

Master's thesis

# Deployment of semi-unsupervised learning in the search for new physics at the LHC with the ATLAS detector

Benchmarking autoencoders for anomaly detection at the LHC with the ATLAS detector

**Sakarias Garcia de Presno Frette**

Computational Science: Physics  
60 ECTS study points

Department of Physics  
Faculty of Mathematics and Natural Sciences

11th May 2023





**Sakarias Garcia de Presno Frette**

**Deployment of semi-unsupervised learning  
in the search for new physics at the LHC  
with the ATLAS detector**

Benchmarking autoencoders for anomaly detection at the  
LHC with the ATLAS detector

Supervisors:  
Professor Farid Ould-Saada  
Dr. James Catmore



# Abstract

This master thesis investigates the performance and usage of autoencoders in Beyond Standard Model (BSM) searches, using n-tuples from ATLAS that are converted to python dataframe structures. The Rapidity-Mass matrix (RMM) is proposed as the input data features, with 6 b-jets and 6 l-jets, and 5 of each lepton. The goal was to test and understand the performance in the 3 lepton +  $e_T^{miss}$  final state, but due to poor results, the 2 lepton +  $e_T^{miss}$  dataset was used instead. To deal with the large dataset size, megasets were used to conserve the overall distribution in smaller batches. The autoencoders were benchmarked by creating anomalous events by altering the  $p_T$  of standard model events and testing on two supersymmetric signal models. The performance was measured in three categories: reconstruction error, background and signal reduction, and significance when performing cuts. The regular autoencoder performed better in the first and second categories, while the variational autoencoder performed slightly better in the third. Increasing the training data improved the performance in all categories. A blind test with ATLAS data and BSM signals showed that the autoencoder, when trained on the 2 lepton +  $e_T^{miss}$  dataset, managed to separate out some signals from the ATLAS data, indicating its potential use in more rigorous analyses. The thesis also discusses future work and challenges, such as computational bottlenecks, further investigation of the RMM, and better feature engineering.



# Acknowledgments

To be blunt, this exercise is the equivalent of fishing in the dark, with a blindfold on, with a net of an arbitrary size, in an ocean trying to not catch fish, but something else that may or may not look like fish that might or might not be in the ocean.

---

*Sakarias Frette / Spring 2023*

This thesis has been a rollercoaster of a project, with its ups and downs, periods of joy and of mild clinical depression. Nevertheless, it is finally done, my master project. It, like so much in my life could not have been done without help. First, thanks to the No Carbs Company for creating the most delicious and addictive energy drink, the NOCCO. They have served my limbic system well and kept my need for caffeine somewhat at bay. I would also thank Bunnpris at Frederikkes plass for selling them for as long as you did, although I have to pick a bone with you guys about the somewhat axiomatically wrong choice to stop selling them. On the other hand, I enjoyed your warm burgers as well, I guess that makes a bit up for it.

Throughout my education here at the University of Oslo, I have had the pleasure of working with, befriending, and working out with several funny, smart, and close friends. William Hirst, Samir Noor, Anders Vestengen and Mikkel Metzch Jensen, you have all given me five excellent years with a lot of fun. Through difficult exams, long days, deadlines, heavy workouts, fun parties, UFC, Formula 1, movie nights and much, much more we have made some beautiful bonds of friendship that I will cherish forever. This is just the beginning. A special thanks to you William Hirst. It's weird to look back at the fateful day in StoreFy, and then 5 years later, with the same bachelor, same supervisors and almost same thesis subject. We are indeed Knoll and Tott, a nickname I wear proudly. Thanks for an excellent time at uni. I look forward to the many more years to come my good friend.

To my mum and dad, Live and Jarle. You have guided me through thick and thin with your excellent guidance and wisdom. You are what all parents should aspire to be. Loving, just, caring, strict but fair, full of insight and interests in your different offsprings. Dad, your longstanding fascination and curiosity of nature is admirable. Your ability to keep a cool head is envious, and you are very, very funny. You saw a potential within me to pursue the natural sciences. You have always been helpful and supportive with good advice. Thank you for this. Mum, your love knows no boundurries. You have children all over the world, as you should, for it is selfish of us to not share your heart with others. Where the natural sciences have been dad's department, the ways of the heart and soul have been yours. You are what I aspire to be in matters of the heart and soul. This I know for a fact. Thank you both for my upbringing and for the parents you are to me. I am forever in your debt.

To Ern. My lovely girlfriend, training partner and tickle monster. You are inspiring, with your hard work ethics, your ambition and your drive. I would not have thought in October how much time we would spend together, how much fun we have had, and how happy I would be. You keep me on my toes, you push me when I need it, and hugs me when I need it. Truly you are one of a kind. And although I tend to make a face when bug med and poke me, and it hurts a bit, I do actually like it ;). Sometimes. Love you boo.

Finally, to Professor Farid Ould-Saada, Dr. Eirik Gramstad and Dr. James Catmore. Thank you for an exiting and difficult project. It is funny to look back to the first weeks of my masters program and reminisce about how little I actually knew about particle physics, the process of science research, machine learning applications and much more. These past two years have been an education to say the least. The tools I bring with me are credited to you. Thanks for being patient with me, as I know I had a lot of questions. The weekly meetings, the questionnaires, and bugfixing are just some many moments I look back fondly on, and will bring with me. My hope is that my work will help the next masters students. I hope you have had some fun and interesting talks and discoveries with me. Until we meet again.



# Contents

<b>Introduction</b>	<b>1</b>
<b>1 Data Analysis</b>	<b>3</b>
1.1 Anomaly detection	3
1.2 Neural Networks	3
1.3 Autoencoders	8
1.4 Other tools and algorithms	10
<b>2 The Standard Model and Beyond Standard Model physics</b>	<b>13</b>
2.1 Structure and composition of the Standard Model	13
2.2 Beyond Standard Model (BSM) physics	16
<b>3 Implementation</b>	<b>19</b>
3.1 The ATLAS detector	19
3.2 ROOT	23
3.3 Background samples	25
3.4 The dataset features	27
3.5 Code implementation	32
3.6 The chosen neural network architectures	34
3.7 The search strategy	37
<b>4 Results and Discussion</b>	<b>41</b>
4.1 Non signal testing of the regular and variational autoencoder	41
4.2 3 lepton training for high $e_T^{miss}$ and invariant mass search	45
4.3 2 lepton training for high $e_T^{miss}$ and invariant mass search	50
4.4 Blind ATLAS data sample testing	54
4.5 Final remarks on the results	56
4.6 Execute summary	59
4.7 Challenges with the search method and tools	61
4.8 Future work	63
<b>5 Conclusion</b>	<b>67</b>
<b>Conclusion</b>	<b>67</b>
<b>Appendices</b>	<b>71</b>
<b>Appendix A</b>	<b>73</b>
A.1 Channel removal testing	73
A.2 Transverse momentum altering	79
A.3 Reconstruction error cuts for 3 leptons + $e_T^{miss}$	83
A.4 Reconstruction error cuts for 2 leptons + $e_T^{miss}$	99
<b>Appendix B</b>	<b>117</b>
B.1 Algorithmic implementation	117



# List of Figures

1.1	Simple diagram of a neural network	4
1.2	Explaining consequence of choice of learning rate	6
1.3	Conceptual autoencoder	9
1.4	Figure depicting a model for a variational autoencoder. Found 14.01.23 here [1].	10
2.1	The Standard Model	13
2.2	Electron scattering diagram	15
2.3	Muon decay diagram	15
2.4	$q\bar{q}$ collision into lepton pair	16
2.5	gluon-gluon interaction into $t\bar{t}$ production	16
2.6	SUSY feynman diagram	17
3.1	ATLAS detector longitudinal and azimuthal diagrams	19
3.2	Detector tracking of particles	21
3.3	Steps from data collection to physics results	22
3.4	Jet produciton from pp-collisions to detector	23
3.5	RDataFrame code example	24
3.6	C++ function example	25
3.7	Conversion from RDataFrame to NumPy	25
3.8	$t\bar{t}$ production diagram	26
3.9	Higgs production diagram	26
3.10	Zeejets channel diagram	27
3.11	3 lepton + $e_T^{miss}$ Monte Carlo and ATLAS data comparison	29
3.12	2 lepton + $e_T^{miss}$ Monte Carlo and ATLAS data comparison	30
3.13	Functional structure	32
3.14	Sequential structure	33
3.15	Single event RMM plot	34
3.16	Megaset structure diagram	35
3.17	Tensorflow neural network training	35
3.18	AE   Small network architecture	36
3.19	AE   Large network architecture	36
3.20	VAE   Small network architecture	37
3.21	Large variational autoencoder architecture.	37
4.1	AE   Reconstruction error using Higgs channel as signal	41
4.2	AE   Reconstruction error using Singletop channel as signal	42
4.3	AE   Reconstruction error using ttbar channel as signal	42
4.4	VAE   Reconstruction error using Higgs channel as signal	42
4.5	VAE   Reconstruction error using Singletop channel as signal	43
4.6	VAE   Reconstruction error using ttbar channel as signal	43
4.7	AE   Reconstruction error $p_T$ altering of 10	44
4.8	VAE   Reconstruction error $p_T$ altering of 10	44
4.9	3lep deep network   450p300   AE	45
4.10	3lep shallow network   450p300   AE	46
4.11	3lep deep network   800p50   AE	47
4.12	3lep shallow network   800p50   AE	48
4.13	3lep deep network   450p300   VAE	49
4.14	3lep shallow network   450p300   VAE	50

4.15	3lep deep network   800 <p>50   VAE</p>	51
4.16	3lep shallow network   800 <p>50   VAE</p>	52
4.17	2lep deep network   450 <p>300   AE</p>	53
4.18	2lep shallow network   450 <p>300   AE</p>	54
4.19	2lep deep network   800 <p>50   AE</p>	55
4.20	2lep shallow network   800 <p>50   AE</p>	56
4.21	2lep deep network   450 <p>300   VAE</p>	57
4.22	2lep shallow network   450 <p>300   VAE</p>	58
4.23	2lep deep network   800 <p>50   VAE</p>	59
4.24	2lep shallow network   800 <p>50   VAE</p>	60
4.25	Reconstruction error blind test	61
4.26	Reconstruction error unblind test	62
4.27	LHC nominal luminosity projections	63
1	AE   Channel removal, diboson2l, diboson3l, diboson4l	74
2	AE   Channel removal, Wjets, topOther, triboson	75
3	AE   Channel removal, Zeejets, Zmmjets, Zttjets	76
4	VAE   Channel removal, diboson2l, diboson3l, diboson4l	77
5	VAE   Channel removal, Wjets, topOther, triboson	78
6	VAE   Channel removal, Zeejets, Zmmjets, Zttjets	79
7	AE   Reconstruction error $p_T$ altering of 1.5	80
8	AE   Reconstruction error $p_T$ altering of 3	80
9	AE   Reconstruction error $p_T$ altering of 5	81
10	AE   Reconstruction error $p_T$ altering of 7	81
11	VAE   Reconstruction error $p_T$ altering of 1.5	82
12	VAE   Reconstruction error $p_T$ altering of 3	82
13	VAE   Reconstruction error $p_T$ altering of 5	83
14	VAE   Reconstruction error $p_T$ altering of 7	83
15	3lep deep network   450 <p>300   AE   2</p>	84
16	3lep shallow network   450 <p>300   AE   2</p>	85
17	3lep deep network   800 <p>50   AE   2</p>	86
18	3lep shallow network   800 <p>50   AE   2</p>	87
19	3lep deep network   450 <p>300   AE   3</p>	88
20	3lep shallow network   450 <p>300   AE   3</p>	89
21	3lep deep network   800 <p>50   AE   3</p>	90
22	3lep shallow network   800 <p>50   AE   3</p>	91
23	3lep deep network   450 <p>300   VAE   2</p>	92
24	3lep shallow network   450 <p>300   VAE   2</p>	93
25	3lep deep network   800 <p>50   VAE   2</p>	94
26	3lep shallow network   800 <p>50   VAE   2</p>	95
27	3lep deep network   450 <p>300   VAE   3</p>	96
28	3lep shallow network   450 <p>300   VAE   3</p>	97
29	3lep deep network   800 <p>50   VAE   3</p>	98
30	3lep shallow network   800 <p>50   VAE   3</p>	99
31	2lep deep network   450 <p>300   AE   2</p>	100
32	2lep shallow network   450 <p>300   AE   2</p>	101
33	2lep deep network   800 <p>50   AE   2</p>	102
34	2lep shallow network   800 <p>50   AE   2</p>	103
35	2lep deep network   450 <p>300   AE   3</p>	104
36	2lep shallow network   450 <p>300   AE   3</p>	105
37	2lep deep network   800 <p>50   AE   3</p>	106
38	2lep shallow network   800 <p>50   AE   3</p>	107
39	2lep deep network   450 <p>300   VAE   2</p>	108
40	2lep shallow network   450 <p>300   VAE   2</p>	109
41	2lep deep network   800 <p>50   VAE   2</p>	110
42	2lep shallow network   800 <p>50   VAE   2</p>	111
43	2lep deep network   450 <p>300   VAE   3</p>	112
44	2lep shallow network   450 <p>300   VAE   3</p>	113
45	2lep deep network   800 <p>50   VAE   3</p>	114

46 2lep shallow network | 800 $p_{\text{50}}$  | VAE | 3

115



# List of Tables

1.1	Neural network notation	5
2.1	Table showing properties of all the fermions, including name, symbol, antiparticle, spin, charge, generation and mass. The masses were found here [2] and [3].	14
3.1	SM MC channels	26
3.2	2015 triggers table	31
3.3	2016 triggers table	31
3.4	2017 triggers table	31
3.5	2018 triggers table	31
4.1	Executive summary table	60



# Introduction

Not only is the Universe stranger than we think, it is stranger than we can think.

---

*Werner Heisenberg*[4]

So goes the quote by Werner Heisenberg, acclaimed for his work in quantum physics in the early to mid 20th century. The quote is a reminder and a statement of the fact that the world we live in is immensely strange, beautiful, complex and interesting. From the fundamental particles to the largest galaxy clusters, the universe is a place of wonder and mystery. It is perhaps easy to forget what science tries to do when studying nature. Its fundamental duty is to model the universe as well as possible given the tools available. These models get better over time, but unlike what scientific absolutists might think and argue for, we will never know the whole truth. One should always remember Heisenberg's quote, for it illustrates the very point that nature is indeed stranger than we can think. Science with its predictive power is only an approximation, one can never truly know if the model we have of nature is a hyperfitted model or the actual instruction manual for nature itself.

As physicists, we develop and extend, replace and debunk models at the most fundamental level of nature, one of which is the Standard Model (SM) of particle physics. At higher energies, it is the most accurate, experimentally tested theory to date, only rivalled by general relativity. From the 1930s to around 1973, there were huge leaps within the field of particle physics. Even then, the SM leaves several important questions unaddressed. Dark matter, dark energy and the energy density are phenomena that we observe around us but cannot be answered by the SM. Attempts have been made to create theoretical frameworks that could extend the SM with the strange behavior, but all have yet to be experimentally verified. One could ask oneself why this is the case. Why is this New Physics, what ever it may look like, so difficult to find? Is the framework wrong? Are the theories not well enough understood or wrong? Or it could be that the New Physics is hiding within the data already collected, in some set of features, too subtle for traditional analysis techniques, but available through advanced data analysis tools? The answer is, perhaps not to anyone's shock, we have no idea. In fact, they may all be true or false.

This story does not end here, as there are countless departments all over the world searching for this New Physics. The ATLAS experiment at CERN is one organization that has taken upon itself this task, including my supervisors Professor Farid Ould-Saada and Dr. James Catmore working on searches for New Physics at the University of Oslo. This thesis will take a somewhat different search approach than conventional analyses done at ATLAS. In a humble attempt, the assumption is made that if the New Physics exist, it is too subtle for existing analysis techniques, and that it is hiding in the data in some set of features. Further, it is assumed that by focusing on data we can label and that we know from experiment to exist, deviations from this would be of interest for more narrow searches. The hope is to filter out the events of interest, that with some certainty differs from the established theory, and then try to understand them better.

In the last decade, data analysis tools such as neural networks have become more and more available to the public, getting optimized, upgraded and extended more computationally powerful every day. Google's Tensorflow[5] and Facebook's PyTorch[6] are two increasingly popular frameworks that are used within industry, academia, and even within the particle physics community. Tensorflow was chosen for this thesis, and all the neural networks are using this framework, together with several other third party pieces of software.

## Outline of the Thesis

The master thesis is outlined in the following way. The first two chapters are dedicated to machine learning and SM physics background required to understand the analysis done and tools used in the thesis. The third chapter goes through the implementation of the project, the input dataset, the ATLAS architecture, the programming libraries and feature choice. Chapter four goes through the results from the implementation as

well as discussion and interpretation of the results, the pros and cons of the implementation, aspects for future improvement, and other thoughts around the process. The final chapter is dedicated to the conclusion, where the results are summarized.

# Chapter 1

## Data Analysis

### 1.1 Anomaly detection

Anomaly detection is a versatile tool that finds application in a diverse range of scenarios, including fraud detection, anomalous sensor data analysis and time series data. The primary objective of this tool is to identify data that deviates from a predetermined standard of normal behavior. The definition of this standard can vary from situation to situation, based on the context and the expected anomalous behavior. According to Chandola, Banerjee, and Kumar [7], anomalies can be classified into three categories: *point anomalies*, *contextual anomalies*, and *collective anomalies*. *Point anomalies* represent singular or few outliers from a larger group or context and can occur in various situations. A notable example of a point anomaly is Michael Phelps, who is able to swim intensively for longer periods due to his body producing less lactic acid. *Contextual anomalies*, on the other hand, are determined based on the context of the anomaly and data, rather than as a whole. For instance, in the case of continuous gas flow data, a sudden change in flow on a Saturday, despite being within the range of Friday's flow, could be categorized as a contextual anomaly. The third type, *collective anomalies*, represents a group of anomalies that deviate from the expected behavior of the dataset. In particle physics experiments, collective anomalies are of particular interest as there are many sources of anomalous behavior where only collective anomalies are worth investigating. A single anomalous event in the detector could be explained by electronic noise, a cosmic ray or radioactive decay. Additionally, the noise generated by numerous components in such experiments makes it essential to consider collective anomalies.

### 1.2 Neural Networks

In the field of machine learning, statistical algorithms are commonly used for data analysis. Neural networks, a specific category of such algorithms, have experienced growth in usage in both industry and academia over the past decade. Although most of the theory behind it was developed as far back as the 1980s, the technology has only now in the last 10 to 15 years become good enough. These statistical models are of extensive use in a variety of applications, ranging from image analysis to weather prediction.

The fundamental principle behind feed forward neural networks (FFNN) involves the data being fed forward through the network, with the end output evaluated and corrections then back propagated through the network to update the weights and biases. This training process is repeated until a certain threshold is met. Figure 1.1 shows a general layout of a neural network, wherein the input layer consists of one node per feature in the dataset. The number of hidden layers and nodes per layer can be fine-tuned, with the last hidden layer connected to the output layer. The latter is determined by the problem being addressed, and in the case of the binary classification problem shown in figure 1.1, the nodes interact via tunable weights  $w$  and biases  $b$  that must be trained on the dataset prior to making predictions. The neural network, especially deep<sup>1</sup> ones become black boxes, meaning that once the training data or the test data is fed in through the input layer it is hard to know exactly what happens with the data until it comes out as a prediction. It is because of this that some<sup>2</sup> have shown some hesitancy with using neural networks for problems of high importance. Nonetheless, they can be very effective if used correctly.

<sup>1</sup>Deep here refers to a neural network with more than one hidden layer, and often also a network where the layers have many neurons. One example would be a network with say a 200 - 500 - 500 - 700 - 500 - 200 - 1 network where the numbers correspond to number of nodes in their layers.

<sup>2</sup>In cases where a lot of money is at stake or lives are dependent on the output and performance of the neural network, it is reasonable to expect some explainability from the engineers if something goes wrong. There are other algorithms that are less

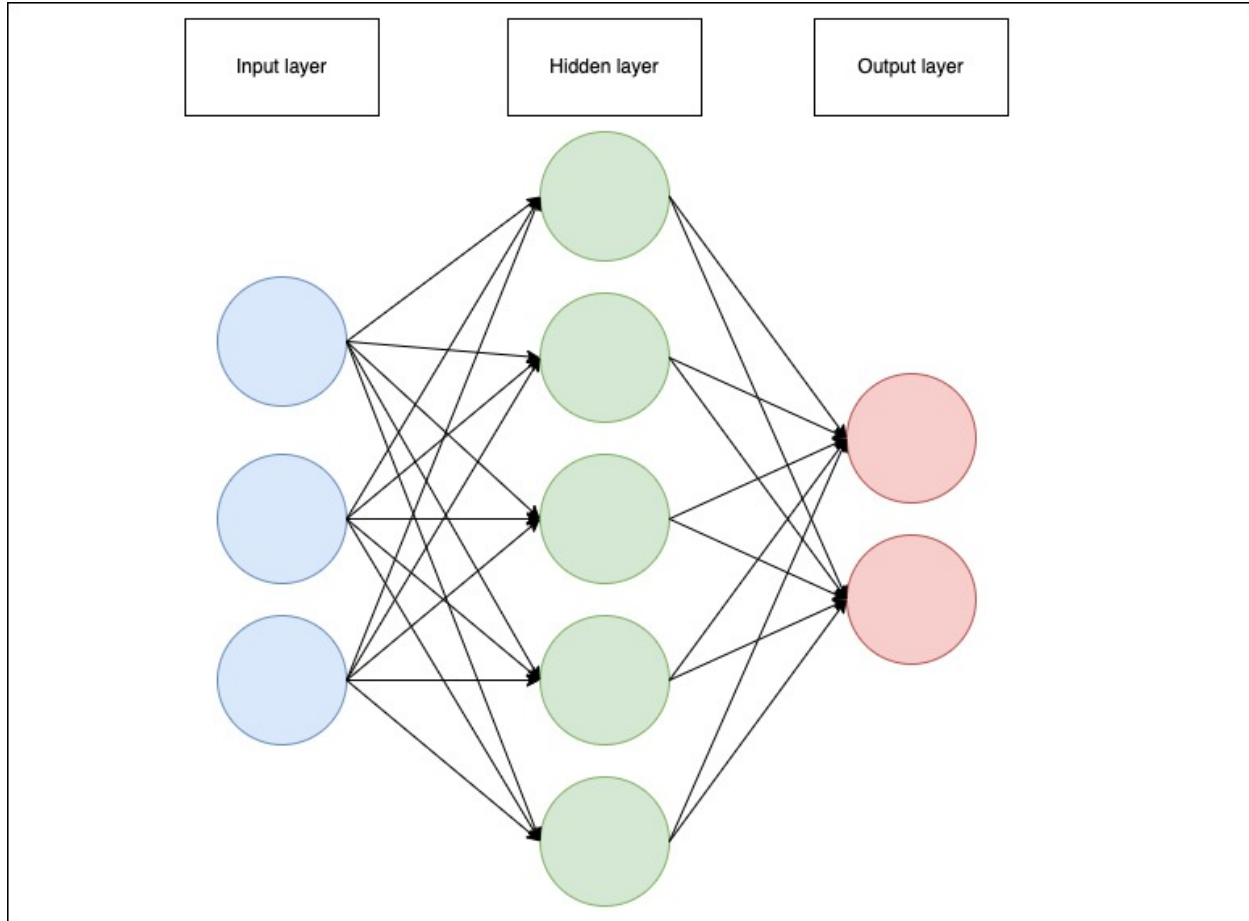


**Figure 1.1:** Simple neural network diagram drawn using Draw.io. Here the blue dots constitute the input layer, the green dots constitute the hidden layer, and the red dots constitute the output layer. The arrows show the connections between the nodes.

In order to avoid confusion, we will adhere to table 1.1 for the notation used in the following sections. Some of the following subsections contain work previously done by myself and two co-students, and can be found here[10].

## Gradient descent

Let us now consider a general n-dimensional problem, with parameters  $\boldsymbol{\theta} = \{\theta_1, \theta_2, \dots, \theta_n\}$ . Our objective is to find the set of  $\boldsymbol{\theta}$  that minimize a cost function with respect to the data and target. One way to solve this problem is using ordinary least squares. For this approach, the optimal parameters  $\boldsymbol{\theta}_{opt}$  are derived from minimizing the cost function, as shown here:

$$\boldsymbol{\theta}_{opt} = (\mathbf{X}^T \mathbf{X})^{-1} \mathbf{X}^T \mathbf{t},$$

where  $\mathbf{X}$  is the design matrix containing the data, and  $\mathbf{t}$  is the target vector. This could however lead to a problem. Suppose the design matrix is sufficiently large, then the matrix inversion will get computationally expensive, or it might not even exist for a given  $\mathbf{X}$ . Thus, an alternative approach is to iteratively approximate the ideal parameters  $\boldsymbol{\theta}_{opt}$ .

Suppose we have a cost function  $C(\boldsymbol{\theta})$  for a given problem. We can approximate the minimum of the cost function by calculating the gradient  $\nabla_{\boldsymbol{\theta}} C$  with respect to  $\boldsymbol{\theta}$ . The negative of this gradient indicates the direction for the minimum of  $C$  when evaluating it in a specific point  $\boldsymbol{\theta}_i$  in the parameter space [10]. This is expressed as follows

$$\boldsymbol{\theta}_{i+1} = \boldsymbol{\theta}_i - \eta \nabla_{\boldsymbol{\theta}} C(\boldsymbol{\theta}_i), \quad (1.1)$$

---

"black box" machines, such as decision trees[8] or support vector machines[9], both of which have their pros and cons compared to neural networks.

Matrices and vectors		
Notation	Description	Type
$X$	Design Matrix (input data).	$\mathbb{R}^{N \times \# \text{features}}$
$t$	Target values.	$\mathbb{R}^{N \times \# \text{categories}}$
$y$	Model output, the prediction from our network.	$\mathbb{R}^{N \times \# \text{categories}}$
$W^l$	The weight matrix associated with layer $l$ which handles the connections between layer $l - 1$ and $l$ .	$\mathbb{R}^{n_{l-1} \times n_l}$
$B^l$	The bias vector associated with layer $l$ which handles the biases for all nodes in layer $l$ .	$\mathbb{R}^{n_l \times 1}$
Elements		
$w_{ij}^l$	The weight connecting node $i$ in layer $l - 1$ to node $j$ in layer $l$ .	$\mathbb{R}$
$b_j^l$	Bias acting on node $j$ in layer $l$ .	$\mathbb{R}$
$z_j^l$	Node output before activation on node $j$ on layer $l$ .	$\mathbb{R}$
$a_j^l$	Activated node output on node $j$ on layer $l$ .	$\mathbb{R}$
Functions		
$C$	Cost function.	
$\sigma^l$	Activation function associated with layer $l$ .	
Quantities		
$n_l$	The number of nodes in layer $l$ .	
$L$	Number of layers in total with $L - 2$ hidden layers.	
$N$	Total number of data points.	
All indexing starts from 1: $i, j, k, l = 1, 2, \dots$		

**Table 1.1:** Table containing notation used for deriving the mathematical formulas for the neural network found in previous work[10]. The # here refers to number of.

where  $\eta$  is a step size, also called the learning rate. The choice of  $\eta$  is not a trivial case. It is one of several hyperparameters[11] that can be altered, and that highly depend on the given problem. With regard to the learning rate, there are only three situations to consider, shown in figure 1.2.

Figure 1.2 visualizes the relation between the learning rate and the cost function. In the left most figure we note that the learning rate is too small. This leads to many iterations before you reach a minimum. In the rightmost figure we note that the learning rate is too high, and the result is that we get divergent behavior. Thus, the goal is to find the optimal learning rate, shown in the middle figure. There are several algorithms that try to do what is shown in the middle figure above, one of which is Adaptive Moment Estimation (ADAM)[12].

A modified and preferred version of gradient descent is the so-called stochastic gradient descent. Regular gradient descent can, for large datasets be quite slow, and is prone to getting stuck in a local minimum. To

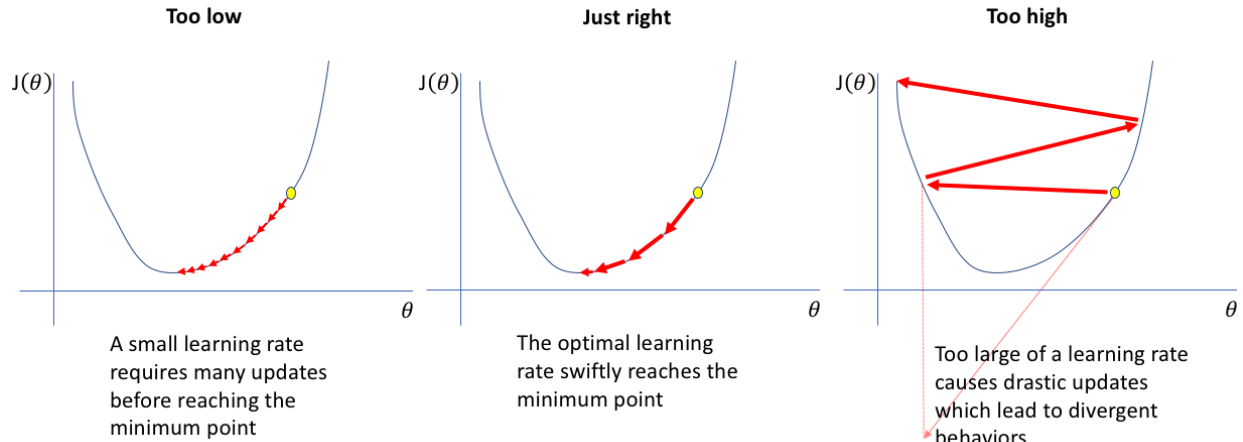


**Figure 1.2:** Figures showing different choices of learning rate for a given cost function, with respect to the tunable parameters. Source: [Jeremy Jordan](#), accessed 03.10.22.

circumvent this issue, mini batches are introduced. For each epoch (training step) the input data is divided into  $M$  mini batches of size  $m$ . For each batch we compute the gradient and update the unknown parameter according to equation 1.1. The parameter  $\theta_{i+1}$  is then updated  $M$  times for each epoch. This will reduce computation time as well as reduce the risk of getting stuck in local minima. [10].

## Feed forwarding

Inference (prediction) and training both use the same feed-forward algorithm. Let's then assume that we have generated a network. The network initializes the weights and biases usually with normal or uniformly distributed values, that can later be adjusted. The procedure is to send the data through the network, weighting each connection according to the neural network's architecture, and produce an output. The procedure can be summarized in the following steps[10]:

- The data is received by the input nodes in the network for each feature.
- Each input node weights the data value according to the connection of each node in the next layer.
- Every node in the hidden layers sums the weighted data values and adds the bias associated to the given node. The resulting number is denoted as  $z$ .
- This value  $z$  is then sent through an activation function  $\sigma$ , which produces the output of the node, denoted as  $a = \sigma(z)$ .
- This process is repeated for each hidden layer, and it is important to note that the number of nodes in the hidden layers is not dependent on the number of features in the original dataset.
- The last hidden layer then sends the activated values to the output layer, where the number of nodes and choice of activation function depends on the problem to solve.

Mathematically this is expressed as follows:

$$z_j^l = \sum_{i=1}^{n_{l-1}} w_{ij}^l a_i^{l-1} + b_j^l, \quad a_j^l = \sigma^l(z_j^l), \quad (1.2)$$

where  $l$  is the layer index,  $j$  is the node index, and  $i$  is the index of the node in the previous layer, and  $l \neq 1$ , as it is not used on the input layer.

## Backpropagation

The way neural networks learn is conventionally by the use of the backpropagation algorithm, first proposed by Rumelhart et al[13]. This is a bit misleading, as the backpropagation algorithm actually only refers to how to compute the gradient with respect to the weights at each unit[11]. The algorithm allows us to alter the weights and biases such that we get an ideal output. Assuming a cost function  $C$ , we can calculate the

gradient  $\nabla_{w,b}C$ , and use this to back propagate the error correction from the last to the first layer. The gradient  $\nabla_{w,b}C$  comprises two derivatives.

$$\nabla_{w,b}C = \left( \frac{\partial C}{\partial w_{i,j}^l}, \frac{\partial C}{\partial b_j^l} \right).$$

We have to use the chain rule to calculate the derivatives, and using that the last layer is  $l = L$ , we get the derivative with respect to the weights as

$$\frac{\partial C}{\partial w_{i,j}^L} = \frac{\partial C}{\partial a_j^L} \frac{\partial a_j^L}{\partial z_j^L} \frac{\partial z_j^L}{\partial w_{i,j}^L},$$

where

$$a_j^L = \sigma(z_j^L), \quad z_j^L = \sum_{i=1}^{n_L-1} w_{i,j}^L a_i^{L-1} + b_j^L.$$

This then gives us

$$\frac{\partial C}{\partial w_{i,j}^L} = \frac{\partial C}{\partial a_j^L} \sigma'(z_j^L) a_i^{L-1},$$

where we defined that

$$\sigma'(z_j^L) = \frac{\partial a_j^L}{\partial z_j^L}. \quad (1.3)$$

This derivative is very easy to calculate given a specific cost function and activation function. The derivative with respect to the bias is given as follows:

$$\frac{\partial C}{\partial b_j^L} = \frac{\partial C}{\partial a_j^L} \frac{\partial a_j^L}{\partial z_j^L} \frac{\partial z_j^L}{\partial b_j^L},$$

which gives us the final expression as

$$\frac{\partial C}{\partial b_j^L} = \frac{\partial C}{\partial a_j^L} \sigma'(z_j^L).$$

We will now introduce a new notation, a local gradient commonly called the "error". It reflects how the rate of change of the cost function depends on the  $j$ 'th node in the  $l$ 'th layer.

$$\delta_j^l \equiv \frac{\partial C}{\partial z_j^l}.$$

Using this we get the following expression:

$$\delta_j^L = \frac{\partial C}{\partial z_j^L} = \frac{\partial C}{\partial a_j^L} \frac{\partial a_j^L}{\partial z_j^L} = \frac{\partial C}{\partial a_j^L} \sigma'(z_j^L),$$

giving us the more compact forms of the derivatives with respect to the weights and biases:

$$\frac{\partial C}{\partial w_{i,j}^L} = \delta_j^L a_i^{L-1}, \quad \frac{\partial C}{\partial b_j^L} = \delta_j^L.$$

We can now let  $\boldsymbol{\delta}^l$  be the vector of all the errors in the  $l$ 'th layer, and  $\boldsymbol{\delta}^L$  be the vector of all the errors in the last layer. The error in the  $l$ 'th layer can then be expressed as a matrix equation for the last layer as follows:

$$\boldsymbol{\delta}^l = \nabla_a C \odot \frac{\partial \sigma}{\partial z^l}, \quad \nabla_a C = \left[ \frac{\partial C}{\partial a_1^L}, \frac{\partial C}{\partial a_2^L}, \dots, \frac{\partial C}{\partial a_{n_L}^L} \right]^T.$$

Here  $\odot$  is the Hadamard product (element wise product). This local gradient can now be defined recursively for the  $j$ 'th node in a layer  $l$  as a function of the local error in the next layer:

$$\delta_j^l \equiv \frac{\partial C}{\partial z_j^l} = \sum_k \frac{\partial C}{\partial z_k^{l+1}} \frac{\partial z_k^{l+1}}{\partial z_j^l} = \sum_k \frac{\partial z_k^{l+1}}{\partial z_j^l} \delta_k^{l+1}. \quad (1.4)$$

We also note that

$$z_k^{l+1} = \sum_{j=1}^{n_l} w_{j,k}^{l+1} a_j^l + b_k^{l+1} = \sum_{j=1}^{n_l} w_{j,k}^{l+1} \sigma(z_j^l) + b_k^{l+1},$$

thus the partial derivative is given as

$$\frac{\partial z_k^{l+1}}{\partial z_j^l} = w_{j,k}^{l+1} \sigma'(z_j^l), \quad (1.5)$$

using the substitution from equation 1.3. This allows us to substitute equation 1.5 into equation 1.4 to get the following expression:

$$\delta_j^l = \sum_k w_{j,k}^{l+1} \sigma'(z_j^l) \delta_k^{l+1}. \quad (1.6)$$

Using this, we can derive a three-step formula for the backpropagation algorithm:

- Compute the local gradient for the last layer,  $\delta^L$ .
- Recursively compute the local gradient for the remaining layers,  $\delta^l$  for  $l = L - 1, L - 2, \dots, 1$ .
- Update the weights and biases via gradient descent<sup>3</sup> for all layers,  $l = 1, 2, \dots, L$ , given the learning rate  $\eta$  as shown below:

$$\begin{aligned} w_{i,j}^l &\leftarrow w_{i,j}^l - \eta \delta_j^l a_i^{l-1}, \\ b_j^l &\leftarrow b_j^l - \eta \delta_j^l. \end{aligned}$$

### 1.3 Autoencoders

Autoencoders are a subset of neural networks. Whereas a general neural network in principle can take any shape, autoencoders are more restrictive. This restrictiveness can in its most general sense be condensed into the following points:

- Same number of output categories as input categories
- A latent space with smaller dimensionality than the input/output layer
- The autoencoders are trained on their own input, using reconstruction as metric

What we end up with are two funnel shaped parts linked together. The two funnels are called the encoder (left funnel) and decoder (right funnel) respectively. This architecture is not accidental, but rather designed with a very specific solution of problems in mind, namely reconstruction. A good example to illustrate this is image reconstruction, illustrated in figure 1.3. Suppose you have an image, and want to reconstruct it. By feeding the encoder an image, and comparing the decoder output to the actual image, the autoencoder can tune itself to recreate the image it trained on.

#### Regular autoencoder

Mathematically the regular autoencoder is represented according to reference [1]. Using the annotations of each component in figure 1.3 the decoded information is defined as follows

$$\mathbf{z} = \mathbf{g}_\phi(\mathbf{x}),$$

and the reconstruction given as

$$\mathbf{x}' = \mathbf{f}_\theta(\mathbf{g}_\phi(\mathbf{x})).$$

To achieve  $(\phi, \theta)$  are the tuneable parameters adjusted according to the loss function. In our case, the goal is reconstruction without copying<sup>4</sup>, thus we can use the mean squared error (MSE), given as

$$L_{AE}(\phi, \theta) = \frac{1}{N} \sum_{i=0}^{N-1} (\mathbf{x}^i - \mathbf{f}_\theta(\mathbf{g}_\phi(\mathbf{x}^i)))^2. \quad (1.7)$$

---

<sup>3</sup>In practice one would use gradient descent with an optimizer, such as ADAgrad or ADAM as mentioned in section 1.4

<sup>4</sup>In some cases one can train the autoencoder to learn the identity matrix, which leads to reconstruction by copying, not training.

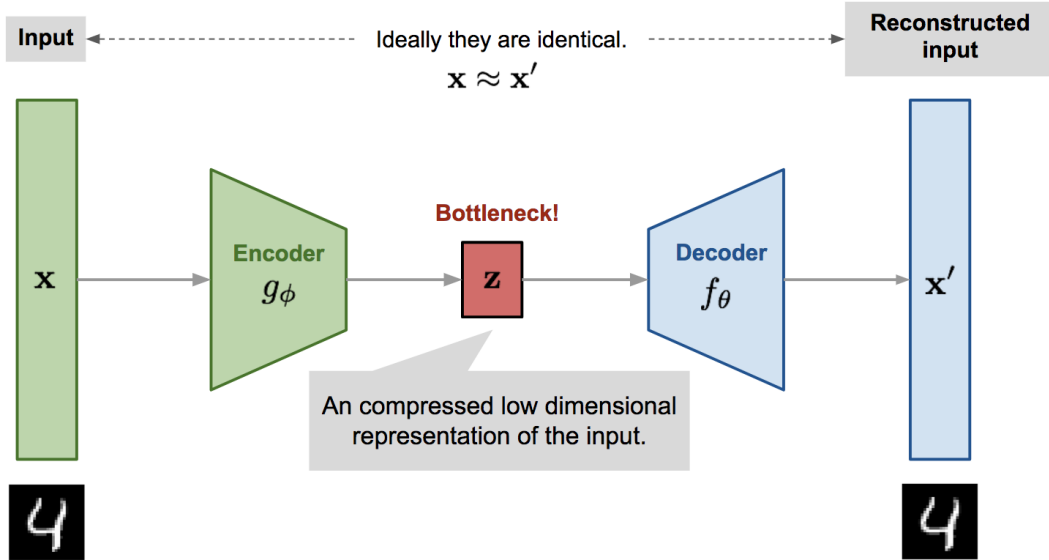


**Figure 1.3:** Figure depicting a model for an autoencoder. Here the input  $\mathbf{x}$  is the original image,  $\mathbf{x}'$  is a reconstructed version of  $\mathbf{x}$ ,  $g_\phi$  is the encoder,  $f_\theta$  is the decoder, and  $\mathbf{z}$  is the latent space. The term bottleneck here only refers to the fact that the latent space have fewer nodes than the two funnels on either side. Found 14.01.23 at [lilianweng.github.io](https://lilianweng.github.io) [1].

### Variational autoencoders

Another popular method for reconstruction is the so-called variational autoencoder. The work by Kingman and Welling [14] showed how one can use the variational bayesian approach for efficient approximate posterior inference, leading to the use of variational autoencoders. Here, contrary to regular autoencoders, the latent space is a distribution that can be sampled from. In the context of reconstruction, this means that we want to create a latent space distribution based on the true distribution in the data, and use this latent space distribution to then generate data given that latent space.

The variational autoencoder contains two neural networks. The generative model  $p_\theta(x|z)$  is the decoder of the network and  $q_\phi(z|x)$  is the encoder. One of the ways a variational autoencoder learns is through the Kullback-Leibler (KL) divergence[15]. The KL divergence is a measure of how one probability distribution is different from a second reference propability distribution, and is related to the cost function via the marginal likelihood

$$\log p_\theta(x^{(i)}) = D_{KL}(q_\phi(z|x^{(i)})||p_\theta(z|x^{(i)})) + \mathcal{L}(\theta, \phi; x^{(i)}). \quad (1.8)$$

Under certain conditions[14] the KL divergence can be computed analytically, and it can then be showed[14] that the variational approximate posterior is:

$$\mathcal{L}(\theta, \phi; x^{(i)}) \simeq \frac{1}{2} \sum_{j=1}^J \left( 1 + \log((\sigma_j^{(i)})^2) - (\mu_j^{(i)})^2 - (\sigma_j^{(i)})^2 \right) + \frac{1}{L} \sum_{l=1}^L \log p_\theta(x^{(i)}|z^{(i,l)}), \quad (1.9)$$

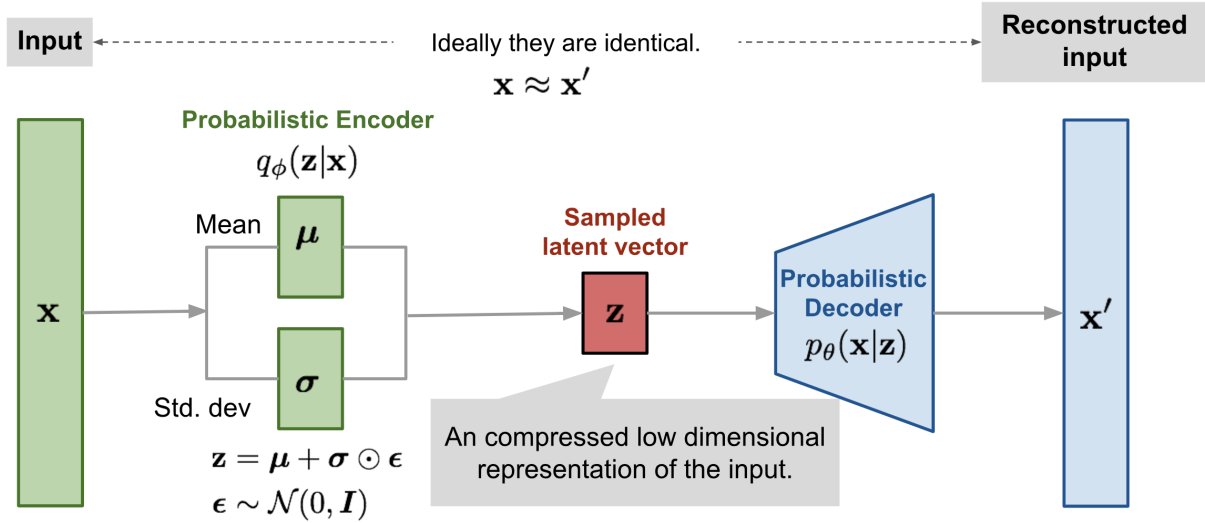
where  $z^{(i,l)} = \mu^{(i)} + \sigma^{(i)} \odot \epsilon^{(l)}$  and  $\epsilon^{(l)} \sim \mathcal{N}(0, I)$ .  $\odot$  is the elementwise product, and  $\mathcal{N}(0, I)$  is a normal distribution with the identity as variance.  $\mathcal{L}(\theta, \phi; x^{(i)})$  is then the cost function for the variational autoencoder.

Figure 1.4 is a graphical representation of a variational autoencoder. The encoder produces a mean and a standard deviation based on the input data, which then produce a latent space distribution from which the decoder can sample and produce an output.

### Inference

As with the cost function for the autoencoder, the inference evaluation is also done by reconstruction. To look for anomalies in the data, the reconstruction error will span a range of values, where the lower end represents events that the autoencoder reconstructed well. The reconstruction error used in the analysis is defined in equation 1.10

$$err = \log_{10} \left[ \sum_i (x_i - \tilde{x}_i)^2 \right], \quad (1.10)$$



**Figure 1.4:** Figure depicting a model for a variational autoencoder. Found 14.01.23 [here \[1\]](#).

where  $x$  is the input data and  $\tilde{x}$  is the output from inference. The distributions produced from the reconstruction error is key to analyse the performance of the autoencoders.

## 1.4 Other tools and algorithms

### Adaptable moment estimation (ADAM) Optimizer

Stochastic gradient descent, though very useful, lack the ability to adapt to the feature space. One algorithm that address this issue is the ADAM optimizer[12]. The Adaptable Moment Estimation (ADAM) algorithm uses stochastic gradient descent, but with an adaptive learning rate. This learning rate is adjusted by calculating estimates for the first and second moment<sup>5</sup>. Thus, a large gradient would indicate proximity to a minimum in feature space, thus a lower learning rate would yield a more accurate result. A small gradient would suggest far proximity to a local minimum, and thus a larger learning rate would increase the chance of approaching a minimum.

### Activation functions

Several activation functions are used in neural networks, and how one chooses the best combination for a given problem is not trivial. This often leads to the use of tuning. In bulletlist 1.4 we have the activation functions used in this thesis, and their mathematical definitions.

1.  $\text{sigmoid}(x) = \frac{1}{1+e^{-x}}$
2.  $\tanh(x) = \frac{e^x - e^{-x}}{e^x + e^{-x}}$
3.  $\text{ReLU}(x) = \max(0, x)$
4.  $\text{LeakyReLU}(\alpha, x) = \max(\alpha x, x)$
5.  $\text{Softmax}(x_j) = \frac{e^{x_j}}{\sum_{i=1}^n e^{x_i}}$
6.  $\text{Linear}(x) = x$

<sup>5</sup>In statistics the first moment is the expectation value for a distribution,  $E[X - \mu]$ . The second moment is the expectation value of the distribution squared, i.e the variance,  $E[(X - \mu)^2]$

### Statistical significance

In the frequentist statistics, the Poisson distribution can be approximated with a Gaussian distribution in the limit of large number of events[16]. The expression for the expected significance is given then as

$$Z = \frac{s}{\sqrt{b}}, \quad (1.11)$$

where  $s$  is the amount of signal, and  $b$  is the amount of background. For low statistics we have that the significance is given as

$$Z = \sqrt{2 \left[ (s + b) \ln \left( 1 + \frac{s}{b} \right) - s \right]}. \quad (1.12)$$

It can be shown that in the limit where  $s \ll b$ , the two expressions are approximately the same[16].



## Chapter 2

# The Standard Model and Beyond Standard Model physics

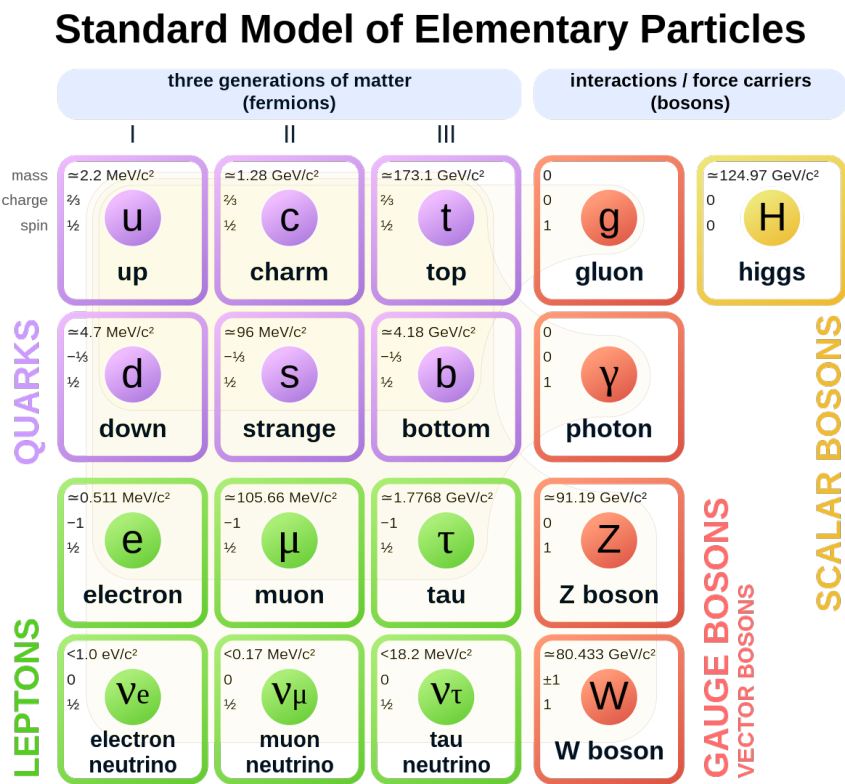


Figure 2.1: The SM of elementary particles. Source [here](#). Accessed 07.10.22

## 2.1 Structure and composition of the Standard Model

This section will briefly describe the Standard Model (SM) in a phenomenological way, as the mathematics and physical reasoning behind the theory is not of great importance to understand the work, results and discussions in this thesis. For a more technical explanation, see (Pich, 2008)[17] for a well written paper containing some more SM fundamentals as well as summarizing the experimental status regarding the SM. For more mathematical understanding of the SM, Peskin and Schroeder's "An introduction to Quantum Field theory" (Peskin and Schroeder, 1995)[18] is highly recommended. Finally, see Thomson's "Modern Particle physics" (Thomson, 2013) [19] for a very comprehensive and up-to-date book that is easy to read and understand.

The SM is to physicists what the periodic table is to chemists, and is to this day the most fundamental description of matter as we know it at the subatomic scale. It comprises two parent class particles, fermions with half integer spin and bosons with full integer spin. The model contains 6 leptons, 6 quarks, coming in 3 colors each, 4 gauge bosons mediating the electroweak interactions ( $\gamma, W^\pm, Z^0$ ), 8 gluons behind the strong interaction and one scalar Higgs boson explaining particle masses, all of which are shown in figure 2.1 together with some quantum numbers.

## Fermions

The fermions are the building blocks of matter, and contain two types of particles, leptons and quarks. The up and down quarks form protons and neutrons, which together with electrons form the atoms. Fermions, unlike bosons, are spin half particles. The fermions are grouped into three so-called families:

$$\begin{bmatrix} \nu_e & u \\ e^- & d' \end{bmatrix}, \quad \begin{bmatrix} \nu_\mu & c \\ \mu^- & s' \end{bmatrix}, \quad \begin{bmatrix} \nu_\tau & t \\ \tau^- & b' \end{bmatrix}$$

The left column contains the leptons whilst the right column contains the quarks. Within the left column, the subscripted  $\nu$  denotes what kind of neutrino that corresponds to the given lepton<sup>6</sup>. Here, the first family consists of the electron, the electron neutrino, the up and down quarks. The second family consists of the muon and the muon neutrino, the charm and strange quarks. The third family consists of the tau and the tau neutrino, the top and bottom quarks. The masses of these particles increases for each particle in the matrix as the family number increases, i.e. the muon is heavier than the electron, and the tau is heavier than the muon, and so on for the other charged fermions. It is not known whether or not the neutrinos follow this pattern as well due to their very low mass. Below is a table with specific properties of the fermions.

Generation	Name	Symbol	Antiparticle	Spin	Charge	Mass (MeV/c <sup>2</sup> )
<b>Quarks</b>						
1	up	u	$\bar{u}$	1/2	2/3	$2.2^{+0.6}_{-0.4}$
	down	d	$\bar{d}$	1/2	-1/3	$4.6^{+0.5}_{-0.4}$
2	charm	c	$\bar{c}$	1/2	2/3	$1280 \pm 30$
	strange	s	$\bar{s}$	1/2	-1/3	$96^{+8}_{-4}$
3	top	t	$\bar{t}$	1/2	2/3	$172100 \pm 600$
	bottom	b	$\bar{b}$	1/2	-1/3	$4180^{+40}_{-30}$
<b>Leptons</b>						
1	electron	$e^-$	$\bar{e}^-$	1/2	-1	0.511
	electron neutrino	$\nu_e$	$\bar{\nu}_e$	1/2	0	$< 9 \cdot 10^{-7}$
2	muon	$\mu^-$	$\bar{\mu}^-$	1/2	-1	105.7
	muon neutrino	$\nu_\mu$	$\bar{\nu}_\mu$	1/2	0	$< 0.170$
3	tau	$\tau^-$	$\bar{\tau}^-$	1/2	-1	$1776.86 \pm 0.12$
	tau neutrino	$\nu_\tau$	$\bar{\nu}_\tau$	1/2	0	$< 15.5$

**Table 2.1:** Table showing properties of all the fermions, including name, symbol, antiparticle, spin, charge, generation and mass. The masses were found here [2] and [3].

Another mystery regarding the neutrinos is the relation to antiparticles. To each particle corresponds an antiparticle, i.e. for  $l^- \rightarrow l^+$ ,  $q \rightarrow \bar{q}$ , where the antiparticle and particle are different. With neutrinos however it is not known whether the neutrinos and antineutrinos are the same particle  $\nu = \bar{\nu}$  (Majorana neutrino), or if they are different  $\nu \neq \bar{\nu}$  (Dirac neutrino).

Quarks are fractional charge particles, with defined charge of either 2/3 or -1/3, as shown in table 2.1. Among them are the main building blocks of protons and neutrons, the up and down quarks, and are bound by the strong force, the strongest of the four fundamental forces. The force mediator is the gluon. The other half of fermions are the leptons. They are split into the charged leptons (electrons, muons and taus), and the uncharged leptons (neutrinos). The charged leptons can interact via the electroweak force, where the Z, W bosons as well as the photon can be a mediator. Note that the neutrinos can only interact through the weak force.

<sup>6</sup>The d', s', b' weak eigenstates are linear combinations of the mass eigenstates d, s, b.

## Bosons

Bosons are integer number spin particles, with spin 0, 1, 2, .... Within bosons there are so-called elementary bosons, some of which are force carriers or mediators such as the  $W^\pm$ , Z and the photon. The Higgs boson is the only elementary scalar boson, but it is not a force carrier. It is the excitation of the Higgs field which is responsible for providing masses to the fermions via a process called spontaneous symmetry breaking[17]. Other bosons are so-called composite bosons, such as mesons ( $q\bar{q}$ ). Baryons ( $qqq$ ) are fermion particles constructed from half integer spin quarks. Bosons also have antiparticles, where  $(\gamma, g, H^0, Z^0)$  are equal to their respective antiparticle, and the  $W^- \rightarrow W^+$  are not equal.

## Feynman diagrams

A graphical way to understand particle interactions are through Feynman diagrams. Feynman diagrams are drawn based on the Feynman rules for a given Lagrangian[17][20], and each component can be linked to a part in the Lagrangian for the system.

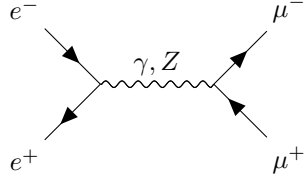


**Figure 2.2:** Feynman diagram of muon pair production from electron annihilation. Here, both Z and  $\gamma$  can work as the propagator.

In figure 2.2 we have a Feynman diagram describing electron-positron annihilation into muon-antimuon pairs. In this thesis, all diagrams will be interpreted from left to right with positive time direction, i.e. figure 2.2. The diagram contains all the components in the Lagrangian, and arrows, curly lines and so on all have their own meaning. A straight line with an arrow usually means a fermion, where the direction of the arrow tells if the particle is a particle (arrow towards the vertex) or an antiparticle (arrow away from the vertex). There is often also a propagator between the left and right side of the Feynman diagram, and they depend on the processes we want to study. In the diagram above we have lepton annihilation, thus we can both have the photon and the Z-boson as a propagator. This process is called a neutral current[17], as the charge is the same before and after the vertex is 0. There are also so-called charged currents, where the charge is different before and after the vertex. Note that we only require charge conservation, thus there is nothing wrong with either having a neutral or a charged current, as long as charge conservation is preserved.

Feynman diagrams are used for both visualizing scatterings, annihilations and decays. An example is provided in figure 2.3.

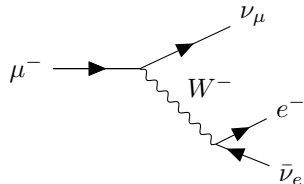


**Figure 2.3:** Muon decay into an electron, an electron neutrino and a muon neutrino via the  $W^-$  boson. Read the graph from left to right.

In figure 2.3 we have a decay of a muon into an electron and two neutrinos through a charged current. The examples above in figure 2.2 and 2.3 show interactions with the electroweak force. Quantum chromodynamics (QCD) is responsible for interactions between quarks and gluons. A strange property of QCD, is that the coupling constant  $\alpha_S$ , contrary to the  $\alpha_{EM}$  for electromagnetism, gets stronger as the distances decreases. This is because QCD (and weak interactions) are based on non-abelian groups[18], thus to study such interactions, one needs to create collisions at very high energies, where  $\alpha_s$  gets small and perturbation theory applies.

### Proton-proton collisions

During an interaction between the protons in proton-proton collisions both the quarks and gluons can interact as shown below:

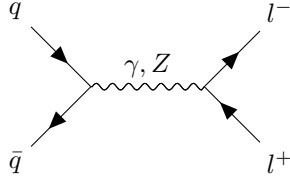


**Figure 2.4:** Proton-proton collision with lepton pair production via the Z boson or photon. Read from left to right.

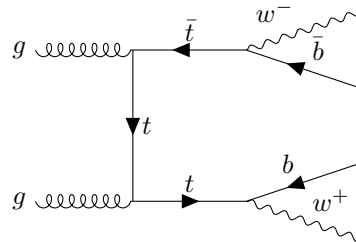


**Figure 2.5:** Proton-proton collision showing the  $t\bar{t}$  channel. Read from left to right.

In figure 2.4 and figure 2.5 we have two examples of Feynman diagrams of possible interactions in proton-proton collisions. Figure 2.4 displays a lepton pair production via the Z boson or photon from quark-antiquark annihilation, and figure 2.5 displays the  $t\bar{t}$  production via gluon-gluon fusion.

### Some limitations

Although the SM has had great success comparing predictions with experiments, there are still several problems not addressed by it. Gravity is one example. The SM as described above cannot incorporate gravity in a quantized way. There are models that try, without success so far, to address this problem, by supplementing the SM. Another problem with the SM is a curious property of the weak interaction, namely that parity is broken. Parity as a mathematical operation is equivalent to the spatial inversion through the origin[19]:

$$x \rightarrow -x. \quad (2.1)$$

In other words, parity can be thought of as left-right symmetry, or mirror symmetry. Breaking of parity is observed in weak currents, where the mediator of the charged currents  $W^\pm$ , only interacts with left-handed fermions and right-handed antifermions. In the SM, neutrinos are assumed to be massless, and the righthanded neutrinos are sterile, i.e. they do not interact in the SM.

This asymmetry is strange, and hints towards new physics that perhaps can restore the parity symmetry at much higher energies. Another note to make is that it has been experimentally verified through observation of neutrino oscillations that the neutrinos are massive. An upper limit on the mass for the anti electron neutrino of  $m_\nu < 0.8 eVc^2$  at 90% confidence level[21]. This is direct experimental evidence that the SM is wrong, as the tiny masses of the neutrinos are not predicted by the SM.

## 2.2 Beyond Standard Model (BSM) physics

The approach of using an autoencoder is an attempt to try and detect BSM physics in an as model agnostic way as possible. This is because there are numerous amounts of possible BSM physics signals some of which could exist in nature. To test the autoencoder two signals from supersymmetry were used. The testing was performed only after having trained on SM only background.

### Supersymmetry

Supersymmetry is a BSM theory that attempts to solve two problems that the SM has. First we have the hierarchy problem. As the SM is a perturbative theory, the Higgs mass increases at higher energies. The

problem is that when you approach higher and higher energies, the Higgs mass goes to infinity, which is not physical. Supersymmetry solves this problem by introducing a supersymmetric partner to each particle in the SM. The result is that the contributions to the Higgs mass from fermions and bosons mainly cancel each other out, thus fixing the hierarchy problem. Another problem we have with the SM is that it does not have a candidate for dark matter, whereas some supersymmetry models have a dark matter candidate. As supersymmetry in theory could solve some problems with the SM it is a topic of great interest with both theoretical and experimental physicists. Still, after two LHC runs supersymmetry has not been observed[22].

To test the autoencoders, two simplified signal models from SUSY were picked up. The chosen signal samples have a final state with 3 leptons +  $e_T^{miss}$ , as the background does. The signal final state is shown below in figure 2.6.

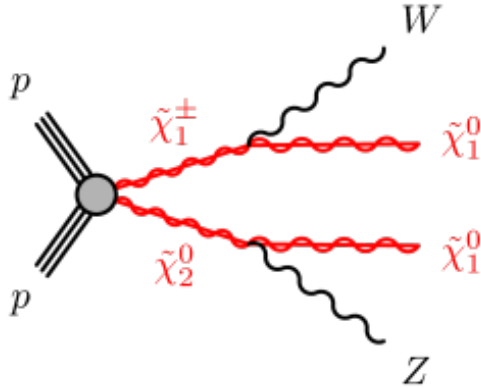


**Figure 2.6:** SUSY diagram showing chargino-neutralino production in proton-proton collision. The test samples we look for with this signal is where the  $W$  and  $Z$  boson decay leptonically.

Figure 2.6 shows chargino( $\tilde{\chi}_2^\pm$ )-neutralino( $\tilde{\chi}_1^0$ ) production via proton-proton collisions. The charginos are the supersymmetric partners to the charged bosons and the neutralinos are the supersymmetric partner of the neutral bosons ( $\gamma, Z^0$ ) and the neutral Higgs bosons ( $h, H^0$ )<sup>7</sup>. The neutralino is the lightest stable supersymmetric particle, and is therefore a good candidate for dark matter. The search for these particles was similarly done by ATLAS in 2021[22].

---

<sup>7</sup>Supersymmetry spontaneous symmetry breaking leads to 5 physical Higgs bosons:  $H^0, h^0, A^0, H^\pm$



# Chapter 3

## Implementation

This section contains the implementation of the analysis. It provides a description of the ATLAS detector, the data collection and event selection, feature engineering, machine learning setup, search strategy and testing setup.

### 3.1 The ATLAS detector

The ATLAS detector comprises several main components for recording proton-proton collisions. Amongst them are the muon detectors, the electromagnetic calorimeters, the hadronic calorimeters and the inner detector. The kinematics and geometry describing the collisions are written below.

#### Kinematics and detector geometry

Before the data can be analysed, it has to be collected and processed in a detector. The data used in the work of this thesis are generated from proton-proton collisions in the ATLAS detector at the Large Hadron Collider (LHC) during the Run 2 period from 2015 to 2018. The ATLAS inner detector itself is contained in a solenoid field, and the kinematic variables are measured based on the following coordinate system. The z-axis is defined to go along the center axis of the solenoid, whereas the y-axis points upwards in the detector and the x-axis radially outwards from the center axis. This allows for all transverse variables to be defined in the x-y plane[23]. From this we construct the azimuthal and polar angles  $\phi$  and  $\theta$ , where the azimuthal angle  $\phi$  is the angle around the z-axis, and the polar angle  $\theta$  is the angle from the z-axis, as shown in figure 3.1.

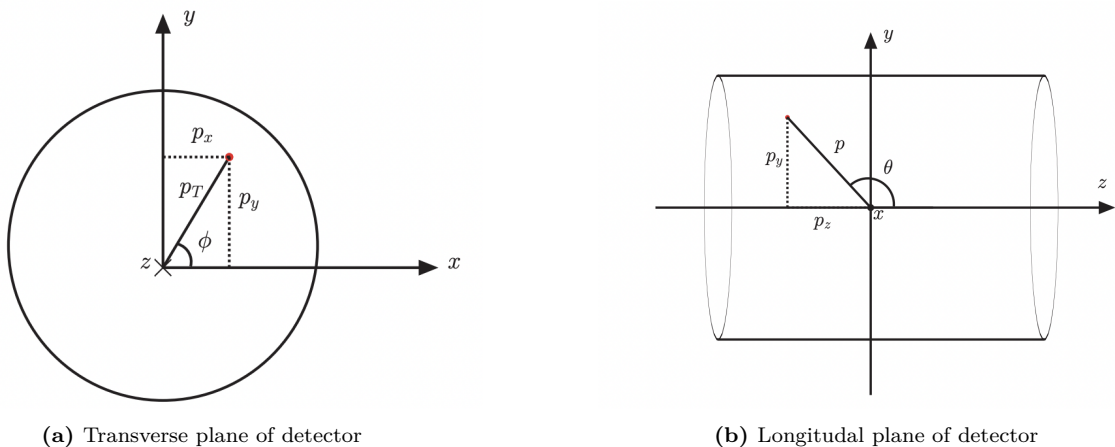


**Figure 3.1:** Spherical coordinate definitions with the azimuthal and polar angles  $\phi$  and  $\theta$ . Here figure 3.1a of the transverse plane shows the z-axis into the paper, whereas figure 3.1b of the longitudinal plane shows the positive x-axis going out of the paper. Figure taken from [23].

In figure 3.1 the kinematic variables for proton-proton collisions are described by the energy, rest mass and momentum, given as  $E$ ,  $m$ , and  $\mathbf{p} = (p_x, p_y, p_z)$  respectively. As the particles move with very high energy,

we will use the relativistic four momentum<sup>8</sup>, given as  $\mathbf{P} = (E, \mathbf{p})$ . We also have that

$$\gamma = \frac{1}{\sqrt{1 - \beta^2}},$$

where  $\gamma$  is the Lorentz factor, and  $\beta = \frac{v}{c}$ , which gives us the following definitions for energy  $E = \gamma m$  and momentum  $\mathbf{p} = \beta \gamma m$ [23]. From this we can derive the energy momentum formula:

$$\begin{aligned}\mathbf{p}^2 &= \beta^2 \gamma^2 m^2 \\ \mathbf{p}^2 + m^2 &= m^2(\beta^2 \gamma^2 + 1) \\ \mathbf{p}^2 + m^2 &= m^2 \gamma^2 \\ \mathbf{p}^2 + m^2 &= E^2\end{aligned}$$

$$E = \sqrt{p^2 + m^2}. \quad (3.1)$$

It can be shown that the phase space of a particle is given by[24]:

$$d\mathbf{p} = dp_x dp_y dp_z = p^2 dp d\Omega = dp_z p_T dp_T d\phi, \quad (3.2)$$

where  $p_z$  is the momentum along the beam direction,  $p_T$  is the projected momentum on the transverse plane, and  $\Omega$  is the solid angle. An analog to the relativistic longitudinal velocity is the rapidity  $y$ . To define this we have that the relativistic generalization of equation 3.2 is given by:

$$d^4 p \delta(E^2 - p^2 - m^2) = d\mathbf{p} \frac{1}{E} = p_T dp_T d\phi dy, \quad dy = \frac{dp_z}{E}.$$

Using the fact that  $p = \sqrt{p_T^2 + p_z^2}$  and equation 3.1 we can integrate  $dy$  to get the rapidity:

$$\begin{aligned}\int dy &= \int \frac{dp_z}{\sqrt{p_T^2 + p_z^2 + m^2}} \\ y &= \cosh^{-1} \left( \frac{E}{\sqrt{p_T^2 + m^2}} \right)\end{aligned} \quad (3.3)$$

For particles with little to no mass relative to the transverse momentum, we have that  $p_T^2 + m^2 \approx p_T^2$  where  $p_T = E \sin(\theta)$ , which gives us the following relations:

$$\begin{aligned}\cosh(y) &= \frac{1}{\sin(\theta)}, \\ \sinh(y) &= \frac{1}{\tan(\theta)}, \\ \tanh(y) &= \cos(\theta).\end{aligned}$$

which can be used to show that  $e^{-y} = \tan \frac{\theta}{2}$ . From this we define the pseudorapidity  $\eta$  as:

$$\eta = -\ln \left( \tan \frac{\theta}{2} \right), \quad (3.4)$$

which is, in the relativistic limit, the same as the rapidity  $y$ . A useful property of the pseudorapidity is that the phase space of a single particle is uniformly distributed for both  $\eta$  and  $\phi$ , making them good features for controls and verification of SM MC.

## Data collection

The features in the dataset used in this analysis are computed with or fetched from the quantities measured from the detector itself. Such measured properties include the momentum, energy, angles etc., all of which are either measured or computed based on the measurements in the detector. In figure 3.2 a visualization shows how different particles move through the detector and how they are detected. For example, energy deposits

---

<sup>8</sup>In special relativity, four momentum is used as both energy and momentum are conserved, and thus by creating the four momentum, you achieve a Lorentz invariant quantity[19].

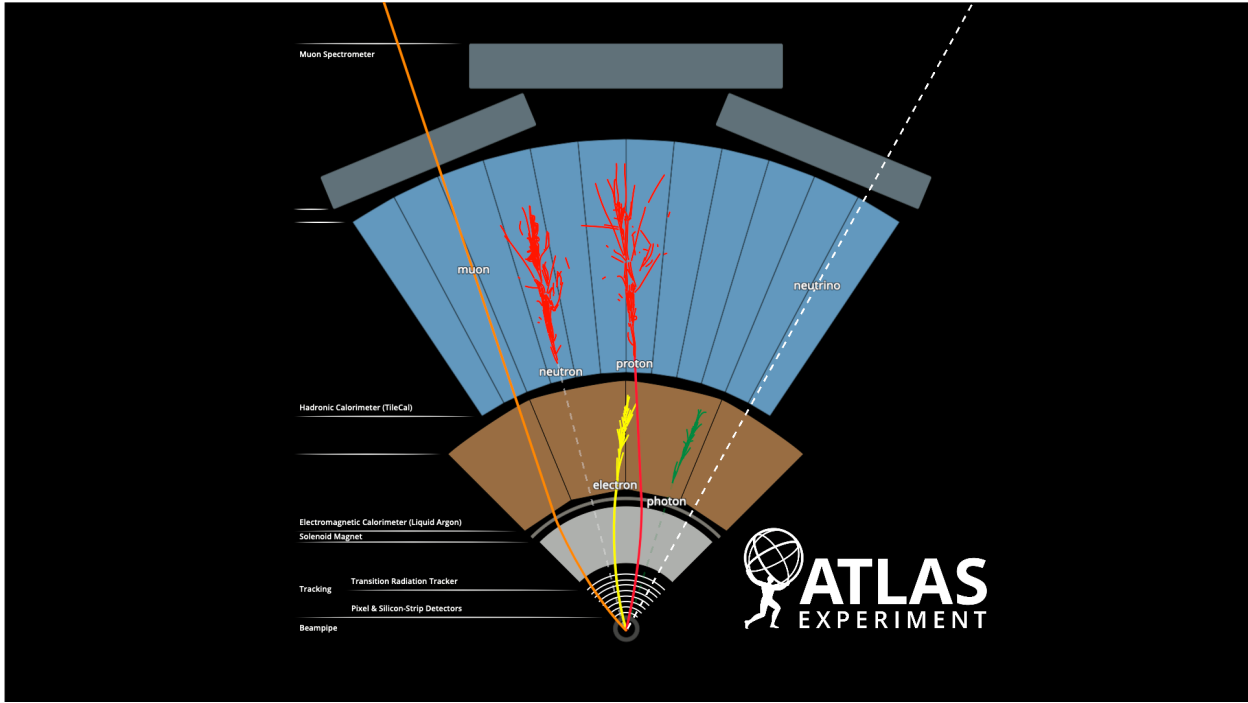


**Figure 3.2:** Figure describing how particles are detected at ATLAS, fetched from [ATLAS detector slice \(and particle visualisations\)](#), by Sascha Mehlhase [25].

are measured using electromagnetic and hadronic calorimeters, specifically designed to efficiently measure the energy of all particles interacting through the electromagnetic and strong interactions, respectively. Charged particles leave tracks in the inner tracking device. Thus, electrons leaves tracks in the inner tracker and deposit energy in the electromagnetic calorimeter, muons pass through the muon spectrometer leaving electrical signal and momentum and energy of a muon is then based on the curvature of the track of the muon in the muon detector. Between the calorimeters and the muon detector there is another magnetic field to help on the measure of the muons. Photons only deposit energy in the electromagnetic calorimeter. Hadrons such as protons and neutrons deposit energy in the hadronic calorimeters, and charged hadrons also leaves tracks in the inner tracker. This is shown in figure 3.2.

The ATLAS detector has a few selection stages before the data is stored. In order to reach the highest intensity of collisions, the LHC accelerates packets of around  $10^{11}$  protons, and collides each batch every 25 nanoseconds, yielding a collision rate of 40 MHz[26].

### Data preparation

During data recording at the ATLAS detector, triggers on the hardware and software level select out the events<sup>9</sup> that are of most interest. Most of the initial collisions are discarded with about 1 in 40000 events being accepted. This is because the amount of recorded events simply are too high to realistically analyse and store. Also, most of the events are of no interest for BSM searches anyway as they do not yield massive particles. There are therefore no large deposits of energy or tracks with high transverse momentum. Instead, these collision fragments leave the interaction region with very small angles between their trajectory and the beam pipe.

Once the trigger selection is done, the data is reconstructed. This means that the objects in the recorded events are being reconstructed into particles like jets and photons using advanced software algorithms. The reconstruction is done based on the tracks and measurements in the detector, but it is not perfect, and can lead to fake leptons or jets. By fake, it is meant that an object might look like a lepton but is in reality a jet or vice versa[27]. Once the reconstruction is done, further slimming of the data is done. Derivations are slimmings of the data where the selection of events are further reduced to match the needs of the different analysis groups.

The simulated data go through parts of the same process as the recorded data from ATLAS. These events are first generated by software that simulates the initial interaction and then run through the detector to simulate the interaction of the particles with the detector and the resulting production of digital signals.

<sup>9</sup>An event here is defined as a collision recorded and reconstructed.

Since these signals mimic the real detector signals, the events can be reconstructed and go through derivations just like the proton-proton collision data, and then be used in analysis.

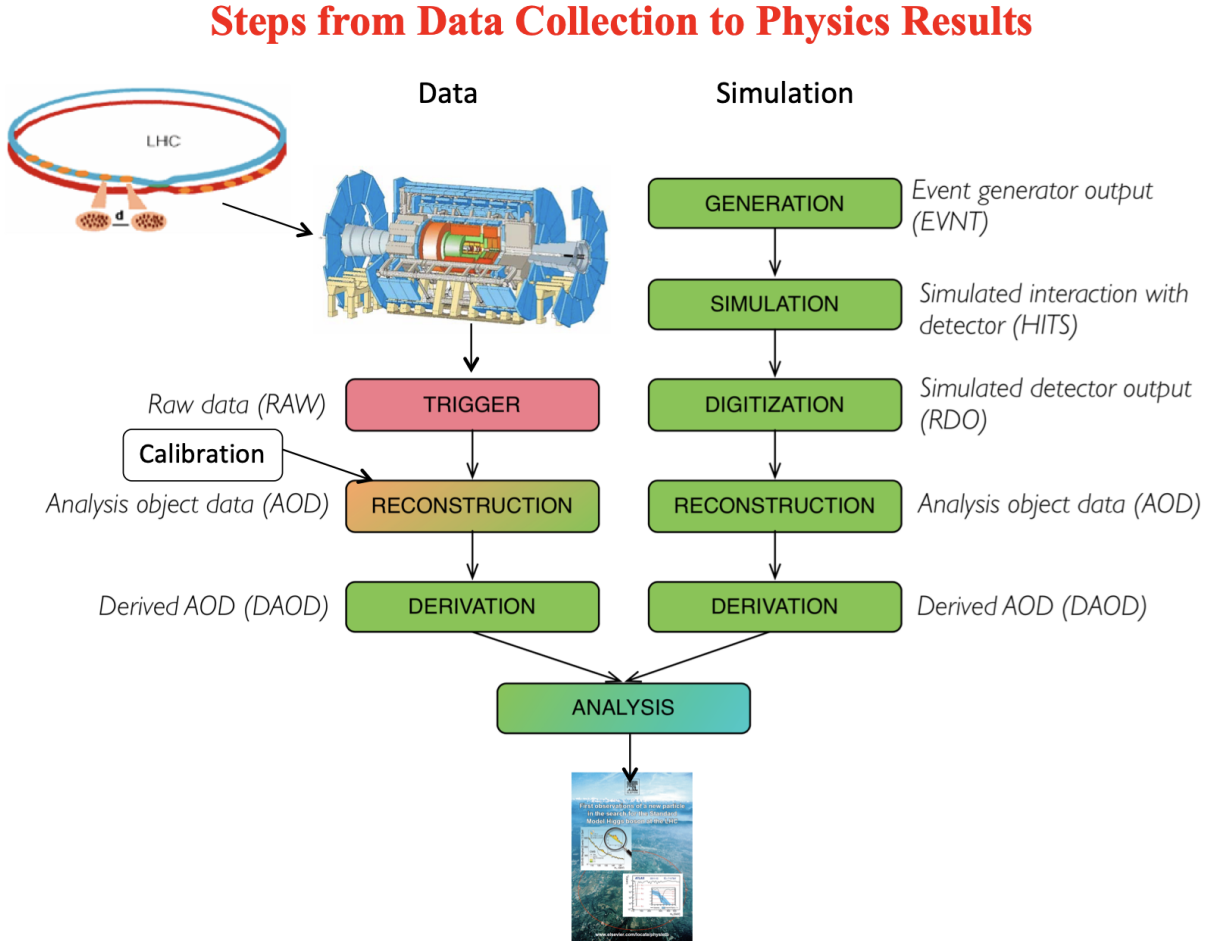


**Figure 3.3:** Figure describing the steps to take for data collection at ATLAS, fetched from [Hybrid ATLAS Induction Day + Software Tutorial workshop](#), part [Computing and Data preparation](#), initially drawn by Dr. James Catmore, later held by S.M Wang [26].

## Jets

Photons and electrons are detected in the electromagnetic calorimeter, and are easy to track and detect as they separate easily. Quarks, however, are bound by QCD and thus cannot be separated as individual particles. An illustration of how quarks and gluons materialise as jets during a proton-proton collision is shown below in figure 3.4.

In a proton-proton collision, the quarks and gluons form stable or unstable hadrons such that the color confinement is upheld[28]. These particles then decay to other stable hadrons that can be tracked, and these collimated tracks and energy deposits are called jets. The jets are defined through complex algorithms. Another point to make is that some quarks yield more information than others. Using the properties of heavy quarks such as the b- and c-quarks and their non-negligible lifetime allows us to differentiate jets containing these quarks from jets only consisting of light quarks. The b-jet coming from a b quark are particularly interesting as they are produced in the decay of top quarks. The Higgs can be produced from, and in association with, top-quarks. The behavior of hadrons containing b-quarks may be indirectly sensitive to BSM physics as well.

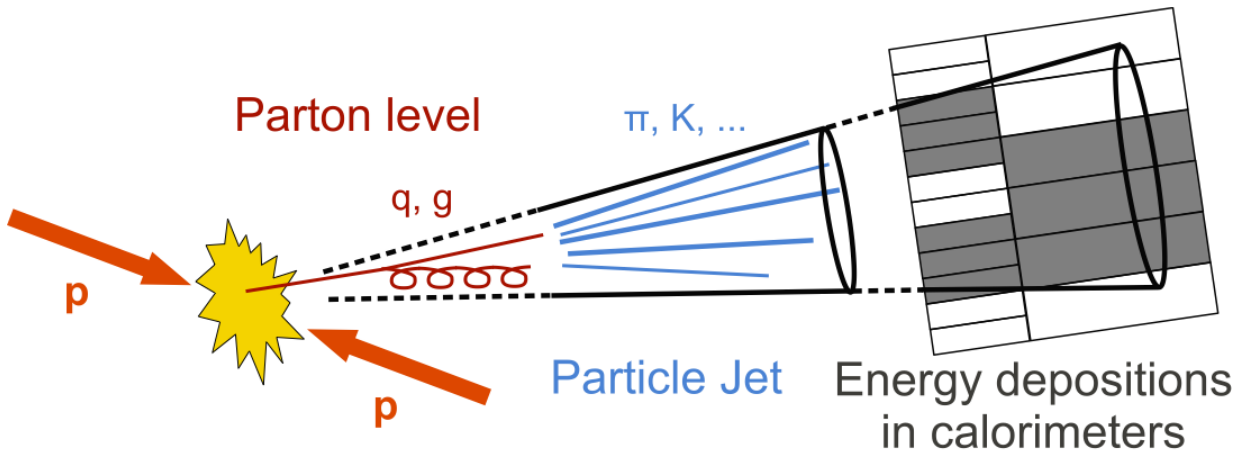


**Figure 3.4:** Figure describing how quarks and gluons are treated in the detector, and thus why we name them jets, fetched from [the CMS webpage](#).

## 3.2 ROOT

ROOT is an open-source data analysis framework used in high energy physics. It can do fast data manipulation, save and access data, create graphics for publication, and even combine with high level languages such as R and Python.

### RDataFrame

RDataFrame's main purpose is to make reading and handling of ROOT files easier, especially in relation to modern machine learning tools and their respective frameworks and environments. This is done by creating a dataframe type of structure of the ROOT n-tuples, and then lazily<sup>10</sup> apply constraints to the data. Using PyROOT<sup>11</sup>, RDataFrame can be accessed in Python, as the functionality is wrapped around a C++ class. Below is a code example of how to create a RDataFrame object, apply a cut and then create a column for later use. Here, good leptons are defined first, denoted as "ele\_SG" and "muo\_SG". A cut is then applied where we require that the number of good leptons is always 3<sup>12</sup>. Finally, a column is created where the combination of type of leptons in the 3 lepton system is stored, as well as creating a histogram containing the results for that given channel<sup>13</sup> k. Notice here that if the variable already exists as a column in the dataframe, arithmetic and logic can be applied directly using those columns to create new one. More complicated variables, such as the flavor combination for the leptons, or the invariant mass of two particles must be found or calculated using C++ functions. An example of such a C++ function is shown in code example ??.

In the code example ?? we see how RDataFrame can be used for event selection. Line 1-9 are settings for ROOT, number of threads to use in the parallelization, extra helper functions written in C++ with .h and .so files and the path to the folder. Lines 11-13 create a dictionary containing the ROOT RDataFrames used for event selection. These are categorized by channel name. The loop on line 15 does event selection for each channel sample, defining new variables in the RDataFrame, applying filters and creating histograms. Some variables are constructed using variables already in the ROOT files such as energy and mass. Through custom C++ functions these properties can be added to the RDataFrames. Code example ?? shows a custom C++ function which is used in work of this thesis.

This C++ function creates Lorentz vectors for two particles, and then returns the invariant mass based on the parameters sent in. This function will be used on all the leptons in a given event. If one particle or both do not exist, the C++ function will return zero as the invariant mass<sup>14</sup>.

Once the event selection is done, the features have been chosen and histograms have been drawn, the RDataFrame can be converted to a Pandas dataframe. This is a very popular choice for data structure when performing data analysis in python. This is done through an intermediate step of converting the RDataFrame

<sup>10</sup>In this context lazily means that the functions and/or cuts are done first after all have been registered, see [ROOT guidelines](#) for more.

<sup>11</sup>[PyROOT website](#)

<sup>12</sup>Final states with two leptons present were also analysed

<sup>13</sup>A channel here refers to a certain decay channel. The simulations of the SM is divided into several channels, and some look more alike than others. One example is the Higgs decay channel, with possible decays such as two photons, W bosons or Z bosons. This pertains to simulated events only, as we cannot control what decay channels we get in the data recorded at ATLAS

<sup>14</sup>The invariant mass function getM is used for jet-jet, jet-lepton and lepton-lepton invariant masses

```

1 import ROOT as R
2
3 R.EnableImplicitMT(200) # Enable multithreading, sets number of threads to 200 or the highest
4 # number possible if the number of threads is less than 200
5 R.gROOT.ProcessLine(".L helperFunctions.cxx+") # Load the C++ helper functions in ROOT
6 # interpreter
7 R.gSystem.AddDynamicPath(str(dynamic_path)) # Add the path to the library with the helper
8 # functions to the ROOT interpreter
9 R.gInterpreter.Declare(
10 '#include "helperFunctions.h"'
11 ) # Header with all helper functions
12 R.gSystem.Load("helperFunctions_cxx.so") # Library with the myFilter function
13
14 df_mc = getDataFrames(mypath_mc) # Function to create a dictionary of RDataFrames for each
15 # channel in the SM MC and possible signal samples
16 df_data = getDataFrames(mypath_data) # Function to create a dictionary of RDataFrames for ATLAS
17 df = {**df_mc, **df_data} # Combine the two dictionaries
18
19
20
21
22
23
24
25
26
27
28
29
30
31
32
33
34
35
36
37
38
39
40
41
42
43
44
45
46
47
48
49
50
51
52
53
54
55

```

**Figure 3.5:** Example of event selection done using RDataFrame. Four example features are created here, the "good electrons", "good muons", "good leptons" and flavor combination of leptons. Then a filter is applied to the RDataFrame structure, and finally a histogram is created. In section B.1 it is shown how to implement the Rapidity-Mass matrix from section 3.4 in event selection.

to a numpy filestructure, which then can be converted to a Pandas[29] dataframe or some other framework. The new Pandas dataframes are stored as HDF5[30] files to be used later. This is because the HDF5 format has a very good compression ratio, and is very fast to read and write.

```

1 double getM(VecF_t &pt_i, VecF_t &eta_i, VecF_t &phi_i, VecF_t &e_i,
2             VecF_t &pt_j, VecF_t &eta_j, VecF_t &phi_j, VecF_t &e_j,
3             int i, int j)
4 {
5     /*
6      * Calculates the invariant mass between two particles.
7      * If the particles are not found, or the index is out of range,
8      * function returns zero, else returns the invariant mass.
9      */
10    const auto size_i = int(pt_i.size());
11    const auto size_j = int(pt_j.size());
12
13    if (size_i == 0 || size_j == 0){return 0.;}
14    if (i > size_i-1){return 0.;}
15    if (j > size_j-1){return 0.;}
16
17    TLorentzVector p1;
18    TLorentzVector p2;
19
20    p1.SetPtEtaPhiM(pt_i[i], eta_i[i], phi_i[i], e_i[i]);
21    p2.SetPtEtaPhiM(pt_j[j], eta_j[j], phi_j[j], e_j[j]);
22
23    double inv_mass = (p1 + p2).M();
24
25    return inv_mass;
26 }
27 }
```

**Figure 3.6:** Example of a C++ function used in event selection. This function is used to calculate the invariant mass between two particles. It takes the kinetic parameters for both particles and the index for which of the leptons available to compute for. If the particles do not exist for that event, it returns zero.

```

1 import pandas as pd
2
3 def Convert_RDF_to_numpy(df, PATH_TO_STORE):
4
5     cols = df.keys()
6
7     for k in cols:
8
9         print(f"Transforming {k}.ROOT to numpy")
10        numpy = df[k].AsNumpy(DATAFRAME_COLS) ## DATAFRAME_COLS is a list of columns to be
11        converted to a numpy array
12        print(f"Numpy conversion done for {k}.ROOT")
13        df1 = pd.DataFrame(data=numpy) ## Convert to pandas dataframe
14        print(f"Transformation done")
15
16        ## Convert to HDF5
17        df1.to_hdf(
18            PATH_TO_STORE + f"/{k}_3lep_df_forML_bkg_signal_fromRDF.hdf5", "mini"
19        )
20
21        ## Flush memory for new dataframe
22        df1 = pd.DataFrame()
```

**Figure 3.7:** Loop converting RDataFrames to NumPy structures, before being stored as HDF5 files. Her  $df[k]$  is a dictionary containing each channel, with channel name as key.

### 3.3 Background samples

To look for anomalies in the 2 or 3 lepton final states we need to train on background Monte Carlo samples with that specific final state. This means in a sense that we want the autoencoder to learn what is expected from the SM in terms of this final state. The 2 and 3 lepton +  $e_T^{miss}$  background Monte Carlo contains the following channels:

Below are three Feynmann diagrams, two of which are both represented in the 2 and 3 lepton +  $e_T^{miss}$  background MonteCarlo shown in table 3.1. The selected ones are likely Feynman diagrams for  $t\bar{t}$ , Higgs and

<b>3 lepton + <math>e_T^{miss}</math></b>	<b>2 lepton + <math>e_T^{miss}</math></b>
<b>Channel names:</b>	
Wjets	Wjets
ttbar	ttbar
Singletop	Singletop
ZeeJets	ZeeJets
ZmmJets	ZmmJets
ZttJets	ZttJets
Higgs	Diboson
Triboson	
TopOther	
Diboson2L	
Diboson3L	
Diboson4L	

**Table 3.1:** SM MC channels for both the 2 and 3 lepton +  $e_T^{miss}$  final state background.

Zeejets channels. The  $t\bar{t}$  process shown in figure 3.8 leads to two leptons +  $e_T^{miss}$  from the W-decays, as well as to two b-jets. One jet can be mis-identified as a lepton.

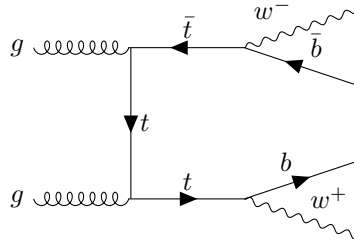


**Figure 3.8:** Proton-proton collision showing the  $t\bar{t}$  channel. Here the w bosons decay leptonically and one or more jets can be misreconstructed as fake leptons by the detector.

The Higgs process in figure 3.9 can lead to four leptons. One or two leptons can be misidentified and therefor constitute a background for the 2 lepton +  $e_T^{miss}$  or 3 lepton +  $e_T^{miss}$  analyses.

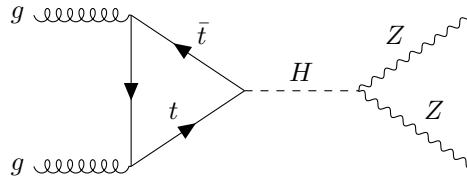


**Figure 3.9:** Proton-proton collision showing the Higgs channel. Here the Z bosons decay leptonically, leading to a four lepton final state.

The Z + jets process in figure 3.10 can lead to two leptons and two b-jets. If one or both of the jets are fakd as leptons, the process constitutes a source of background for the 3 lepton +  $e_T^{miss}$  or 2 lepton +  $e_T^{miss}$  analysis.

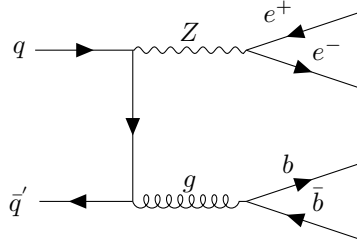


**Figure 3.10:** Proton-proton collision showing the Zeejets channel. Here one of the Z bosons decay leptonically and the gluon decays hadronically.

## 3.4 The dataset features

### The Rapidity-Mass matrix (RMM)

Most of the features in the analysis are elements in the Rapidity-Mass matrix (RMM) inspired by the work of Chekanov [31]. The RMM is a convenient structure to create a feature space for the dataset. It contains information of various reconstructed objects and their combinations about mass, rapidity, momenta and missing transverse energy, all of which are useful in searches for new physics in HEP[32]. One example of an analysis that has used some features from the RMM is demonstrated in [33]. The main reason however for using this structure is the systematic layout and automated feature space, that maintains low to no correlation between the cells in the matrix, which is optimal when using neural networks.

The RMM is determined as a square matrix of  $1 + \sum_{i=1}^T N_i$  columns and rows, where T is the total number of objects (i.e. jets, electrons etc.), and  $N_i$  is the multiplicity of a given object. In the case where the multiplicity of a particle is equal to the number of different particles, we can denote the RMM matrix as a  $TmNn$  matrix, where m is the number of objects, and n is the multiplicity of each object. One should already here choose appropriately the number of objects and the multiplicity of each, as the computation time increases significantly when expanding the RMM. Each cell in the matrix contains information about either single or two particle properties. It is also important to remember that each event gets its own RMM, therefor each event creates its own signature that the autoencoder hopefully can learn trends from. An example of a small RMM is shown in matrix 3.5.

$$\begin{pmatrix} \mathbf{e}_T^{miss} & m_T(j_1) & m_T(j_2) & m_T(e_1) & m_T(e_2) \\ h_L(j_1) & \mathbf{e}_T(j_1) & m(j_1, j_2) & m(j_1, e_1) & m(j_1, e_2) \\ h_L(j_2) & h(j_2, j_1) & \delta\mathbf{e}_T(j_2) & m(j_2, e_1) & m(j_2, e_2) \\ h_L(e_1) & h(e_1, j_1) & h(e_1, j_2) & \mathbf{e}_T(e_1) & m(e_1, e_2) \\ h_L(e_2) & h(e_2, j_1) & h(e_2, j_2) & h(e_2, e_1) & \delta\mathbf{e}_T(e_2) \end{pmatrix} \quad (3.5)$$

In matrix 3.5 we have the RMM matrix for a T2N2 system, in other words we have two types of objects, jets <sup>15</sup> and electrons, and for each object we consider a multiplicity of two. The matrix itself is partitioned into three parts. The diagonal represents energy properties, the upper triangle represents mass properties and the lower triangle represents longitudinal properties related to rapidity. The diagonal has three different properties,  $\mathbf{e}_T^{miss}$ ,  $\mathbf{e}_T$  and  $\delta\mathbf{e}_T$ .  $\mathbf{e}_T^{miss}$  is placed in the (0,0) position in the matrix. It accounts for the missing transverse energy of the system, which is of high interest for analyses in searches for BSM physics such as heavy neutrinos or supersymmetric particles.  $\mathbf{e}_T$  is the transverse energy defined as

$$\mathbf{e}_T = \sqrt{m^2 + p_T^2} \quad (3.6)$$

but for light particles such as electrons, this can be approximated to  $\mathbf{e}_T \approx p_T$ .  $\delta\mathbf{e}_T$  is the transverse energy imbalance. It is defined as

$$\delta\mathbf{e}_T = \frac{E_T(i_{n-1}) - E_T(i_n)}{E_T(i_{n-1}) + E_T(i_n)}, \quad n = 2, \dots, N, \quad (3.7)$$

where  $i_n$  is the nth entry of object i. The first column in the RMM matrix, except the first element, is related to the longitudinal property of the given particle. It is defined as

$$h_L(i_n) = C(\cosh(y(i_n)) - 1).$$

<sup>15</sup>Jets here can both be b- or l-jets. Ljet is defined as jets with  $\text{jetd1r} < 0.665$ , whereas  $\text{bjet77}$  is defined as jets with  $\text{jetd1r} \geq 2.195$ .  $\text{jetd1r}$  is a machine learning output from a network trained to distinguish b- and l-jets.

$C$  is a constant to ensure that the average  $h_L(i_n)$  values do not deviate too much from the ranges of the invariant masses or the transverse masses, found to be 0.15, as it ensures that rapidity ranges in the range  $[-2.5, 2.5]$  produces  $h_L(i_n)$  values in the  $[0, 1]$  interval[31].  $y(i_n)$  is the rapidity of the particle, and  $i_n$  is the particle number. In the lower triangle we have the longitudinal properties of the combinations of particles. Similar to  $h_L(i_n)$ , this property is defined as

$$h(i_n, j_k) = C(\cosh(\Delta y) - 1),$$

where  $\Delta y = y_{i_n} - y_{j_k}$  is the rapidity difference between particle  $i_n$  and  $j_k$ .

## Tabular and sparse data

A consequence of using the RMM structure is that the RMM for the data and SM MC can be sparse for some events. This is due to the fact that the RMM allows for the variety of final states of the reconstructed events, i.e. that one event has two ljets, zero bjets, one electron and two muons, whereas another event can have four ljets, three bjets and three electrons. This means that the non-zero elements of the RMM will vary from event to event, and for neural networks this is a problem. To solve this problem, Chekanov simply pads the missing values with zeros[31].

## Standard Model Monte Carlo and data comparison

Before we can start the analysis, we need to compare the SM MC and data. This is done to ensure that the measured features used are well modelled by the SM MC training samples we use. As described by R. Stuart Geiger et al. [34], the concept of "Garbage in, garbage out" is of key importance in computer science, and is indeed important in high energy physics. To ensure that the models we train actually learn physical processes, the training set must closely resemble the data. The SM MC simulations are indeed very good, but they are numerical approximations and can sometimes be off. Thus, every feature that will be used for training must be checked before being used. This is done by comparing the distributions of the features in the SM MC and ATLAS data. Monte Carlo simulations are based on the actual theory itself, and comparisons with data taken from ATLAS and other detectors alike are necessary to ensure that the SM background events look like data. This is done by creating control regions where there with high confidence is no signatures of New Physics. This of course becomes problematic if the New Physics are embedded in the background.

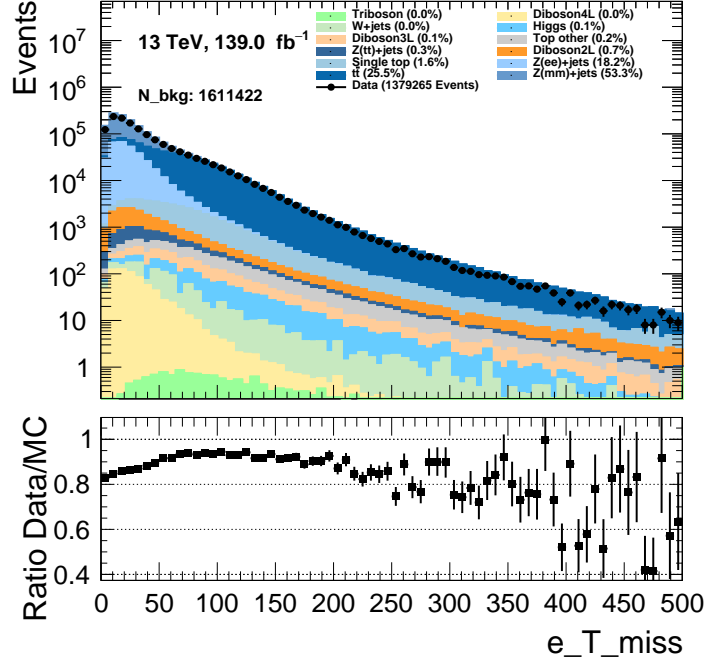
Now, if we compare all SM MC and ATLAS data, we would usually expect there to be a good agreement. To ensure that the SM MC actually represents the physics, we create signal and background regions to optimize for amount of signal and amount of background. If we can create a background region where we believe with very high certainty that only SM processes can occur, and we get a good match, we usually conclude that the SM MC is good enough. Since the data from ATLAS used in the work for this thesis has been thoroughly analysed for New Physics without finding any, it is not needed here to create these control regions. Traditional searches using rectangular cuts have only excluded some models, which is why machine learning is getting more popular. The hope is that the signal, whatever it might be, can be revealed with more clever feature engineering and smart machine learning algorithms. Particle physics differs here from more day-to-day machine learning as the recorded data from ATLAS, the true data, is completely unlabeled.

In figure 3.11 two features have been selected to visualize the comparison between SM MC and ATLAS data,  $e_T^{\text{miss}}$  and  $m(\text{ele}_0, \text{ele}_1)$  in the 3 lepton +  $e_T^{\text{miss}}$  dataset<sup>16</sup>. The  $e_T^{\text{miss}}$  and  $m(\text{ele}_0, \text{ele}_1)$  shows a ratio between SM MC and ATLAS data reasonably close to 1, thus we can safely move forward with the analysis. All features were checked, and can be found in the GitHub repository for this thesis at [Figures/Histo\\_var\\_check<sup>17</sup>](#) under the 3lep folder.

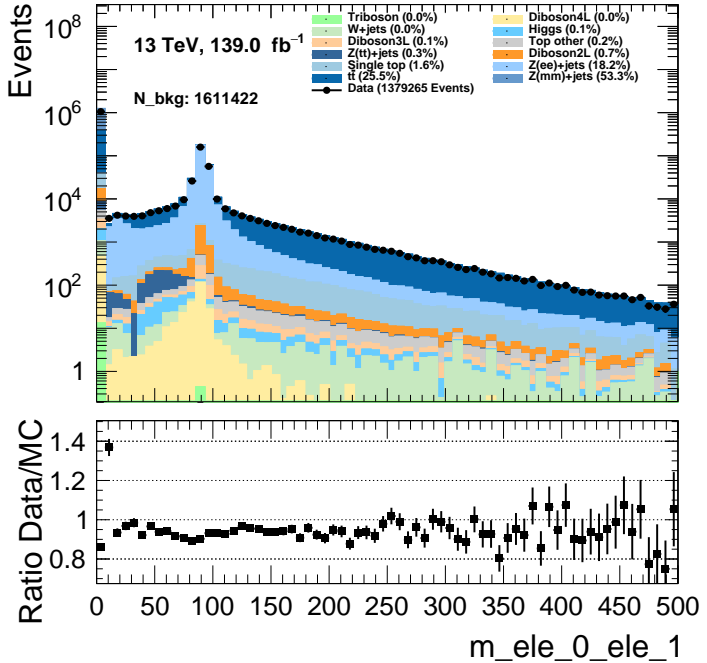
Similar checks were done for the 2 lepton +  $e_T^{\text{miss}}$  dataset. In figure 3.12 the features  $e_T^{\text{miss}}$  and  $m(\text{ele}_0, \text{ele}_1)$  do not satisfy the same ratio between SM MC and ATLAS data, as with the 3 lepton +  $e_T^{\text{miss}}$  case. It appears that RDataframe struggles with some diboson events, leading to a discrepancy. This could be a trigger matching issue or an issue with RDataFrame. The samples were run using both C++ ROOT event selection and RDataFrame by one of the supervisors, and the issue seems to only occur with RDataFrame. Therefore all results regarding the 2 lepton +  $e_T^{\text{miss}}$  dataset should be interpreted with this in mind. One attempt can be shown in figure 3.12b where a cut on the invariant mass above 70 GeV of at least the two leptons with the highest energy was done to try to accommodate the trigger issue. There is some improvement needed, but we proceeded with the dataset, keeping a cut on the leading lepton pair invariant mass > 70 GeV. All features

<sup>16</sup>Full treatment of systematic uncertainties, which is beyond this work, covers for the apparent deviations between MC and data.

<sup>17</sup>Full link: [https://github.com/Gadangadang/MasterThesis/tree/main/Figures/histo\\_var\\_check/LEP3](https://github.com/Gadangadang/MasterThesis/tree/main/Figures/histo_var_check/LEP3)



(a) Missing transverse energy for the three lepton final state in GeV. The histogram contains the entire Run 2 dataset.

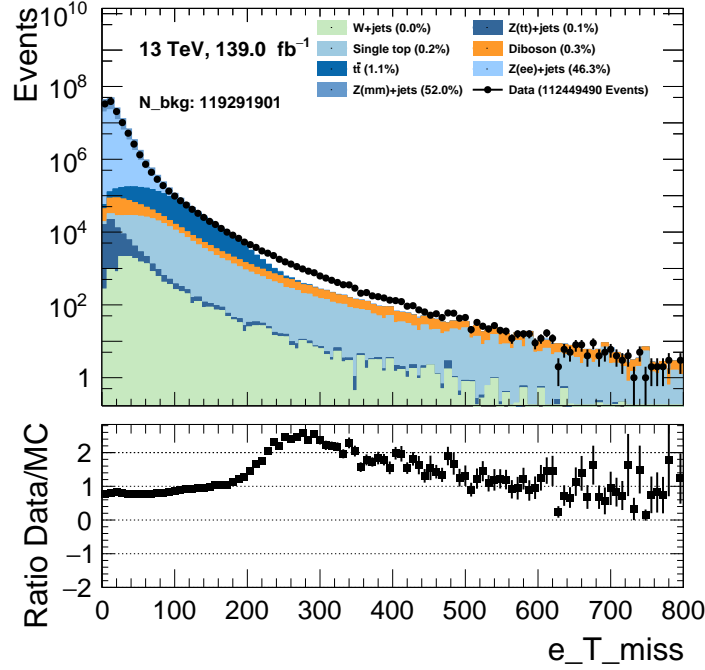


(b) Invariant mass for the first and second electron in GeV. The histogram contains the entire Run 2 dataset.

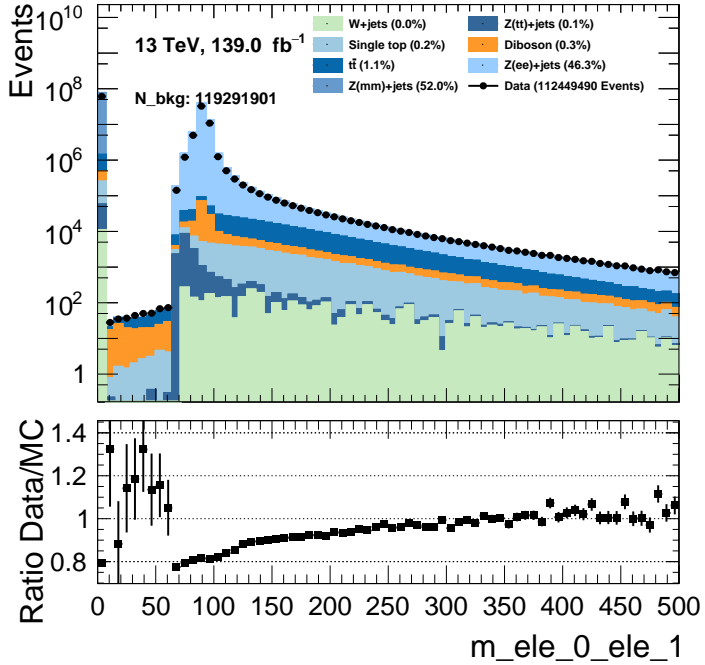
**Figure 3.11:** Comparison of the Monte Carlo and data for the three lepton +  $e_T^{miss}$  final state with the features  $e_T^{miss}$  and flavor composition.

were checked, and can be found in the GitHub repository for this thesis at [Figures/Histo\\_var\\_check<sup>18</sup>](https://github.com/Gadangadang/MasterThesis/tree/main/FIGURES/histo_var_check) under the 2lep folder.

<sup>18</sup>Full link: [https://github.com/Gadangadang/MasterThesis/tree/main/FIGURES/histo\\_var\\_check](https://github.com/Gadangadang/MasterThesis/tree/main/FIGURES/histo_var_check)



(a) Missing transverse energy for the three lepton final state in GeV. The histogram contains the entire Run 2 dataset.



(b) Invariant mass for the first and second electron in GeV. The histogram contains the entire Run 2 dataset. Note the sharp reduction of events from 10-70 GeV.

**Figure 3.12:** Comparison of the SM MC and data for the 2 lepton +  $e_T^{miss}$  final state with the features  $e_T^{miss}$  and flavor composition. In figure 3.12b a cut on the invariant mass above 70 GeV of the leading lepton pair. In some cases the first and second electron are not the leading pair, thus there will be some events in this histogram below 70 GeV.

## Triggers

The triggers used in the 2 lepton +  $e_T^{miss}$  and 3 lepton +  $e_T^{miss}$  datasets are shown in Table 3.2, 3.3, 3.4 and 3.5 for the 2015, 2016, 2017 and 2018 data taking periods.

	Name
2015	<i>HLT_2e15_lhvloose_nod0_L12EM13VH</i>
	<i>HLT_2e12_lhloose_L12EM10VH</i>
	<i>HLT_2mu10</i>
	<i>HLT_mu18_mu8noL1</i>
	<i>HLT_e17_lhloose_mu14</i>
	<i>HLT_e7_lhmedium_mu24</i>

**Table 3.2:** Triggers used in the 2015 SM MC and ATLAS data samples for the 2 lepton 0  $e_T^{miss}$  dataset.

	Name
2016	<i>HLT_2e15_lhvloose_nod0_L12EM13VH</i>
	<i>HLT_2e17_lhvloose_nod0</i>
	<i>HLT_2mu10</i>
	<i>HLT_2mu14</i>
	<i>HLT_mu20_mu8noL1</i>
	<i>HLT_mu22_mu8noL1</i>
	<i>HLT_e17_lhloose_nod0_mu14</i>
	<i>HLT_e24_lhmedium_nod0_L1EM20VHI_mu8noL1</i>
	<i>HLT_e7_lhmedium_nod0_mu24</i>

**Table 3.3:** Triggers used in the 2016 SM MC and ATLAS data samples for the 2 lepton 0  $e_T^{miss}$  dataset.

	Name
2017	<i>HLT_2e17_lhvloose_nod0_L12EM15VHI</i>
	<i>HLT_2e24_lhvloose_nod0</i>
	<i>HLT_2mu14</i>
	<i>HLT_mu22_mu8noL1</i>
	<i>HLT_e17_lhloose_nod0_mu14</i>
	<i>HLT_e26_lhmedium_nod0_mu8noL1</i>
	<i>HLT_e7_lhmedium_nod0_mu24</i>

**Table 3.4:** Triggers used in the 2017 SM MC and ATLAS data samples for the 2 lepton 0  $e_T^{miss}$  dataset.

	Name
2018	<i>HLT_2e17_lhvloose_nod0_L12EM15VHI</i>
	<i>HLT_2e24_lhvloose_nod0</i>
	<i>HLT_2mu14</i>
	<i>HLT_mu22_mu8noL1</i>
	<i>HLT_e17_lhloose_nod0_mu14</i>
	<i>HLT_e26_lhmedium_nod0_mu8noL1</i>
	<i>HLT_e7_lhmedium_nod0_mu24</i>

**Table 3.5:** Triggers used in the 2018 SM MC and ATLAS data samples for the 2 lepton 0  $e_T^{miss}$  dataset.

Each trigger is designed to detect certain base expectations in the detector, for example reconstructed leptons. In the tables above, the triggers are laid out, showing which were used for a given data taking year. For a more in-depth understanding of trigger, it is recommended to look at the "Performance of

the ATLAS Trigger System in 2015” paper[35], as well as the paper for the electron and photon triggers paper[36] and the muon trigger paper[37]. The most important thing to note about these triggers is that the second argument in the trigger, in other words the component after ”HLT\_” indicates the leptons and their transverse momentum criteria. The trigger ”HLT\_2mu14” requires two reconstructed muons with a transverse momentum of at least 14 GeV to be triggered for a given event. The other components in some other triggers are more complicated, and describe reconstruction quality working points and more.

For the 3 lepton +  $e_T^{miss}$  final state, applying the trigger system on the data did not work as expected, thus a simple cut of requiring at least two leptons with a  $p_T$  above 20 GeV was implemented. Note that further triggers would refine the dataset even more.

### 3.5 Code implementation

#### Machine learning implementation

The machine learning analysis was written with Keras[38] using the Tensorflow api[5]. The machine learning structure was written using a functional structure<sup>19</sup>. In practice, this model could just as well have been written as a Sequential model<sup>20</sup>, but at a cost of flexibility and lack of the possibility for creating non-linear structure in the architecture. The code consists of one general class for the autoencoder, where the different testing cases are different classes inheriting from the parent class.

#### Construction of a neural network in Tensorflow

Using the functional structure, a general neural network in the Tensorflow API can be constructed as shown in code example ??.

```

1 import tensorflow as tf
2
3
4 inputs = tf.keras.layers.Input(shape=data_shape, name="input")
5
6 # First hidden layer
7 First_layer = tf.keras.layers.Dense(
8     units=30,
9     activation="relu"
10 )(inputs)
11
12 # Second hidden layer
13 Second_layer = tf.keras.layers.Dense(
14     units=45,
15     activation="relu"
16 )(First_layer)
17
18 # Third hidden layer
19 output_layer = tf.keras.layers.Dense(
20     units=1,
21     activation="sigmoid"
22 )(Second_layer)
23
24
25 # Model definition
26 nn_model = tf.keras.Model(inputs, output_layer, name="nn_model")
27
28 hp_learning_rate = 0.0015
29 optimizer = tf.keras.optimizers.Adam(hp_learning_rate)
30 nn_model.compile(loss="mse", optimizer=optimizer, metrics=["mse"])

```

**Figure 3.13:** Functional structure for Tensorflow neural network.

The neural network in the code above contains one input layer, one hidden layer and an output layer. The choice of nodes and activation functions are arbitrary here as the use case has not been defined. Note that code example 3.14 is exactly the same as code example 3.13, but using the sequential structure.

<sup>19</sup>Functional structure uses a function call for layers, i.e. for layers a, b, then b(a) will connect the two layers, and equals a sequential link a → b. This allows for more flexible structures. More on the functional api can be found [here](#).

<sup>20</sup>Sequential structure adds layers in sequence, i.e. for layers a, b, c we have that a → b → c, with a strict structure. This allows for more organized code. More on sequential models can be found [here](#).

```

1 import tensorflow as tf
2
3 nn_model = tf.keras.Sequential(
4     [
5         tf.keras.layers.Dense(30, activation="relu", input_shape=data_shape),
6         tf.keras.layers.Dense(45, activation="relu"),
7         tf.keras.layers.Dense(1, activation="sigmoid"),
8     ]
9 )
10
11 hp_learning_rate = 0.0015
12 optimizer = tf.keras.optimizers.Adam(hp_learning_rate)
13 nn_model.compile(loss="mse", optimizer=optimizer, metrics=["mse"])

```

**Figure 3.14:** Sequential structure for Tensorflow neural network.

## Data handling python side

### Implementation of the RMM matrix

Examples of RMM matrices used in this thesis are shown in figure 3.15.

The two RMM matrices in figure 3.15 are created from two different channels in the MC samples. This RMM is of type T4N5<sup>21</sup>. For easier interpretability, the gray area corresponds to a missing value, leading to so-called "islands" in the RMM matrix. Note here that the y-axis for the RMM's lack every other label, due to lack of space in the y-axis of the plot. If looked more closely upon, one can see that each figure has all RMM cells, just that the labels, which are identical to the x-axis label, only show for 1, 3, 5, ... The RMM plots were created using Plotly[39].

### Setup for 3 lepton dataset

The 3 lepton dataset is about 96 GB of data or circa 381873 events when implementing the RMM structure for 6 b- and ljets, 5 electrons and 5 muons. The dataset is converted from a ROOT N-tuple using RDataframe to a Pandas dataframe[29] for further preprocessing. Having added the channel name column<sup>22</sup>, weights, trilepton mass<sup>23</sup> as well as the RMM structure, the datasets are divided into a training and a validation/test set in an 80-20 split<sup>24</sup>. The split was done using the `train_test_split()` function from the Scikit-learn library[40]. Then the data and SM MC was scaled using the MinMax scaler via the `".fit_transform()"` and `".transform()"` functions from the Scikit-learn library. The training and validation/test set are then converted to numpy arrays[41] for faster loading and easier indexing, and saved as `".npy"` files. This allows for faster reuse of the arrays.

### Setup via iterative training for 2 lepton dataset

The two lepton dataset contains about 1.5 - 2 TB of data or about 119291900 events when implementing the RMM structure for 6 b- and ljets, 5 electrons and 5 muons, as for the 3 lepton dataset. This is too much to hold in memory at the same time, thus it had to be split into several smaller datasets, called megasets. Figure 3.16 visualize the structure used.

Pandas is not built for very large datasets since it is not running in a parallelized way. To handle this, the library Polars<sup>25</sup> [42] was used instead. When all channels were split, a merging was done combining all the channels in a given megaset to a separate dataset. The selection of events from each channel was done randomly, which is important, as we want to the best of our ability keep the distribution signature of the entire dataset in each megaset. If not, the model will be biased towards those datasets with the most events. Once each of the megasets where merged, the training could begin in an iterative fashion. Because Tensorflow is statically compiled, one cannot call the fit function over and over again. Instead, the weights trained based on one megaset is stored and reloaded into a new model, thus the weights are still trained on

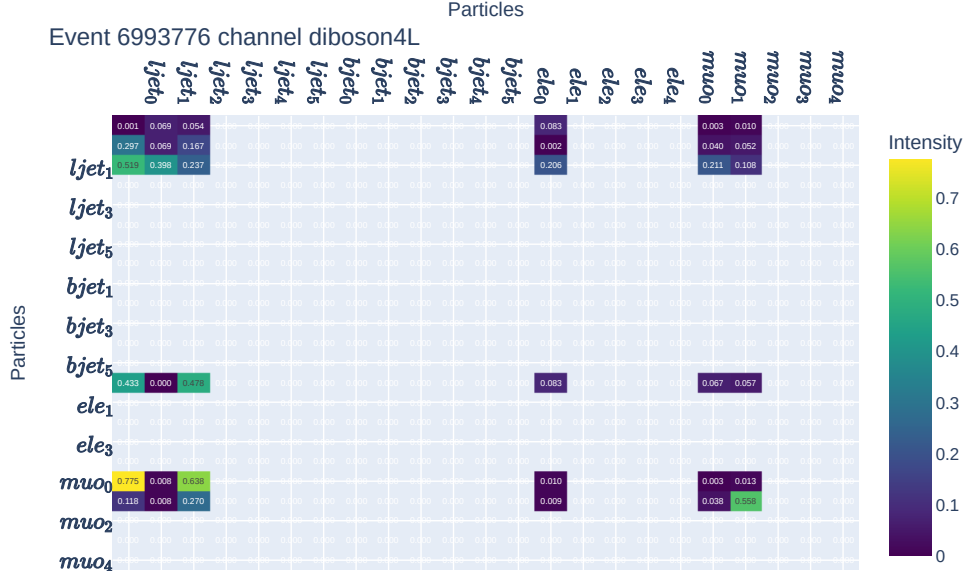
<sup>21</sup>T4 → 4 particle types: bjets, ljets, electrons and muons. N5 → 5 particles per particle type. Note here that we have 5 particles only for the leptons, and 6 particles for each of the types of jets, so it is a almost T4N5 matrix.

<sup>22</sup>This column would in a fully supervised setting be used as a target vector, but in this thesis it will only be used for legends in histograms and to index out certain channels in the validation and training set.

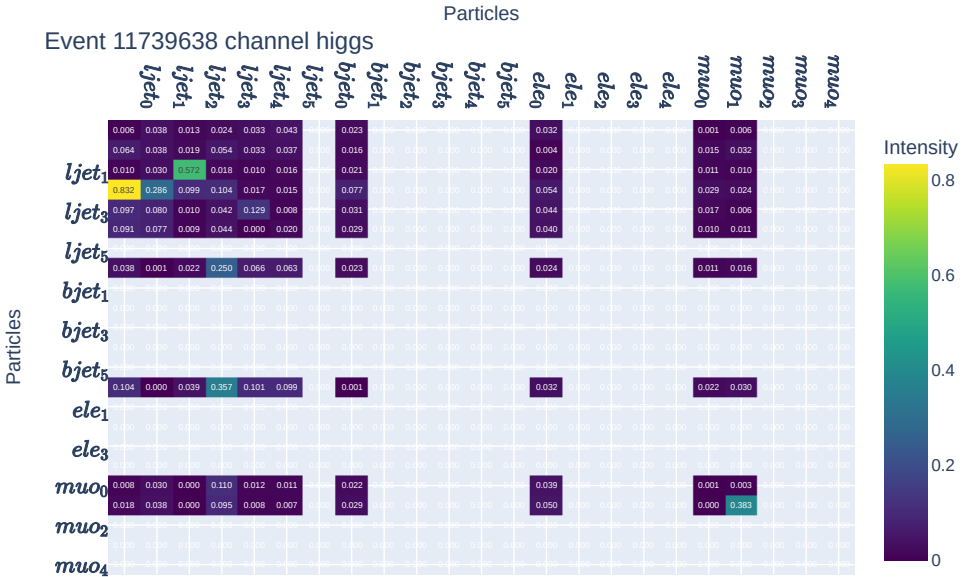
<sup>23</sup>Invariant mass of three leptons. This is assured to exist from event selection in the 3 lepton dataset.

<sup>24</sup>80 percent are reserved for training and 20 percent are reserved for testing/validation. This convention is standard within the machine learning community.

<sup>25</sup>Polars uses all available cores on the system and has excellent memory handling capability, see [Polars User Guide](#)



(a) RMM matrix for event number 6993776 from the Monte Carlo diboson4L event. Each feature is scaled based on a fit for that feature for all events in the training set ( $\approx 80\%$  of total MC). This event contains two ljets, one electron and two muons.



(b) RMM matrix for event number 11739638 from the Monte Carlo Higgs event. Each feature is scaled based on a fit for that feature for all events in the training set ( $\approx 80\%$  of total MC). This event contains five ljets, one bjet, one electron and two muons.

**Figure 3.15:** Two RMM matrices for one diboson4L (3.15a) event and one Higgs (3.15b) event.

the entire set, but in a batch like manner. The implementation used in this thesis is shown in code example 3.17.

### 3.6 The chosen neural network architectures

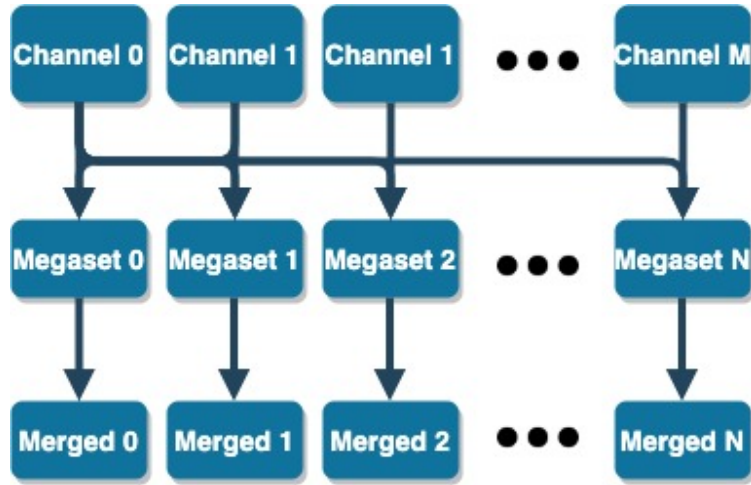


**Figure 3.16:** Megaset structure for the 2lep dataset. This figure generalises to M channels, and N megasets, where M and N does not have to be equal. The more you increase the number of megasets, the smaller each megaset will be in bytesize, but in order to keep the natural distribution in the SM MC distribution, it is not recommended to make too small sets. In this thesis 10 megasets were created where the simulated data contained 7 channels.

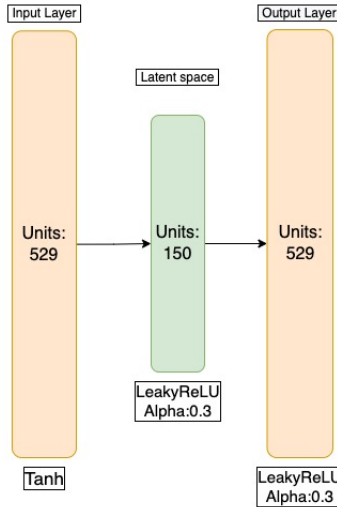
```
1 for megaset in range(totmegaset):
2
3     ## Load model
4
5     autoencoder = getModel()
6
7     if megaset != 0:
8         autoencoder.load_weights('./checkpoints/Megabatch_checkpoint')
9
10
11    ## Run Training
12    with tf.device("/GPU:0"):
13
14        tf.config.optimizer.set_jit("autoclustering")
15
16        autoencoder.fit(
17            xtrain,
18            xtrain,
19            epochs=epochs,
20            batch_size=b_size,
21            validation_data=(xval, xval),
22            sample_weight=x_train_weights,
23        )
24
25
26    AE_model.save_weights('./checkpoints/Megabatch_checkpoint')
```

**Figure 3.17:** Example code for training a neural network on megasets with Tensorflow.

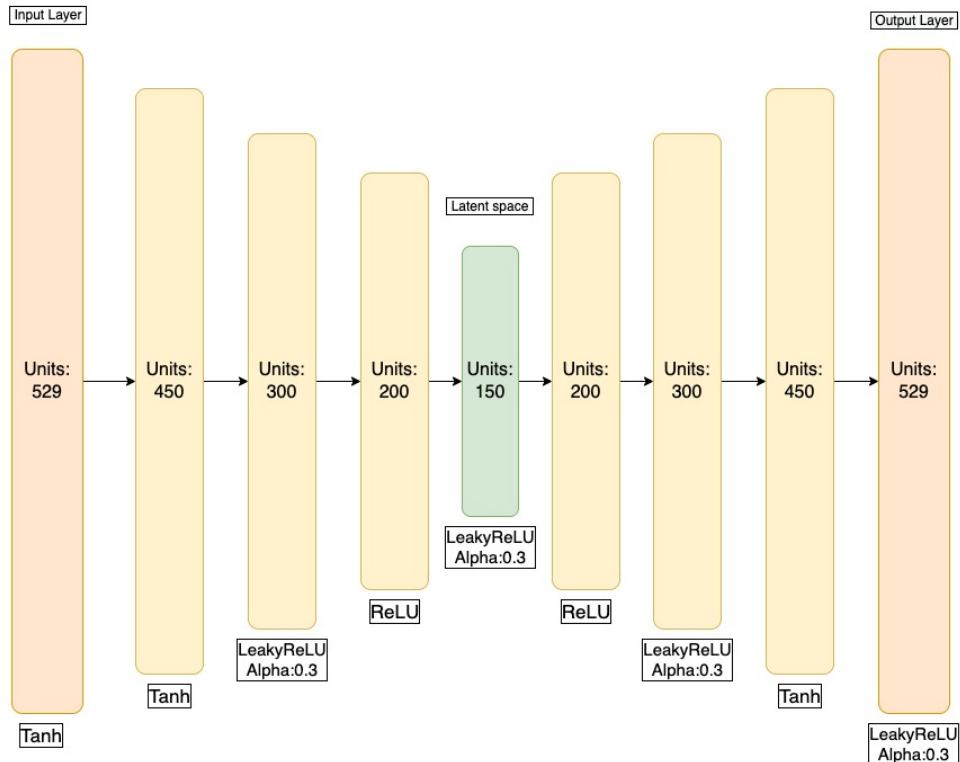
## The regular Autoencoder

Figure 3.18 shows the small autoencoder. It consists of an input and output layer of 529 nodes, with one latent space layer of 150 nodes. The activation functions for the input is Tanh while the latent space and the output layer use LeakyReLU with  $\alpha = 0.3$ .

Figure 3.19 shows the large regular autoencoder. It consists of an input and output layer of 529 nodes, with three hidden layers of 450, 300 and 200 nodes, respectively, in the encoder and three hidden layers of 200, 300 and 450 in the decoder, respectively. The activation functions for the input and output layers are the Tanh and LeakyReLU with  $\alpha = 0.3$ . The encoder layers have the activation functions Tanh, LeakyReLU with  $\alpha = 0.3$  and ReLU. The decoder layers have the activation functions ReLU, LeakyReLU with  $\alpha = 0.3$  and Tanh. The latent space has 150 nodes, with the LeakyReLU activation function with  $\alpha = 0.3$ . The activation functions as well as the number of nodes per layer were chosen based on earlier work done on the ATLAS open data[43], as well as some light hyperparameter testing using Keras-Tuner[44].



**Figure 3.18:** Small autoencoder architecture.



**Figure 3.19:** Large autoencoder architecture.

## The variational Autoencoder

Figure 3.20 and 3.21 summarize the two models used for the variational autoencoder.

In figure 3.20 we have the small variational autoencoder. It consists of an input and output layer of 529 nodes, with one latent space layer of 150 nodes sampling from a mean and variance layer of same size. The activation functions for the input, latent space and output are the Tanh, LeakyReLU with  $\alpha = 0.3$  and Sigmoid, respectively.

The large variational autoencoder in figure 3.21 consists of an input and output layer of 529 nodes, with three hidden layers of 400, 300 and 200 nodes respectively in the encoder and three hidden layers of 200, 300 and 400 in the decoder. The activation functions for the input and ouput layers are the ReLU and Sigmoid, respectively. The hidden layers in the encoder have the activation functions Tanh, ReLU, LeakyReLU with  $\alpha = 0.3$ , respectively. The hidden layers in the decoder have the activation functions LeakyReLU with  $\alpha = 0.3$ , ReLU and Tanh, respectively. The activation functions as well as the number of nodes per layer

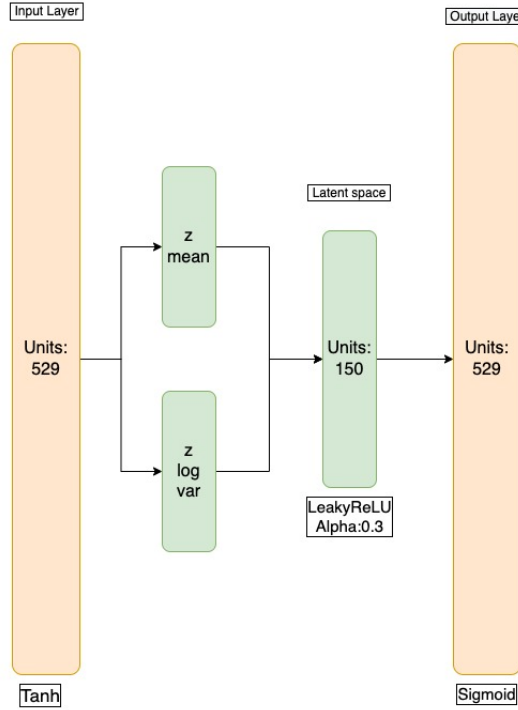


**Figure 3.20:** Small variational autoencoder architecture.

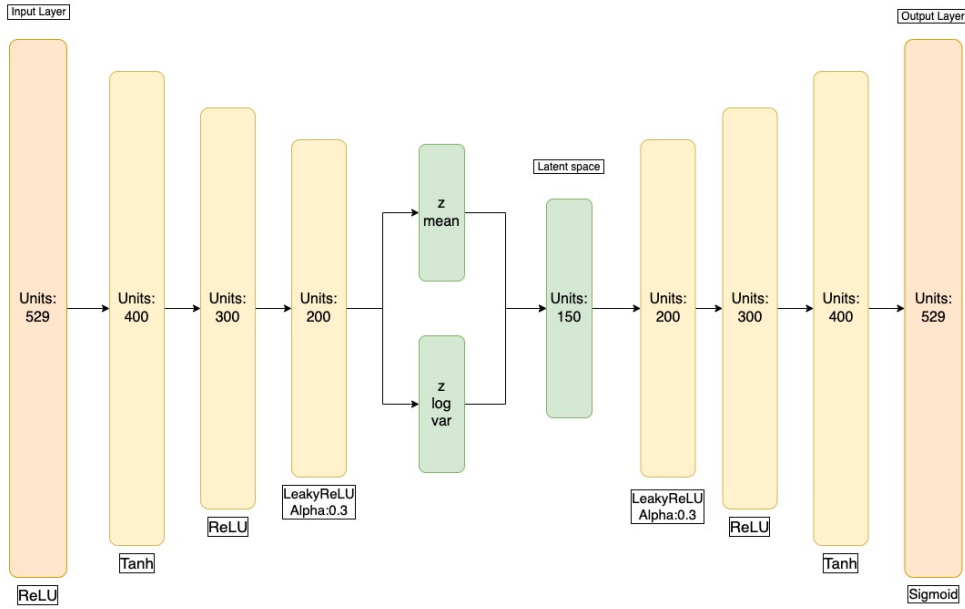


**Figure 3.21:** Large variational autoencoder architecture.

were chosen based on earlier work done on the ATLAS open data[43], as well as some light hyperparameter testing using Keras-Tuner[44].

### 3.7 The search strategy

The strategy used to look for anomalies in the 3 lepton + missing energy final state is presented here. First, the SM MC and ATLAS data for training and inference are constructed with the RMM from section 3.4 as features. After scaling and splitting, 80% of the MC will be used for training the neural network, and the remaining 20% will be used for inference. The reconstruction error from inference will then be used to

separate the anomalies from background. The hope is that the anomalous events will be skewed towards higher reconstruction errors.

Standard analyses rely on what is called a signal region. The signal region is a region in the feature space in which the signal is expected to be enriched. These are often not inspected until all analysis selections are fixed ("blind" analysis). We use this region to calculate the significance of a result in the search, which is really the only metric that is of use. The statistical uncertainty and noise is proportional to the amount of SM MC, thus with lower amounts of SM MC, the better the significance will be. This is *a*) given that the signal does not reduce in the same (or more extreme) manner and *b*) that one does not run out of SM MC statistics. Because otherwise one does not have any predictive power anymore. Using the reconstruction error, the autoencoder can create its own signal region, more specifically the areas of high reconstruction error. By placing a cut at "high" reconstruction error one can look at e.g. the missing transverse energy or other features of interest to see if the AE has managed to select events which have anomalous behavior (wrt. the SM) in these distributions. I.e. the cut on the reconstruction error from the AE replaces the pre-selection cuts one typically design in an ordinary cut-and-count analysis using traditional kinematic variables.

The signal regions for the regular autoencoder models were created by calculating the median  $m_{err}$  of the reconstruction error. Then, 3 cuts were made, starting at  $m_{err} + im_{err}/5$  for  $i = 1, 2, 3$ . This was a direct result of the shape of the background reconstruction error being a hill-like shape. The median then became a good place to start to remove much of the SM MC. This is however just a guess for an optimal signal region, as the true signal is unknown, and the method has to be as unbiased as possible. There is however an issue to keep in mind here. The method to find the cut is in some sense based on the slope shape of the SM MC reconstruction error distribution, thus three cuts based on the median seems like a good choice. However, if one then uses all the events in the signal region, it might be that one misses the ideal amount of background and signal to create the significance<sup>26</sup>. Thus, for each reconstruction error cut, there is an associated plot showing the significance as a function of  $e_T^{miss}$  for the events passing a given cut on the AE reconstruction error. The  $e_T^{miss}$  would be the final discriminating variable for where we look for deviations from the expected SM background. Thus, you can find the ideal cut, within the signal region, for where to choose the amount of background and signal to get a better significance.

Since the analysis is based on semi supervised learning, one should avoid tuning on specific signal models. Therefor one should also prepare a blind test.

## Testing strategy

Before testing the AE and VAE on signal samples, it is interesting to test the sensitivity of both the regular and variational autoencoders on anomalous SM MC events. This can be thought of as initial testing.

### Channel removing

One idea was to test the anomaly detection capability by removing one of the channels in the SM. The idea was that some of the channels differ enough in the final states and thus in their RMM signature that they might be treated like anomalous data by the autoencoders. All channels were tested on as signal.

### Altering transverse momentum

Another idea for anomaly detection testing with the SM MC was to alter the transverse momentum of some particles. Random events were selected, and their transverse energy was changed by scaling it with a factor. The hope is that especially events with at least a scaling of 5 in transverse momentum should be picked up. Note that by changing the transverse momentum, the elements in the RMM related to the difference in transverse energy between the objects change. From equation 3.7 we see that a scale change  $k$  in  $p_T$  yields the following new relation:

$$\delta e_T^k = \frac{kE_T(i_n - 1) - E_T(i_n)}{kE_T(i_n - 1) + E_T(i_n)}, n = 2, \dots, N. \quad (3.8)$$

Thus, both the transverse energy and the difference in transverse energy between the various objets are changed for this test.

---

<sup>26</sup>Only 20% of the background and 100% of the signal are used for inference. This is important to know when evaluating the significance plots, as to not overinflate the results provided by the AE's and VAE's.

## Signal testing

It is not correct to refer to the machine learning algorithm used in this thesis as unsupervised learning. This is mostly due to the fact that we show it labeled MonteCarlo to train on, and thus essentially gives the models a target to aim for. But, since we do not show the autoencoders any signals in training, it can be allowed to name the learning strategy as semi-supervised learning. Because of this, one does not bias oneself too much if the algorithm is tested on one or more signal samples. This type of testing can be separated into two different categories, the open signal testing and the blind signal testing.

The open signal testing first takes a trained model that has only seen SM MC and then runs inference on both SM MC and the given signal. Then the search strategy mentioned in the previous section is done on those collected reconstruction error distributions.

The blind signal testing is the final test, where a dataset is prepared encapsulating SM MC or ATLAS data, and one or multiple signals. The labels are kept, for verification. That way, if one were to do open signal testing on many signal samples from many theories, one could in principle bias oneself too much. This way one can get an unbiased measurement of the performance.



# Chapter 4

## Results and Discussion

### 4.1 Non signal testing of the regular and variational autoencoder

#### Channel removing

Results following removal of specific channels are shown in figures 4.1 - 4.6. The left plots in the figures show the results from the small AE while the right plots show the corresponding result using the large AE. Figure 4.1 - 4.3 show the results where the Higgs, single top and ttbar channel, respectively, has been removed in the training of the AE. The inference of the AE is applied on the removed process (shown as markers in the distributions). Figure 4.4 - 4.6 show the corresponding results using a variational autoencoder. These three channels were chosen since they are the most unlike the rest of the background channels.

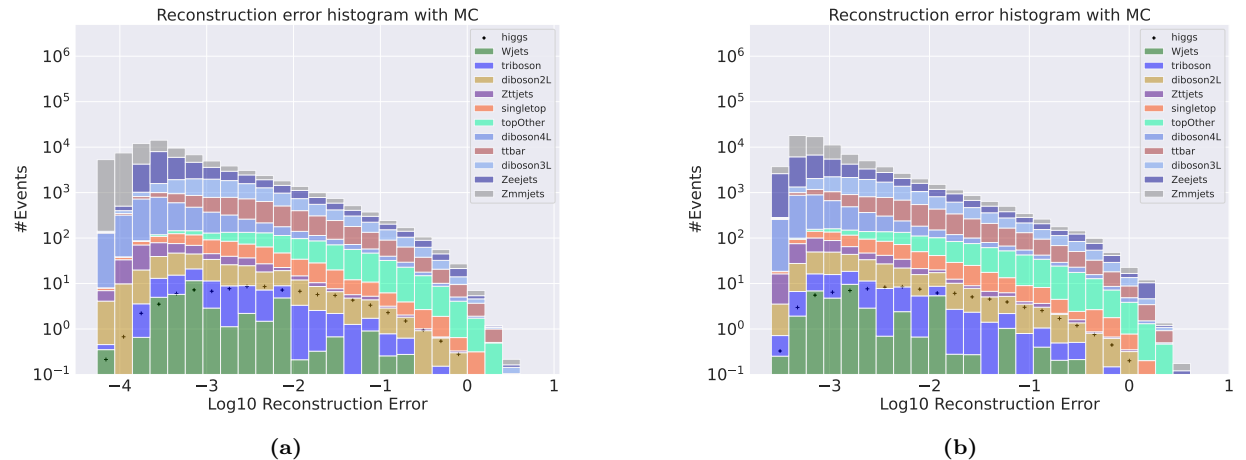


**Figure 4.1:** Reconstruction error on validation SM MC from the small (a) and large (b) autoencoders. The Higgs channel has been removed from training and is used as signal. No significant difference in distributions is found.

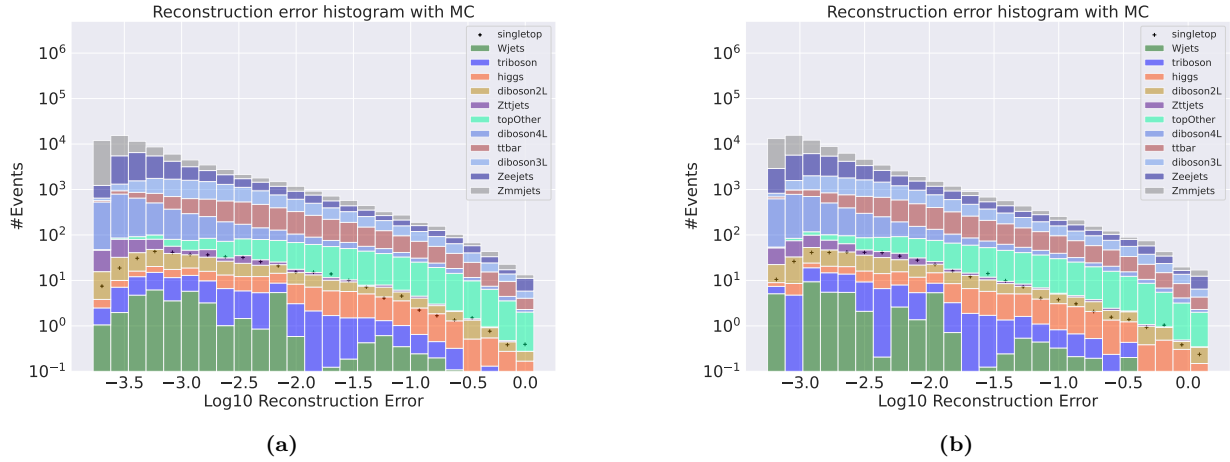


**Figure 4.2:** Reconstruction error on validation SM MC from the small (a) and large (b) autoencoders. The single top channel has been removed from training and is used as signal. No significant difference in distributions is found.

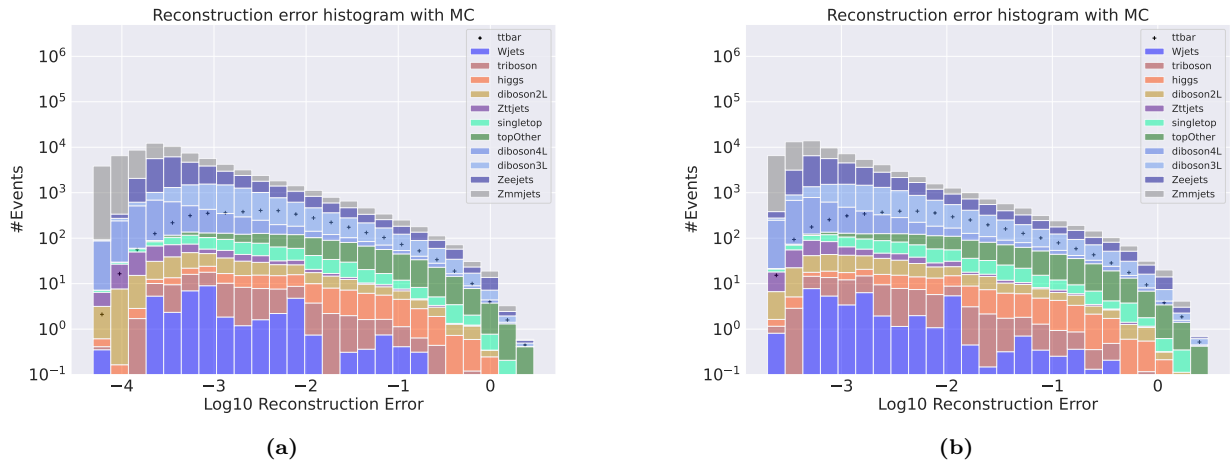


**Figure 4.3:** Reconstruction error on validation SM MC from the small (a) and large (b) autoencoder. The ttbar channel has been removed from training and is used as signal. No significant difference in distributions is found.

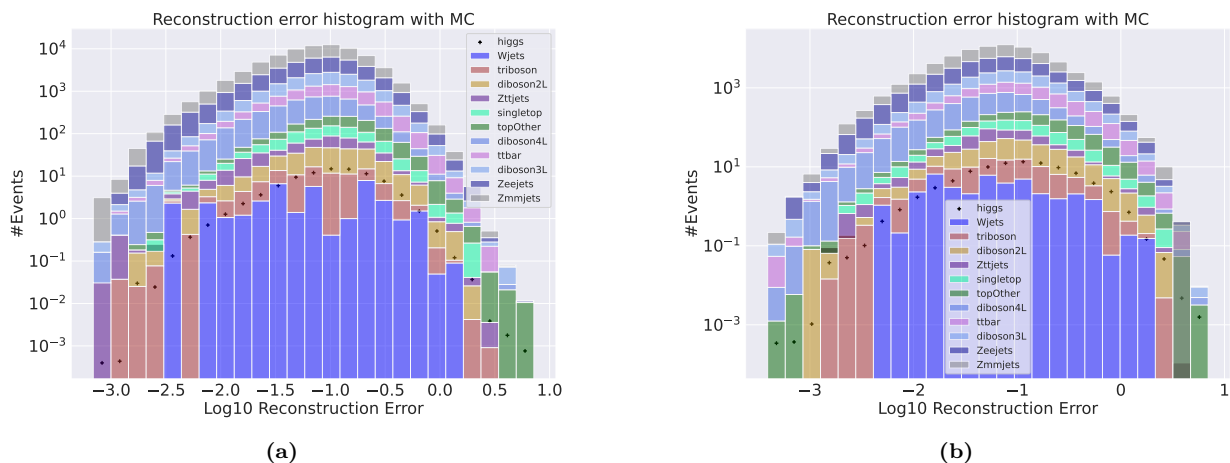


**Figure 4.4:** Reconstruction error on validation SM MC from the small (a) and large (b) variational autoencoder. The Higgs channel has been removed from training and is used as signal. No significant difference in distributions is found.

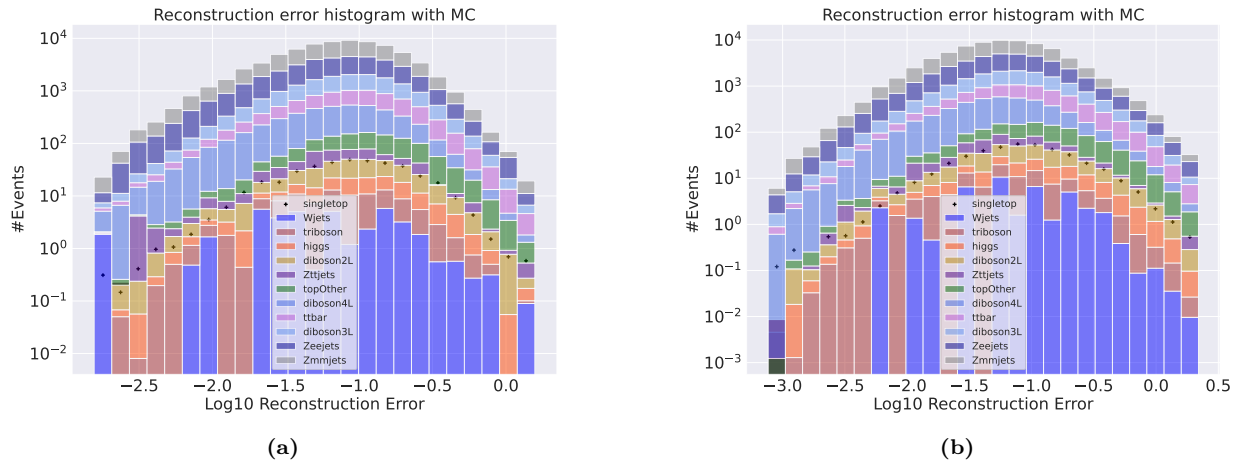


**Figure 4.5:** Reconstruction error on validation SM MC from the small (a) and large (b) variational autoencoder. The single top channel has been removed from training and is used as signal. No significant difference in distributions is found.

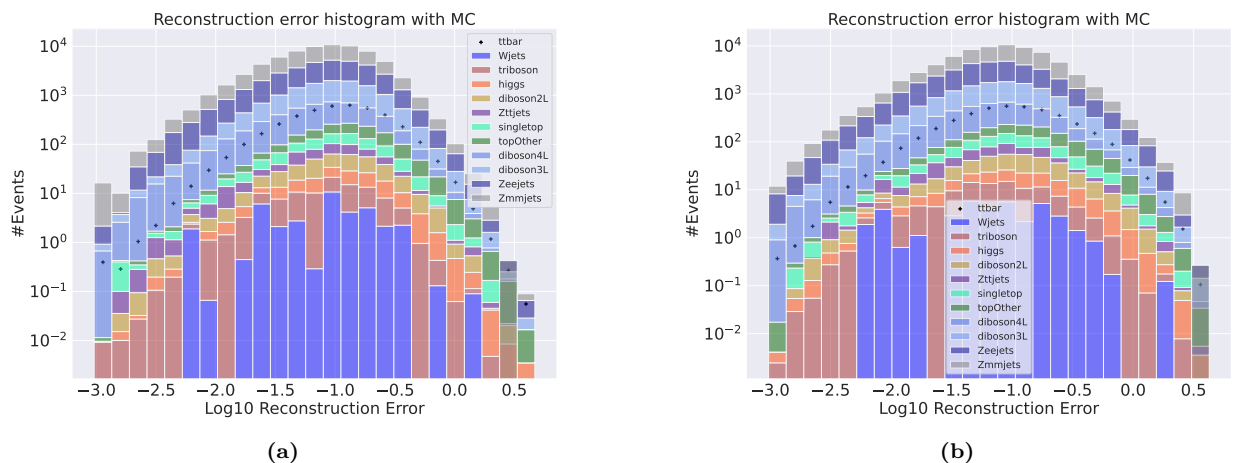


**Figure 4.6:** Reconstruction error on validation SM MC from the small (a) and large (b) variational autoencoder. The ttbar channel has been removed from training and is used as signal. No significant difference in distributions is found.

It is clear from figures that the reconstruction error distributions for the removed SM channel and the remaining SM MC are very similar. The same behavior is also shown for the other channels, which can be found in section A.1 in the appendix. Although the two models did not demonstrate much separation of reconstruction error distributions, the regular autoencoder seems to have a more shifted pattern of reconstruction to lower values than the variational autoencoder. In fact, the regular autoencoder's reconstruction error distribution peak is about 3 order of magnitude lower than the variational autoencoder's error distribution peak along the x-axis. There could be several reasons for this, one of which could be that the variational autoencoder might require more input data to approximate the distribution, as well as the fact that the balance between the KL divergence and MSE loss can be difficult to handle[45]. The variational autoencoder is a larger and more complex model. Given that the natural distributions in the data are quite complex, learning the natural distribution might require more data. This can lead to comparably poorer performance of the neural network compared to the regular autoencoder. It should be noted that although the three channels selected here, as well as the rest in section A.1 in the appendix, do not differ that much from one another, and it was not expected that the networks would be able to separate the two distributions created. However, it does provide us with a baseline, as well as insight for what to expect if we were to test on signals that look a lot like some background channels.

## Altering of transverse momentum

Altering the transverse momentum of some particles would in the extreme be anomalous, and the hypothesis was that some of those trends would be picked up by the autoencoder. Scaling of  $k \in [1.5, 3, 5, 7, 10]$  for the

transverse momentum were used according to equation 3.8. A scaling of  $p_T$  for the regular and variational autoencoder are shown in figures 4.7 and 4.8, respectively. The other scaling plots can be found in section A.2 in the appendix.

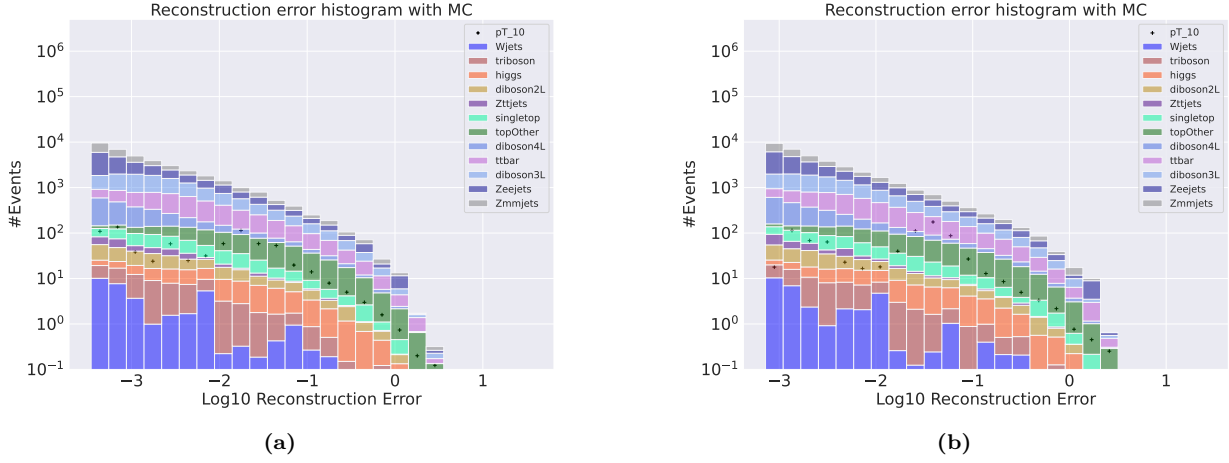


**Figure 4.7:** Reconstruction error on validation SM MC from the small (a) and large (b) regular autoencoder. The signal is a subsample of the validation set where the transverse momentum of the first electron and the first muon has been increased with a scale of 10. The difference in transverse energy between the objects has also been changed according to the scaling of transverse momentum. A peak is found around  $10^{-1.6}$ .

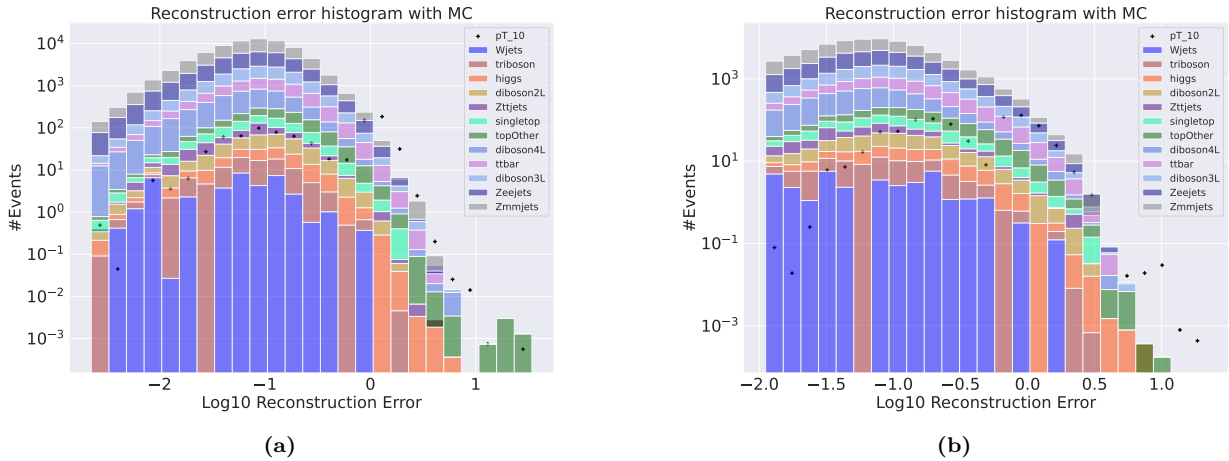


**Figure 4.8:** Reconstruction error on validation SM MC from the small (a) and large (b) variational autoencoder. The signal is a subsample of the validation set where the transverse momentum of the first electron and the first muon has been increased with a scale of 10. The difference in transverse energy between the objects has also been changed according to the scaling of transverse momentum. A peak is found around  $10^{-1.6}$ .

The first thing to notice here is that, as with the channel removal, the distribution shape of the output from the regular autoencoder compared to the variational autoencoder is different. The shape from the regular autoencoder is clearly shifted to the left end, with low reconstruction error compared to the shape from the variational autoencoder, where the peak of the distribution is around -1. From the  $p_T$  altering test we also see here that the variational autoencoder falls short to the regular one. It is also interesting to observe here that the high  $p_T$  events are picked up as anomalous from both autoencoders, with both shallow and deep structure. In the regular autoencoder it is arguably even separated distributions. This is also a good sign as it indicates that the network has learned which ranges the  $p_T$  should be in for the 3 lepton plus missing energy final state. The most extreme case is, as expected, in the case where the  $p_T$  is multiplied by 10. There is a clear separation in reconstruction error distributions for the signal and background for the deep regular autoencoder, and a slightly more subtle separation of reconstruction error distributions for the shallow regular autoencoder. For the variational autoencoder, the separation in figure 4.8 is not as clear, but the signal is still picked up as anomalous. The peaks are separated, but not to the same degree.

## 4.2 3 lepton training for high $e_T^{miss}$ and invariant mass search

To better ascertain and map the usefulness of the regular and variational autoencoder in the search for new physics, two MC signals were used as test cases. They are both 3 lep + $e_T^{miss}$  final state SUSY signals, and thus are a suitable fit to use for testing. The two autoencoders were tested on four metrics.

- Low reconstruction error on SM MC
- Background to signal ratio in  $e_T^{miss}$  signal region
- Large tail or possible resonance in trilepton signal region
- Significance scan in  $e_T^{miss}$  signal region

### Regular autoencoder output

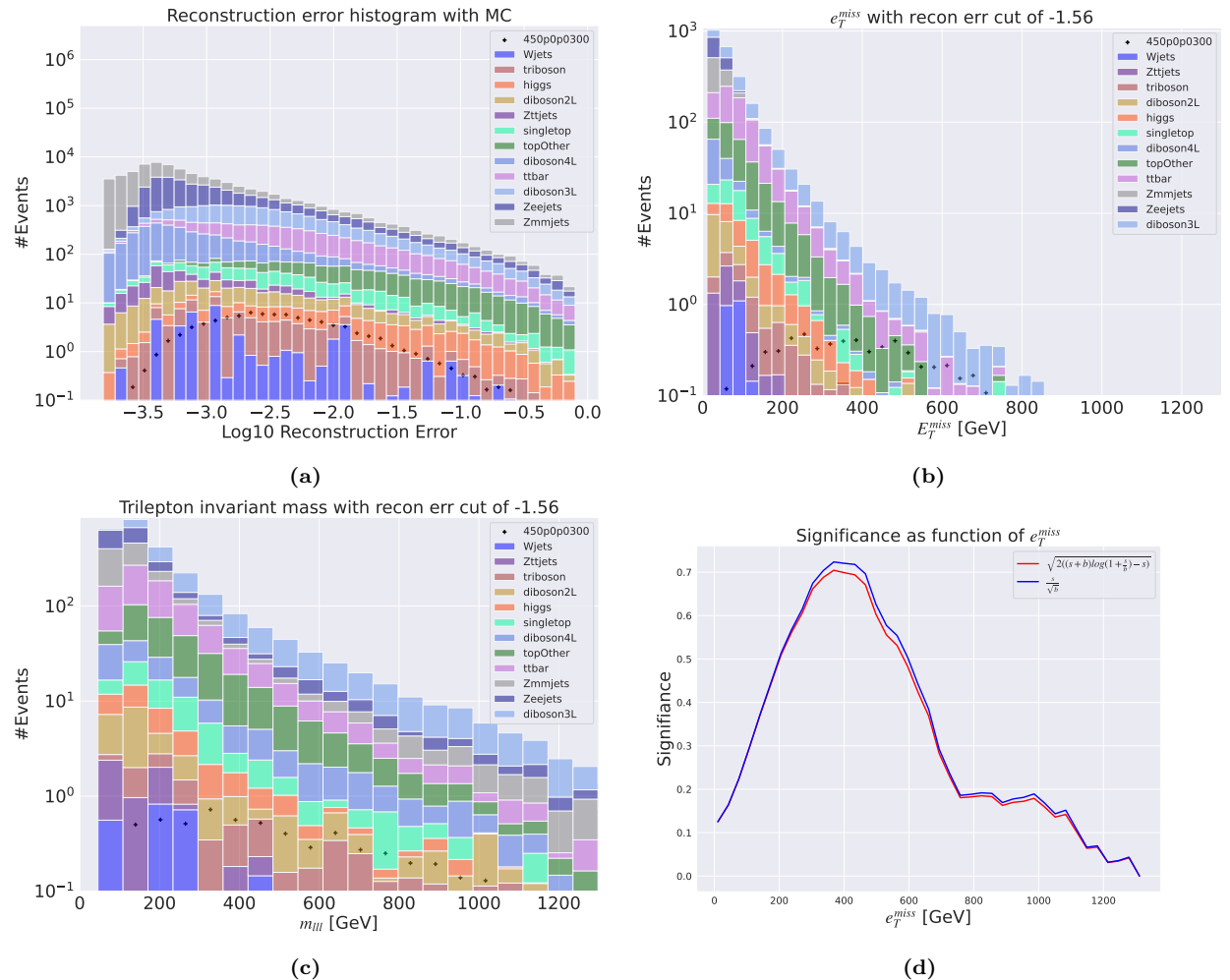


**Figure 4.9:** Reconstruction error,  $e_T^{miss}$  signal region,  $m_{lll}$  signal region and significance as function of  $e_T^{miss}$  for the deep regular autoencoder using the SUSY 450p300. Figure 4.9a shows the reconstruction error distribution for the SM MC and the SUSY signal. Here the autoencoder produces the same reconstruction error shape for both background and signal. Figure 4.9b shows the  $e_T^{miss}$  distribution for the SM MC and the SUSY signal in the signal region, defined as the region having a  $\log_{10}$  reconstruction error above -1.56. Most of the background is removed, and the signal distribution is clearly shifted towards higher values of  $e_T^{miss}$  compared with SM MC. Figure 4.9c shows the  $m_{lll}$  distribution for the SM MC and the SUSY signal. The shape of the SM MC and the signal distributions are too similar to distinguish. Figure 4.9d shows the significance as function of  $e_T^{miss}$ . The maximum significance is found when applying a cut of about > 380 GeV in the  $e_T^{miss}$ , with a significance of around 0.7.

Figures 4.9, 4.10, 4.11 and 4.12 contain four subplots each showing the total reconstruction error distributions (a), the  $e_T^{miss}$  signal regions (b), the  $m_{lll}$  signal regions (c) and the significances as function of

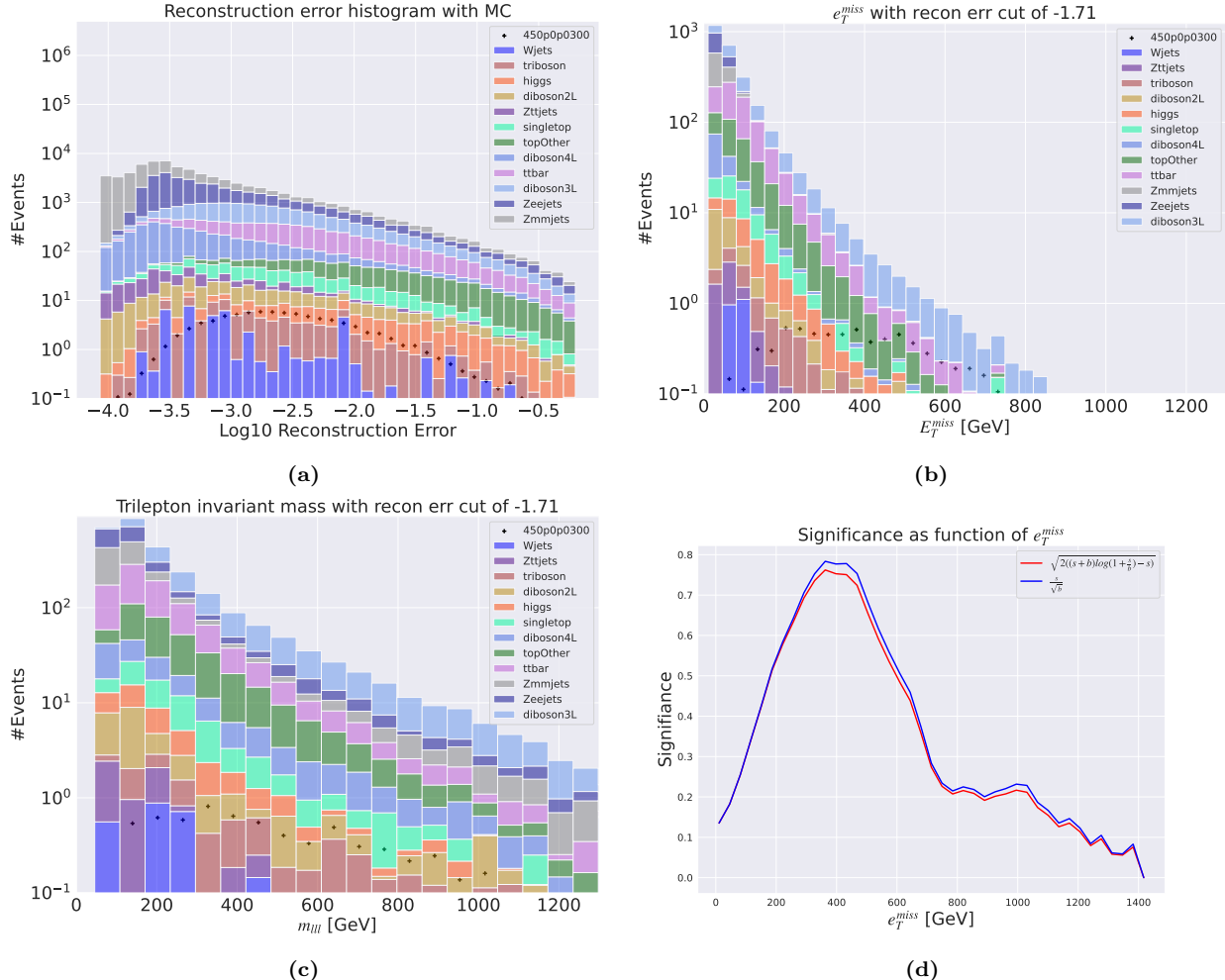


**Figure 4.10:** Reconstruction error,  $e_T^{\text{miss}}$  signal region,  $m_{lll}$  signal region and significance as function of  $e_T^{\text{miss}}$  for the shallow regular autoencoder using the SUSY 450p300 model. Figure 4.10a shows the reconstruction error distribution for the SM MC and the SUSY signal. Here the autoencoder produces the same reconstruction error shape for both background and signal, but with a small separation of the peaks of the distributions. Figure 4.10b shows the  $e_T^{\text{miss}}$  distribution for the SM MC and the SUSY signal in the signal region, defined as the region having a  $\log_{10}$  reconstruction error above -1.71. Most of the background is removed, and the peaks of the SM MC and signal distributions are somewhat separated. Figure 4.10c shows the  $m_{lll}$  distribution for the SM MC and the SUSY signal. The shape of the SM MC and the signal distributions are too similar to distinguish. Figure 4.10d shows the significance as function of  $e_T^{\text{miss}}$ . The maximum significance is found when applying a cut of about  $> 380$  GeV in the  $e_T^{\text{miss}}$ , with a significance of around 0.78.

a lower cut on  $e_T^{\text{miss}}$  curve (d) for the shallow (figure 4.10 and 4.12) and deep (figure 4.9 and 4.11) regular autoencoder using two different SUSY scenarios for inference. From figures 4.9a - 4.12a it is clear that the autoencoders struggles more to reconstruct the 800p50 point (i.e. more anomalous, higher reconstruction error) compared with the 450p300 point, which is expected from the fact that the 800p50 point has a larger mass difference between the chargino and the lightest supersymmetric particle and thus would lead to more missing transverse energy in the events. The steepness of the slopes of the reconstruction error show quite similar behavior for both the shallow and deep regular autoencoders, indicating that the performance of these two models does not differ. The bulk of the events are below  $10^{-2}$  reconstruction error, indicating that the autoencoder has learned a lot of the internal RMM structures for the 3 lepton +  $e_T^{\text{miss}}$  final state MC.

In figures 4.9b, 4.10b, 4.11b and 4.12b signal regions are created for each of the two SUSY models for both the shallow and deep regular autoencoder. The cuts were created using the median and then iteratively increasing the error requirement, as explained in section 3.7. Only one of the three cuts done are shown here, the rest can be found in appendix A.3. The most inclusive signal region is chosen in order to illustrate the difficulty of the anomaly detection method since we do not have any idea how anomalous (i.e. how large reconstruction error) we expect a BSM signal to have. A too strict a cut could possibly eliminate a large

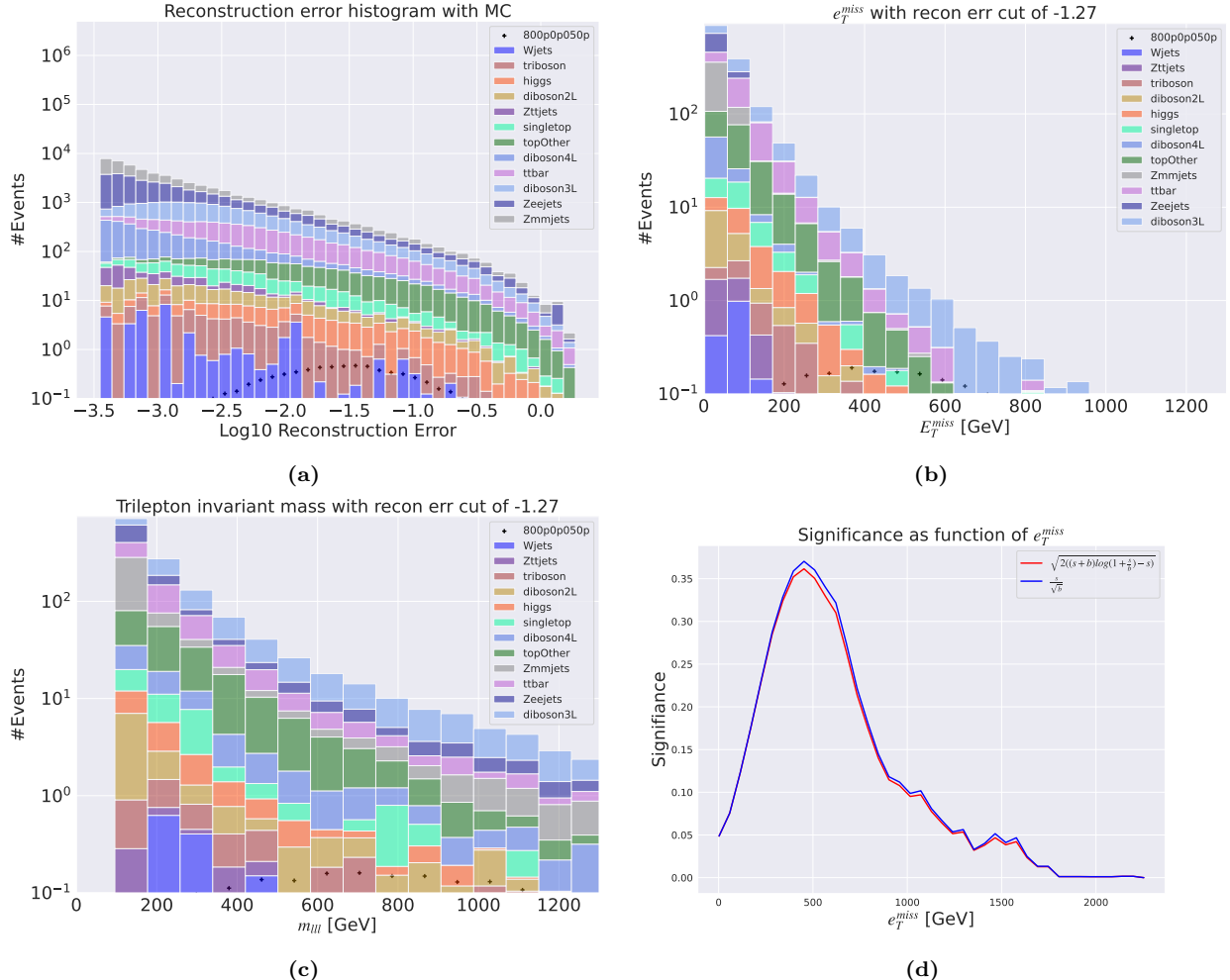


**Figure 4.11:** Reconstruction error,  $e_T^{miss}$  signal region,  $m_{lll}$  signal region and significance as function of  $e_T^{miss}$  for the deep regular autoencoder using the SUSY 800p50. Figure 4.11a shows the reconstruction error distribution for the SM MC and the SUSY signal. Here the autoencoder produces a mirrored reconstruction error shape for background and signal. The peaks of the two distributions are separated with two orders of magnitude in reconstruction error. Figure 4.11b shows the  $e_T^{miss}$  distribution for the SM MC and the SUSY signal in the signal region, defined as the region having a  $\log_{10}$  reconstruction error above -1.27. Most of the background is removed, and the peaks of the SM MC and signal distributions are separated. Figure 4.11c shows the  $m_{lll}$  distribution for the SM MC and the SUSY signal. The shape of the SM MC and the signal distributions are somewhat separated. Figure 4.11d shows the significance as function of  $e_T^{miss}$ . The maximum significance is found when applying a cut of about  $> 430$  GeV in the  $e_T^{miss}$ , with a significance of around 0.37.

fraction of the signal events in the signal region, whereas a too loose a cut would result in the SM MC background dominating completely.

In figures 4.9c, 4.10c, 4.11c and 4.12c the  $m_{lll}$  distributions for the most inclusive signal regions from both the shallow and deep regular autoencoder for both of the SUSY signals. The results from the most inclusive signal region is shown here while the rest can be found in appendix A.3. The difference observed in the  $m_{lll}$  distribution between the SM MC and signal are small for both the shallow and deep autoencoders. This is expected considering the signal modeling being used, which do not have any particular resonance in the three-lepton invariant mass.

In figures 4.9d, 4.10d, 4.11d and 4.12d the significance as a function of applying a lower cut on  $e_T^{miss}$  is shown. It displays that an additional cut on  $e_T^{miss}$  leads to an increased significance. The best case is achieved for the SUSY 450p300 signal using the shallow autoencoder, leading to a significance of 0.78. Although the autoencoders gave a larger reconstruction error for the high-mass SUSY signal the final significance is found to be higher for the low mass SUSY signal. This is due to the cross section being a factor of 15 larger for the 450p300 model compared with the 800p50 model.

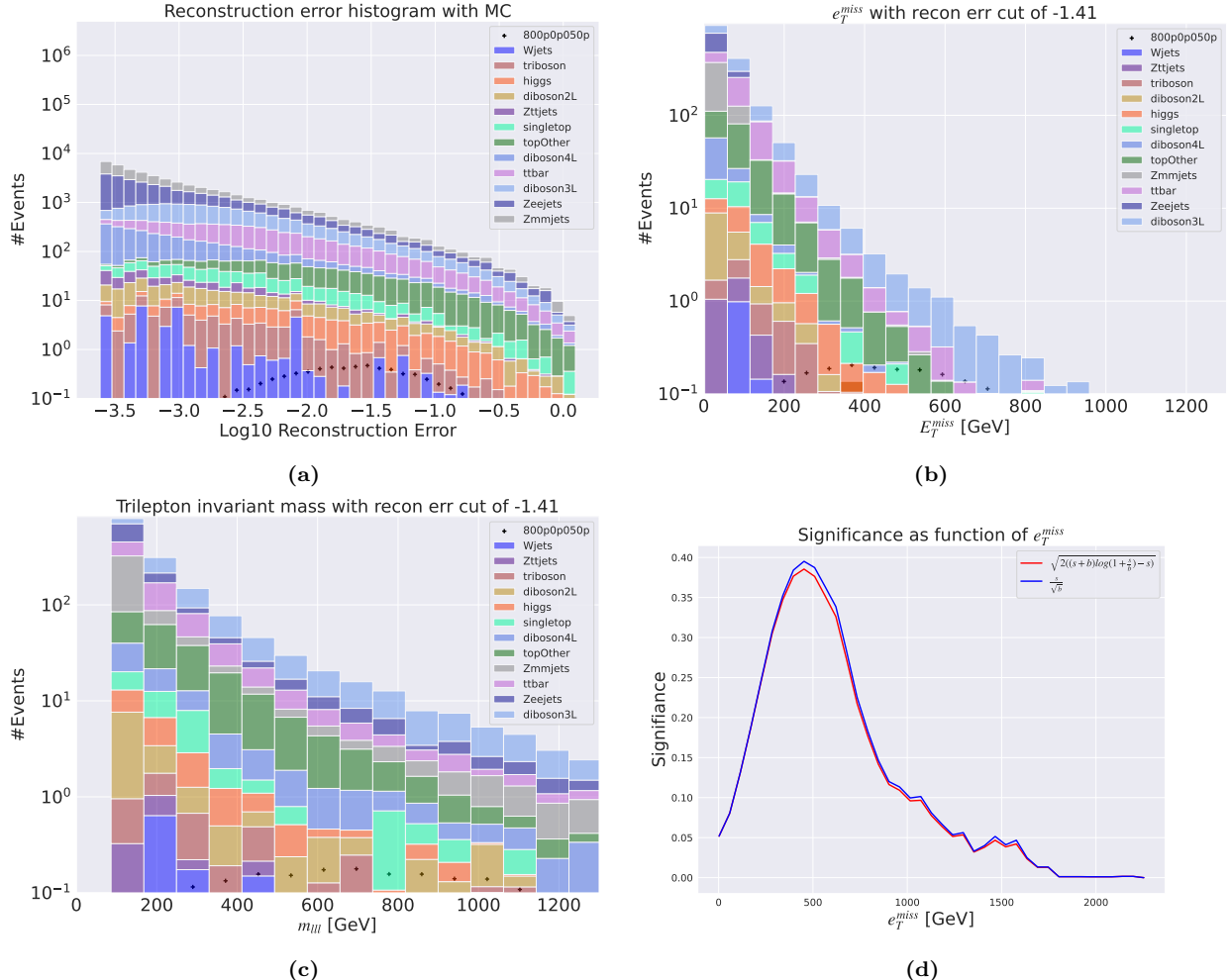


**Figure 4.12:** Reconstruction error,  $e_T^{miss}$  signal region,  $m_{lll}$  signal region and significance as function of  $e_T^{miss}$  for the shallow regular autoencoder using the SUSY 800p50. Figure 4.12a shows the reconstruction error distribution for the SM MC and the SUSY signal. Here the autoencoder produces a mirrored reconstruction error shape for background and signal. The peaks of the two distributions are separated with two orders of magnitude in reconstruction error. Figure 4.12b shows the  $e_T^{miss}$  distribution for the SM MC and the SUSY signal in the signal region, defined as the region having a  $\log_{10}$  reconstruction error above -1.41. Most of the background is removed, and the peaks of the SM MC and signal distributions are separated. Figure 4.12c shows the  $m_{lll}$  distribution for the SM MC and the SUSY signal. The shape of the SM MC and the signal distributions are somewhat separated. Figure 4.12d shows the significance as function of  $e_T^{miss}$ . The maximum significance is found when applying a cut of about > 450 GeV in the  $e_T^{miss}$ , with a significance of around 0.39.

### Variational autoencoder output

The corresponding results for the variational autoencoders are shown in Figure 4.13 - 4.16 following the same outline as used in section ???. From figures 4.13a, 4.14a, 4.15a and 4.16a we observe that the variational autoencoder seems to struggle with differentiating between background and signal. There is however a slight difference in the shape of the distributions from the shallow and deep network shown for both of the SUSY signal samples. The shallow VAEs have typically a more narrow and slightly more left-skewed shape, whereas the deep network has a slightly more broad distribution shifted a bit to the right. The bulk of the events for all four histograms are between  $10^{-2}$  and  $10^{-0.5}$  reconstruction error, indicating that the autoencoder struggles to learn the internal RMM structures for the 3 lepton +  $e_T^{miss}$  final state MC.

In figures 4.13b, 4.14b, 4.15b and 4.16b we have the reconstruction error cut imposed on the SM MC and the signal samples. Interestingly, one should note that although the total reconstruction error distributions are not well separated, the signal regions show a separation in the  $e_T^{miss}$  distribution. Unlike in the regular autoencoder case, the variational autoencoder allows for almost two orders of magnitude more background events in the signal region. This is because of the signal region definition from section 3.7 where the median for all four cases with the variational autoencoder is exactly at the peak of the reconstruction error distribution

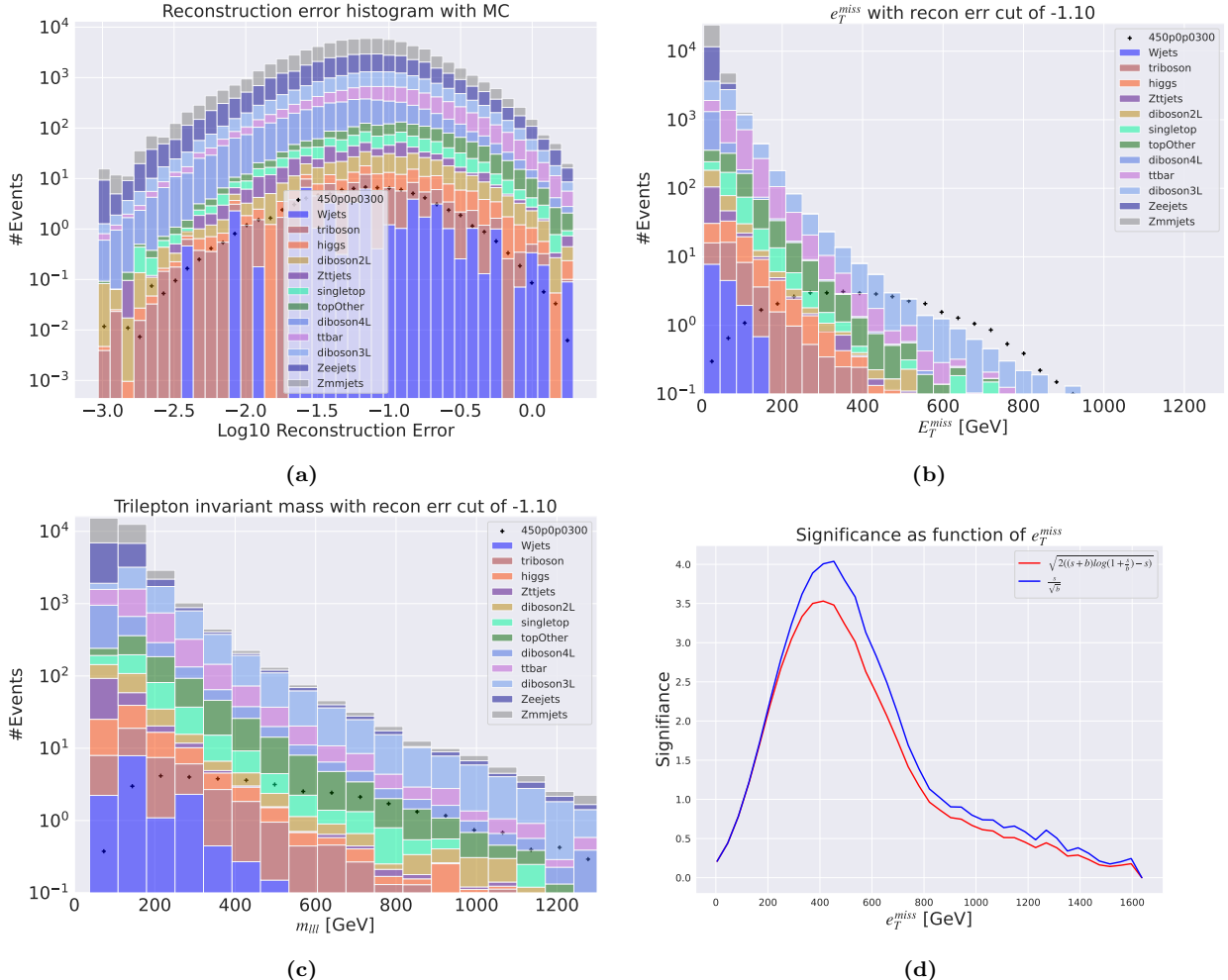


**Figure 4.13:** Reconstruction error,  $e_T^{miss}$  signal region,  $m_{lll}$  signal region and significance as function of  $e_T^{miss}$  for the deep variational autoencoder using the SUSY 450p300. Figure 4.13a shows the reconstruction error distribution for the SM MC and the SUSY signal. Here the autoencoder produces a hill-like for background and signal with little distinction. The peaks of the two distributions are not separated in reconstruction error. Figure 4.13b shows the  $e_T^{miss}$  distribution for the SM MC and the SUSY signal in the signal region, defined as the region having a  $\log_{10}$  reconstruction error above -1.10. Some background is removed, and the peaks of the SM MC and signal distributions are separated. Figure 4.13c shows the  $m_{lll}$  distribution for the SM MC and the SUSY signal. The shape of the SM MC and the signal distributions are displaying almost the same shape. Figure 4.13d shows the significance as function of  $e_T^{miss}$ . The maximum significance is found when applying a cut of about > 450 GeV in the  $e_T^{miss}$ , with a significance of around 4.1.

for the background. Therefor we also get the peak of the signal distributions, which is why we see so much signal in the signal region in figures 4.13b, 4.14b, 4.15b and 4.16b.

As expected the separation between SM MC and signal in the  $m_{lll}$  distribution, shown in Figure 4.13c - 4.16c, is less prominent compared with the  $e_T^{miss}$  distribution. The performance of the deep and shallow VAE, based on the separation of SM MC and signal in the signal regions, are very similar.

In figures 4.13d, 4.14d, 4.15d and 4.16d we have the significance as a function of the  $e_T^{miss}$ . Interestingly, for the SUSY 450p300 case, we have that both the deep and shallow autoencoder manages to get a significance of around 4, which is much better than the regular autoencoder which got around 0.7. For the SUSY 800p50 signal the difference between the significance from the AE and VAE was small. A cut at  $e_{T}^{miss} > 400$  GeV provided the best significance of around 4.5 for the 450p300 signal point using the signal region defined by a cut in the reconstruction error of  $10^{-1.1}$  ( $10^{-1.06}$ ) using a deep (shallow) VAE.

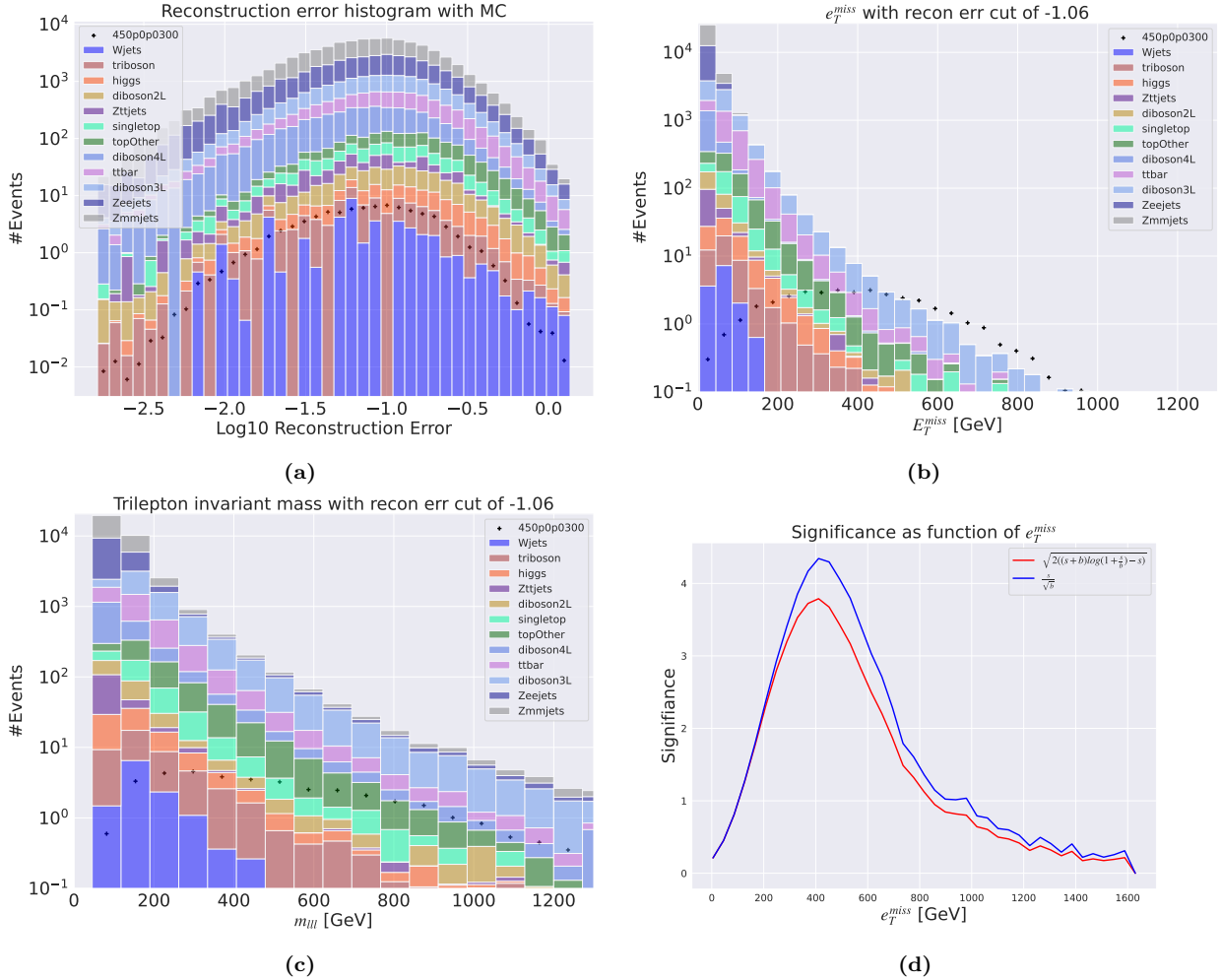


**Figure 4.14:** Reconstruction error,  $e_T^{miss}$  signal region,  $m_{lll}$  signal region and significance as function of  $e_T^{miss}$  for the shallow variational autoencoder using the SUSY 450p300. Figure 4.14a shows the reconstruction error distribution for the SM MC and the SUSY signal. Here the autoencoder produces a hill-like for background and signal with little distinction. The peaks of the two distributions are not separated in reconstruction error. Figure 4.14b shows the  $e_T^{miss}$  distribution for the SM MC and the SUSY signal in the signal region, defined as the region having a  $\log_{10}$  reconstruction error above -1.06. Some background is removed, and the peaks of the SM MC and signal distributions are separated. Figure 4.14c shows the  $m_{lll}$  distribution for the SM MC and the SUSY signal. The shape of the SM MC and the signal distributions are displaying almost the same shape. Figure 4.14d shows the significance as function of  $e_T^{miss}$ . The maximum significance is found when applying a cut of about > 400 GeV in the  $e_T^{miss}$ , with a significance of around 4.5.

### 4.3 2 lepton training for high $e_T^{miss}$ and invariant mass search

An important factor for how well AEs and VAEs perform is the availability of sufficient amount of training data. In order to better understand the effect of introducing more data for training the same procedure as in section 4.2 was followed, but now considering a data set requiring at least 2 leptons. The increase in events is from 81873 → 19291900. The requirement of at least two leptons would imply that the 3 lepton dataset used in the previous section is a subset of the 2 lepton set exploited in the following and thus the same signal samples can be used for inference. The same studies of shallow and deep regular and variational autoencoders as in section 4.2 will be performed, except that the distribution of the  $m_{lll}$  will not be considered in the following.

#### Regular autoencoder performance

This section presents some results from training the shallow and deep regular AEs and VAEs on the 2 lepton case, using the same two SUSY signals as test cases.

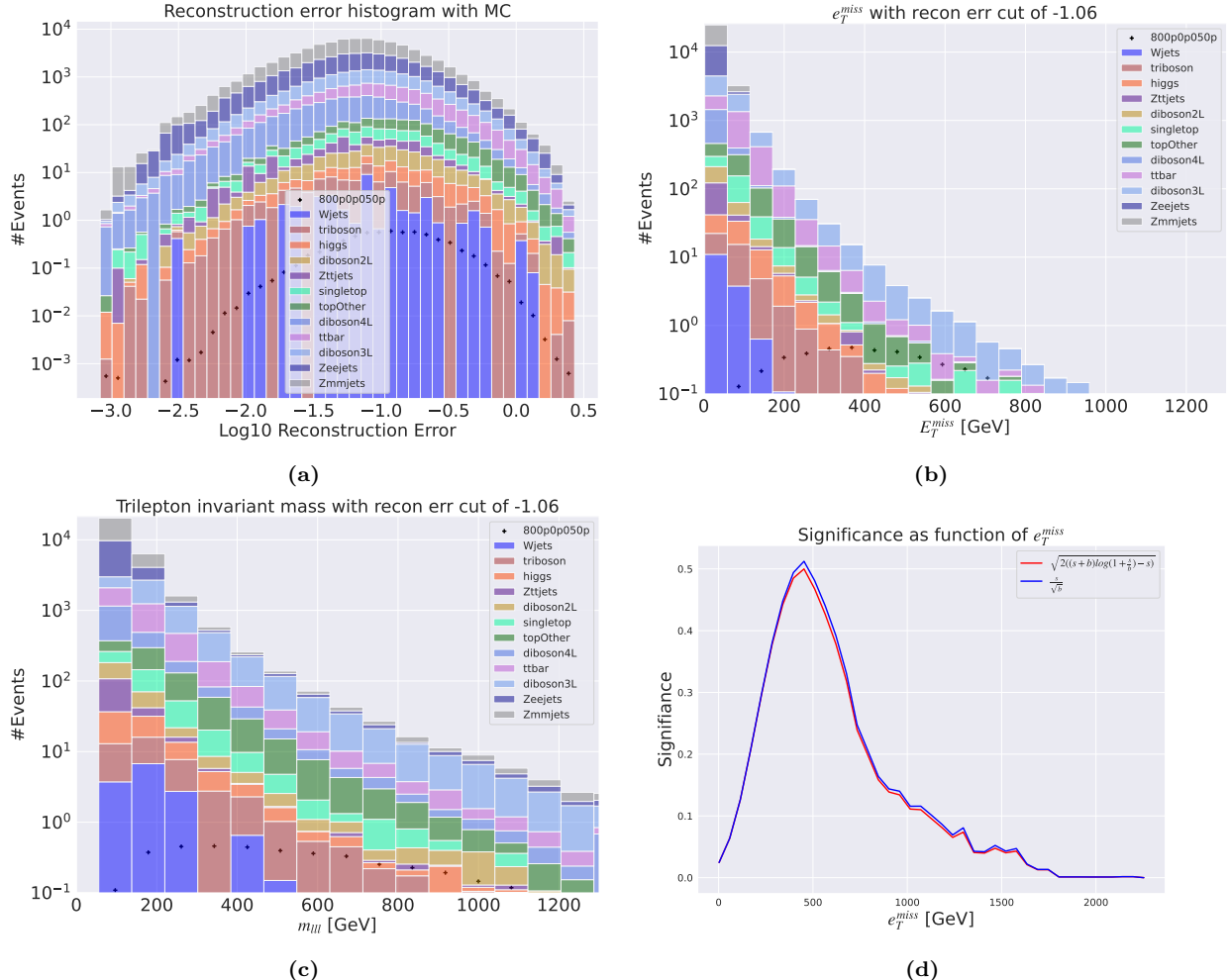


**Figure 4.15:** Reconstruction error,  $e_T^{miss}$  signal region,  $m_{lll}$  signal region and significance as function of  $e_T^{miss}$  for the deep variational autoencoder using the SUSY 800p50. Figure 4.15a shows the reconstruction error distribution for the SM MC and the SUSY signal. Here the autoencoder produces a hill-like for background and signal with little distinction. The peaks of the two distributions are not separated in reconstruction error. Figure 4.15b shows the  $e_T^{miss}$  distribution for the SM MC and the SUSY signal in the signal region, defined as the region having a  $\log_{10}$  reconstruction error above -1.06. Some background is removed, and the peaks of the SM MC and signal distributions are separated. Figure 4.15c shows the  $m_{lll}$  distribution for the SM MC and the SUSY signal. The shape of the SM MC and the signal distributions are displaying almost the same shape. Figure 4.15d shows the significance as function of  $e_T^{miss}$ . The maximum significance is found when applying a cut of about > 480 GeV in the  $e_T^{miss}$ , with a significance of around 0.6.

Figures 4.17, 4.18, 4.19 and 4.20 display three subplots each, containing the total reconstruction error distributions (a), the  $e_T^{miss}$  signal regions (b), and the significance as function of a cut in  $e_T^{miss}$  (c). By comparing the reconstruction error distributions of the AEs trained on the two lepton dataset (Figure 4.17a - 4.20a) with the corresponding figures from ones trained on the 3 lepton dataset (Figure 4.9a - 4.12a.) we see a clear tendency towards the signals having a larger reconstruction error compared with the SM MC. This indicates that as we increase the statistics, in other words the amount of background events used for training, the ability of the autoencoder to learn the internal structure increases. As expected, Z-boson production in association with jets along with  $t\bar{t}$  are the channels with the highest statistics in the 2 lepton +  $e_T^{miss}$  dataset, thus it should be easier to for the AEs to better reconstruct those events. However, note the amount of diboson in the higher end of the reconstruction error histograms, as well as in the  $e_T^{miss}$  distribution after applying a cut on the reconstruction error.

In figures 4.17b, 4.18b, 4.19b and 4.20b we have the  $e_T^{miss}$  distributions for the least strict cuts for the regular autoencoder models. The corresponding significances obtained by applying a cut in the  $e_T^{miss}$  distribution of the most inclusive signal regions are shown in figures 4.17c, 4.18c, 4.19c and 4.20c. The highest significance (of about 1.75) was found with the shallow autoencoder with the SUSY 450p300 signal model. It

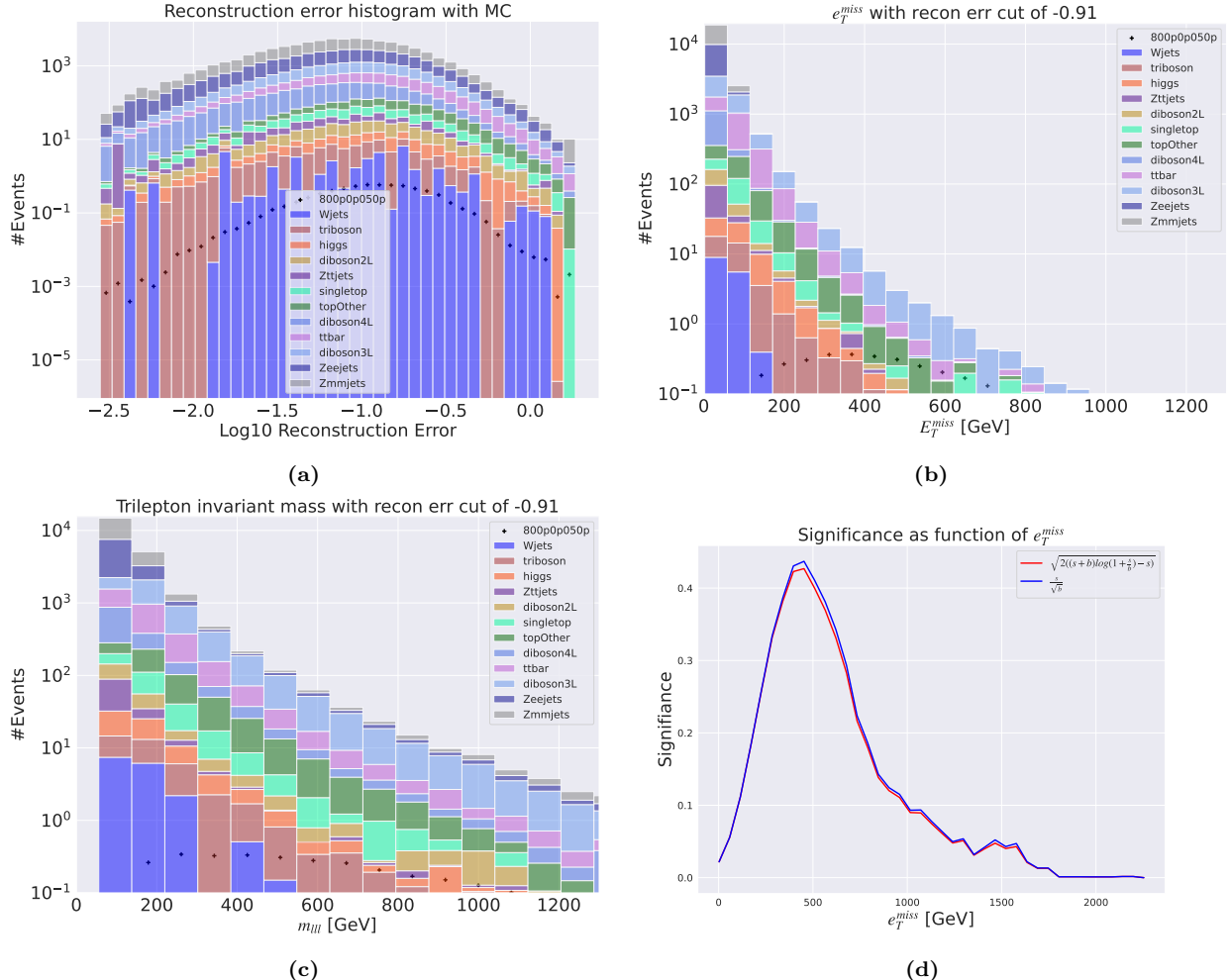


**Figure 4.16:** Reconstruction error,  $e_T^{\text{miss}}$  signal region,  $m_{lll}$  signal region and significance as function of  $e_T^{\text{miss}}$  for the shallow variational autoencoder using the SUSY 800p50. Figure 4.16a shows the reconstruction error distribution for the SM MC and the SUSY signal. Here the autoencoder produces a hill-like for background and signal with little distinction. The peaks of the two distributions are not separated in reconstruction error. Figure 4.16b shows the  $e_T^{\text{miss}}$  distribution for the SM MC and the SUSY signal in the signal region, defined as the region having a  $\log_{10}$  reconstruction error above -0.91. Some background is removed, and the peaks of the SM MC and signal distributions are separated. Figure 4.16c shows the  $m_{lll}$  distribution for the SM MC and the SUSY signal. The shape of the SM MC and the signal distributions are displaying almost the same shape. Figure 4.16d shows the significance as function of  $e_T^{\text{miss}}$ . The maximum significance is found when applying a cut of about > 480 GeV in the  $e_T^{\text{miss}}$ , with a significance of around 0.45.

should be noted that the significance for the 800p50 signal model is a lot smaller than for the 450p300 signal model, even though the separation shown in figures 4.17a, 4.18a, 4.19a, 4.20a would suggest otherwise. In order to better understand the performance of the AEs a comparison of the maximum significance obtained from a cut in  $e_T^{\text{miss}}$  before and after imposing a requirement on the reconstruction error was performed. Before any cut in reconstruction error the maximum significances obtained were 0.017 and 0.0014 for the 450p300 and 800p50 points, respectively. This can be compared with the significances of 2.4 and 0.42 obtained after the cut in reconstruction error. Note that for the results without the reconstruction error cut no other cuts were applied to enhance the signal over background ratio and thus a better significance would be expected in a more comprehensive analysis.

### Variational autoencoder performance

In figures 4.21, 4.22, 4.23 and 4.24 we have three subplots containing the total reconstruction error distributions, the  $e_T^{\text{miss}}$  signal region, and the significance as function of  $e_T^{\text{miss}}$  curve respectively. They were created using the shallow and deep regular autoencoder with the 2 lepton +  $e_T^{\text{miss}}$  dataset.

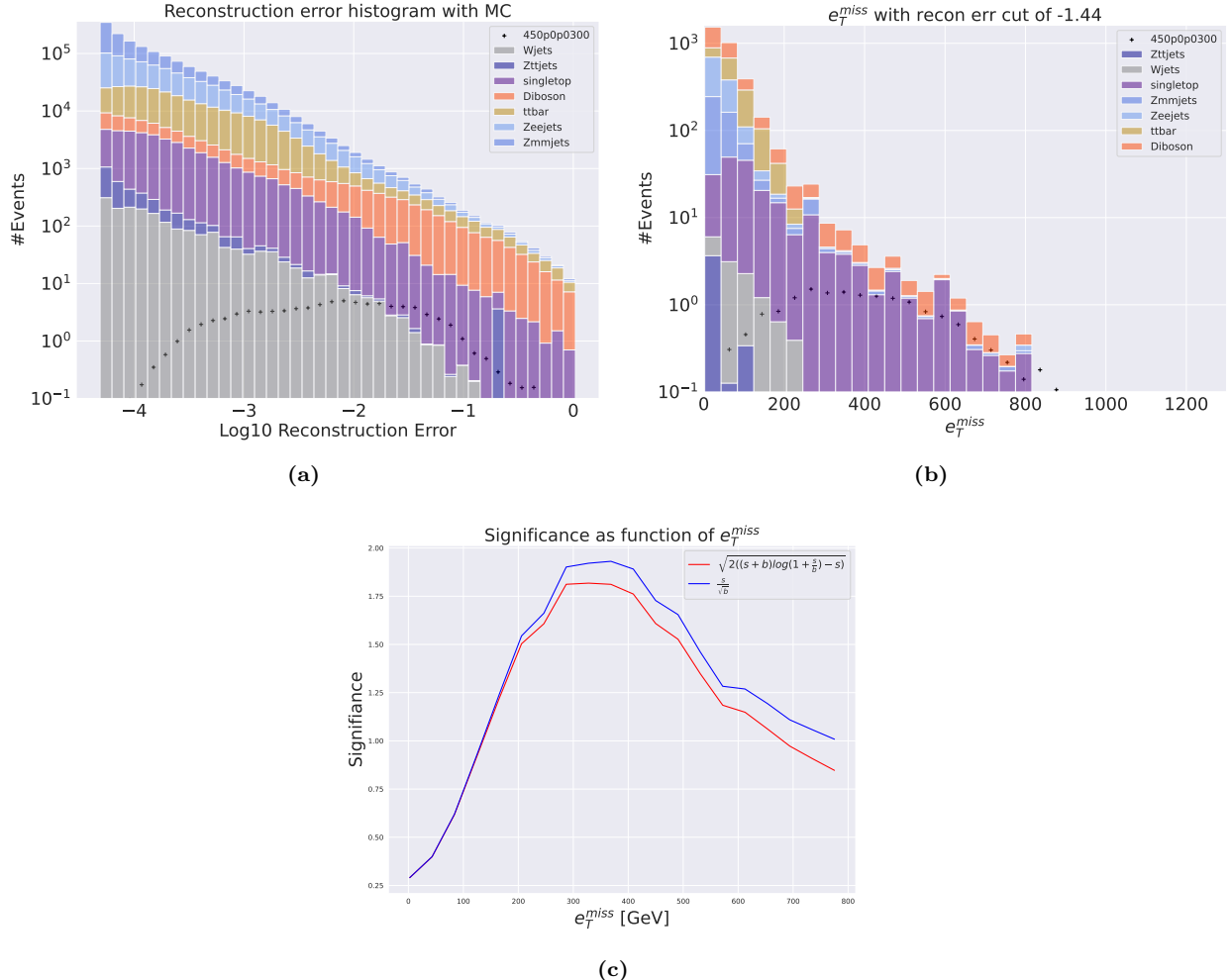


**Figure 4.17:** Reconstruction error (a),  $e_T^{miss}$  signal region (b) and significance as function of  $e_T^{miss}$  (c) for the deep regular autoencoder using SUSY 450p300. (a) shows the reconstruction error distribution for the SM MC and the SUSY signal. The autoencoder produces a slope-like shape that is highly shifted to the lower end of the reconstruction error range for the background. The signal is more evenly spread out along the x-axis. The peaks of the two distributions are totally separated with two orders of magnitude in reconstruction error. (b) shows the  $e_T^{miss}$  T distribution for the SM MC and the SUSY signal in the signal region. The signal region is made using a cut around  $10^{-1.44}$ . Most of the background is removed, and the peaks of the SM MC and signal distributions are somewhat separated. (c) shows the significance as function of  $e_T^{miss}$ . The peak is put around a cut of about 380 GeV in the  $e_T^{miss}$ , with a significance of around 1.85.

In figures 4.21a, 4.22a, 4.23a, 4.24a we have the reconstruction error distributions for both SUSY signals for the small and large variational autoencoder. The steepness here differs from the steep slope in figures 4.17a, 4.18a, 4.19a, 4.20a. Interestingly, we see here that the deepness of the neural network here plays a role, which is different from the regular autoencoder output, where both the small and large autoencoder made a steep slope shape of the SM MC reconstruction error distribution. The peak of the distribution here is slightly shifted to the left for the shallow autoencoder model, and slightly shifted to the right of the center with the deep autoencoder model. One possible reason for this somewhat hill-like distribution could be that the variational autoencoder samples from a Gaussian distribution that has yet to be trained on enough data to produce a good enough error distribution.

In figures 4.21b, 4.22b, 4.23b and 4.24b the  $e_T^{miss}$  distribution is shown after imposing least strict cut for each signal on the reconstruction error. We see that the cuts are somewhat similar to the regular autoencoder, but with two key differences. First, because the peaks of the distributions from figures 4.21a, 4.22a, 4.23a, 4.24a are so close, the cuts allowed for more background events in the signal region. Here, as with the regular autoencoder output, the reconstruction cut from section 3.7  $m_{err}$  was used to create the signal region, but was not a good discriminator for the background events. Still, because we set cuts based on reconstruction

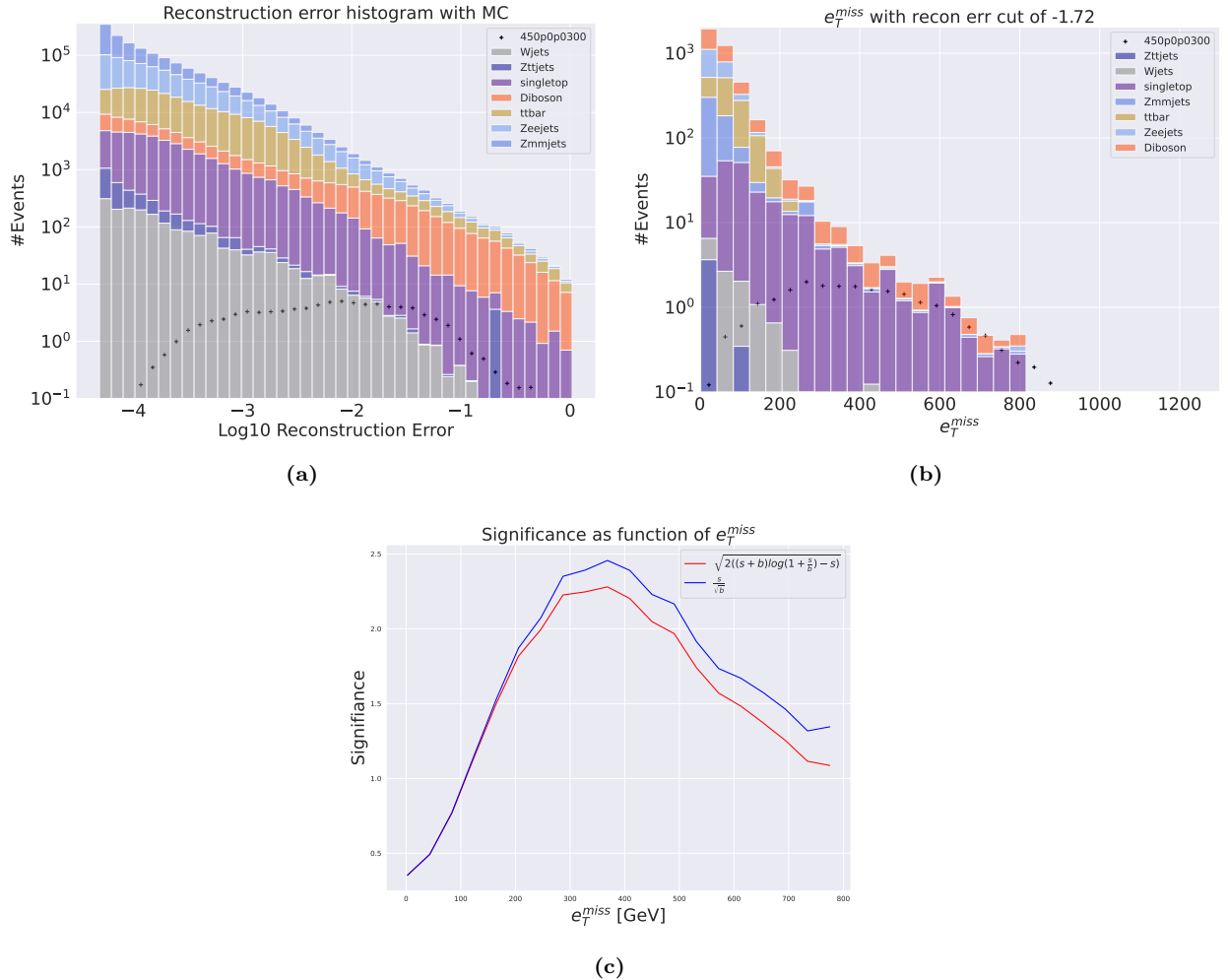


**Figure 4.18:** Reconstruction error (a),  $e_T^{\text{miss}}$  signal region (b) and significance as function of  $e_T^{\text{miss}}$  (c) for the shallow regular autoencoder using SUSY 450p300. (a) shows the reconstruction error distribution for the SM MC and the SUSY signal. The autoencoder produces a slope-like shape that is highly shifted to the lower end of the reconstruction error range for the background. The signal is more evenly spread out along the x-axis. The peaks of the two distributions are totally separated with two orders of magnitude in reconstruction error. (b) shows the  $e_T^{\text{miss}}$  T distribution for the SM MC and the SUSY signal in the signal region. The signal region is made using a cut around  $10^{-1.72}$ . Most of the background is removed, and the peaks of the SM MC and signal distributions are somewhat separated. (c) shows the significance as function of  $e_T^{\text{miss}}$ . The peak is put around a cut of about 380 GeV in the  $e_T^{\text{miss}}$ , with a significance of around 2.4.

error to minimize the background in the signal region, if one does have overlapping distributions with similar slopes, the results will be poor in comparison.

Secondly, the background that remains are slightly separated from the peak of the SM MC, the SUSY 800p50 signal model is shifted a bit more to the right end. The reason for the low significance is that the cross-section is much lower for the different from the signal region from the regular autoencoder. In the lower energy range there is a large excess of Zeejets, Zmmjets and ttbar events that have a high reconstruction error, which is not the case for the variational autoencoder, dominated by diboson events in all bins. In the higher energy range, diboson are largest contributor to the background, but the number of bins are exceptionally smaller than the Zmmjets/Zeejets/ttbar events, by a magnitude of 3 at the most.

## 4.4 Blind ATLAS data sample testing

The final test to run on the autoencoder is a blind test. The blind test will compare the reconstruction error from the autoencoder on an ATLAS dataset with the reconstruction error on the same ATLAS dataset where about 1.6 million events have been randomly removed and switched with samples from many BSM samples.

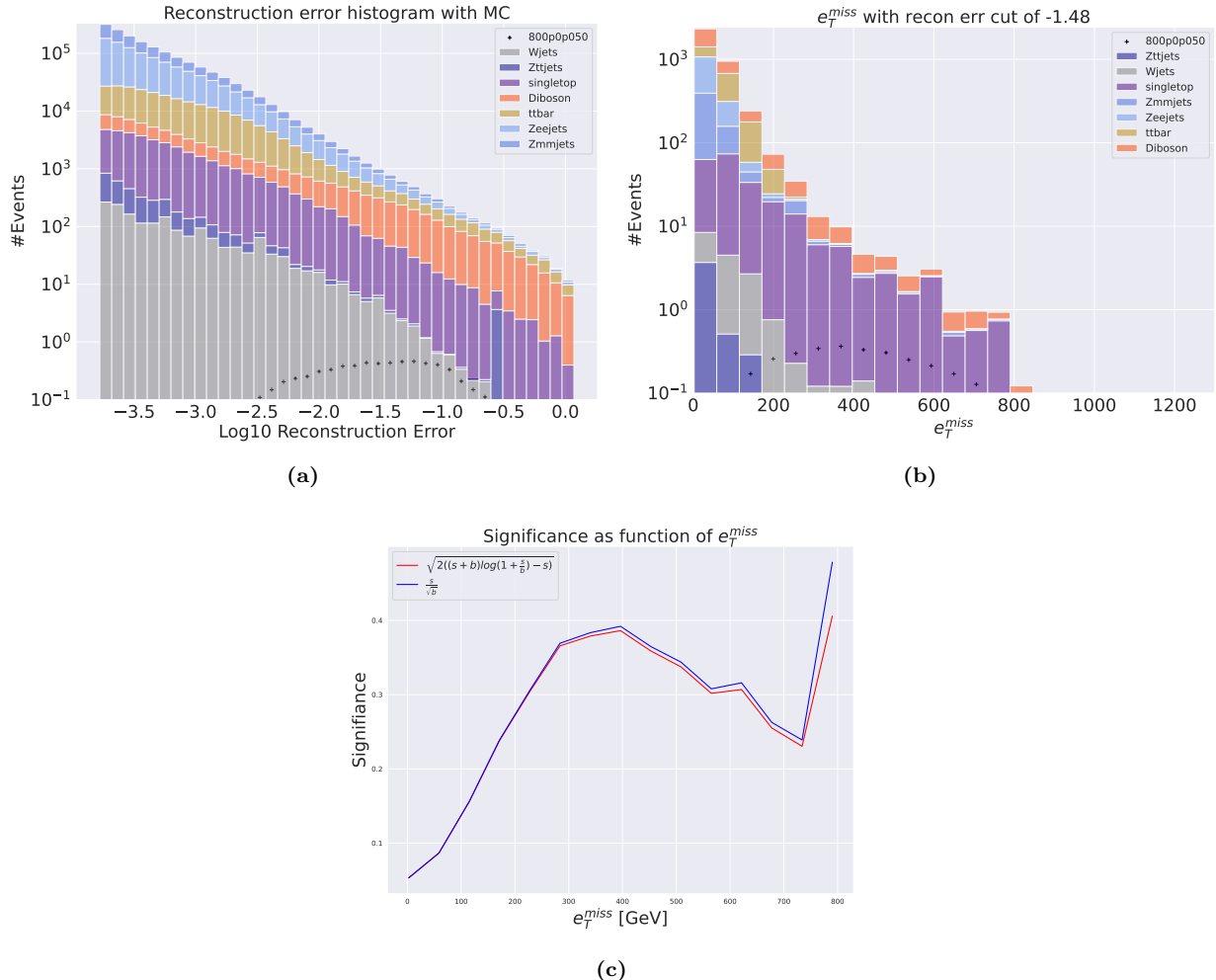


**Figure 4.19:** Reconstruction error (a),  $e_T^{miss}$  signal region (b) and significance as function of  $e_T^{miss}$  (c) for the deep regular autoencoder using SUSY 800p50. Figure 4.19a shows the reconstruction error distribution for the SM MC and the SUSY signal. Here the autoencoder produce slope-like shape that is highly shifted to the lower end of the reconstruction error range for the background. The signal has a peak around  $10^{-1.5}$  with a mirrored distribution shape from the background. The peaks of the two distributions are separated with two orders of magnitude in reconstruction error. Figure 4.19b shows the  $e_T^{miss}$  distribution for the SM MC and the SUSY signal in the signal region. The signal region is made using a cut around  $10^{-1.48}$ . Most of the background is removed, and the peaks of the SM MC and signal distributions are somewhat separated. Figure 4.19c shows the significance as function of  $e_T^{miss}$ . The peak is put around a cut of about 400 GeV in the  $e_T^{miss}$ , with a significance of around 0.38.

The signal samples have been given the same weight as the ATLAS data. Therefor the total amount of events before eventselection are the same in both datasets. The dataset was prepared by one of the supervisors of this thesis, and not shown to the author. The ATLAS data contains events from the data collection from 2015 and 2016, and the signal samples are created according to those runs. The ATLAS data will therefor be referred to as ATLAS data 15 and data 16 for the ATLAS events, and the mix set will be referred to data1516 mix.

In figure 4.25 the reconstruction error for the blind test is shown. The ratio subplot beneath the histogram shows the reconstruction error discrepancy. This indicates that the autoencoder is able to distinguish between the ATLAS data 15 and data 16, and BSM samples. The highest ratio difference is around 15 between the two datasets. The ratio discrepancy is also due to event selection. The mix set contains the same events as the ATLAS data 15 and data 16 sample set, but has around 1.6 million ATLAS events removed and replaced with BSM events. It appears that a higher number of BSM signal samples than the events that was removed passed the cuts in event selection.

The model has not been changed after running inference on the blind test, and we can therefor unblind the test, and see how well the autoencoder actually did in separating out the BSM events.

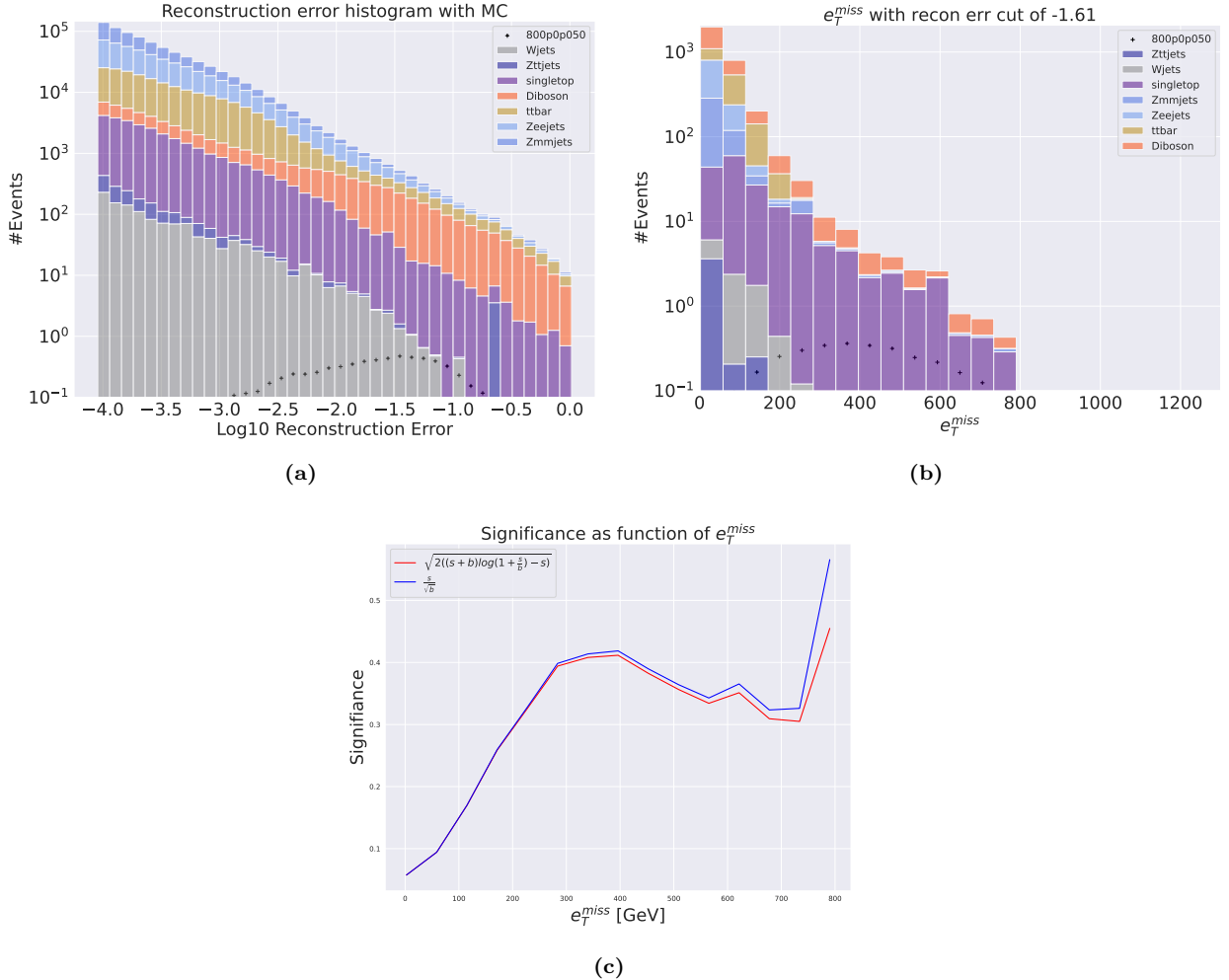


**Figure 4.20:** Reconstruction error (a),  $e_T^{\text{miss}}$  signal region (b) and significance as function of  $e_T^{\text{miss}}$  (c) for the shallow regular autoencoder using SUSY 800p50. (a) shows the reconstruction error distribution for the SM MC and the SUSY signal. The autoencoder produces a slope-like shape that is highly shifted to the lower end of the reconstruction error range for the background. The signal is more evenly spread out along the x-axis. The peaks of the two distributions are totally separated with two orders of magnitude in reconstruction error. (b) shows the  $e_T^{\text{miss}}$  T distribution for the SM MC and the SUSY signal in the signal region. The signal region is made using a cut around  $10^{-1.61}$ . Most of the background is removed, and the peaks of the SM MC and signal distributions are somewhat separated. (c) shows the significance as function of  $e_T^{\text{miss}}$ . The peak is put around a cut of about 400 GeV in the  $e_T^{\text{miss}}$ , with a significance of around 0.42.

In figure 4.26 the reconstruction error distributions for both ATLAS data 15 and data 16 samples, and BSM signals samples are shown. Allthough some samples have low reconstruction error, the peak is between  $10^{-2}$  and  $10^{0.5}$  reconstruction error. The hishget ratio discrepancy is around 15 between the two distributions, and it is shown to be in the same area of the peak.

## 4.5 Final remarks on the results

In sections 4.1, 4.2, 4.3 and 4.4 the performance of the regular and variational autoencoder with respect to usage in BSM searches has been shown through various tests. The final remarks can be summed up in five points:

- Shape of SM MC reconstruction error distribution
- Dataset altering testing
- Megaset changes
- Network architecture

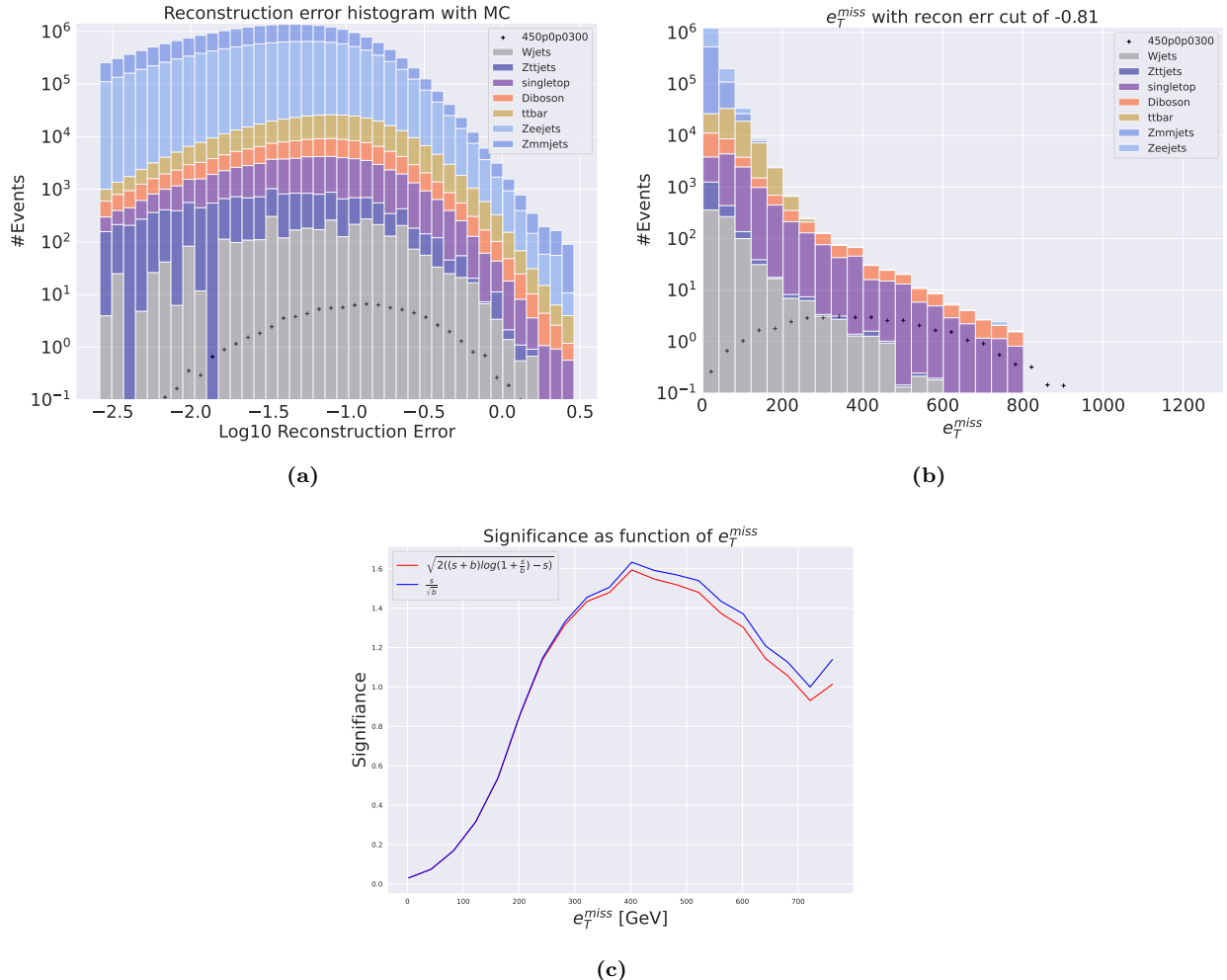


**Figure 4.21:** Reconstruction error (a),  $e_T^{\text{miss}}$  signal region (b) and significance as function of  $e_T^{\text{miss}}$  (c) for the deep variational autoencoder using SUSY 450p300. (a) shows that the peak of the distribution is somewhat centered in the middle of the reconstruction error range forming a hill-like shape. The peaks of the background and signal distributions are not well separated, with almost identical reconstruction error pattern. (b) shows a signal region with large background distribution. The signal region is made using a cut around  $10^{-0.81}$ . The peaks in the signal region are also somewhat separated, but the overall distributions are overlapping still. (c) shows the significance as function of  $e_T^{\text{miss}}$ . The peak significance is around 1.61 at around 400 GeV.

- Blind tests

First, it appears that the shape of the reconstruction error is more sensitive to the choice between variational and regular autoencoder than it is to the number of training samples it uses. However, the skewedness of the reconstruction error produced by the regular autoencoder increases with the size of the training data. From this observation it is reasonable to assume that to improve on the performance of the autoencoder, large amounts of training data is needed. This is also observed in the case of the variational autoencoder, where if one increases the amount of training data by going from the 3 lepton +  $e_T^{\text{miss}}$  case to the 2 lepton +  $e_T^{\text{miss}}$  case we observe a shift towards lower reconstruction error. It was not investigated further why the outputs of the two models are so different, but one reason could be that the decoder that samples from the latent space distribution in the variational autoencoder needs even more training data to get good separation.

Secondly, with the increase in training data it would be interesting to do the "altering  $p_T$ " test, as well as some other SM MC altering tests with especially the regular autoencoder. Based on the signal tests and the "altering  $p_T$ " test done with the 3 lepton +  $e_T^{\text{miss}}$  trained regular autoencoder, it is reasonable to assume that the autoencoder would perform even better. Other tests could for example be to swap certain features in the RMM, or swap events from one decay channel with another in order to create unphysical events. Essentially, by making these anomalous events and testing the autoencoder, one would get a better picture on the reach and ability of the autoencoder. This is of importance given the fact that the target signal or signals could in theory look very strange or perhaps in some feature space very similar to the SM MC.

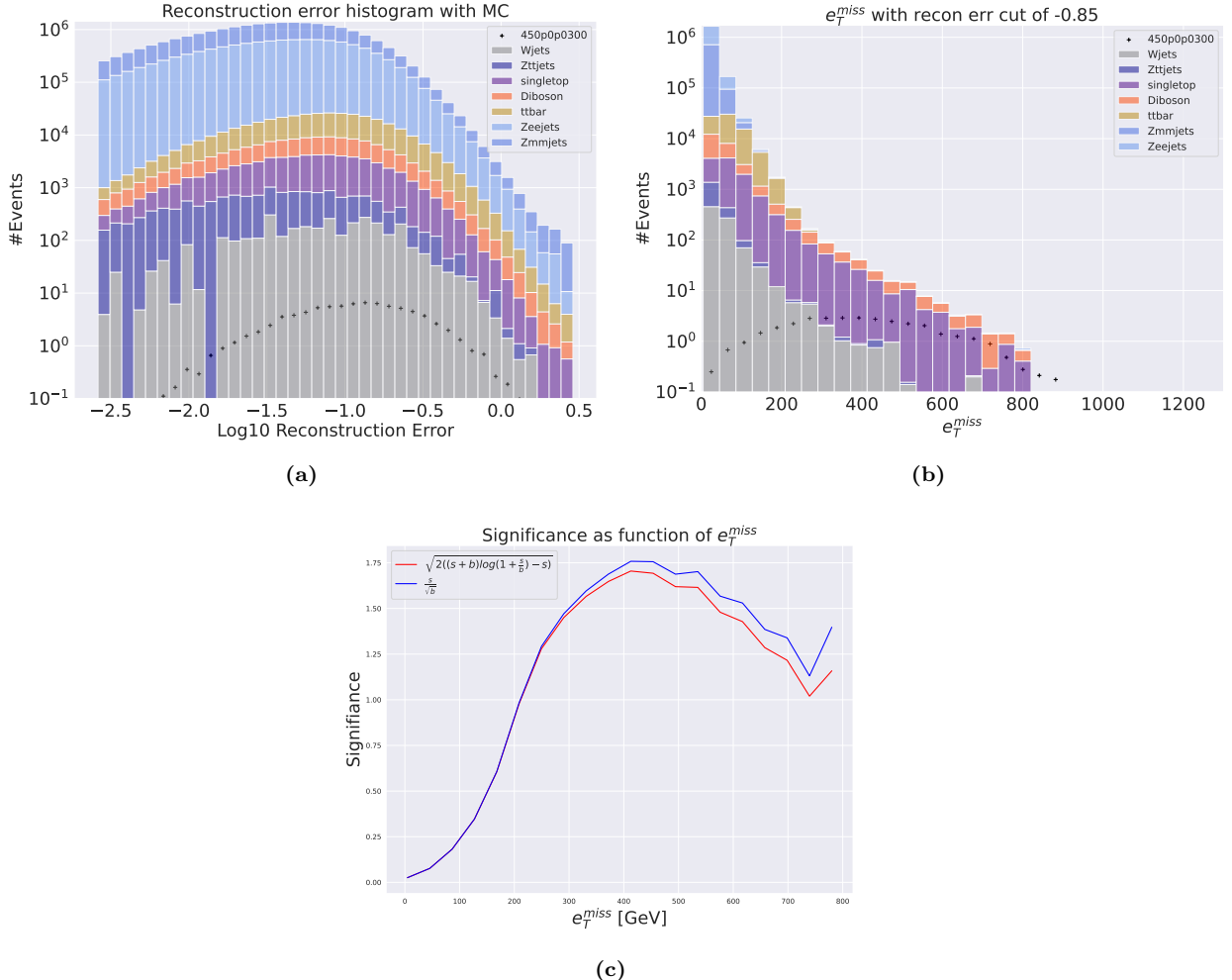


**Figure 4.22:** Reconstruction error (a),  $e_T^{miss}$  signal region (b) and significance as function of  $e_T^{miss}$  (c) for the shallow variational autoencoder using SUSY 450p300. (a) shows that the peak of the distribution is somewhat centered in the middle of the reconstruction error range forming a hill-like shape. The peaks of the background and signal distributions are not well separated, with almost identical reconstruction error pattern. (b) shows a signal region with large background distribution. The signal region is made using a cut around  $10^{-0.85}$ . The peaks in the signal region are also somewhat separated, but the overall distributions are overlapping still. (c) shows the significance as function of  $e_T^{miss}$ . The peak significance is around 1.75 at around 420-450 GeV.

A third point to note is in regard to the megaset training done in the 2 lepton +  $e_T^{miss}$  case. An arbitrary set of 10 megasets was chosen, but it might have been beneficial to choose a larger or smaller number of megasets<sup>27</sup>, and this might have had an impact on how well the autoencoders learn the SM signatures. A key criterion to uphold when doing training is to ensure that the megasets, when sampled, all maintain the natural distribution of the entire training set and thus the SM. If not, the algorithm will learn with a bias that is not constructive.

The fourth point to draw from the results are that it appears that the results are not too sensitive to the architecture of the networks. The two different architectures chosen were one model with only a latent space layer between the input and output layer, and a model with three layers on each side of the latent space. The choice of layers and nodes per layer was somewhat arbitrary, and after inference it was also clear that changes to the latent space affected more a change in the reconstruction error. This is though more related to the size of the input layer and the complexity of the data, more than the number of events in the training and test set.

The fifth point is in regard to the blind test done with the 2 lepton +  $e_T^{miss}$  trained deep autoencoder. This test was done in order to see if the autoencoder could pick up on signals mixed with SM events in ATLAS data. From the results in section 4.4 it appears that the autoencoder is able to some extent separate

<sup>27</sup>As the total amount of events would be the same, the difference with using say 20 megasets would be faster loading and writing time. The batchsize for a given training session with a batch would still be the same.

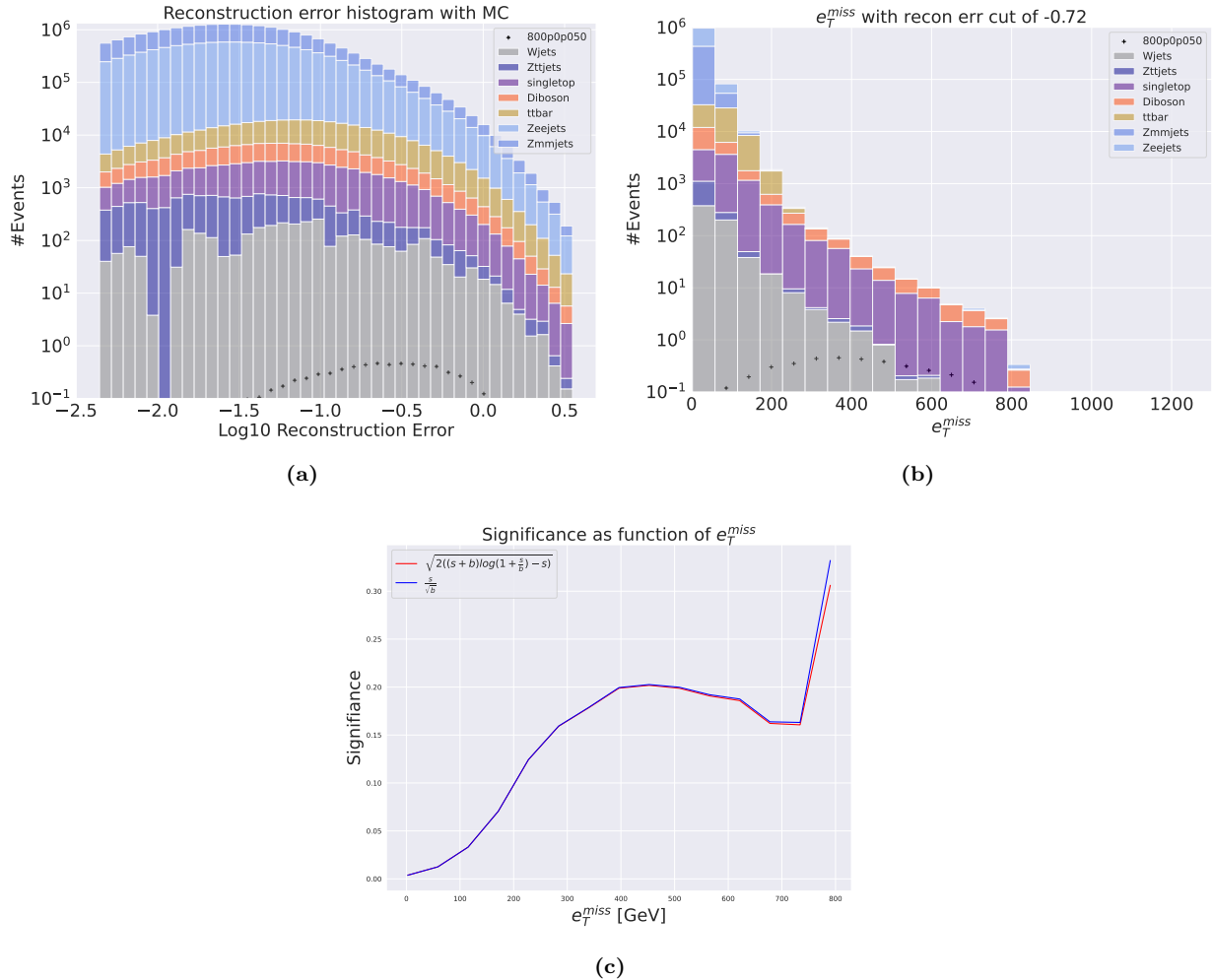


**Figure 4.23:** Reconstruction error (a),  $e_T^{\text{miss}}$  signal region (b) and significance as function of  $e_T^{\text{miss}}$  (c) for the deep variational autoencoder using SUSY 800 $p_{\text{T}}50$ . (a) shows that the peak of the distribution is somewhat centered in the middle of the reconstruction error range forming a hill-like shape. The peaks of the background and signal distributions are not well separated, with some separation of distribution peaks. (b) shows a signal region with large background distribution. The signal region is made using a cut around  $10^{-0.72}$ . The peaks in the signal region are also somewhat separated, but the overall distributions are overlapping still. (c) shows the significance as function of  $e_T^{\text{miss}}$ . The peak significance is around 0.20 at around 450 GeV.

out BSM signals. This indicates that there might be use for this search method and therefore more to learn about the autoencoders. Further in-depth research into the method should be done to figure out its usefulness in high energy physics research.

## 4.6 Execute summary

The results and discussion for the 3 lepton +  $e_T^{\text{miss}}$  dataset be summarized in bullet points for the regular and variational autoencoders, respectively:

- Better separation for high mass SUSY scenarios
- Shallow and deep architecture have similar performance for both signal samples
- In general low reconstruction error (i.e. the AE's have learned well the structures of the RMM)
- Shallow and deep architecture show similar results when looking at distributions of  $m_{lll}$  and  $e_T^{\text{miss}}$  in the signal region
- Best significance of 0.78 is found for the low mass SUSY by cutting at < 380 GeV in  $e_T^{\text{miss}}$  after requiring a reconstruction error of  $10^{-1.71}$  for the shallow AE

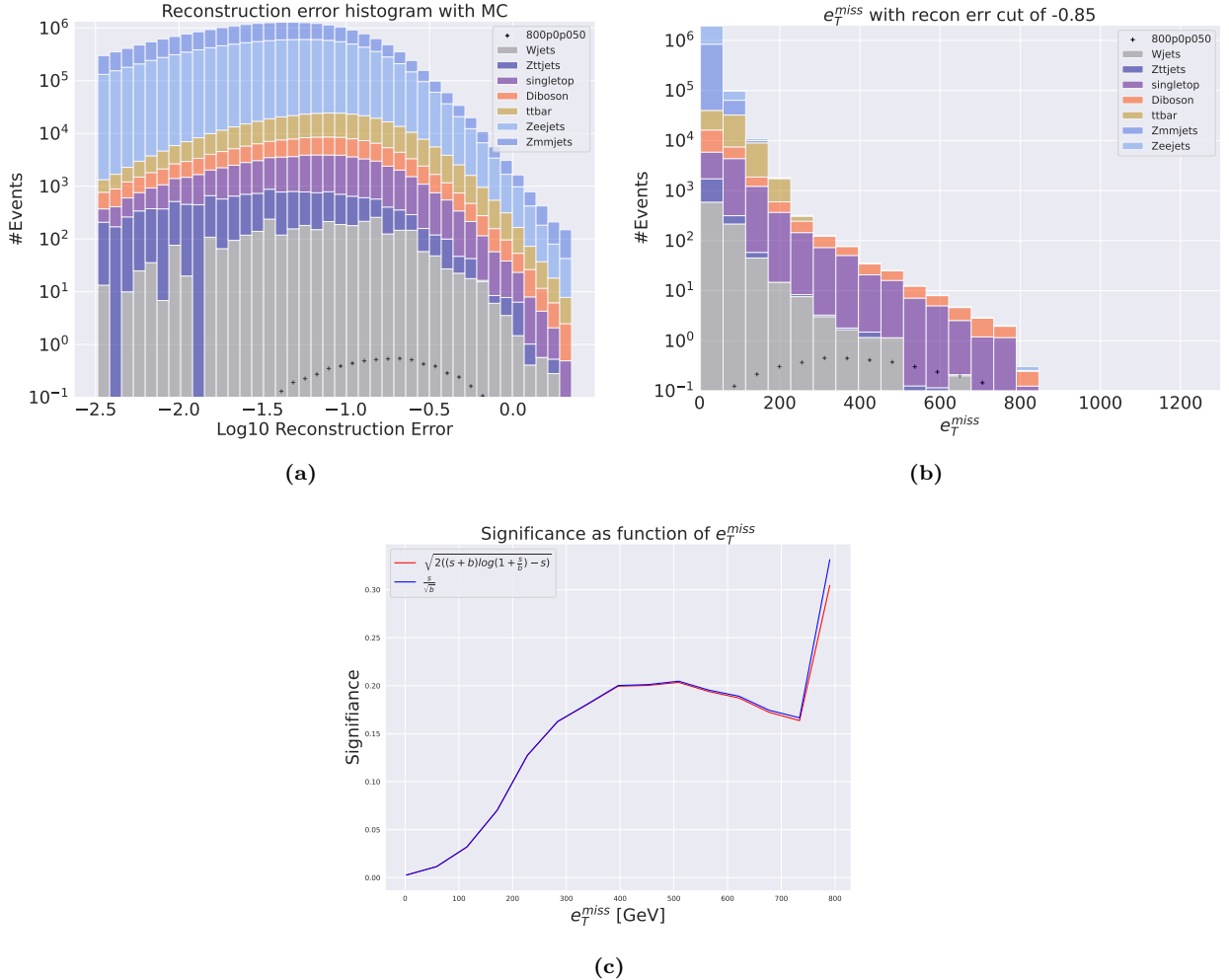


**Figure 4.24:** Reconstruction error (a),  $e_T^{\text{miss}}$  signal region (b) and significance as function of  $e_T^{\text{miss}}$  (c) for the shallow variational autoencoder using SUSY 800p50. (a) shows that the peak of the distribution is somewhat centered in the middle of the reconstruction error range forming a hill-like shape. The peaks of the background and signal distributions are not well separated, with almost identical reconstruction error pattern. (b) shows a signal region with large background distribution. The signal region is made using a cut around  $10^{-0.72}$ . The peaks in the signal region are also somewhat separated, but the overall distributions are overlapping still. (c) shows the significance as function of  $e_T^{\text{miss}}$ .

Model	3 lepton + $e_T^{\text{miss}}$				2 lepton + $e_T^{\text{miss}}$			
	AE	AE	VAE	VAE	AE	AE	VAE	VAE
Signal sample	450p300	800p50	450p300	800p50	450p300	800p50	450p300	800p50
SR cut in reconstruction	$10^{-1.71}$	$10^{-1.41}$	$10^{-1.06}$	$10^{-1.06}$	$10^{-1.72}$	$10^{-1.61}$	$10^{-0.85}$	$10^{-0.85}$
Optimal cut in $e_T^{\text{miss}}$ [GeV]	380	450	400	480	380	400	430	510
Max significance	0.78	0.39	4.5	0.52	2.4	0.42	1.75	0.21
Architecture	Shallow	Shallow	Shallow	Deep	Shallow	Shallow	Shallow	Shallow

**Table 4.1:** Summary of the best results obtained by the regular and variational autoencoders for the 3 lepton and 2 lepton +  $e_T^{\text{miss}}$  datasets

- Worse separation in reconstruction error between SM MC and signal
- Consistently hisgher reconstruction error for both signal and SM MC compared with AE

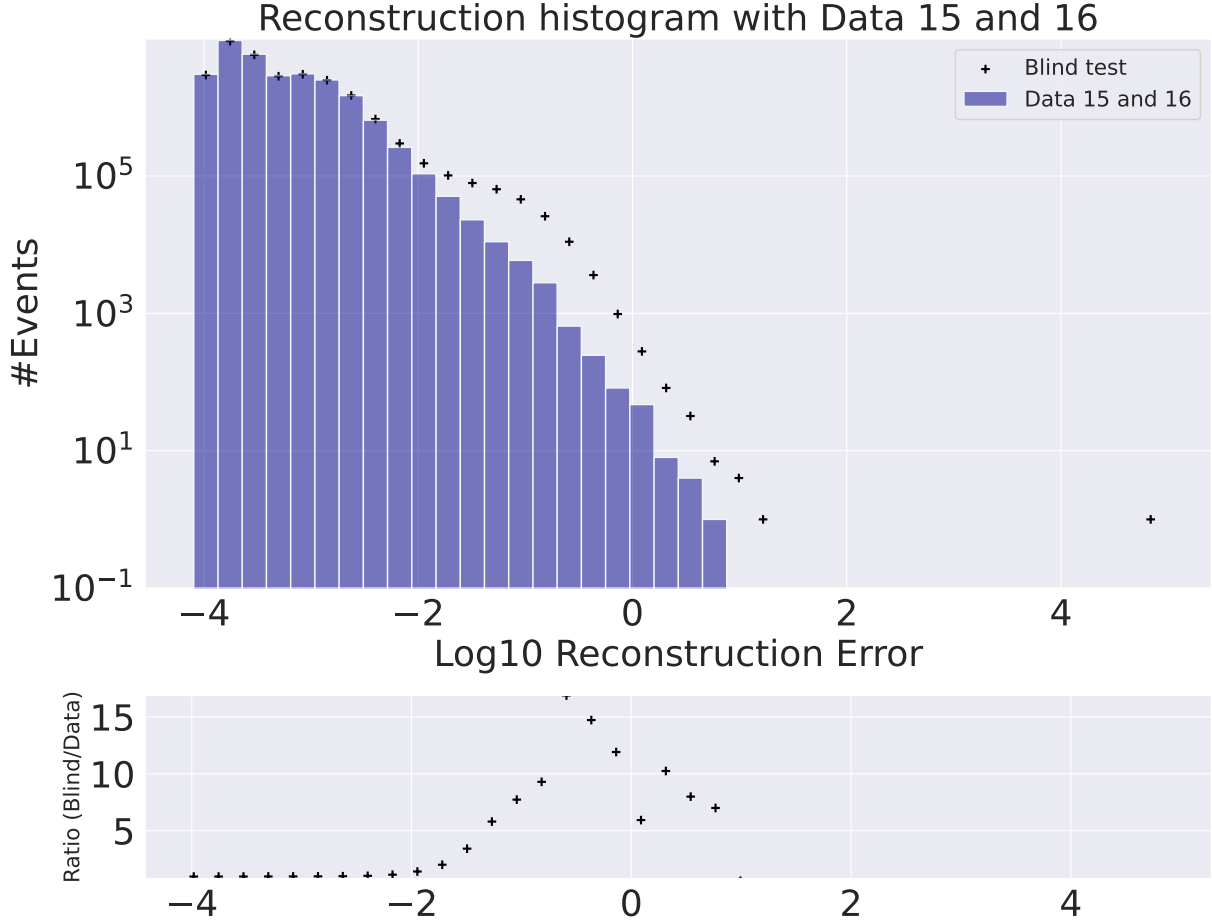


**Figure 4.25:** Reconstruction error for the blind test. The blue histogram is the ATLAS data 15 and data 16 sample and the black crosses are the ATLAS data mixed with BSM samples. Between a reconstruction error of  $10^{-2}$  and  $10^{0.5}$  there is a separation of the peaks of the two distributions. The biggest difference is a ratio difference of around 15.

- The signal region choice for the VAE achieves a better significance although the separation in reconstruction error between SM MC and signal is worse compared with the AE
- Shallow and deep VAE perform similarly in terms of obtained significance

## 4.7 Challenges with the search method and tools

In the previous sections, the output and results of using the autoencoder for anomaly detection have been shown. The method and results, as produced and shown in this thesis, have yielded some promising results given the nature of the search method. However, it should be known what the challenges of the task actually are to truly understand why the results are only promising, and not great compared to other search methods. The challenges can be divided into three main points, all of which are tangled together. The three challenges are listed below.

- Model independence
- Reconstruction error minimization
- Feature engineering

Model independence is the first challenge. By model, it is here referring to signal models.

As mentioned in the theory section for the SM, the SM, although very successful in certain predictions, lack the ability to explain a whole number of behavior around us, and so there have been made many suggested solutions to the issues. These new models are often called extensions to the SM, and although

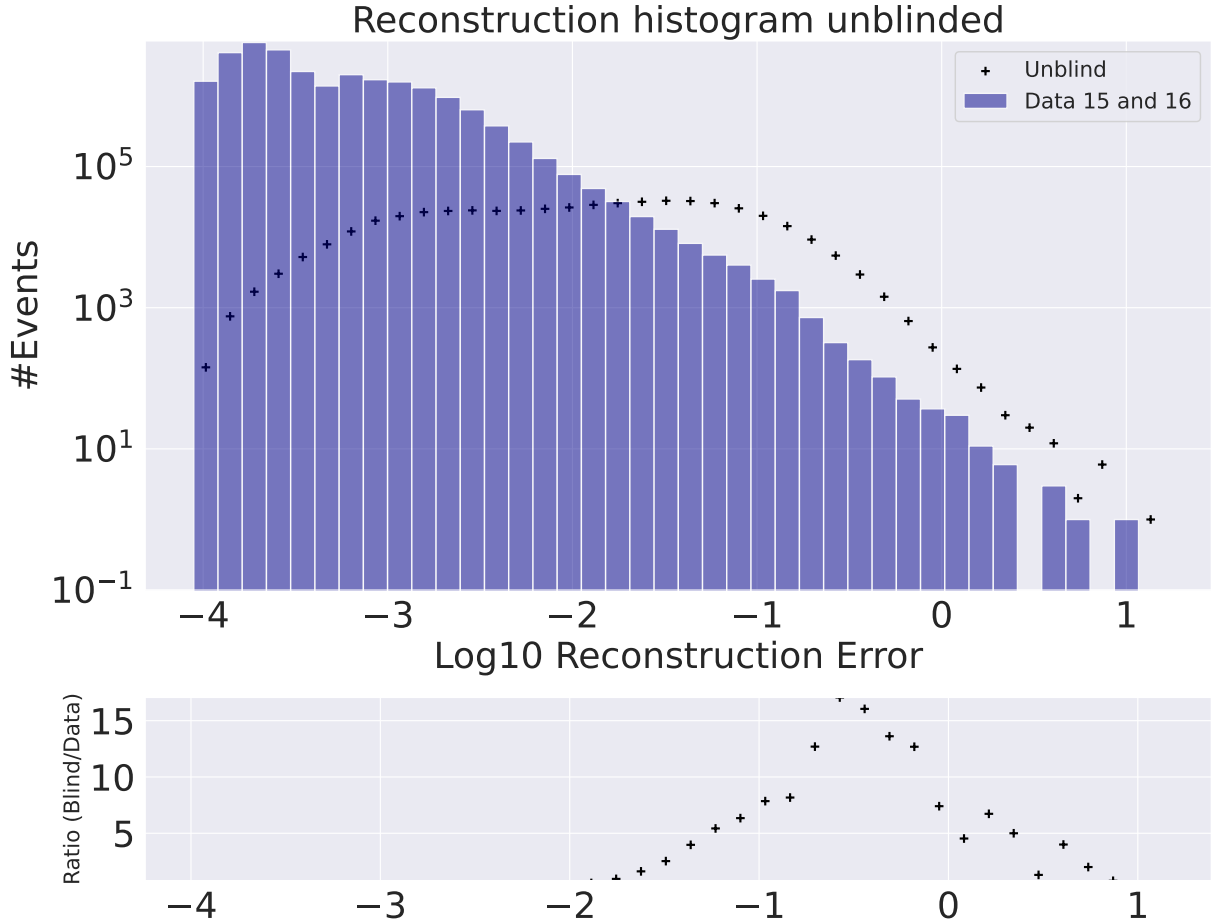


**Figure 4.26:** Reconstruction error for the unblind test. In the histogram the blue bins are the ATLAS data 15 and data 16 samples from the mix dataset and the black crosses are the BSM samples with the legend "Unblind". Between a reconstruction error of  $10^{-2}$  and  $10^{0.5}$  there is a separation of peaks of the two distributions. The biggest difference is a ratio difference of around 15.

mathematically consistent, not necessarily physically possible. And even if they are physically possible, in other words, they adhere to certain fundamental physical principles, they still might not exist, as several searches at ATLAS have excluded but never found any new physics.

The search method is inherently biased as one assumes that the new physics looks like the signal, and thus do analysis, data preparation etc. with that signal in mind. But we do not know, at all, what the new physics looks like, even the assumption that we are looking for particles are implying a bias that might not be true. From the collisions in the detector to the analysis, there are biased decisions, we cannot avoid them, but we can minimize them as much as possible, which is the goal with the search strategy in this thesis.

This leads us to the second challenge, which is reconstruction error minimization. The proposed method in this thesis is to learn the signature of the SM so well, that even subtle anomalous behavior will be picked up by the analysis tool. The autoencoder learns the signature of the SM via reconstruction error minimization, and then hopefully the anomalous data will be picked up in a signal region. One problem with this is that one first blinds oneself to signals that might be very, very similar to the SM in some feature space, but with very low statistics. These events will for a given set of features, never be found.

The third challenge is the choice of features. This thesis utilized the RMM structure by Chekanov et al., as it maximizes the amount of information in the input data by using almost completely uncorrelated features. However, as we do not know the signals we are looking for, there is no way to know if this choice is the optimal choice for new physics. In fact, even if we found an ideal set of features, based on some physical principles or something else, it is not trivial that the reconstruction error calculation should weight the error of each feature equally. It might very well be that some features are less important than others. Essentially, the goal is to optimize for a signal we do not know, using features we don't know are optimal, and weighting them as "unbiased" as possible, simply taking the average, to dictate how the autoencoder learns and updates its internal weights and biases.

## 4.8 Future work

Autoencoders and their applications to anomaly detection in high energy physics are not well understood, and this thesis only scraped on some issues and attempts that needs to be done. It is a recent topic within the HEP community, and consequently much work is needed to reach a better understanding of how autoencoders behave with HEP data. The work done in this thesis has led to three areas of focus that should be explored more, listed below.

- Computational bottlenecks
- Data and feature engineering
- Network and architecture engineering

### Computational bottlenecks

From sections 4.2 and 4.3 there seems to be a positive trend in increasing the amount of training data for the autoencoders, both regular and variational. With a continual increase in data from Run3 and onward [46], the loading and storing time used for doing analyses increase.

**Figure 4.27:** LHC nominal luminosity projections for the next 2 decades

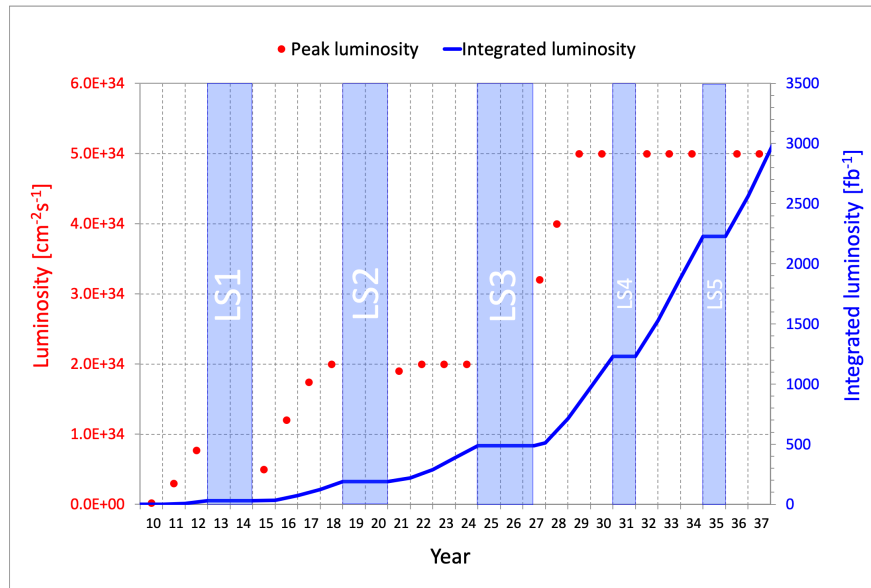


Figure 4.27 shows the expected time periods for data collection and the amount of data expected for the next two decades.

One bottleneck<sup>28</sup> that was discovered during the work with this thesis was the use of Pandas pre the 2.0 version release, which is written on top of NumPy. Although Pandas has many very useful features and is the industry standard for data analysis and feature engineering, it is somewhat slow. NumPy is not parallelized, thus all operations are done in serial. Polars has proven useful as a replacement, and was used for the megaset training. Although in its early stages still, it unlike Pandas has a Rust backend, which natively parallelizes. Thus, if one works with rather large datasets one should use Polars, or some other parallelized tool. Another tool used for training and inference was to store training and test data post-processing in numpy arrays such that one can just load them. NumPy makes this very simple, but as mentioned above it is serial in its execution and thus takes long time for large arrays. In the 2 lepton case the clear bottleneck both in processing of the training and testing data, as well as inference and training of the models, was the loading and storing time using NumPy's load and save functions. Sadly there is not much one can do per now as NumPy's load and save functions are the fastest, provided one has a lot of storage available. This can also be generalised to number of conversion steps from ROOT files to an useable python format. In the future this might be better incorporated in ROOT such that many conversion steps are not needed.

<sup>28</sup>The bottleneck problem explained here is not in regard to the recording of the events. It is rather in the amount of data the analysis tools have to ingest. Figure 4.27 is used as a tool to illustrate the amount that will have to be ingested.

Another bottleneck is computation time of training and inference. There is a continuing battle between speed and accuracy in terms of choosing an appropriate batchsize. The choice of batchsize for this thesis is 8192. It is common to choose a batchsize that is a multiple of two, as this is most optimized for GPU's. 8192 is  $2^{13}$ , and it a rather large batchsize. Although this allows for epoch training time to be as low as less than 2 minutes for 2 lepton case and less than 1 minute for 3 lepton case, it does decrease the model's ability to learn more about the dataset[11]. With better and faster equipment this could be improved whilst decreasing the batchsize.

## Data and feature engineering

### Scaling

One aspect that was not explored in this thesis is the choice of scaling for the data. The choice used for this thesis was the MinMax scaling algorithm from Sci-kit learn. From previous work done on the ATLAS Open data [47] it appeared that MinMax was better for over all accuracy than Standard scaling. Still, it should be looked at and more understood why this is or is not the case for the Run2 dataset used in this thesis.

### Interpretation and possible feature changes

This thesis used the Rapidity-Mass matrix described by Chekanov[31] as features in the dataset. Whilst containing features that are very uncorrelated it creates a feature signature that could be used by the autoencoder to learn underlying structures in the SM. There are however some aspects to discuss. First, every nonexisting entry in the RMM for a given event is replaced with a zero value. This creates "islands" in the RMM structure which contributes to create the signatures for the events. It is however not clear how these zero values propagate through the network, and how they affect the performance and the autoencoder's ability to learn the underlying structures in the SM. In cases where one uses tools like decision trees, this is not an issue, as they can just remove the feature if it holds a certain value, but as we need a tabular and rectangular shape to do the matrix multiplication that is neural network feed forwarding and backpropagation, a value has to be put in the missing entries, and it is not obvious or known what the choice of using zeros does.

Another choice to consider is the amount of particles in the RMM. This thesis tried allowing for 5 electrons and 5 muons, and 6 b- and ljets, yielding a total of 529 elements in the RMM. This choice was an arbitrary one, but it is not unreasonable to think that an even larger RMM would be more beneficial, as it contains more information. Some events might have even more jets in them, or leptons. But with a larger RMM comes a larger amount of zero valued features as well. And also, with a larger RMM, the memory needed for a given array increases, which in the case of the 2 lepton case, would mean more megabytes of smaller size. The computation time, from event selection and conversion from Rdataframe to Numpy, and training and inference, would increase a lot. A third point to make is that the RMM alone might not be the ideal set of features. It would be interesting to test a combination of RMM and some other features, where we remove some of the features that are on average zero and replace them with other useful information. If the goal is to learn the autoencoders the signature of the SM, then it is not unreasonable to assume that more specific information would be better. It should be better understood what it means to learn the signature of a channel, and of the SM as a whole.

## Architecture engineering

The regular autoencoder appears to provide a better anomaly detection performance than the variational autoencoder. The architecture is somewhat simple, given the hard task it is meant to perform. It might be possible to add some more complex layer structures like convolutional neural network (CNN) autoencoders or principal component analysis (PCA) to make a more complicated and better performing network architecture. This is of course only speculation, and was not investigated much in depth. General trends were found to vary depending on the size of the dataset, and it is not trivial that for example a deep neural network is beneficial as the training sample increases. What was important though was to ensure that the latent space was large enough to store enough information for the decoder. In the early attempts the latent space was set between 10 and 50 nodes, which was too little for the encoded information to be useful. As there is no clear way to find the optimal architecture, an educated guess on the number of nodes were done. In theory, one can create a tunable network where the number of layers and nodes in each layer are hyperparameters, but the sheer number of combinations would lead to much longer computation time than what was reasonable within the timescale of this thesis. Tools like Keras-Tuner could facilitate this search, but if this were a PhD thesis or a long term research project it would be beneficial with more significant hardware or a more rigorous way to set an optimal architecture.

Another point to think about is how the autoencoder is trained. As explained in section 1.3 the autoencoder is trained by how well it manages to reconstruct the input data. This is done by calculating the error of each feature for a given event, and averaging the error for all features. This has its pros and cons, and should be investigated further. Suppose one has an RMM which is very sparse, with 10 bjets, 10 ljets, 10 electrons, 10 muons, and 10 photons, i.e a T5N10 matrix of 2601 columns and rows. In this case, one can easily assume that the RMM would be very sparse, as few if any SM events produced at the current energy level at the LHC contains that many particles. Thus, one could argue that some features are more important to learn correctly than others, and thus should be weighted more. It is however difficult to know which features that should be in focus, as the signatures for each event might differ, and some might look completely different from one another. One way to deal with this issue is to calculate the average RMM for a given channel, and then see if there are general trends in the RMM for those channels. Then one could perhaps weigh the most used features more than the sparser areas.



# Chapter 5

## Conclusion

The main goal of this thesis was to benchmark and investigate the performance and usage of autoencoders in BSM searches. The analysis and testing were done using n-tuples from ATLAS that was converted to python dataframe structures. We argued for using the Rapidity-Mass matrix as features in our input data, with 6 bjets and 6 ljets, and 6 of each lepton. The original goal was to test and understand the performance in the case where we have a 3 lepton +  $e_T^{miss}$  final state. In testing, it was shown that the performance was not too impressive, thus the choice was made to use the 2 lepton +  $e_T^{miss}$  dataset which contains much more data. Due to the large size of the total dataset, we proposed a solution where the overall distribution in the total set was conserved in smaller batches, called megasets. Several tests were devised to benchmark the autoencoders, making anomalous events by altering the  $p_T$  of standard model events and testing on two supersymmetric signal models. We showed that the autoencoders performance increased with larger training samples, but argue for more testing as these methods are not well understood yet. The performance was measured in three categories: how well it reconstructs the test dataset; how much background and signal is left in the signal region; and the significance it achieves when performing cuts in the signal region. It was shown that for the reconstruction of the test dataset, the regular autoencoder is much better than the variational autoencoder, creating a reconstruction error distribution with slope like shape pushed to the lower end. In the second category the regular autoencoder is much better at reducing the background, but not that much better at increasing the amount of signal. In the second category the regular autoencoder is much better at reducing the background, but struggles with increasing the amount of signal. The variational autoencoder struggled with reducing the background, but increased the amount of signal relative to the regular autoencoder reconstruction error. On the significance test the regular autoencoder performs better than the variational autoencoder. It was also shown that with an increase in training data, the reconstruction of the test dataset was improved for both the regular autoencoder and the variational autoencoder. The final test of the autoencoder was a blind test with ATLAS data and BSM signals. It showed that the autoencoder, when trained on the 2 lepton +  $e_T^{miss}$  dataset, managed to separate out some signals from the ATLAS data. This indicates that there might be an usecase for it in more rigorous analyses at ATLAS, and should be better understood.

We also argue for future work and challenges with the method. Amongst other issues where computational bottlenecks related to writing and loading of data from training and inference. It is recommended to further investigate the RMM, as well as alter the training process by physics informed or machine learning informed choices, such as a weighted mean squared error (MSE). The autoencoder might perform even better with better feature engineering, and this should be of focus for futher research as well.



# Bibliography

- [1] L. Weng, *From autoencoder to beta-vae*, [lilianweng.github.io](https://lilianweng.github.io) (2018) .
- [2] PARTICLEDATA GROUP collaboration, C. Patrignani, K. Agashe, G. Aielli, C. Amsler, M. Antonelli, D. M. Asner et al., *Review of Particle Physics, 2016-2017*, *Chin. Phys. C* **40** (2016) 100001.
- [3] M. Aker, A. Beglarian, J. Behrens, A. Berlev, U. Besserer, B. Bieringer et al., *Direct neutrino-mass measurement with sub-electronvolt sensitivity*, *Nature Physics* **18** (Feb, 2022) 160–166.
- [4] W. Heisenberg, *Across the Frontiers*. 1974.
- [5] M. Abadi, A. Agarwal, P. Barham, E. Brevdo, Z. Chen, C. Citro et al., *TensorFlow: Large-scale machine learning on heterogeneous systems*, 2015.
- [6] A. Paszke, S. Gross, F. Massa, A. Lerer, J. Bradbury, G. Chanan et al., *Pytorch: An imperative style, high-performance deep learning library*, 2019.
- [7] V. Chandola, A. Banerjee and V. Kumar, *Anomaly detection: A survey*, *ACM Comput. Surv.* **41** (07, 2009) .
- [8] T. Chen and C. Guestrin, *XGBoost*, in *Proceedings of the 22nd ACM SIGKDD International Conference on Knowledge Discovery and Data Mining*, ACM, aug, 2016. DOI.
- [9] C. Cortes and V. Vapnik, *Support-vector networks*, *Machine learning* **20** (1995) 273–297.
- [10] S. Frette, W. Hirst and M. M. Jensen, *A computational analysis of a dense feed forward neural network for regression and classification type problems in comparison to regression methods*, .
- [11] I. Goodfellow, Y. Bengio and A. Courville, *Deep Learning*. MIT Press, 2016.
- [12] D. P. Kingma and J. Ba, *Adam: A method for stochastic optimization*, 2014. 10.48550/ARXIV.1412.6980.
- [13] D. Rumelhart, G. Hinton and R. Williams, *Learning representations by back-propagating errors*, *Nature* (1986) .
- [14] D. P. Kingma and M. Welling, *Auto-encoding variational bayes*, 2013. 10.48550/ARXIV.1312.6114.
- [15] S. Kullback and R. A. Leibler, *On information and sufficiency*, *Ann. Math. Statistics* **22** (1951) 79–86.
- [16] G. Cowan, *Statistical data analysis, lecture week 6*, 2020/21.
- [17] A. Pich, *The Standard Model of Electroweak Interactions; rev. version*, .
- [18] M. E. Peskin and D. V. Schroeder, *An Introduction to Quantum Field Theory*. Westview Press, 1995.
- [19] M. Thomson, *Modern particle physics*. Cambridge University Press, New York, 2013.
- [20] K. Kumericki, *Feynman diagrams for beginners*, 2016. 10.48550/ARXIV.1602.04182.
- [21] M. Aker, A. Beglarian, J. Behrens, A. Berlev, U. Besserer, B. Bieringer et al., *Direct neutrino-mass measurement with sub-electronvolt sensitivity*, *Nature Physics* **18** (Feb, 2022) 160–166.
- [22] *Search for chargino-neutralino pair production in final states with three leptons and missing transverse momentum in  $\sqrt{s} = 13$  TeV pp collisions with the ATLAS detector*, [2106.01676](#).
- [23] E. Gramstad, *Searches for Supersymmetry in Di-Lepton Final States with the ATLAS Detector at  $\sqrt{s} = 7$  TeV*, 2013.
- [24] D. Green, *High pt Physics at Hadron Colliders*. Cambridge University Press, 2004.
- [25] ATLAS collaboration, S. Mehlhase, *ATLAS detector slice (and particle visualisations)*, .
- [26] S.-M. Wang, *ATLAS Computing and Data Preparation. ATLAS Induction Day + Software Tutorial*, .
- [27] T. P. S. Gillam, *Identifying fake leptons in ATLAS while hunting SUSY in 8 TeV proton-proton collisions*. PhD thesis, Cambridge U., 2015. 10.17863/CAM.16619.
- [28] W. Hwang and T. Wu, *Relativistic Quantum Mechanics and Quantum Fields: Second Edition for the 21st Century*. World Scientific, 2018.
- [29] The pandas development team, *pandas-dev/pandas: Pandas*, Feb., 2020. 10.5281/zenodo.3509134.
- [30] The HDF Group, *Hierarchical Data Format, version 5*, 1997–2022.
- [31] S. Chekanov, *Imaging particle collision data for event classification using machine learning*, *Nuclear Instruments and Methods in Physics Research Section A: Accelerators, Spectrometers, Detectors and Associated Equipment* **931** (jul, 2019) 92–99.
- [32] S. V. Chekanov, *Machine learning using rapidity-mass matrices for event classification problems in HEP*, *Universe* **7** (jan, 2021) 19.
- [33] R. Santos, M. Nguyen, J. Webster, S. Ryu, J. Adelman, S. Chekanov et al., *Machine learning techniques in searches for  $t\bar{t}$  in the  $h \rightarrow bb$  decay channel*, *Journal of Instrumentation* **12** (apr, 2017) P04014–P04014.

- [34] R. S. Geiger, D. Cope, J. Ip, M. Lotosh, A. Shah, J. Weng et al., "garbage in, garbage out" revisited: What do machine learning application papers report about human-labeled training data?, *CoRR abs/2107.02278* (2021) , [[2107.02278](#)].
- [35] M. Aaboud, , G. Aad, B. Abbott, J. Abdallah, O. Abdinov et al., *Performance of the ATLAS trigger system in 2015*, *The European Physical Journal C* **77** (may, 2017) .
- [36] G. Aad, B. Abbott, D. Abbott, A. A. Abud, K. Abeling, D. Abhayasinghe et al., *Performance of the ATLAS muon triggers in run 2*, *Journal of Instrumentation* **15** (sep, 2020) P09015–P09015.
- [37] G. Aad, , B. Abbott, D. C. Abbott, A. A. Abud, K. Abeling et al., *Performance of electron and photon triggers in ATLAS during LHC run 2*, *The European Physical Journal C* **80** (jan, 2020) .
- [38] F. Chollet et al., *Keras*, 2015.
- [39] Plotly Technologies Inc., *Collaborative data science*, 2015.
- [40] F. Pedregosa, G. Varoquaux, A. Gramfort, V. Michel, B. Thirion, O. Grisel et al., *Scikit-learn: Machine learning in Python*, *Journal of Machine Learning Research* **12** (2011) 2825–2830.
- [41] C. R. Harris, K. J. Millman, S. J. van der Walt, R. Gommers, P. Virtanen, D. Cournapeau et al., *Array programming with NumPy*, *Nature* **585** (Sept., 2020) 357–362.
- [42] R. Vink, S. de Gooijer, A. Beedie, J. van Zundert, G. Hulselmans, C. Grinstead et al., *pola-rs/polars: Python polars 0.16.14*, Mar., 2023. 10.5281/zenodo.7744139.
- [43] S. Frette, *Deployment of unsupervised learning in a search for new physics with ATLAS Open Data*, .
- [44] T. O’Malley, E. Bursztein, J. Long, F. Chollet, H. Jin, L. Invernizzi et al., "Kerastuner." <https://github.com/keras-team/keras-tuner>, 2019.
- [45] A. Aspertì and M. Trentin, *Balancing reconstruction error and kullback-leibler divergence in variational autoencoders*, 2020. 10.48550/ARXIV.2002.07514.
- [46] LHC, *Lhc nominal luminosity projection*, 2013.
- [47] ATLAS collaboration, *Review of the 13 TeV ATLAS Open Data release*, tech. rep., CERN, Geneva, Jan, 2020.

# Appendices



# Appendix A

## A.1 Channel removal testing

In this section the remaining histograms for the channel removal test are shown. Each figure contains the same subfigure structure as shown in the results and discussion section.

## Regular autoencoder

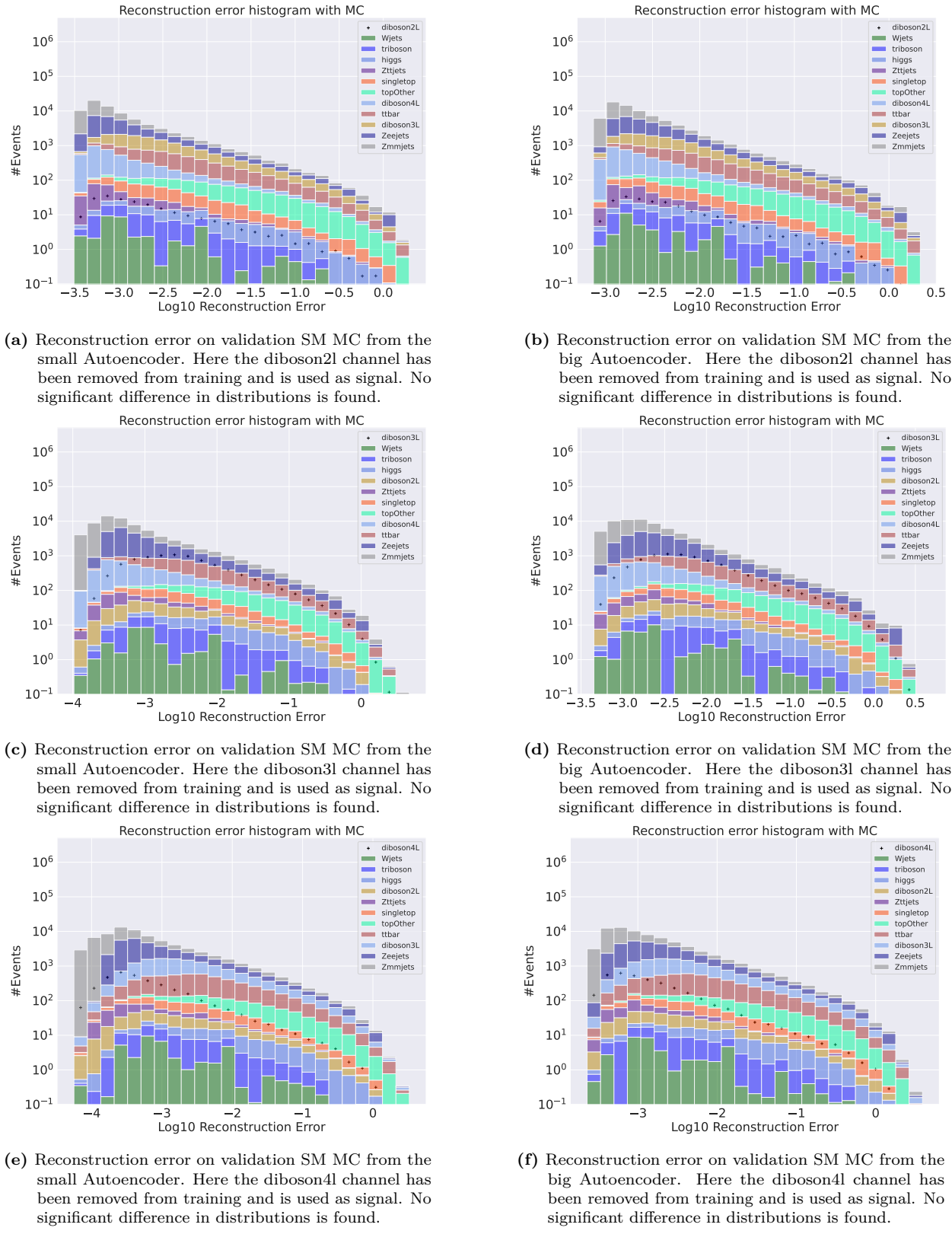


**Figure 1:** Reconstruction error on validation SM MC from the small and big Autoencoder. Here the diboson2L, diboson3L and diboson4L have been used for the small (left) and large (right) regular autoencoder

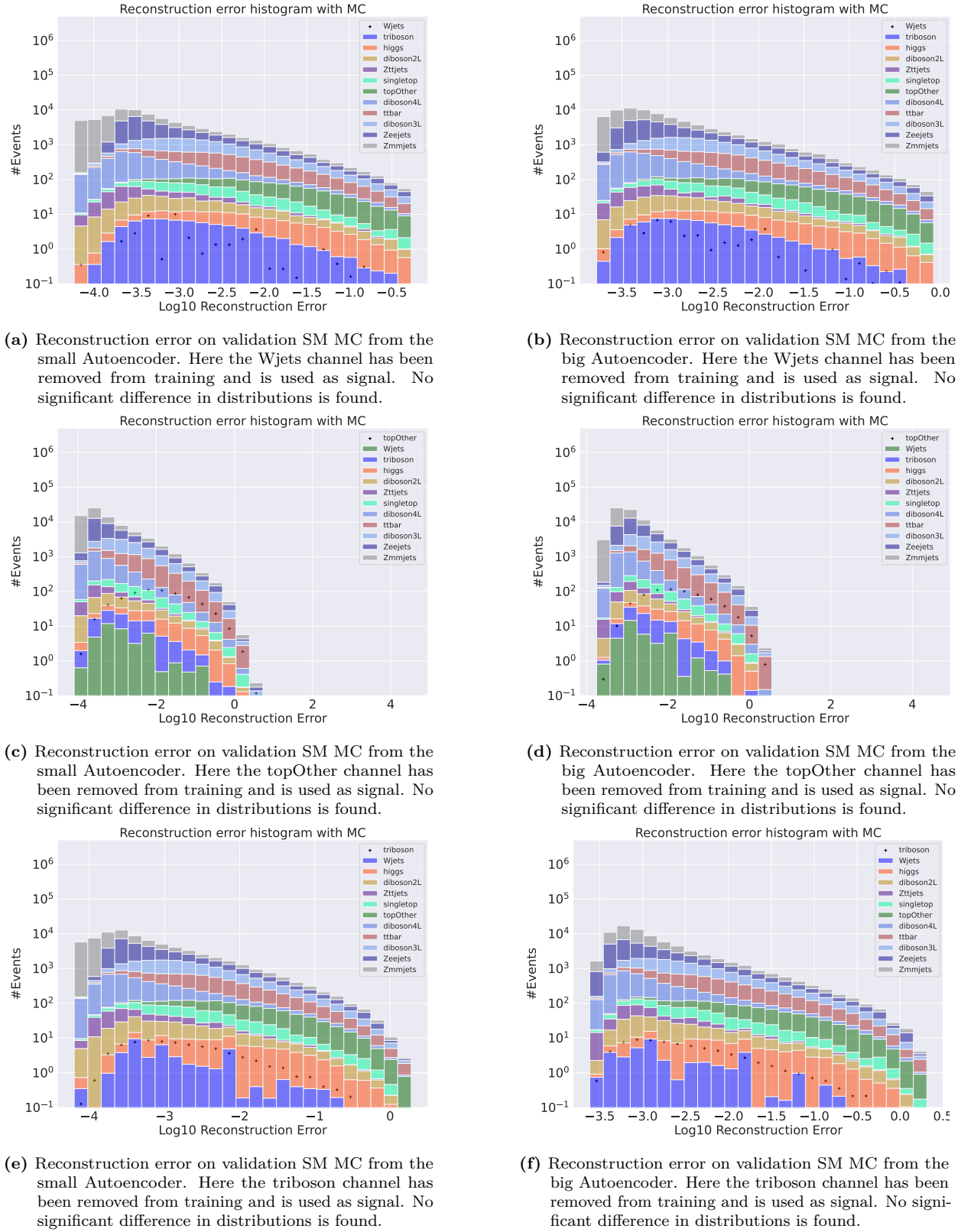


**Figure 2:** Reconstruction error on validation SM MC from the small and big Autoencoder. Here the Wjets, topOther and triboson have been used for the small (left) and large (right) regular autoencoder

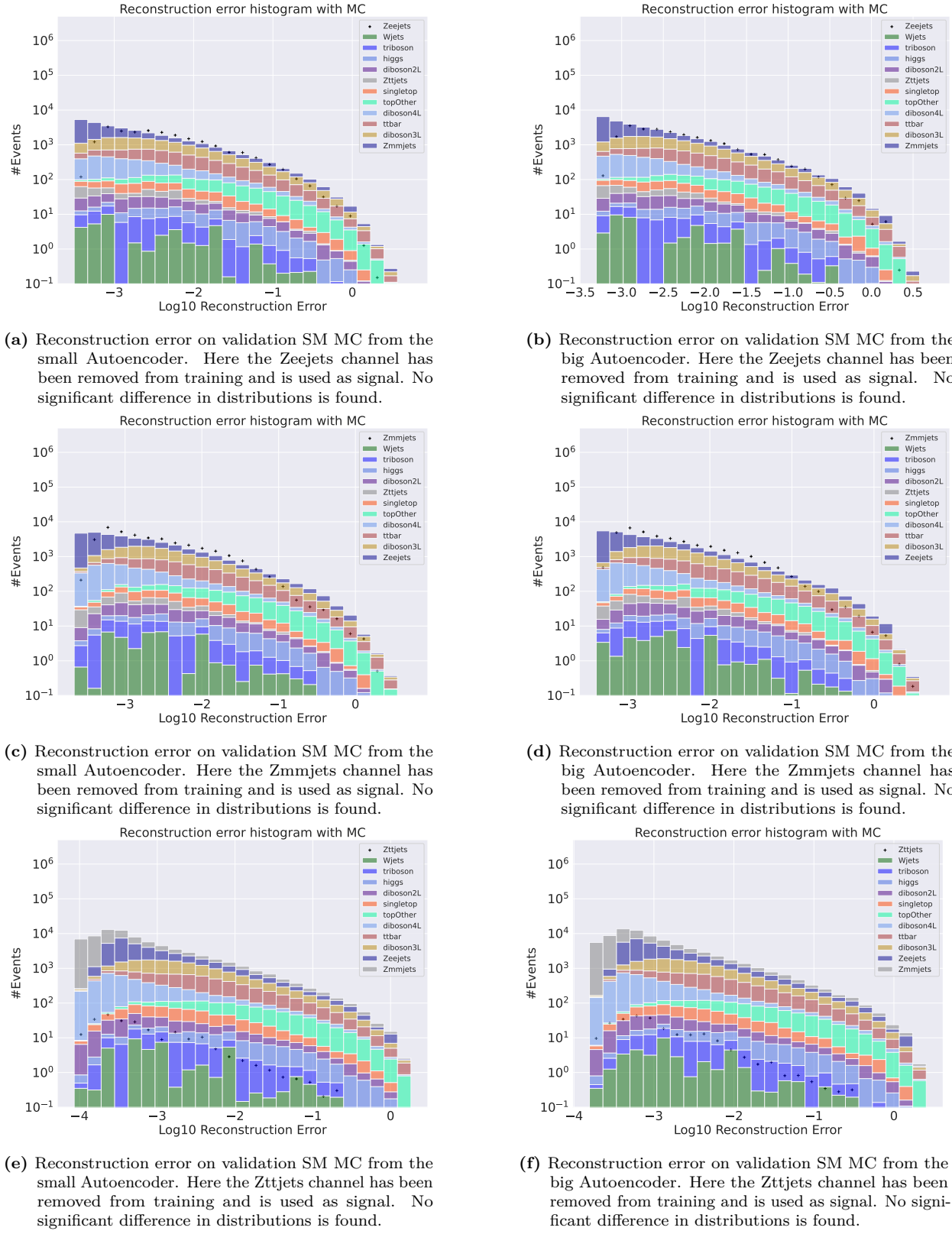


**Figure 3:** Reconstruction error on validation SM MC from the small and big Autoencoder. Here the Zeejets, Zmmjets and Zttjets have been used for the small (left) and large (right) regular autoencoder

## Variational autoencoder

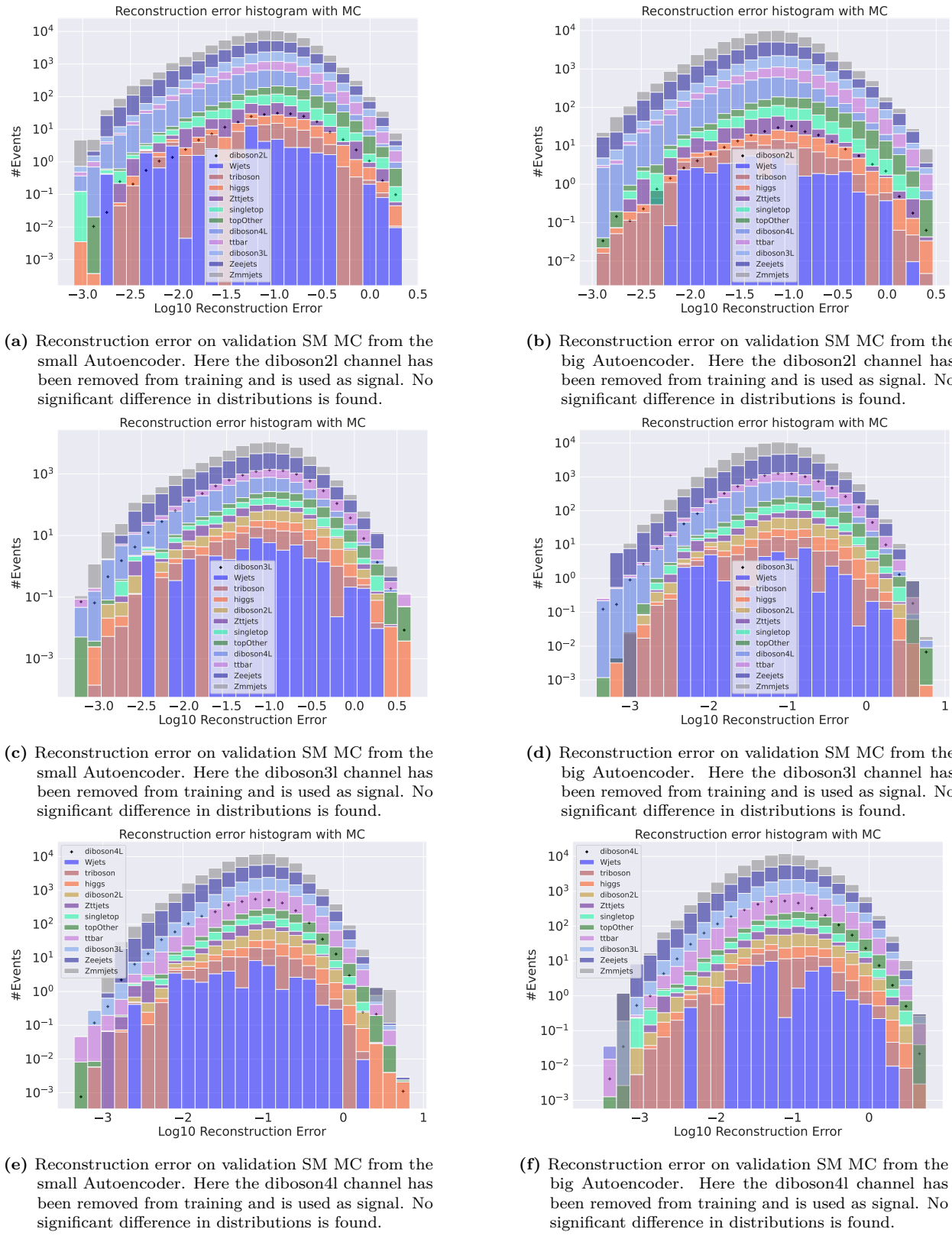


**Figure 4:** Reconstruction error on validation SM MC from the small and big Autoencoder. Here the diboson2L, diboson3L and diboson4L have been used for the small (left) and large (right) variational autoencoder

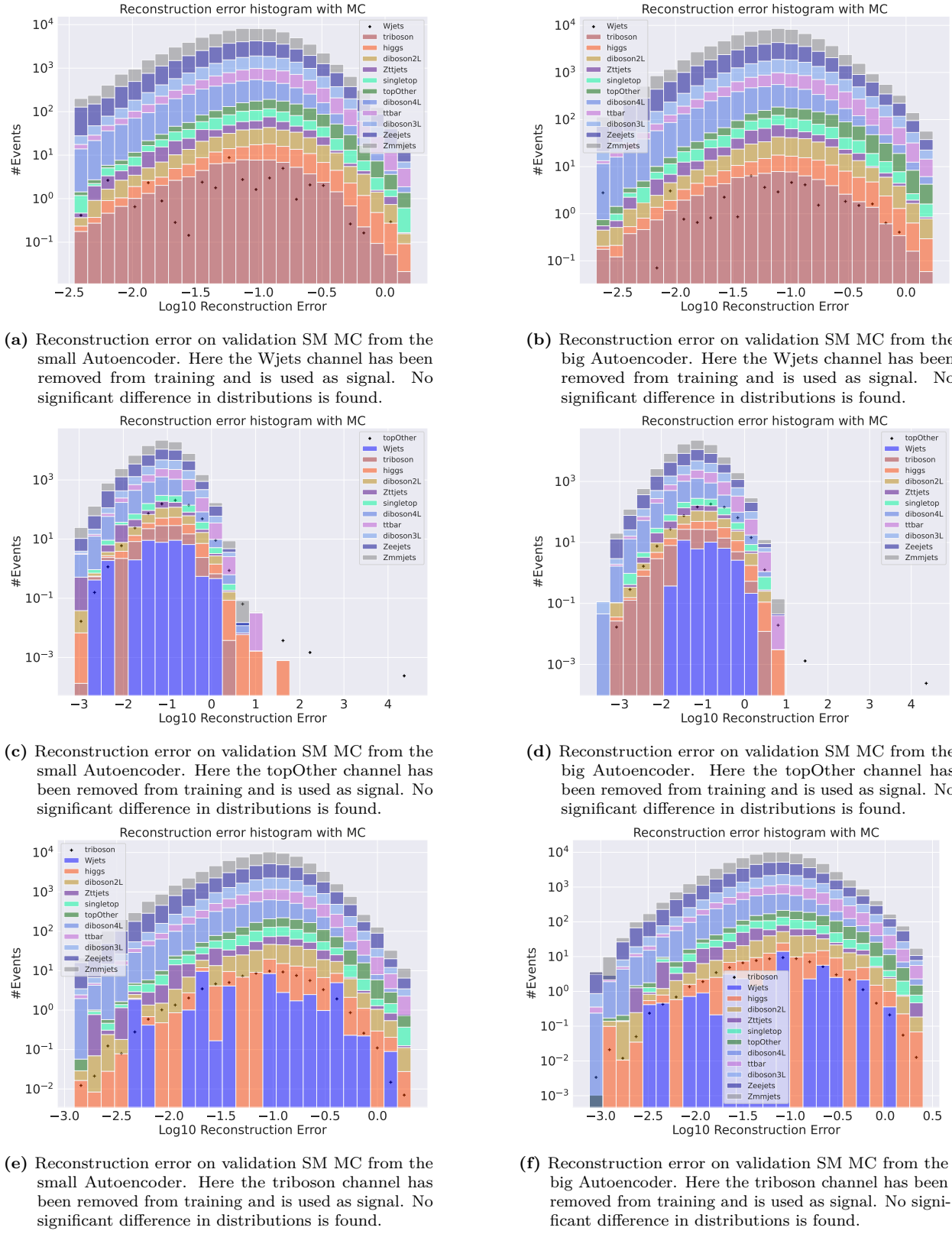


**Figure 5:** Reconstruction error on validation SM MC from the small and big Autoencoder. Here the Wjets, topOther and triboson have been used for the small (left) and large (right) variational autoencoder

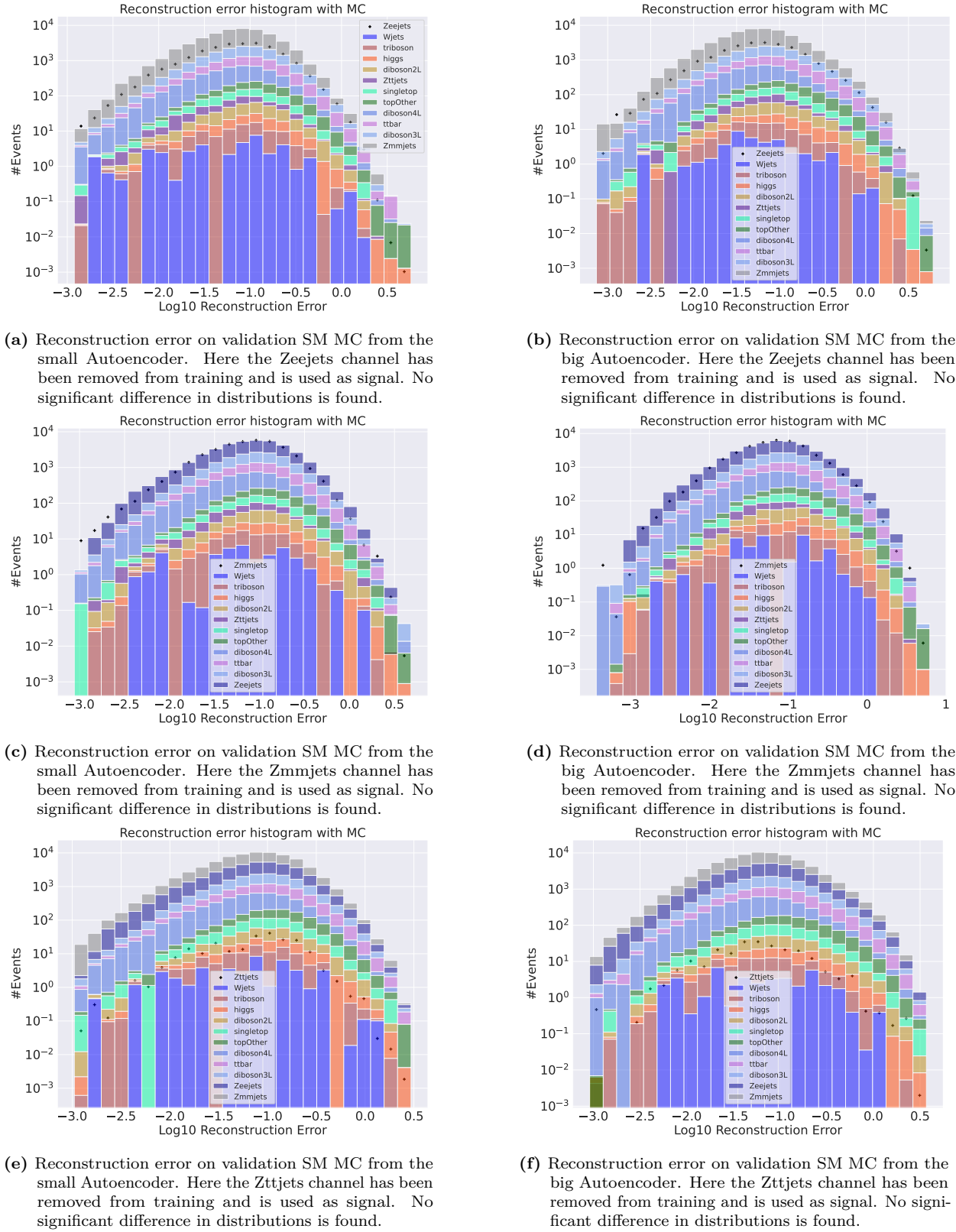


**Figure 6:** Reconstruction error on validation SM MC from the small and big Autoencoder. Here the Zeejets, Zmmjets and Zttjets have been used for the small (left) and large (right) variational autoencoder

## A.2 Transverse momentum altering

## Regular autoencoder output

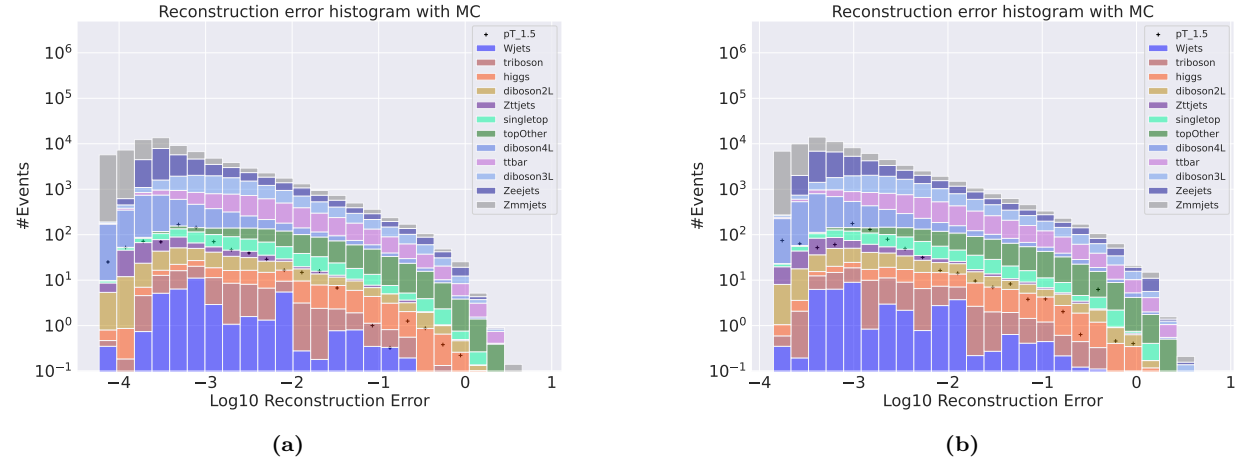


**Figure 7:** Reconstruction error on validation SM MC from the small (a) and large (b) regular autoencoder. The signal is a subsample of the validation set where the transverse momentum of the first electron and the first muon has been increased with a scale of 1.5. The change of transverse energy has also been changed according to the scaling of transverse momentum. A small peak is found around  $10^{-3.3}$ .

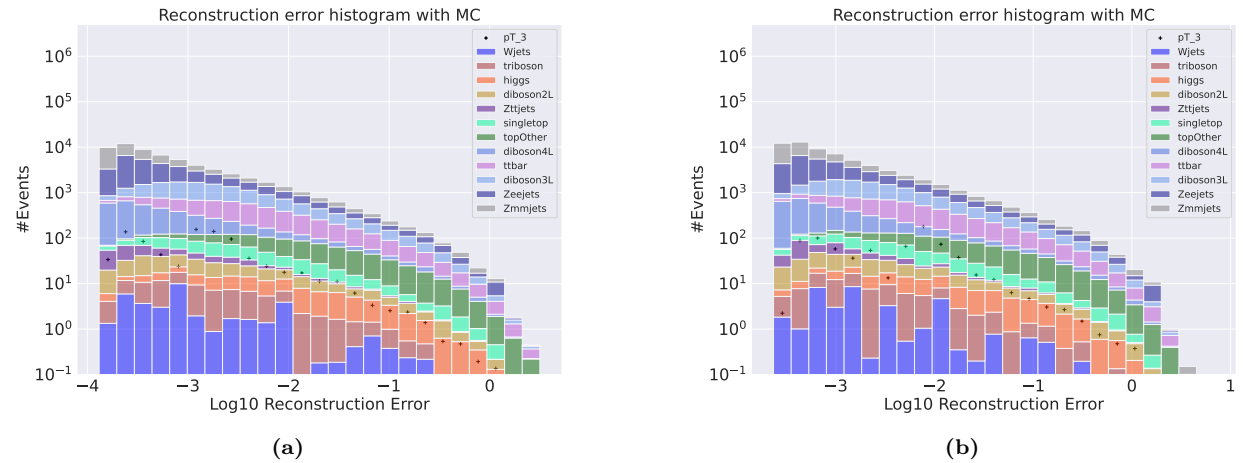


**Figure 8:** Reconstruction error on validation SM MC from the small (a) and large (b) regular autoencoder. The signal is a subsample of the validation set where the transverse momentum of the first electron and the first muon has been increased with a scale of 3. The change of transverse energy has also been changed according to the scaling of transverse momentum. A small peak is found around  $10^{-2.8}$ .

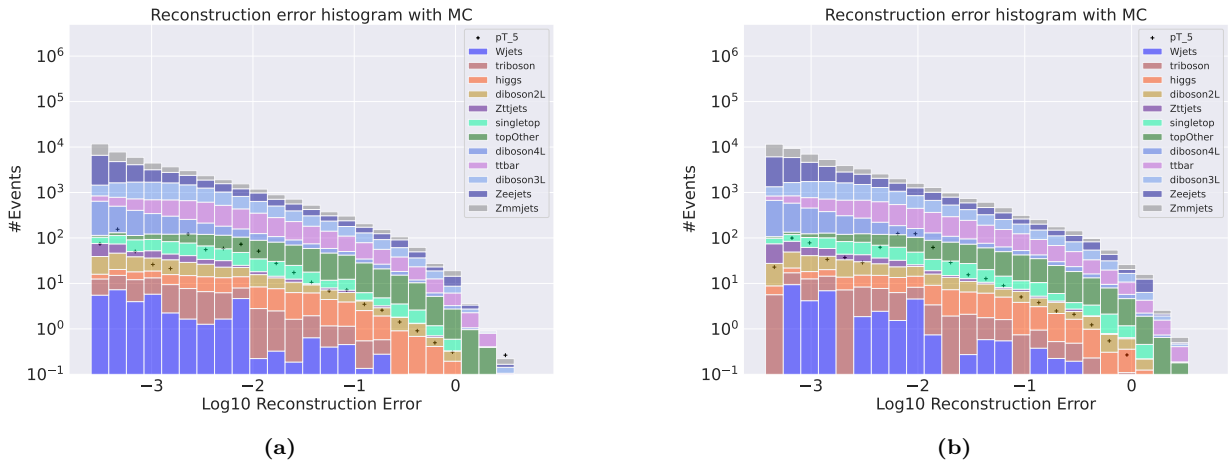


**Figure 9:** Reconstruction error on validation SM MC from the small (a) and large (b) regular autoencoder. The signal is a subsample of the validation set where the transverse momentum of the first electron and the first muon has been increased with a scale of 5. The change of transverse energy has also been changed according to the scaling of transverse momentum. A small peak is found around  $10^{-2}$ .

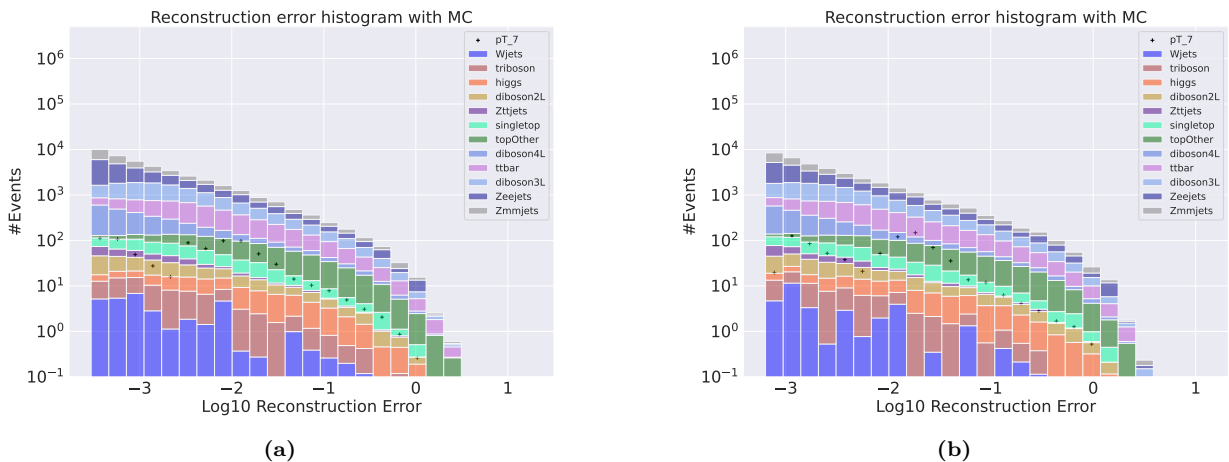


**Figure 10:** Reconstruction error on validation SM MC from the small (a) and large (b) regular autoencoder. The signal is a subsample of the validation set where the transverse momentum of the first electron and the first muon has been increased with a scale of 7. The change of transverse energy has also been changed according to the scaling of transverse momentum. A small peak is found around  $10^{-2}$ .

## Variational autoencoder output

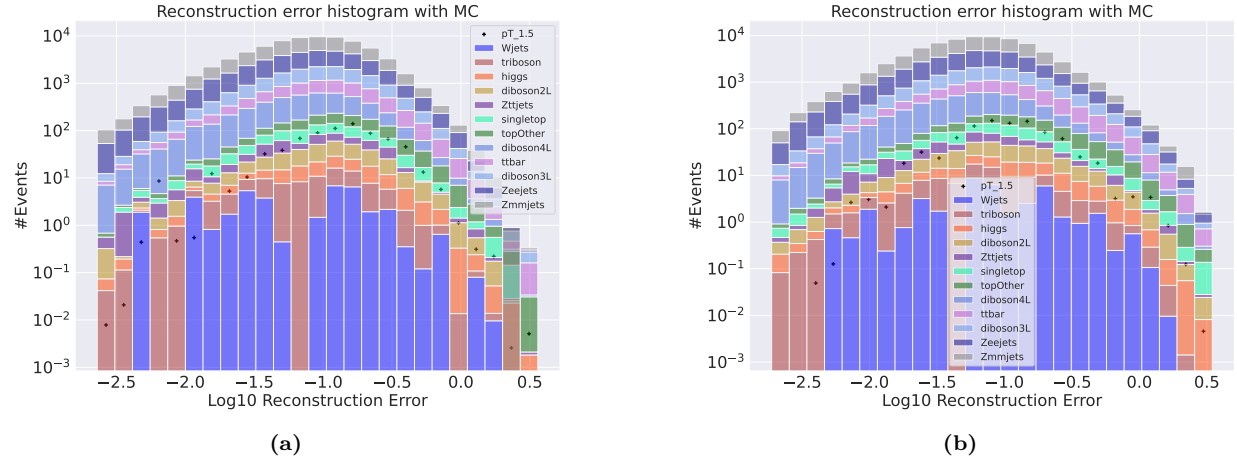


**Figure 11:** Reconstruction error on validation SM MC from the small (a) and large (b) variational autoencoder. The signal is a subsample of the validation set where the transverse momentum of the first electron and the first muon has been increased with a scale of 1.5. The change of transverse energy has also been changed according to the scaling of transverse momentum. A small peak is found around  $10^{-0.8}$ .

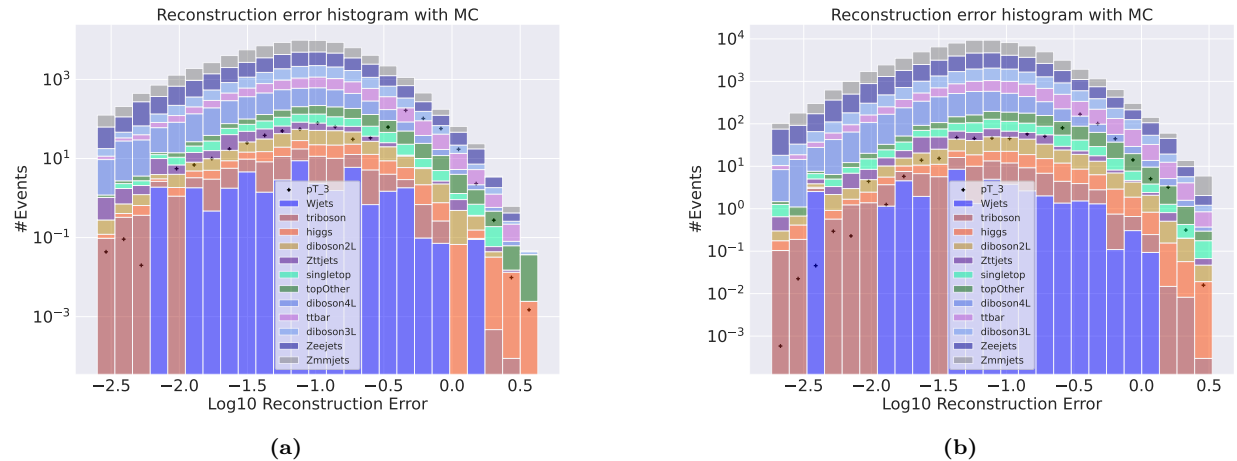


**Figure 12:** Reconstruction error on validation SM MC from the small (a) and large (b) variational autoencoder. The signal is a subsample of the validation set where the transverse momentum of the first electron and the first muon has been increased with a scale of 3. The change of transverse energy has also been changed according to the scaling of transverse momentum. A small peak is found around  $10^{-0.5}$ .

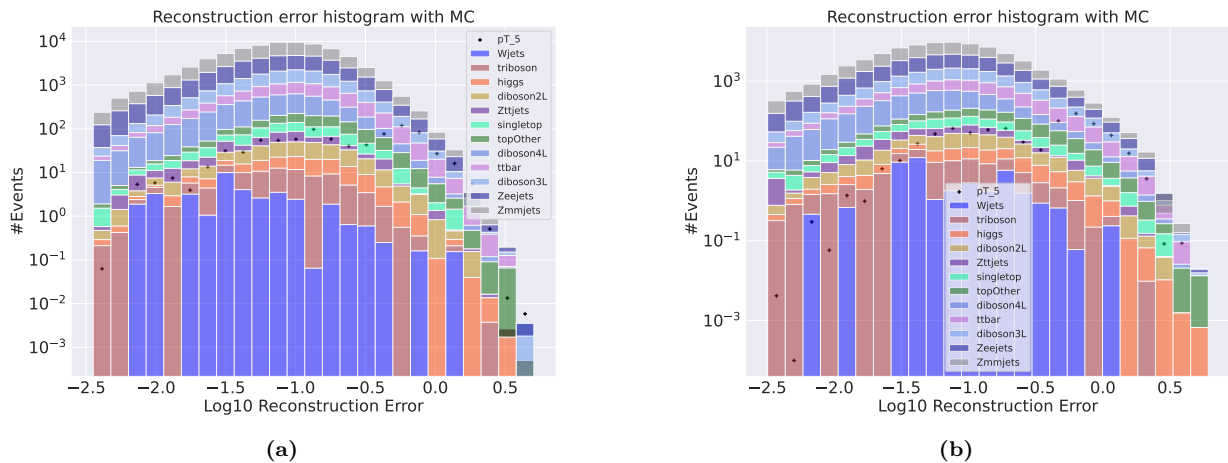


**Figure 13:** Reconstruction error on validation SM MC from the small (a) and large (b) variational autoencoder. The signal is a subsample of the validation set where the transverse momentum of the first electron and the first muon has been increased with a scale of 5. The change of transverse energy has also been changed according to the scaling of transverse momentum. A small peak is found around  $10^{-0.3}$ .

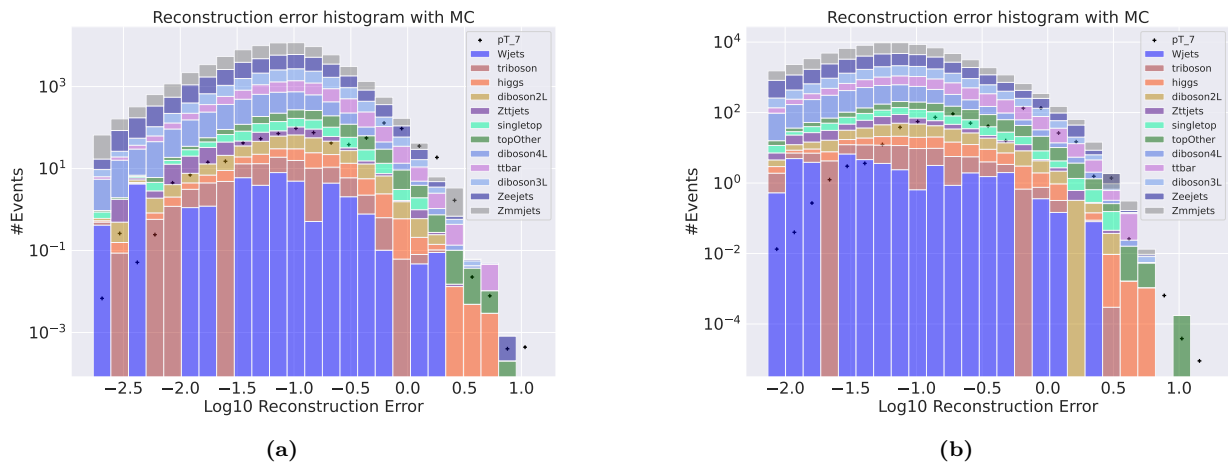


**Figure 14:** Reconstruction error on validation SM MC from the small (a) and large (b) variational autoencoder. The signal is a subsample of the validation set where the transverse momentum of the first electron and the first muon has been increased with a scale of 7. The change of transverse energy has also been changed according to the scaling of transverse momentum. A small peak is found around  $10^{-0.3}$ .

### A.3 Reconstruction error cuts for 3 leptons + $e_T^{miss}$

In this section the remaining two reconstruction error cuts in the 3 lepton +  $e_T^{\text{miss}}$  are shown. The figures here are shaped with the same subfigure structure as the figures in the results and discussion section.

## Regular autoencoder output

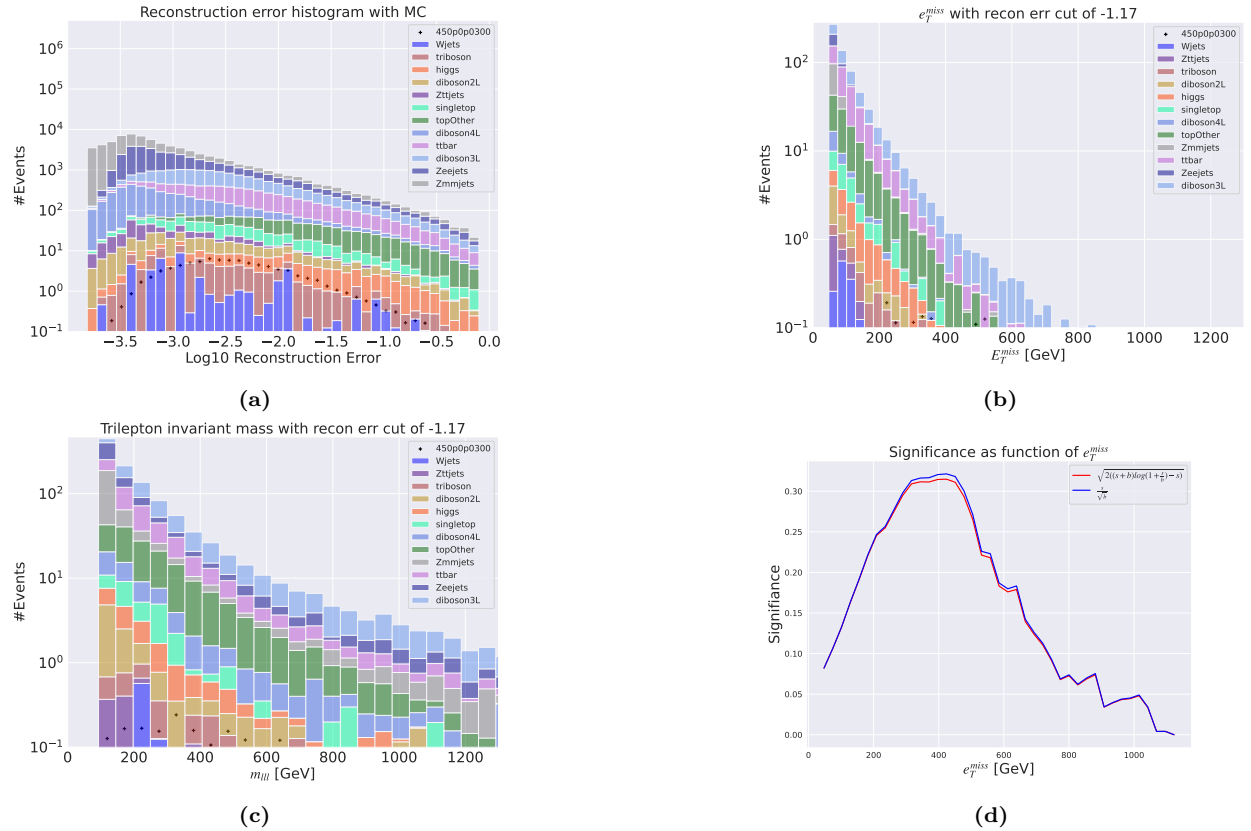


**Figure 15:** Reconstruction error,  $e_T^{\text{miss}}$  signal region,  $m_{ll}$  signal region and significance as function of  $e_T^{\text{miss}}$  for the deep regular autoencoder using the SUSY 450p300. Figure 15a shows the reconstruction error distribution for the SM MC and the SUSY signal. Here the autoencoder produce the same reconstruction error shape for both background and signal. Figure 15b shows the  $e_T^{\text{miss}}$  distribution for the SM MC and the SUSY signal in the signal region. The signal region is made using a cut around  $10^{-1.17}$ . Most of the background is removed, with almost no signal in the signal region. Figure 15c shows the  $m_{ll}$  distribution for the SM MC and the SUSY signal. There is almost no signal in the signal region. Figure 15d shows the significance as function of  $e_T^{\text{miss}}$ . The peak is put around a cut of about 430 GeV in the  $e_T^{\text{miss}}$ , with a significance of around 0.35.

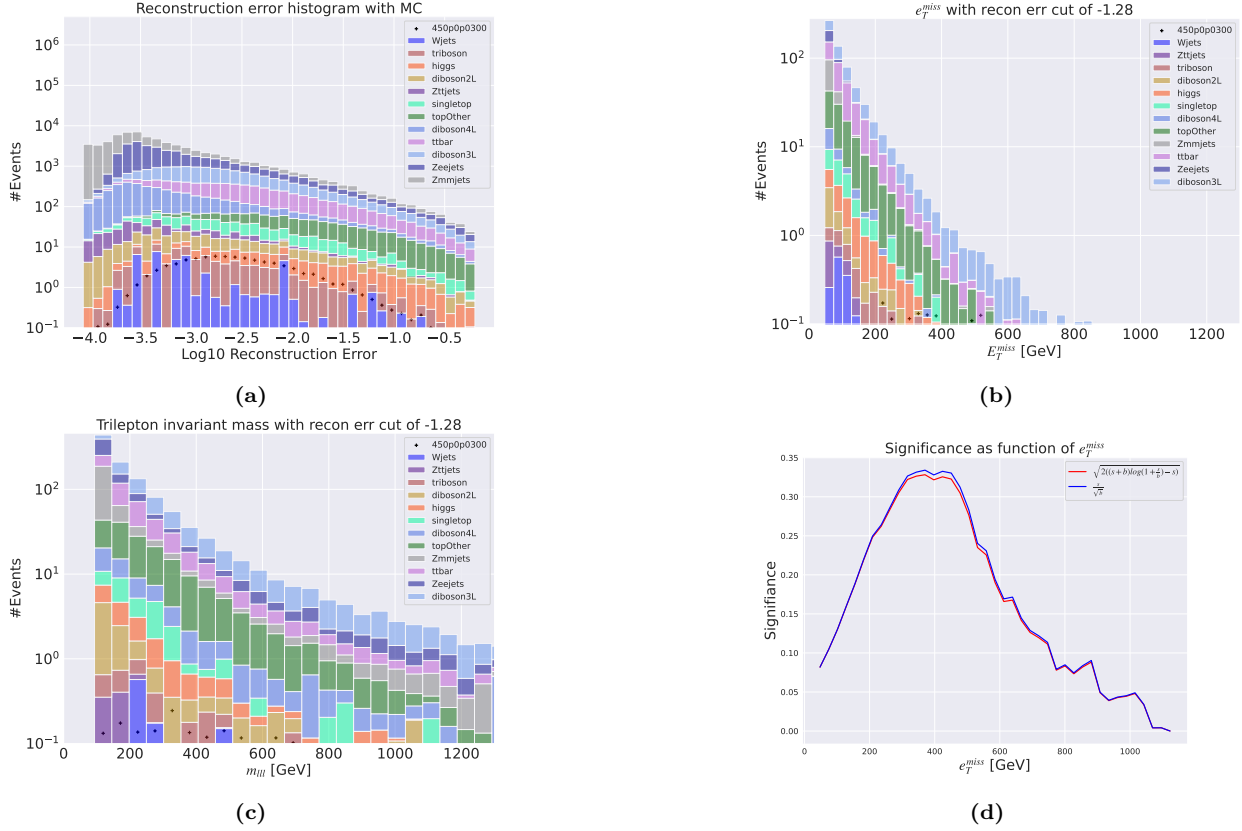


**Figure 16:** Reconstruction error,  $e_T^{miss}$  signal region,  $m_{lll}$  signal region and significance as function of  $e_T^{miss}$  for the shallow regular autoencoder. Here the SUSY 450p300 model is used. Figure 16a shows the reconstruction error distribution for the SM MC and the SUSY signal. Here the autoencoder produce the same reconstruction error shape for both background and signal. Figure 16b shows the  $e_T^{miss}$  distribution for the SM MC and the SUSY signal in the signal region. The signal region is made using a cut around  $10^{-1.28}$ . Most of the background is removed, with almost no signal in the signal region. Figure 16c shows the  $m_{lll}$  distribution for the SM MC and the SUSY signal. There is almost no signal in the signal region. Figure 16d shows the significance as function of  $e_T^{miss}$ . The peak is put around a cut of about 380 GeV in the  $e_T^{miss}$ , with a significance of around 0.33.

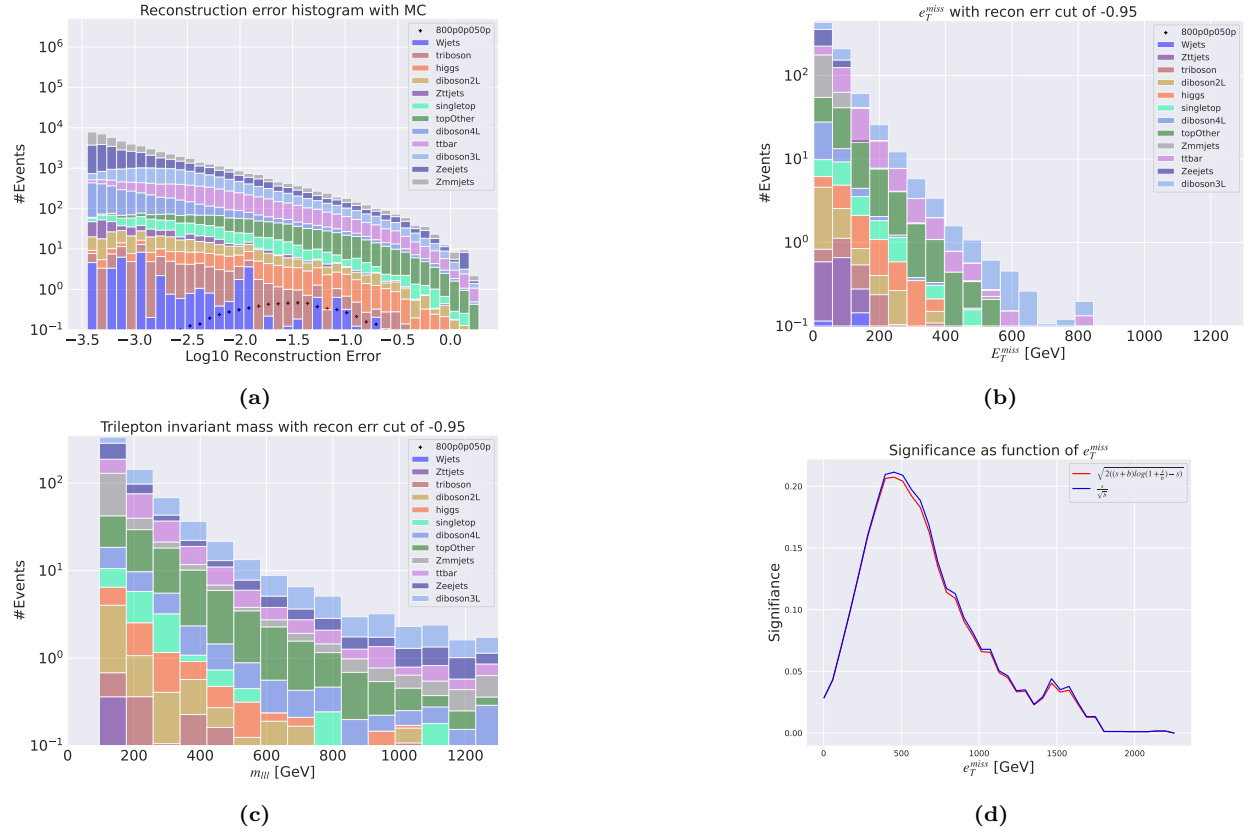


**Figure 17:** Reconstruction error,  $e_T^{\text{miss}}$  signal region,  $m_{lll}$  signal region and significance as function of  $e_T^{\text{miss}}$  for the deep regular autoencoder. Here the SUSY 450p300 model is used. Figure 17a shows the reconstruction error distribution for the SM MC and the SUSY signal. Here the autoencoder produce a mirrored reconstruction error shape for both background and signal. Figure 17b shows the  $e_T^{\text{miss}}$  distribution for the SM MC and the SUSY signal in the signal region. The signal region is made using a cut around  $10^{-0.95}$ . Most of the background is removed, with almost no signal in the signal region. Figure 17c shows the  $m_{lll}$  distribution for the SM MC and the SUSY signal. There is almost no signal in the signal region. Figure 17d shows the significance as function of  $e_T^{\text{miss}}$ . The peak is put around a cut of about 480 GeV in the  $e_T^{\text{miss}}$ , with a significance of around 0.25.

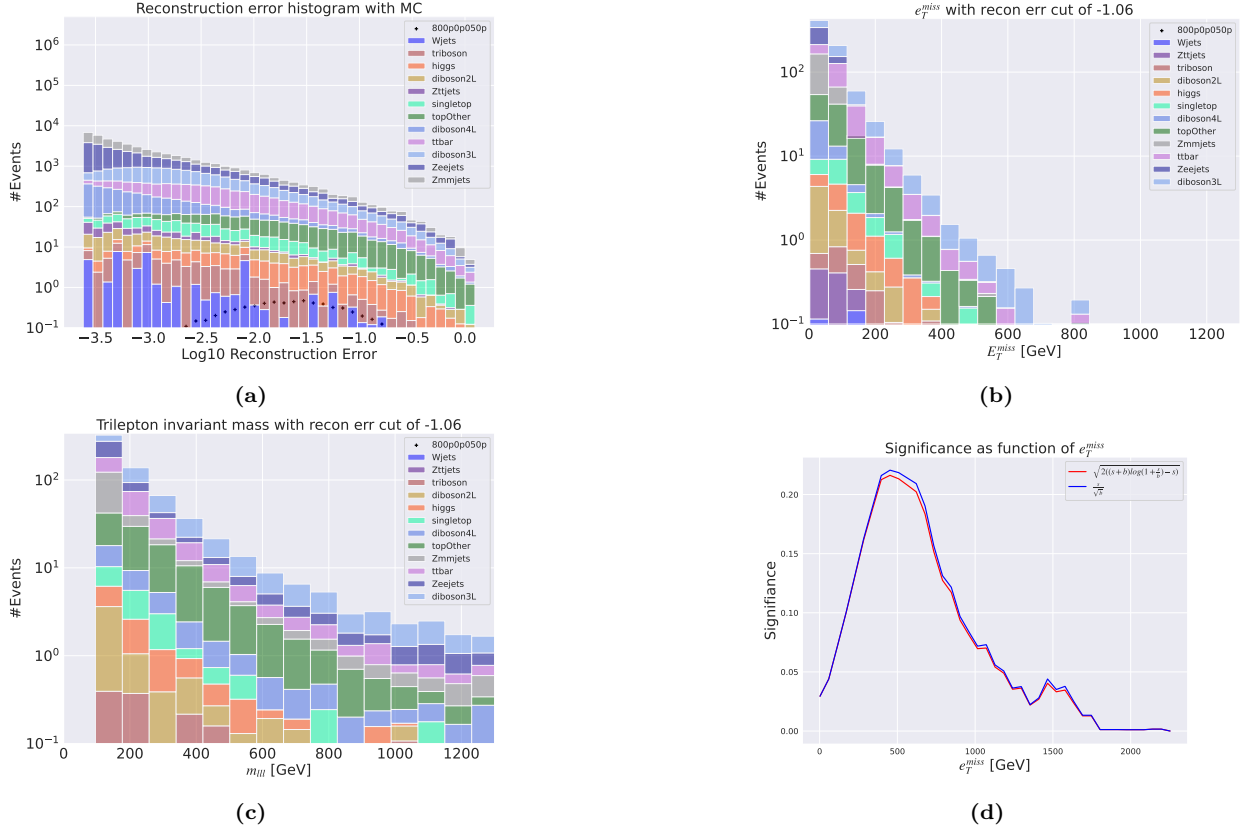


**Figure 18:** Reconstruction error,  $e_T^{miss}$  signal region,  $m_{lll}$  signal region and significance as function of  $e_T^{miss}$  for the shallow regular autoencoder. Here the SUSY 450p300 model is used. Figure 18a shows the reconstruction error distribution for the SM MC and the SUSY signal. Here the autoencoder produce a mirrored reconstruction error shape for both background and signal. Figure 18b shows the  $e_T^{miss}$  distribution for the SM MC and the SUSY signal in the signal region. The signal region is made using a cut around  $10^{-1.06}$ . Most of the background is removed, with almost no signal in the signal region. Figure 18c shows the  $m_{lll}$  distribution for the SM MC and the SUSY signal. There is almost no signal in the signal region. Figure 18d shows the significance as function of  $e_T^{miss}$ . The peak is put around a cut of about 480 GeV in the  $e_T^{miss}$ , with a significance of around 0.23.

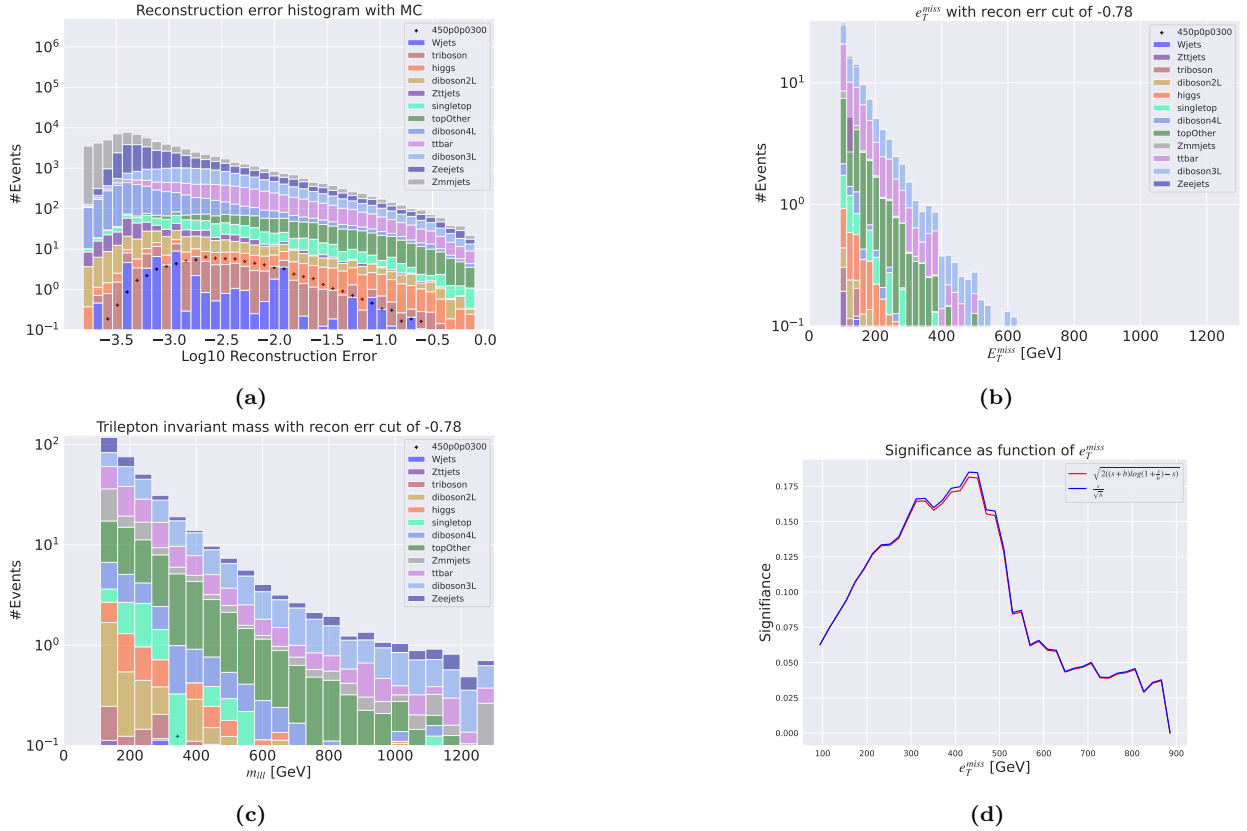


**Figure 19:** Reconstruction error,  $e_T^{\text{miss}}$  signal region,  $m_{lll}$  signal region and significance as function of  $e_T^{\text{miss}}$  for the deep regular autoencoder. Here the SUSY 450p300 model is used. Figure 19a shows the reconstruction error distribution for the SM MC and the SUSY signal. Here the autoencoder produce the same reconstruction error shape for both background and signal. Figure 19b shows the  $e_T^{\text{miss}}$  distribution for the SM MC and the SUSY signal in the signal region. The signal region is made using a cut around  $10^{-0.78}$ . Most of the background is removed, with almost no signal in the signal region. Figure 19c shows the  $m_{lll}$  distribution for the SM MC and the SUSY signal. There is almost no signal in the signal region. Figure 19d shows the significance as function of  $e_T^{\text{miss}}$ . The peak is put around a cut of about 430 GeV in the  $e_T^{\text{miss}}$ , with a significance of around 0.185.

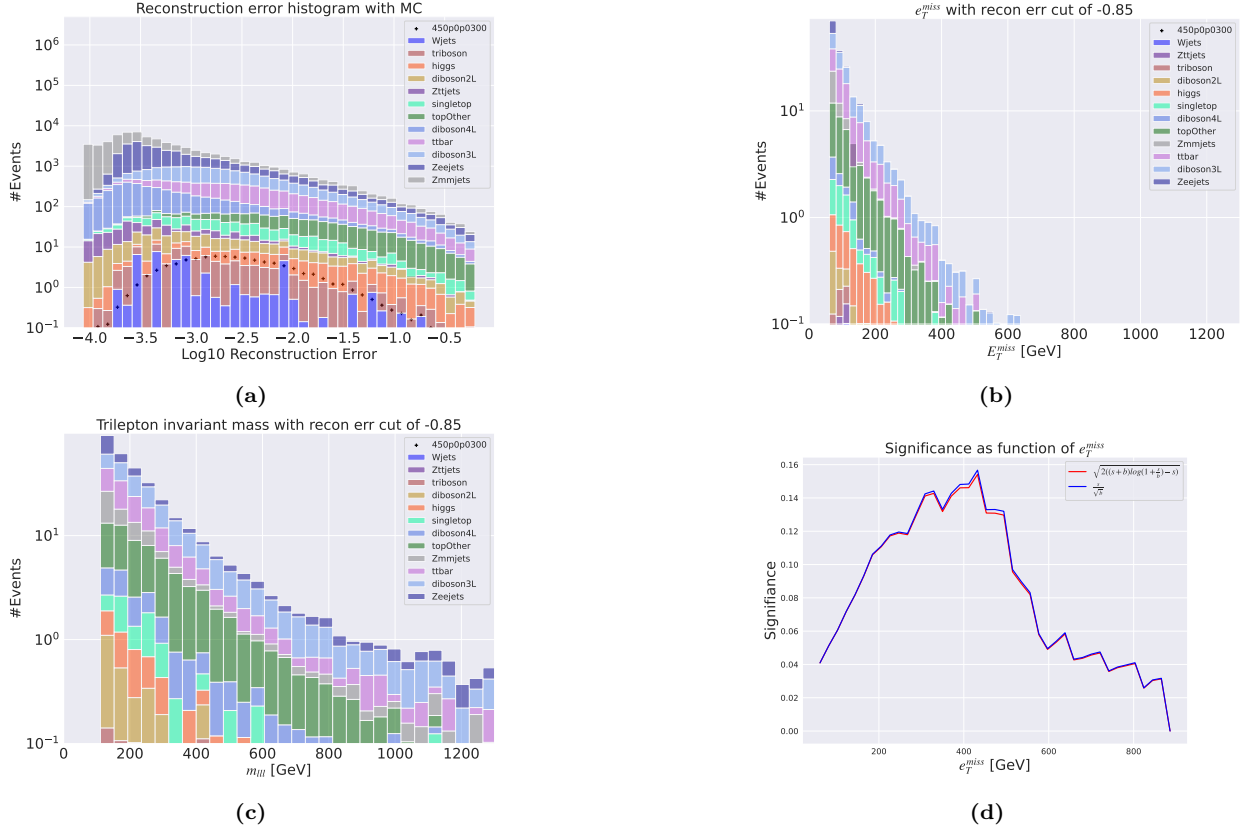


**Figure 20:** Reconstruction error,  $e_T^{miss}$  signal region,  $m_{lll}$  signal region and significance as function of  $e_T^{miss}$  for the shallow regular autoencoder. Here the SUSY 450p300 model is used. Figure 20a shows the reconstruction error distribution for the SM MC and the SUSY signal. Here the autoencoder produce the same reconstruction error shape for both background and signal. Figure 20b shows the  $e_T^{miss}$  distribution for the SM MC and the SUSY signal in the signal region. The signal region is made using a cut around  $10^{-0.85}$ . Most of the background is removed, with almost no signal in the signal region. Figure 20c shows the  $m_{lll}$  distribution for the SM MC and the SUSY signal. There is almost no signal in the signal region. Figure 20d shows the significance as function of  $e_T^{miss}$ . The peak is put around a cut of about 430 GeV in the  $e_T^{miss}$ , with a significance of around 0.155.

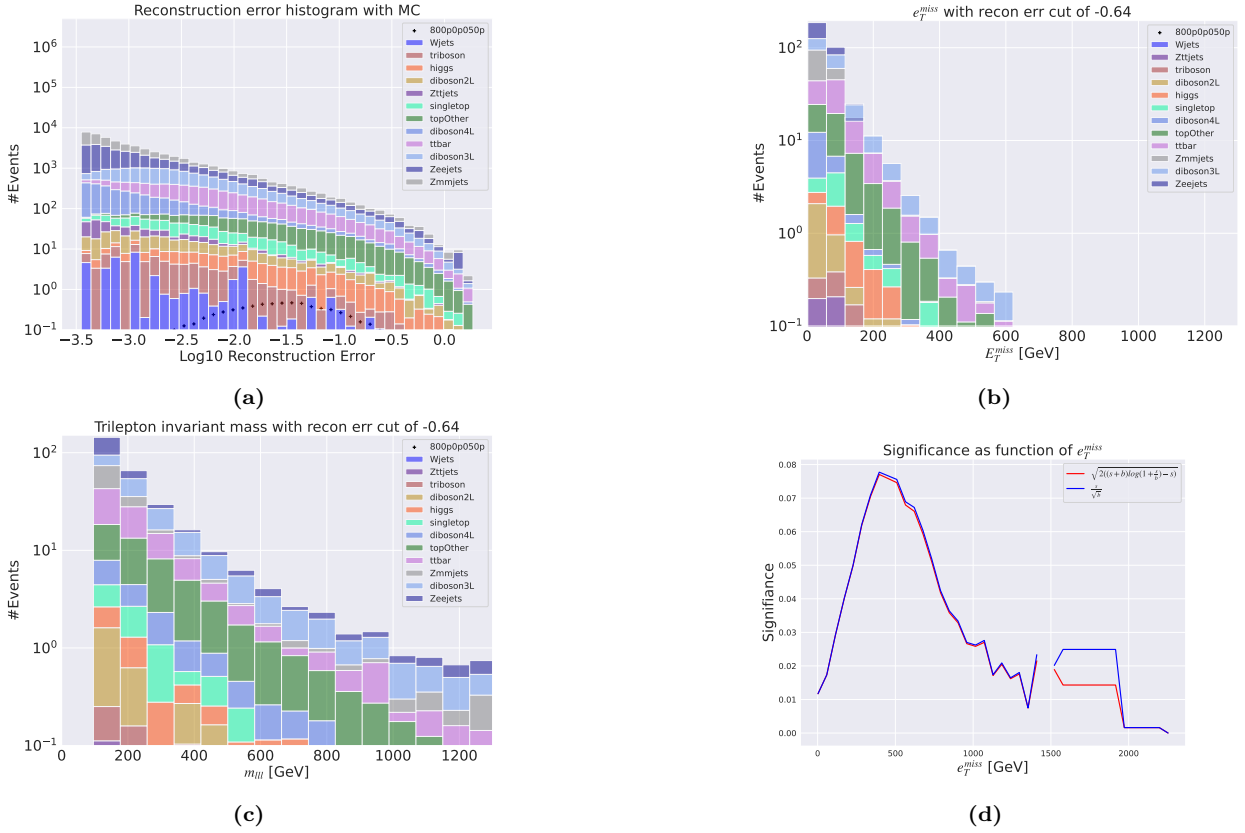


**Figure 21:** Reconstruction error,  $e_T^{\text{miss}}$  signal region,  $m_{lll}$  signal region and significance as function of  $e_T^{\text{miss}}$  for the deep regular autoencoder. Here the SUSY 450p300 model is used. Figure 21a shows the reconstruction error distribution for the SM MC and the SUSY signal. Here the autoencoder produce a mirrored reconstruction error shape for both background and signal. Figure 21b shows the  $e_T^{\text{miss}}$  distribution for the SM MC and the SUSY signal in the signal region. The signal region is made using a cut around  $10^{-0.64}$ . Most of the background is removed, with almost no signal in the signal region. Figure 21c shows the  $m_{lll}$  distribution for the SM MC and the SUSY signal. There is almost no signal in the signal region. Figure 21d shows the significance as function of  $e_T^{\text{miss}}$ . The peak is put around a cut of about 400 GeV in the  $e_T^{\text{miss}}$ , with a significance of around 0.078.

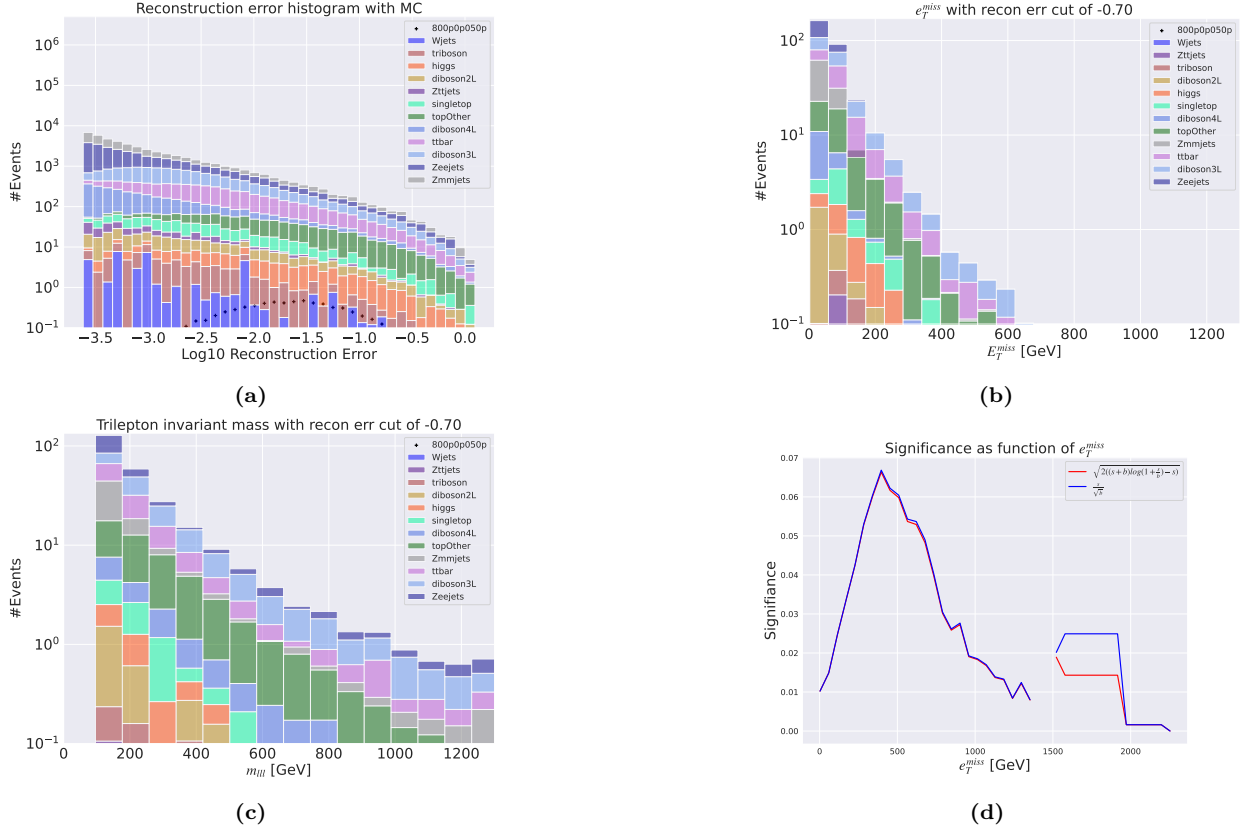


**Figure 22:** Reconstruction error,  $e_T^{miss}$  signal region,  $m_{lll}$  signal region and significance as function of  $e_T^{miss}$  for the shallow regular autoencoder. Here the SUSY 450p300 model is used. Figure 22a shows the reconstruction error distribution for the SM MC and the SUSY signal. Here the autoencoder produce a mirrored reconstruction error shape for both background and signal. Figure 22b shows the  $e_T^{miss}$  distribution for the SM MC and the SUSY signal in the signal region. The signal region is made using a cut around  $10^{-0.95}$ . Most of the background is removed, with almost no signal in the signal region. Figure 22c shows the  $m_{lll}$  distribution for the SM MC and the SUSY signal. There is almost no signal in the signal region. Figure 22d shows the significance as function of  $e_T^{miss}$ . The peak is put around a cut of about 400 GeV in the  $e_T^{miss}$ , with a significance of around 0.067.

## Variational autoencoder output

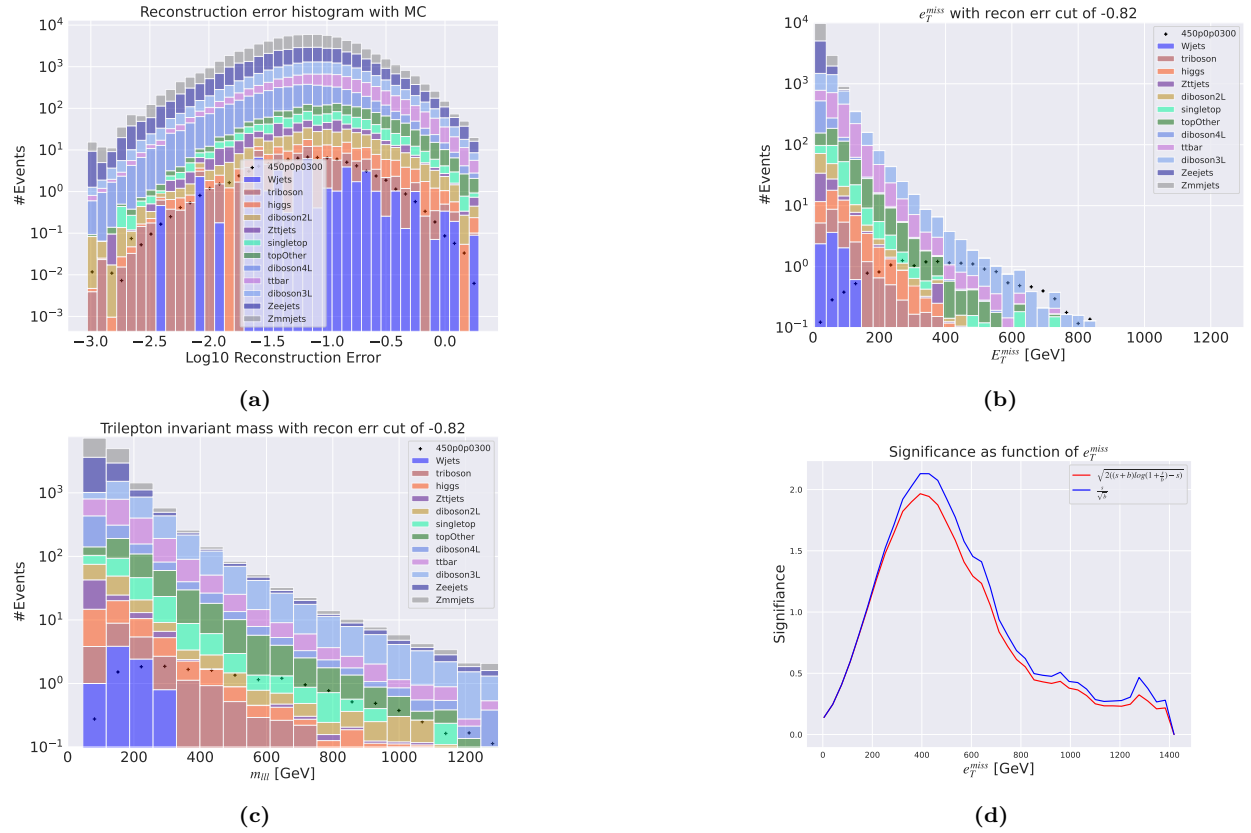


**Figure 23:** Reconstruction error,  $e_T^{\text{miss}}$  signal region,  $m_{lll}$  signal region and significance as function of  $e_T^{\text{miss}}$  for the deep variational autoencoder. Here the SUSY 450p300 model is used. Figure 23a shows the reconstruction error distribution for the SM MC and the SUSY signal. Here the autoencoder produce a bell-shape for background and signal with little distinction. The peaks of the two distributions are not separated in reconstruction error. Figure 23b shows the  $e_T^{\text{miss}}$  distribution for the SM MC and the SUSY signal in the signal region. The signal region is made using a cut around  $10^{-0.82}$ . Some background is removed, and the peaks of the SM MC and signal distributions are separated. Figure 23c shows the  $m_{lll}$  distribution for the SM MC and the SUSY signal. The shape of both distributions are displaying almost the same shape. Figure 23d shows the significance as function of  $e_T^{\text{miss}}$ . The peak is put around a cut of about 400 GeV in the  $e_T^{\text{miss}}$ , with a significance of around 2.5.

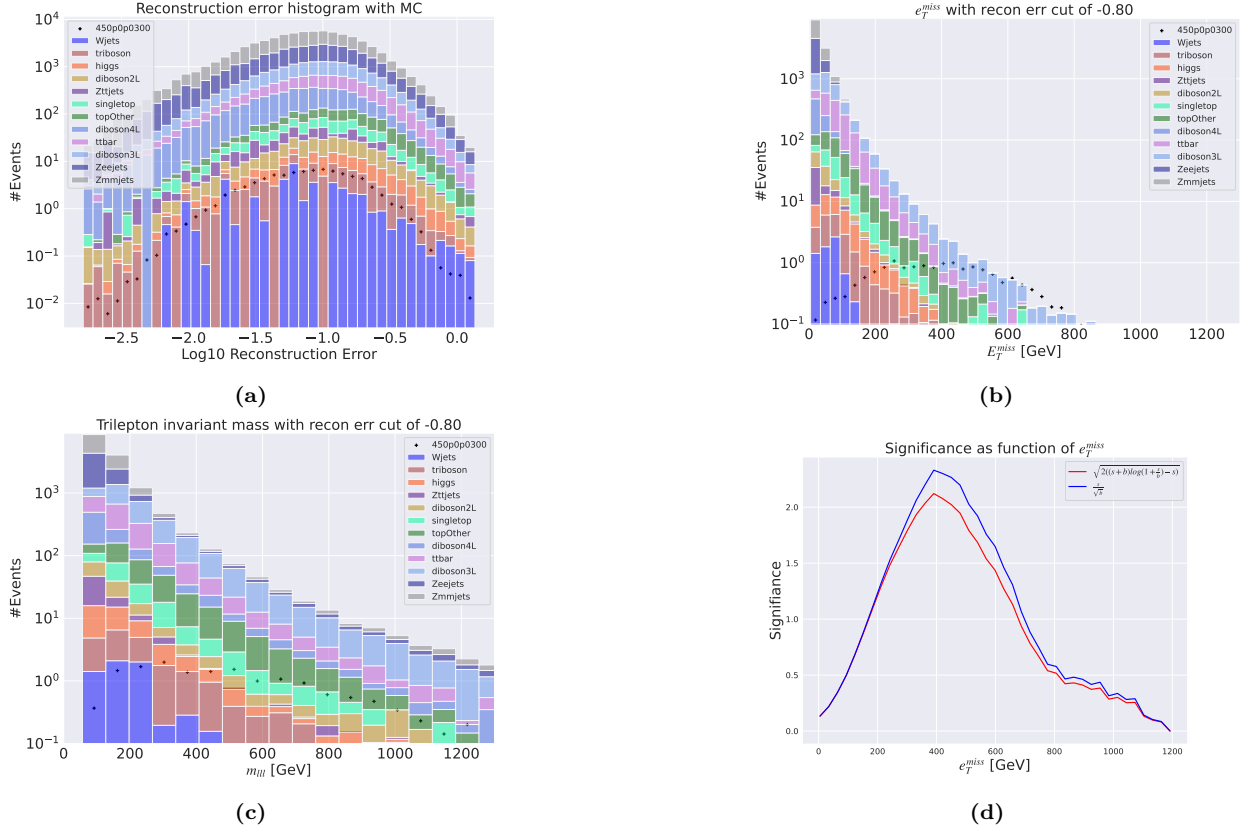


**Figure 24:** Reconstruction error,  $e_T^{miss}$  signal region,  $m_{ll}$  signal region and significance as function of  $e_T^{miss}$  for the shallow variational autoencoder. Here the SUSY 450p300 model is used. Figure 24a shows the reconstruction error distribution for the SM MC and the SUSY signal. Here the autoencoder produce a bell-shape for background and signal with little distinction. The peaks of the two distributions are not separated in reconstruction error. Figure 24b shows the  $e_T^{miss}$  distribution for the SM MC and the SUSY signal in the signal region. The signal region is made using a cut around  $10^{-0.80}$ . Some background is removed, and the peaks of the SM MC and signal distributions are separated. Figure 24c shows the  $m_{ll}$  distribution for the SM MC and the SUSY signal. The shape of both distributions are displaying almost the same shape. Figure 24d shows the significance as function of  $e_T^{miss}$ . The peak is put around a cut of about 400 GeV in the  $e_T^{miss}$ , with a significance of around 2.6.

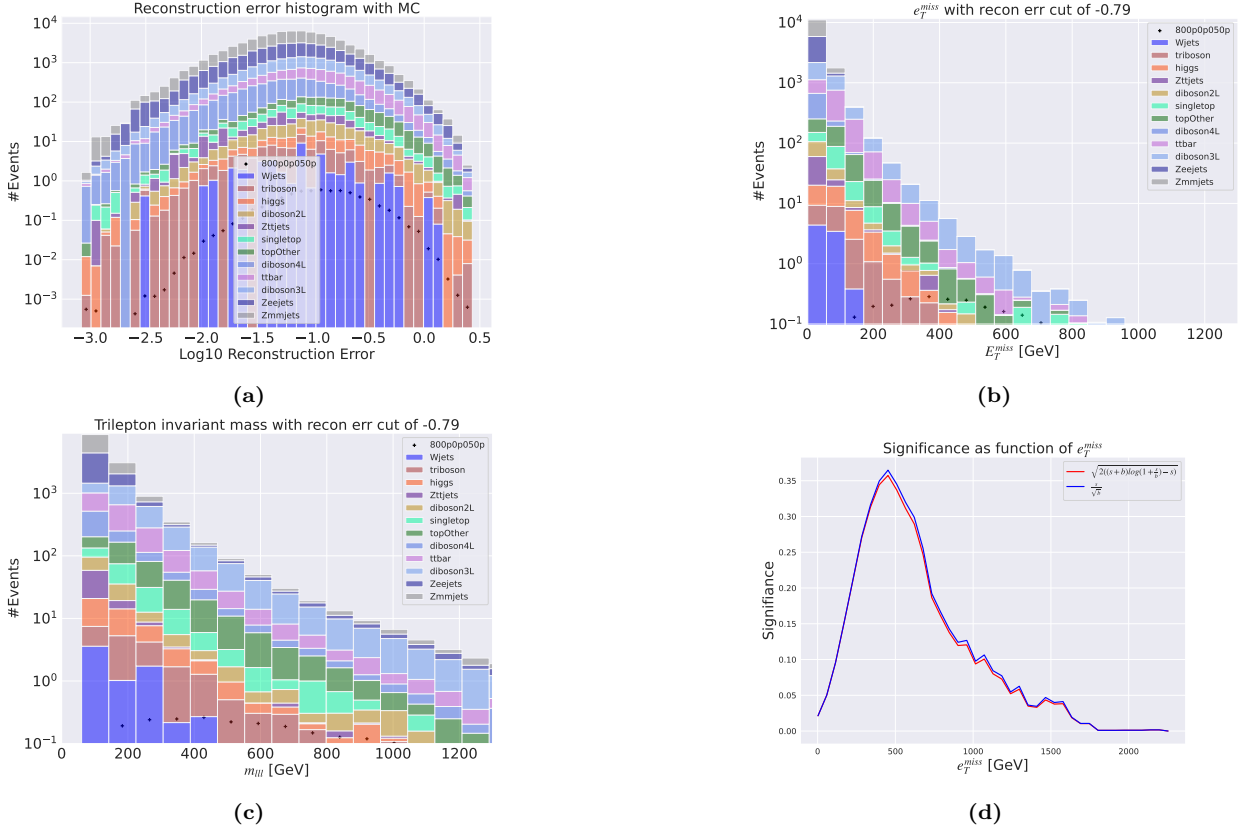


**Figure 25:** Reconstruction error,  $e_T^{\text{miss}}$  signal region,  $m_{lll}$  signal region and significance as function of  $e_T^{\text{miss}}$  for the deep variational autoencoder. Here the SUSY 450p300 model is used. Figure 25a shows the reconstruction error distribution for the SM MC and the SUSY signal. Here the autoencoder produce a bell-shape for background and signal with little distinction. The peaks of the two distributions are not separated in reconstruction error. Figure 25b shows the  $e_T^{\text{miss}}$  distribution for the SM MC and the SUSY signal in the signal region. The signal region is made using a cut around  $10^{-0.79}$ . Some background is removed, and the peaks of the SM MC and signal distributions are separated. Figure 25c shows the  $m_{lll}$  distribution for the SM MC and the SUSY signal. The shape of both distributions are displaying almost the same shape. Figure 25d shows the significance as function of  $e_T^{\text{miss}}$ . The peak is put around a cut of about 400 GeV in the  $e_T^{\text{miss}}$ , with a significance of around 3.3.

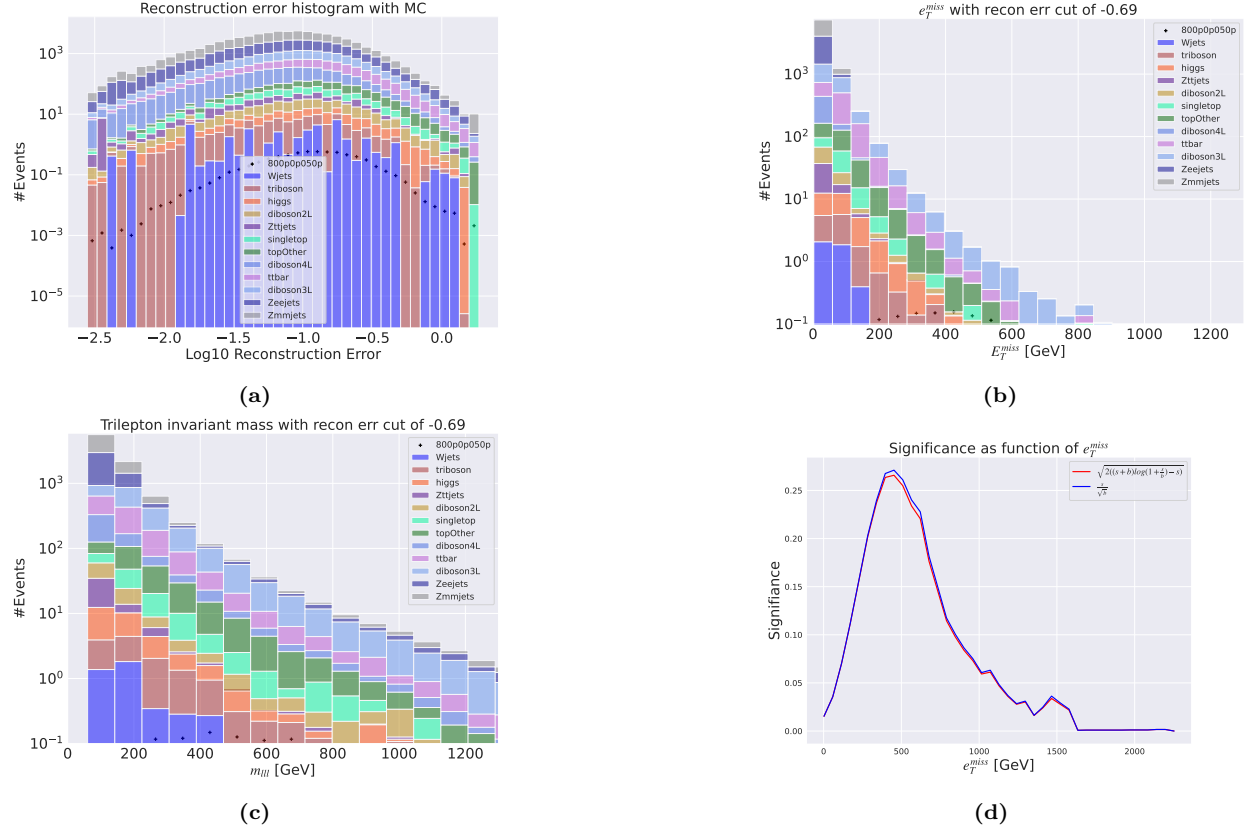


**Figure 26:** Reconstruction error,  $e_T^{miss}$  signal region,  $m_{ll}$  signal region and significance as function of  $e_T^{miss}$  for the shallow variational autoencoder. Here the SUSY 450p300 model is used. Figure 26a shows the reconstruction error distribution for the SM MC and the SUSY signal. Here the autoencoder produce a bell-shape for background and signal with little distinction. The peaks of the two distributions are not separated in reconstruction error. Figure 26b shows the  $e_T^{miss}$  distribution for the SM MC and the SUSY signal in the signal region. The signal region is made using a cut around  $10^{-0.69}$ . Some background is removed, and the peaks of the SM MC and signal distributions are separated. Figure 26c shows the  $m_{ll}$  distribution for the SM MC and the SUSY signal. The shape of both distributions are displaying almost the same shape. Figure 26d shows the significance as function of  $e_T^{miss}$ . The peak is put around a cut of about 450 GeV in the  $e_T^{miss}$ , with a significance of around 0.27.

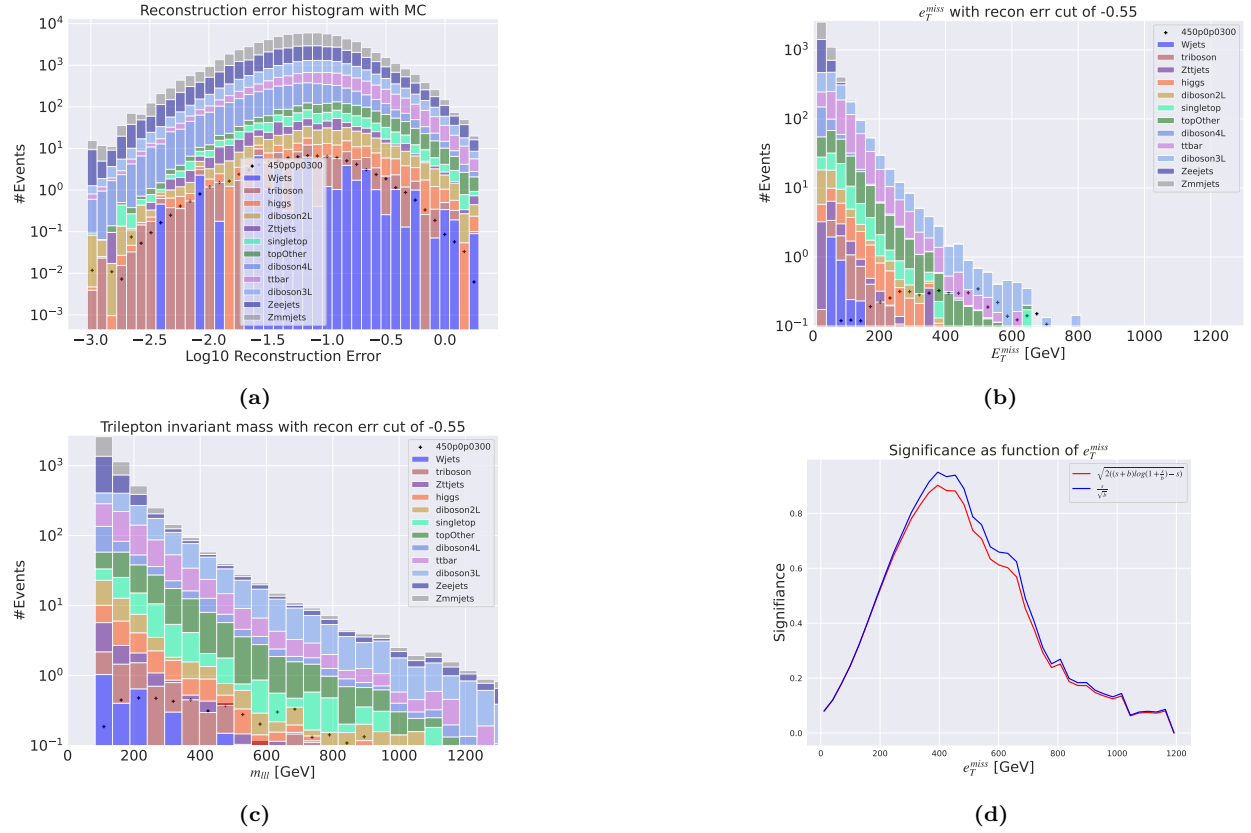


**Figure 27:** Reconstruction error,  $e_T^{\text{miss}}$  signal region,  $m_{lll}$  signal region and significance as function of  $e_T^{\text{miss}}$  for the deep variational autoencoder. Here the SUSY 450p300 model is used. Figure 27a shows the reconstruction error distribution for the SM MC and the SUSY signal. Here the autoencoder produce a bell-shape for background and signal with little distinction. The peaks of the two distributions are not separated in reconstruction error. Figure 27b shows the  $e_T^{\text{miss}}$  distribution for the SM MC and the SUSY signal in the signal region. The signal region is made using a cut around  $10^{-0.55}$ . Some background is removed, and the peaks of the SM MC and signal distributions are separated. Figure 27c shows the  $m_{lll}$  distribution for the SM MC and the SUSY signal. The shape of both distributions are displaying almost the same shape. Figure 27d shows the significance as function of  $e_T^{\text{miss}}$ . The peak is put around a cut of about 400 GeV in the  $e_T^{\text{miss}}$ , with a significance of around 0.94.

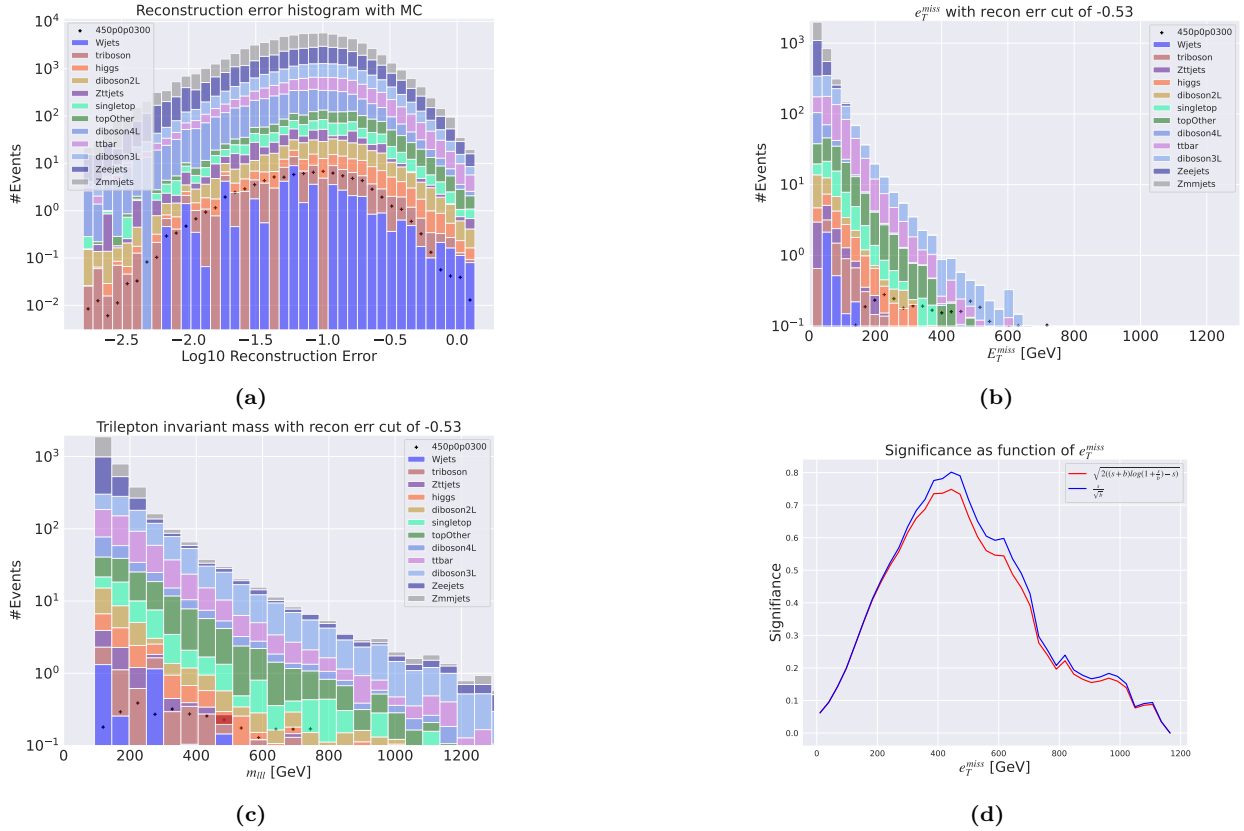


**Figure 28:** Reconstruction error,  $e_T^{miss}$  signal region,  $m_{ll}$  signal region and significance as function of  $e_T^{miss}$  for the shallow variational autoencoder. Here the SUSY 450p300 model is used. Figure 28a shows the reconstruction error distribution for the SM MC and the SUSY signal. Here the autoencoder produce a bell-shape for background and signal with little distinction. The peaks of the two distributions are not separated in reconstruction error. Figure 28b shows the  $e_T^{miss}$  distribution for the SM MC and the SUSY signal in the signal region. The signal region is made using a cut around  $10^{-0.53}$ . Some background is removed, and the peaks of the SM MC and signal distributions are separated. Figure 28c shows the  $m_{ll}$  distribution for the SM MC and the SUSY signal. The shape of both distributions are displaying almost the same shape. Figure 28d shows the significance as function of  $e_T^{miss}$ . The peak is put around a cut of about 450 GeV in the  $e_T^{miss}$ , with a significance of around 0.81.

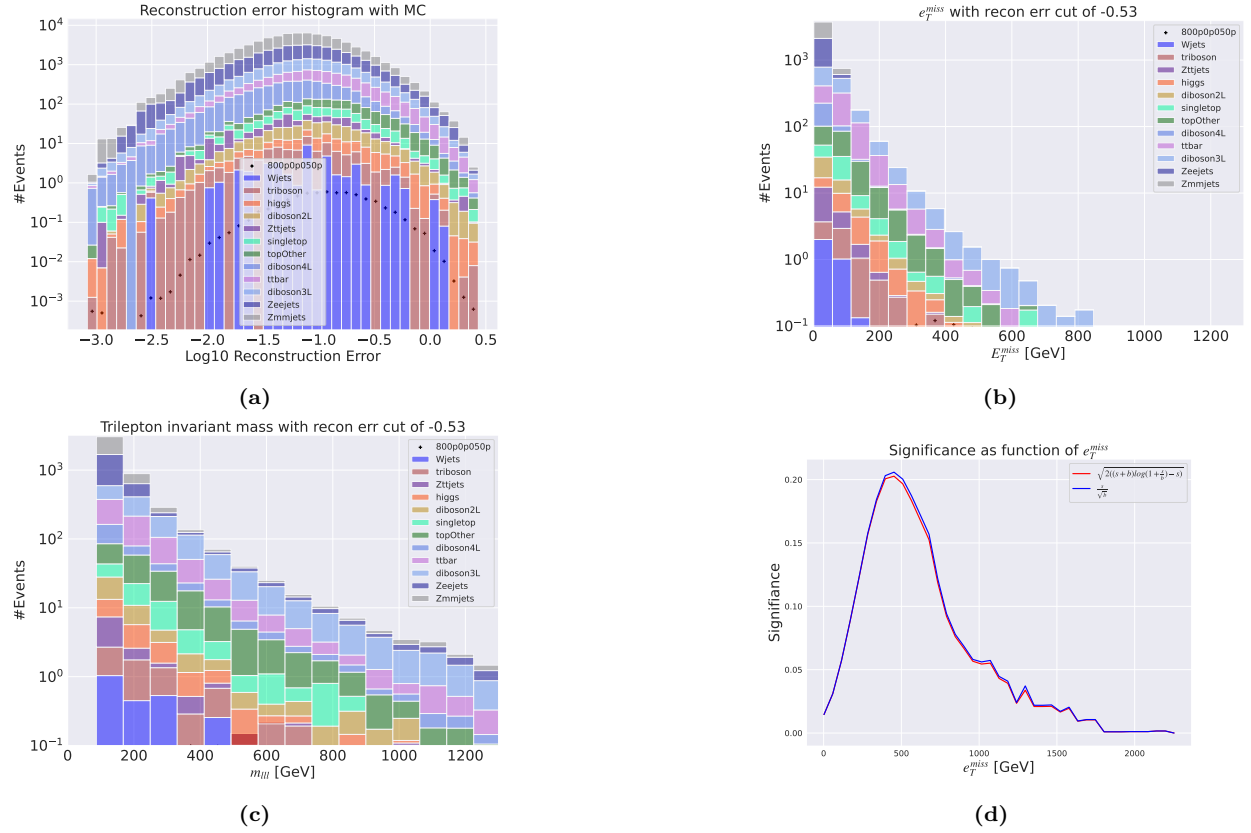


**Figure 29:** Reconstruction error,  $e_T^{\text{miss}}$  signal region,  $m_{lll}$  signal region and significance as function of  $e_T^{\text{miss}}$  for the deep variational autoencoder. Here the SUSY 450p300 model is used. Figure 29a shows the reconstruction error distribution for the SM MC and the SUSY signal. Here the autoencoder produce a bell-shape for background and signal with little distinction. The peaks of the two distributions are not separated in reconstruction error. Figure 29b shows the  $e_T^{\text{miss}}$  distribution for the SM MC and the SUSY signal in the signal region. The signal region is made using a cut around  $10^{-0.53}$ . Some background is removed, and the peaks of the SM MC and signal distributions are separated. Figure 29c shows the  $m_{lll}$  distribution for the SM MC and the SUSY signal. The shape of both distributions are displaying almost the same shape. Figure 29d shows the significance as function of  $e_T^{\text{miss}}$ . The peak is put around a cut of about 480 GeV in the  $e_T^{\text{miss}}$ , with a significance of around 0.21.

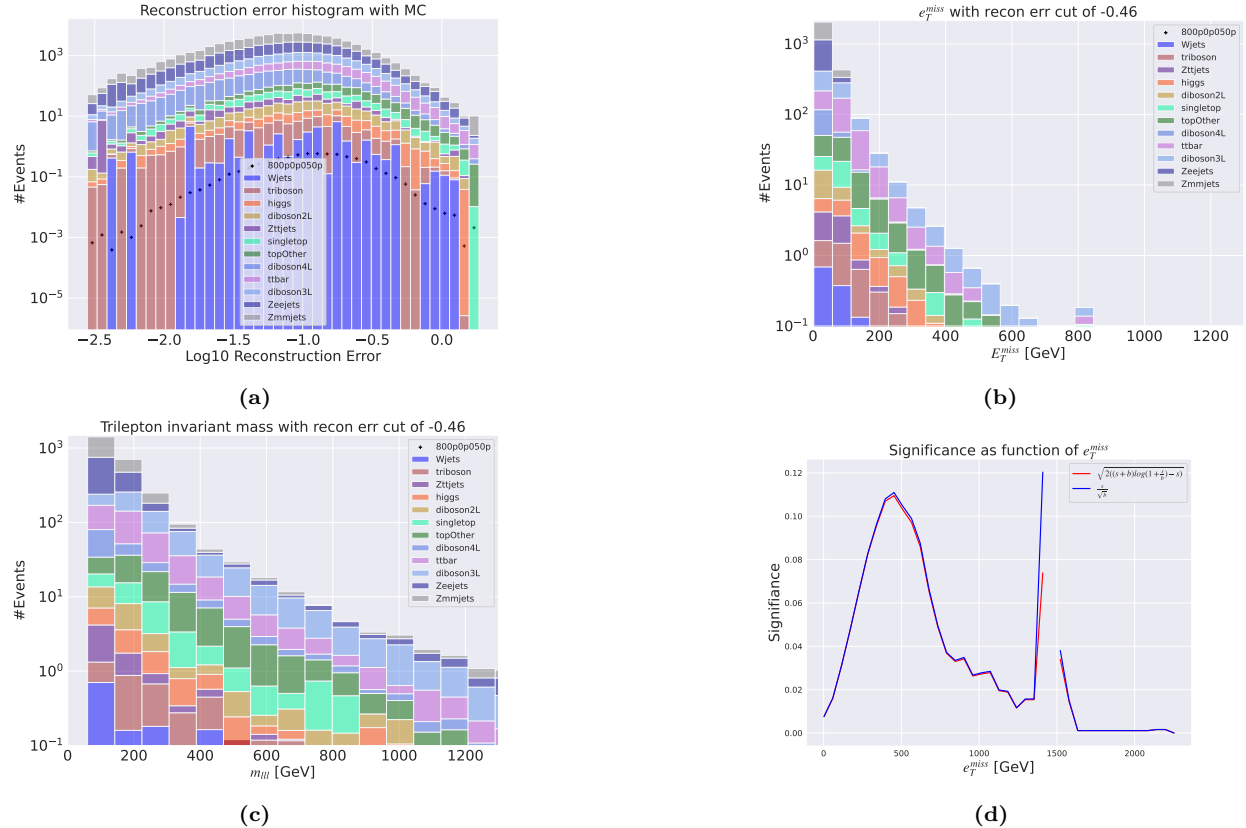


**Figure 30:** Reconstruction error,  $e_T^{miss}$  signal region,  $m_{ll}$  signal region and significance as function of  $e_T^{miss}$  for the shallow variational autoencoder. Here the SUSY 450p300 model is used. Figure 30a shows the reconstruction error distribution for the SM MC and the SUSY signal. Here the autoencoder produce a bell-shape for background and signal with little distinction. The peaks of the two distributions are not separated in reconstruction error. Figure 30b shows the  $e_T^{miss}$  distribution for the SM MC and the SUSY signal in the signal region. The signal region is made using a cut around  $10^{-0.46}$ . Some background is removed, and the peaks of the SM MC and signal distributions are separated. Figure 30c shows the  $m_{ll}$  distribution for the SM MC and the SUSY signal. The shape of both distributions are displaying almost the same shape. Figure 30d shows the significance as function of  $e_T^{miss}$ . The peak is put around a cut of about 480 GeV in the  $e_T^{miss}$ , with a significance of around 0.11.

#### A.4 Reconstruction error cuts for 2 leptons + $e_T^{miss}$

In this section the remaining two reconstruction error cuts in the 2 lepton +  $e_T^{miss}$  are shown. The figures here are shaped with the same subfigure structure as the figures in the results and discussion section.

## Regular autoencoder output

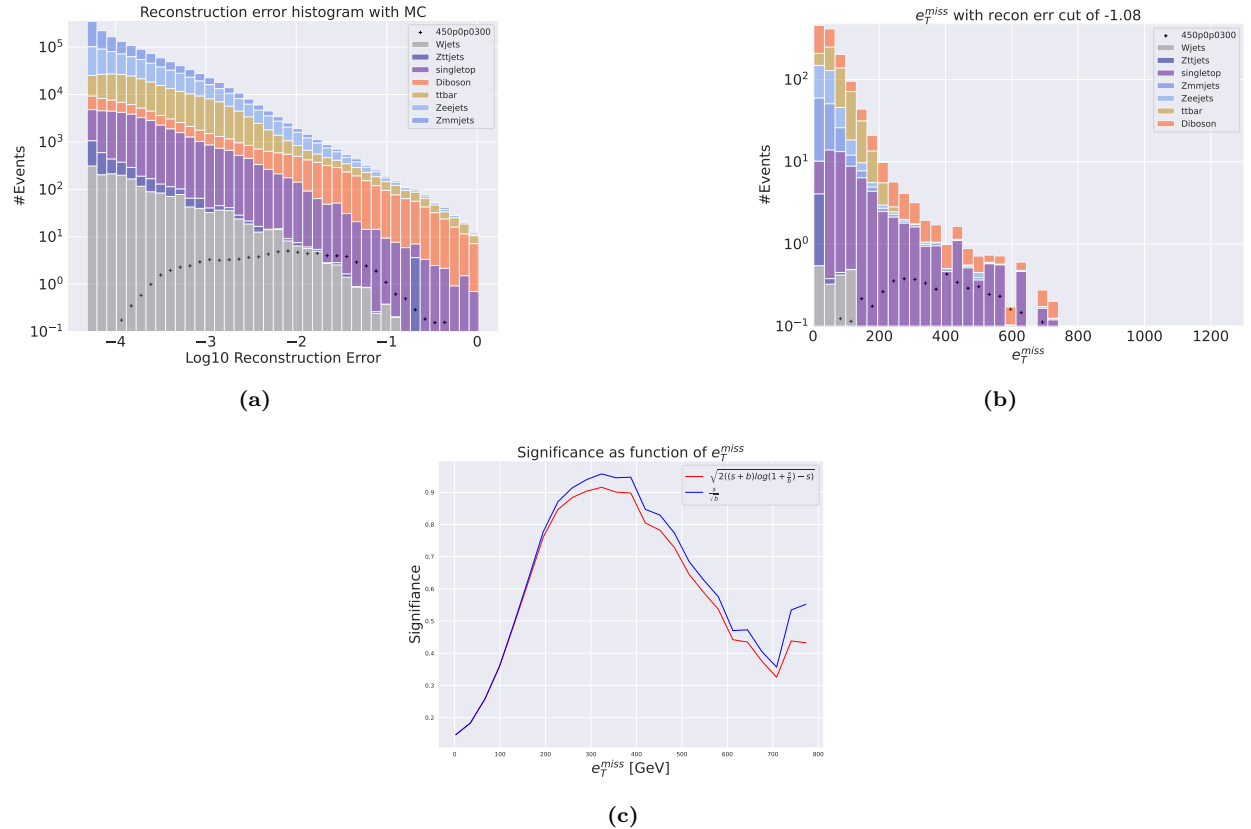


**Figure 31:** Reconstruction error (a),  $e_T^{\text{miss}}$  signal region (b) and significance as function of  $e_T^{\text{miss}}$  (c) for the deep regular autoencoder using SUSY 450p300. (a) shows the reconstruction error distribution for the SM MC and the SUSY signal. The autoencoder produces a slope like shape that is highly shifted to the lower end of the reconstruction error range for the background. The signal is more evenly spread out along the x-axis. The peaks of the two distributions are totally separated with two orders of magnitude in reconstruction error. (b) shows the  $e_T^{\text{miss}}$  T distribution for the SM MC and the SUSY signal in the signal region. The signal region is made using a cut around  $10^{-1.08}$ . Most of the background is removed, and the peaks of the SM MC and signal distributions are somewhat separated. (c) shows the significance as function of  $e_T^{\text{miss}}$ . The peak is put around a cut of about 340 GeV in the  $e_T^{\text{miss}}$ , with a significance of around 0.95.

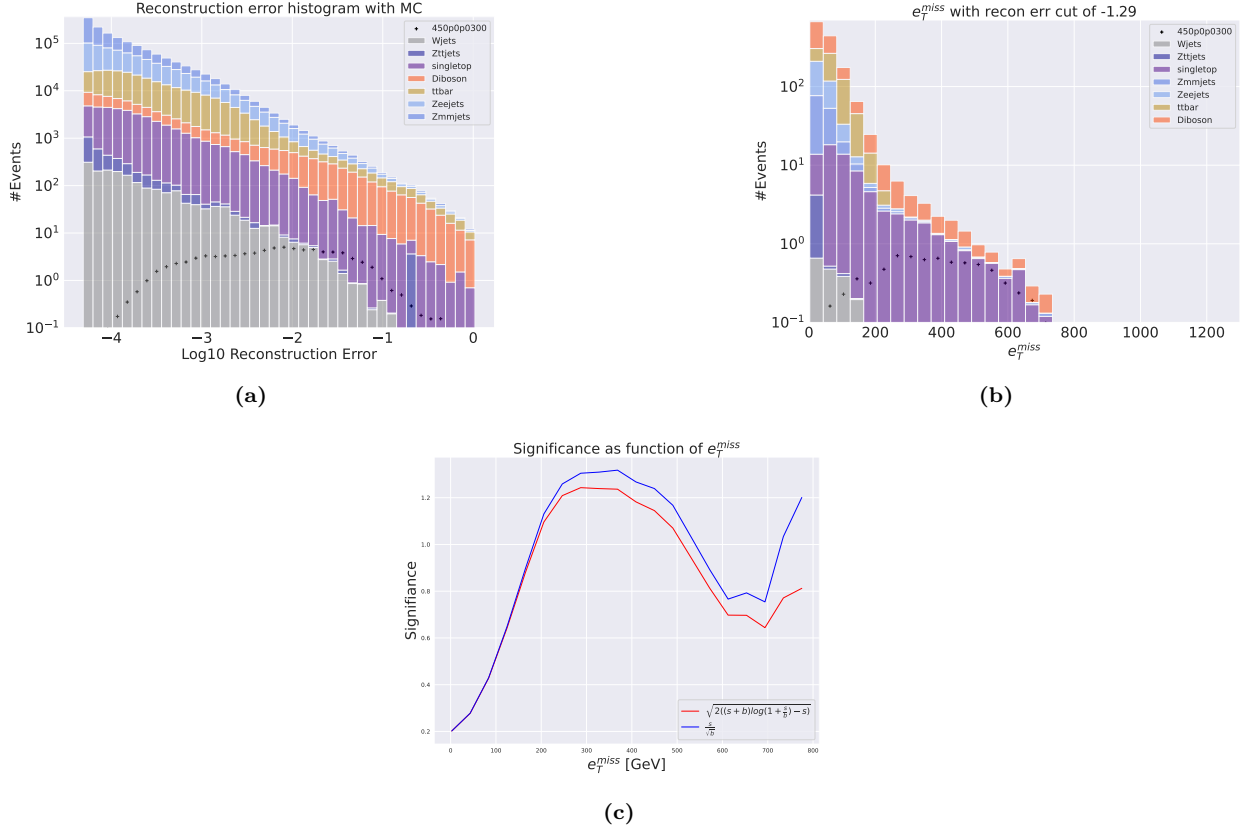


**Figure 32:** Reconstruction error (a),  $e_T^{miss}$  signal region (b) and significance as function of  $e_T^{miss}$  (c) for the deep regular autoencoder using SUSY 450p300. (a) shows the reconstruction error distribution for the SM MC and the SUSY signal. The autoencoder produces A slope like shape that is highly shifted to the lower end of the reconstruction error range for the background. The signal is more evenly spread out along the x-axis. The peaks of the two distributions are totally separated with two orders of magnitude in reconstruction error. (b) shows the  $e_T^{miss}$  T distribution for the SM MC and the SUSY signal in the signal region. The signal region is made using a cut around  $10^{-1.29}$ . Most of the background is removed, and the peaks of the SM MC and signal distributions are somewhat separated. (c) shows the significance as function of  $e_T^{miss}$ . The peak is put around a cut of about 380 GeV in the  $e_T^{miss}$ , with a significance of around 1.3.

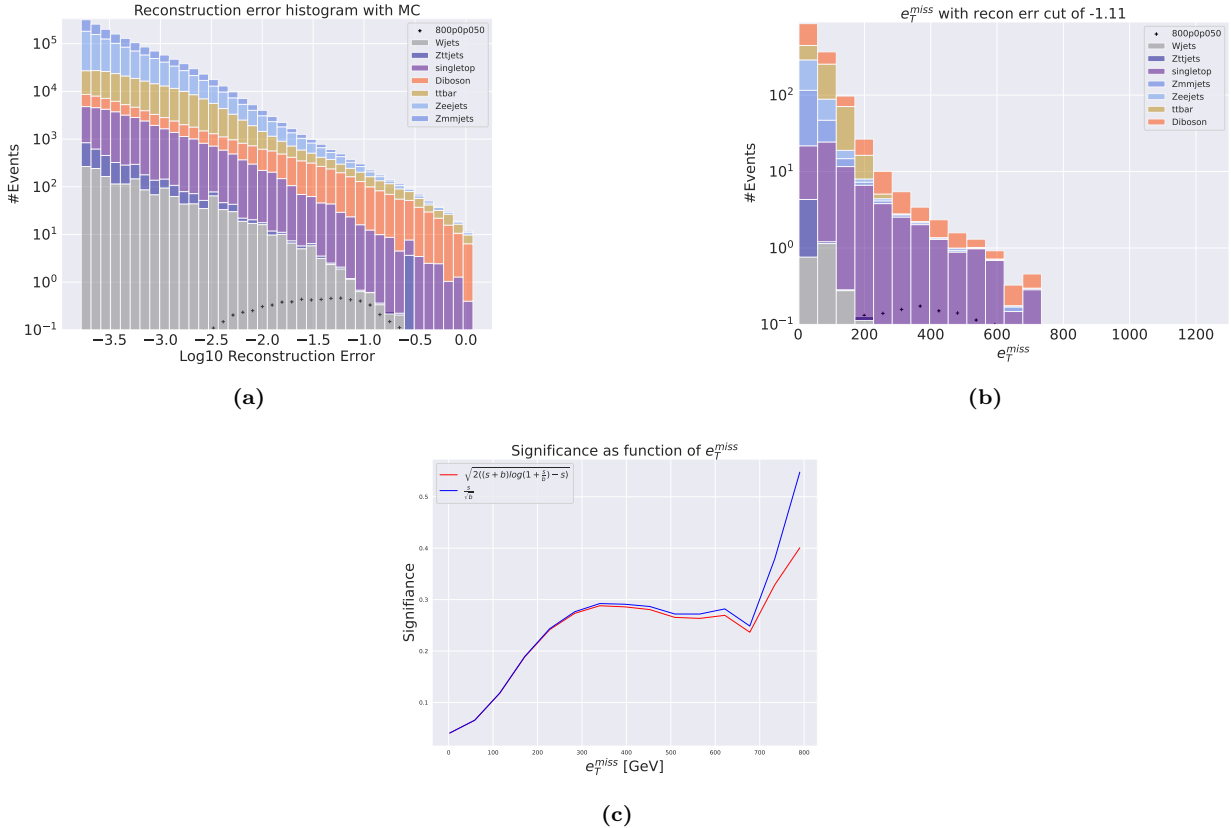


**Figure 33:** Reconstruction error (a),  $e_T^{\text{miss}}$  signal region (b) and significance as function of  $e_T^{\text{miss}}$  (c) for the deep regular autoencoder using SUSY 800p50. (a) shows the reconstruction error distribution for the SM MC and the SUSY signal. The autoencoder produces a slope like shape that is highly shifted to the lower end of the reconstruction error range for the background. The signal is more evenly spread out along the x-axis. The peaks of the two distributions are totally separated with two orders of magnitude in reconstruction error. (b) shows the  $e_T^{\text{miss}}$  T distribution for the SM MC and the SUSY signal in the signal region. The signal region is made using a cut around  $10^{-1.11}$ . Most of the background is removed, and the peaks of the SM MC and signal distributions are somewhat separated. (c) shows the significance as function of  $e_T^{\text{miss}}$ . The peak is put around a cut of about 340 GeV in the  $e_T^{\text{miss}}$ , with a significance of around 0.29.

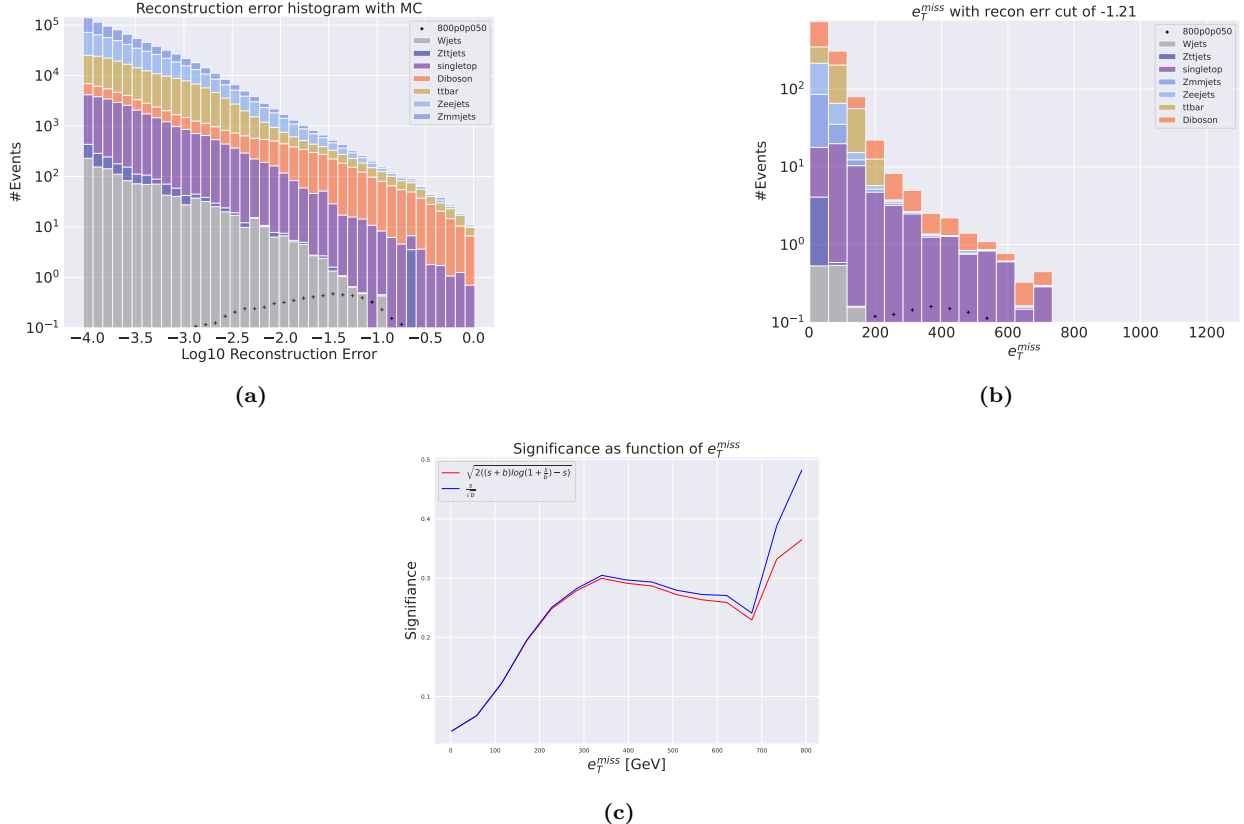


**Figure 34:** Reconstruction error (a),  $e_T^{miss}$  signal region (b) and significance as function of  $e_T^{miss}$  (c) for the deep regular autoencoder using SUSY 800p50. (a) shows the reconstruction error distribution for the SM MC and the SUSY signal. The autoencoder produces A slope like shape that is highly shifted to the lower end of the reconstruction error range for the background. The signal is more evenly spread out along the x-axis. The peaks of the two distributions are totally separated with two orders of magnitude in reconstruction error. (b) shows the  $e_T^{miss}$  T distribution for the SM MC and the SUSY signal in the signal region. The signal region is made using a cut around  $10^{-1.21}$ . Most of the background is removed, and the peaks of the SM MC and signal distributions are somewhat separated. (c) shows the significance as function of  $e_T^{miss}$ . The peak is put around a cut of about 340 GeV in the  $e_T^{miss}$ , with a significance of around 0.31.

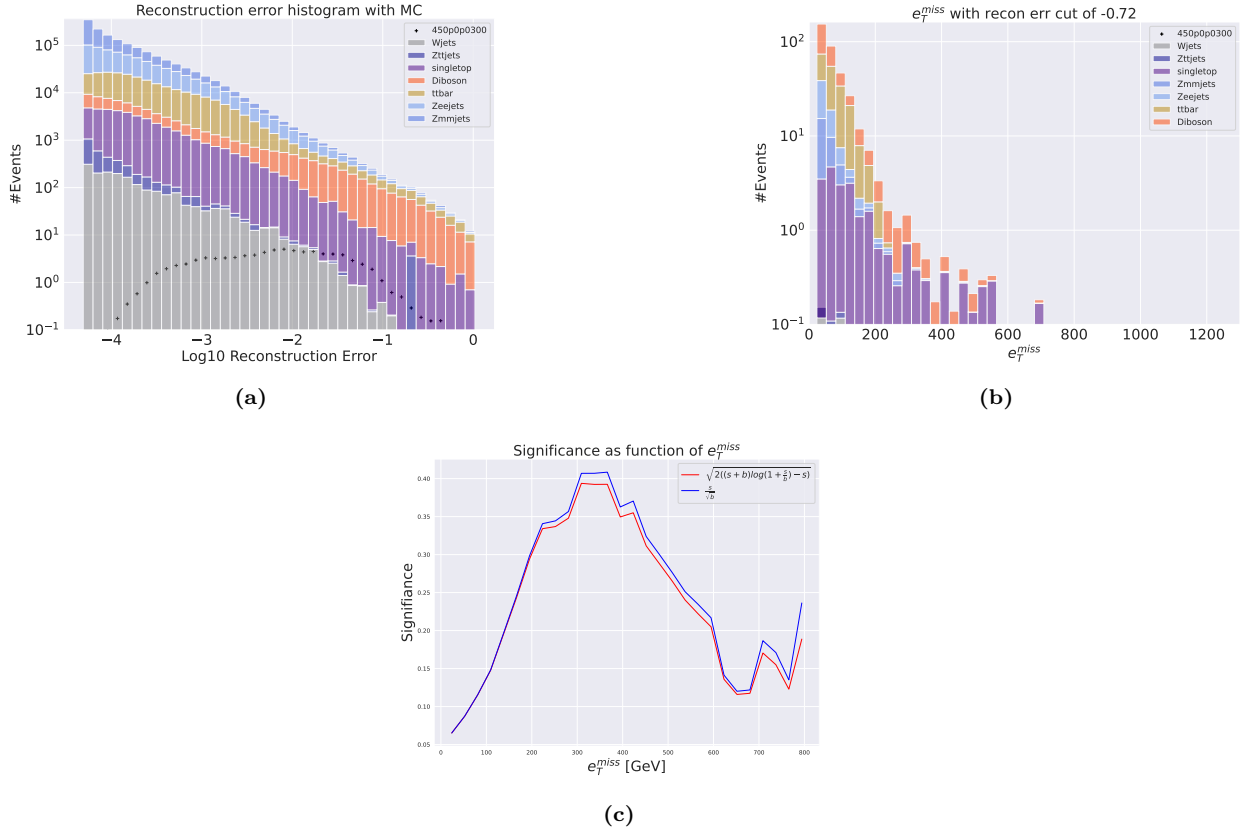


**Figure 35:** Reconstruction error (a),  $e_T^{miss}$  signal region (b) and significance as function of  $e_T^{miss}$  (c) for the deep regular autoencoder using SUSY 450p300. (a) shows the reconstruction error distribution for the SM MC and the SUSY signal. The autoencoder produces a slope like shape that is highly shifted to the lower end of the reconstruction error range for the background. The signal is more evenly spread out along the x-axis. The peaks of the two distributions are totally separated with two orders of magnitude in reconstruction error. (b) shows the  $e_T^{miss}$  T distribution for the SM MC and the SUSY signal in the signal region. The signal region is made using a cut around  $10^{-0.72}$ . Most of the background is removed, and the peaks of the SM MC and signal distributions are somewhat separated. (c) shows the significance as function of  $e_T^{miss}$ . The peak is put around a cut of about 380 GeV in the  $e_T^{miss}$ , with a significance of around 0.42.

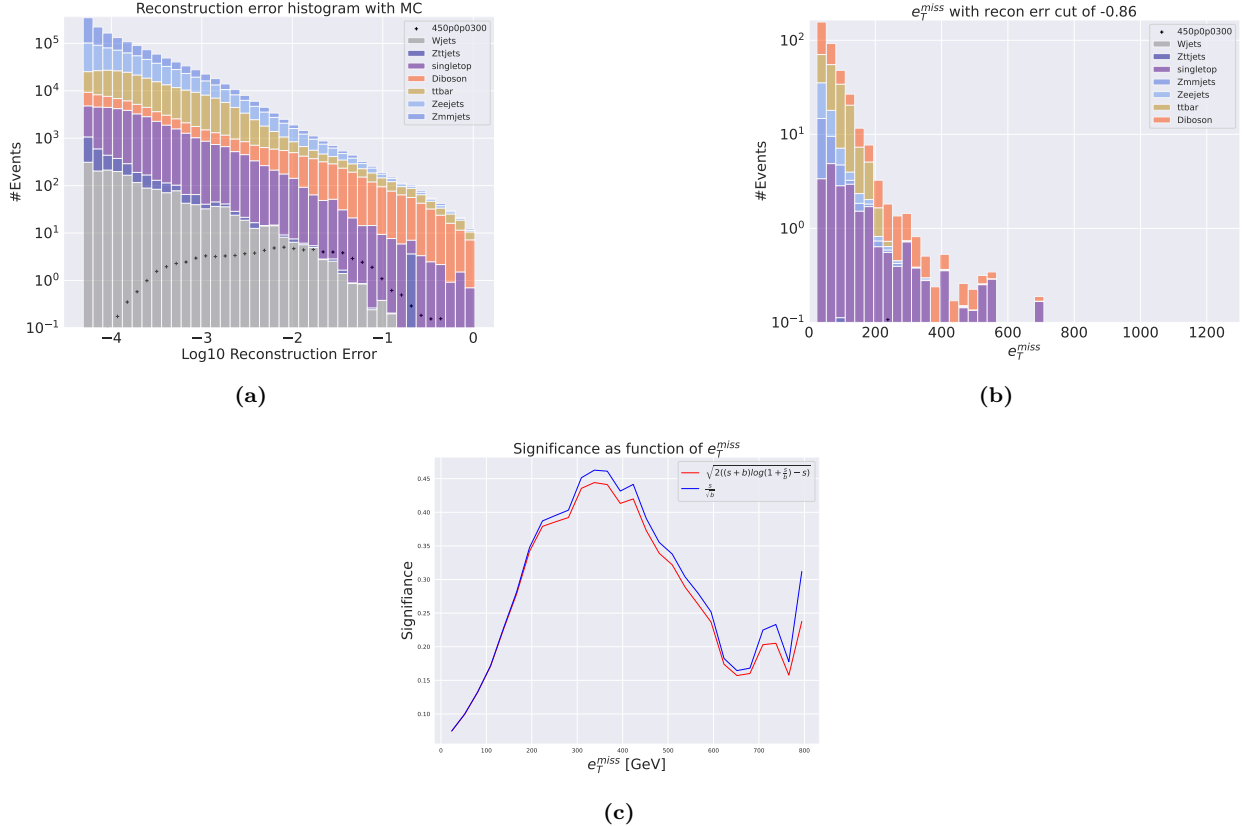


**Figure 36:** Reconstruction error (a),  $e_T^{miss}$  signal region (b) and significance as function of  $e_T^{miss}$  (c) for the deep regular autoencoder using SUSY 450p300. (a) shows the reconstruction error distribution for the SM MC and the SUSY signal. The autoencoder produces A slope like shape that is highly shifted to the lower end of the reconstruction error range for the background. The signal is more evenly spread out along the x-axis. The peaks of the two distributions are totally separated with two orders of magnitude in reconstruction error. (b) shows the  $e_T^{miss}$  T distribution for the SM MC and the SUSY signal in the signal region. The signal region is made using a cut around  $10^{-0.86}$ . Most of the background is removed, and the peaks of the SM MC and signal distributions are somewhat separated. (c) shows the significance as function of  $e_T^{miss}$ . The peak is put around a cut of about 350 GeV in the  $e_T^{miss}$ , with a significance of around 0.47.

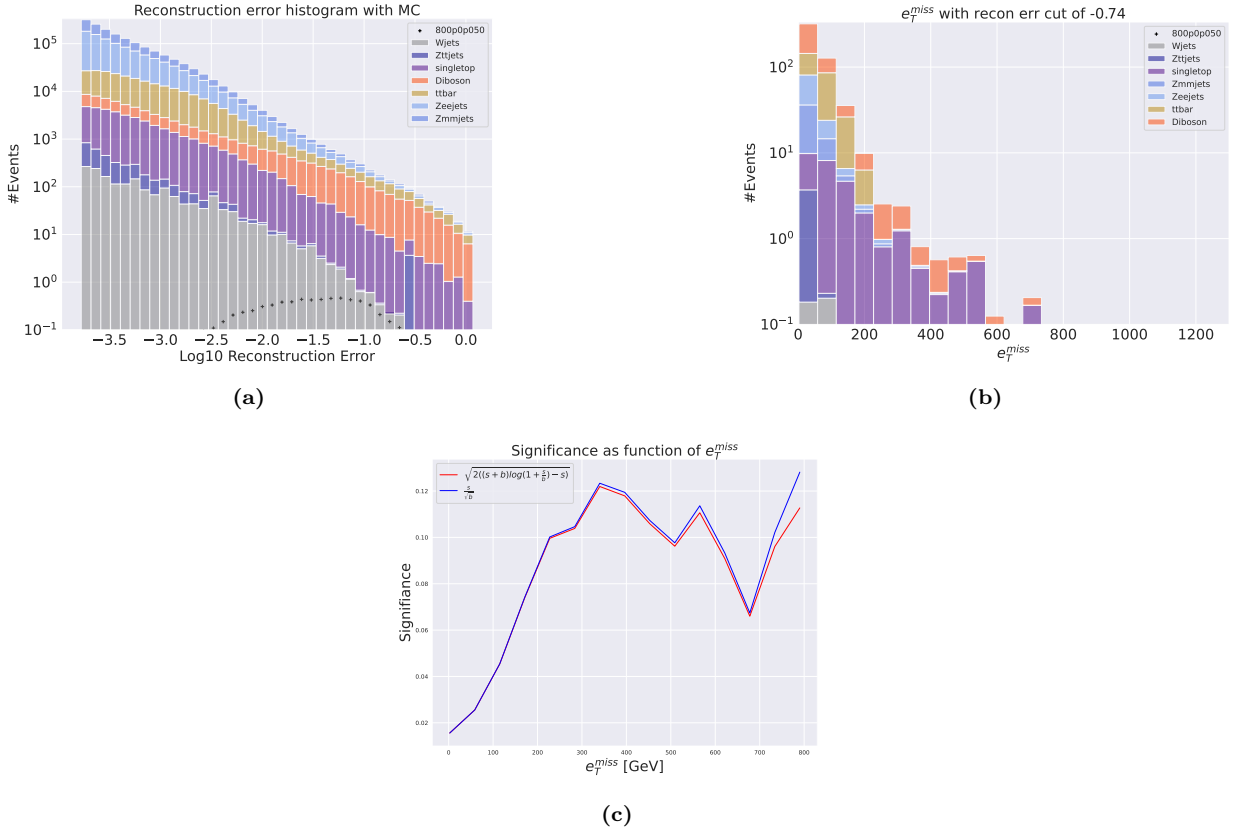


**Figure 37:** Reconstruction error (a),  $e_T^{\text{miss}}$  signal region (b) and significance as function of  $e_T^{\text{miss}}$  (c) for the deep regular autoencoder using SUSY 800p50. (a) shows the reconstruction error distribution for the SM MC and the SUSY signal. The autoencoder produces a slope like shape that is highly shifted to the lower end of the reconstruction error range for the background. The signal is more evenly spread out along the x-axis. The peaks of the two distributions are totally separated with two orders of magnitude in reconstruction error. (b) shows the  $e_T^{\text{miss}}$  T distribution for the SM MC and the SUSY signal in the signal region. The signal region is made using a cut around  $10^{-0.74}$ . Most of the background is removed, and the peaks of the SM MC and signal distributions are somewhat separated. (c) shows the significance as function of  $e_T^{\text{miss}}$ . The peak is put around a cut of about 340 GeV in the  $e_T^{\text{miss}}$ , with a significance of around 0.125.

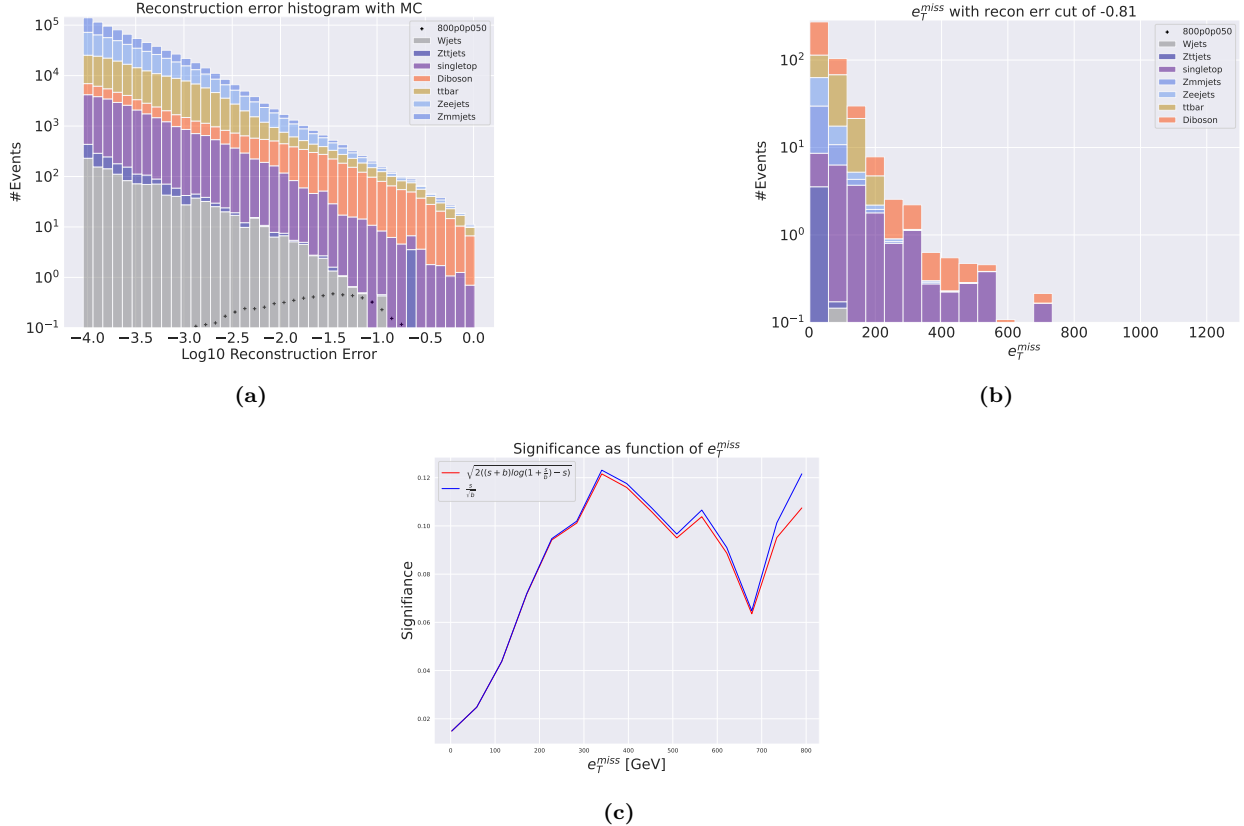


**Figure 38:** Reconstruction error (a),  $e_T^{miss}$  signal region (b) and significance as function of  $e_T^{miss}$  (c) for the deep regular autoencoder using SUSY 800p50. (a) shows the reconstruction error distribution for the SM MC and the SUSY signal. The autoencoder produces A slope like shape that is highly shifted to the lower end of the reconstruction error range for the background. The signal is more evenly spread out along the x-axis. The peaks of the two distributions are totally separated with two orders of magnitude in reconstruction error. (b) shows the  $e_T^{miss}$  T distribution for the SM MC and the SUSY signal in the signal region. The signal region is made using a cut around  $10^{-0.81}$ . Most of the background is removed, and the peaks of the SM MC and signal distributions are somewhat separated. (c) shows the significance as function of  $e_T^{miss}$ . The peak is put around a cut of about 340 GeV in the  $e_T^{miss}$ , with a significance of around 0.125.

## Variational autoencoder output

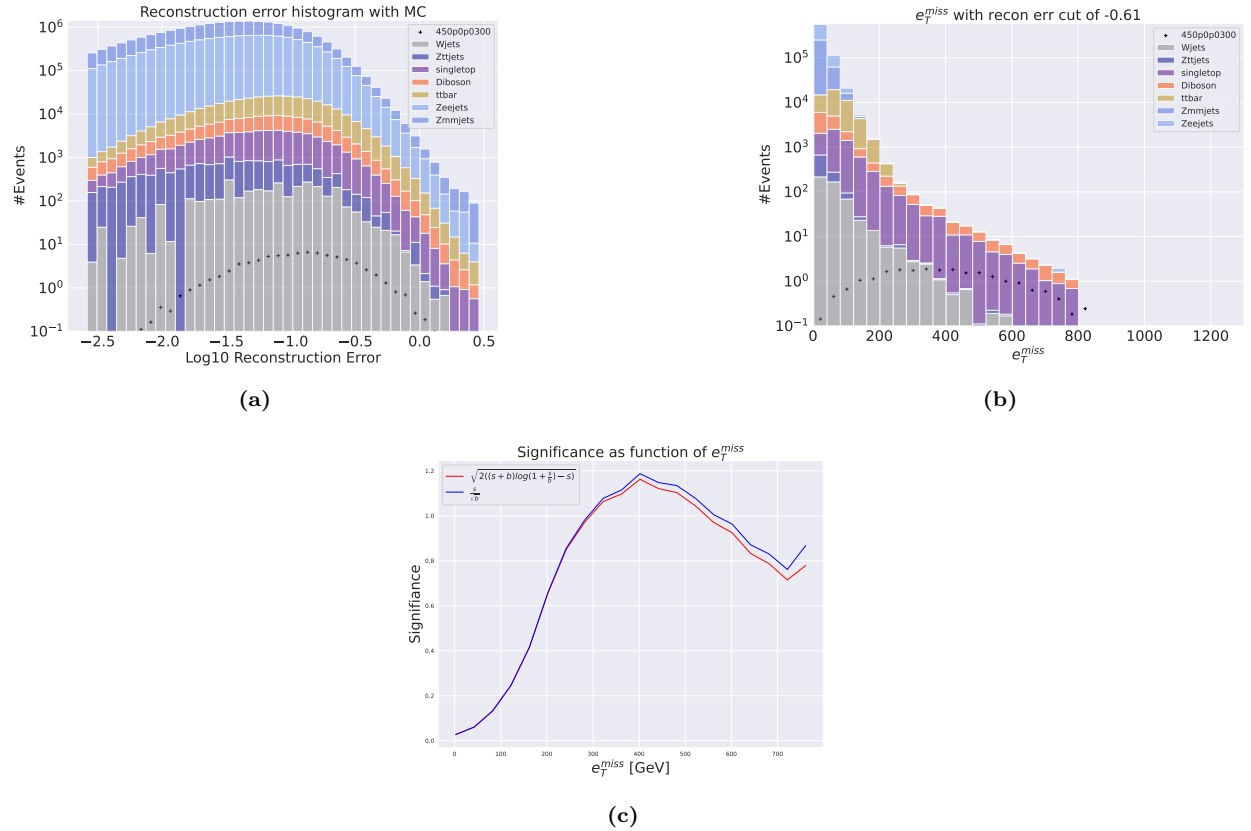


**Figure 39:** Reconstruction error (a),  $e_T^{miss}$  signal region (b) and significance as function of  $e_T^{miss}$  (c) for the deep regular autoencoder using SUSY 450p300. (a) shows that the peak of the distribution is somewhat centered in the middle of the reconstruction error range forming a bell-like shape. The peaks of the background and signal distributions are not well separated, with almost identical reconstruction error pattern. (b) shows a signal region with large background distribution. The signal region is made using a cut around  $10^{-0.81}$ . The peaks in the signal region are also somewhat separated, but the overall distributions are overlapping still. (c) shows the significance as function of  $e_T^{miss}$ . The peak significance is around 1.2 at around 400 GeV.

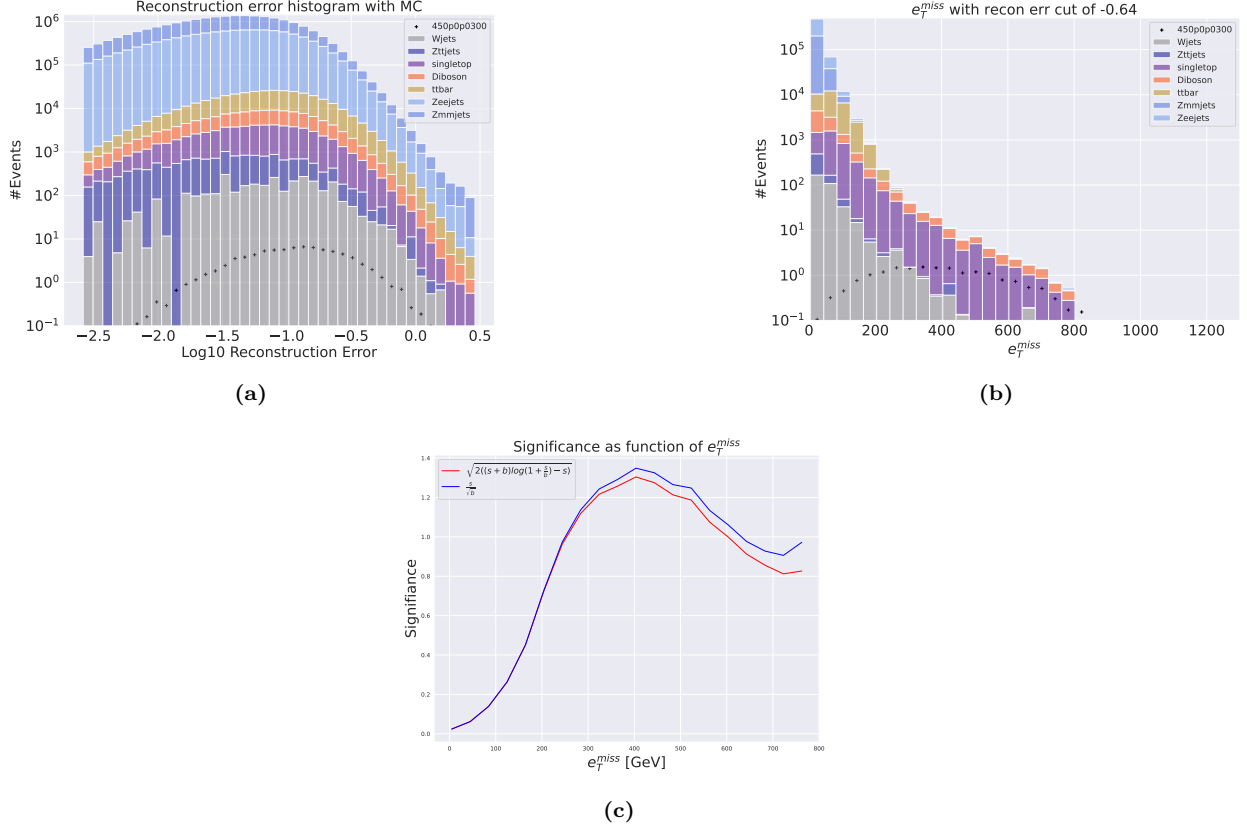


**Figure 40:** Reconstruction error (a),  $e_T^{miss}$  signal region (b) and significance as function of  $e_T^{miss}$  (c) for the deep regular autoencoder using SUSY 450p300. (a) shows that the peak of the distribution is somewhat centered in the middle of the reconstruction error range forming a bell-like shape. The peaks of the background and signal distributions are not well separated, with almost identical reconstruction error pattern. (b) shows a signal region with large background distribution. The signal region is made using a cut around  $10^{-0.61}$ . The peaks in the signal region are also somewhat separated, but the overall distributions are overlapping still. (c) shows the significance as function of  $e_T^{miss}$ . The peak significance is around 1.31 at around 400 GeV.

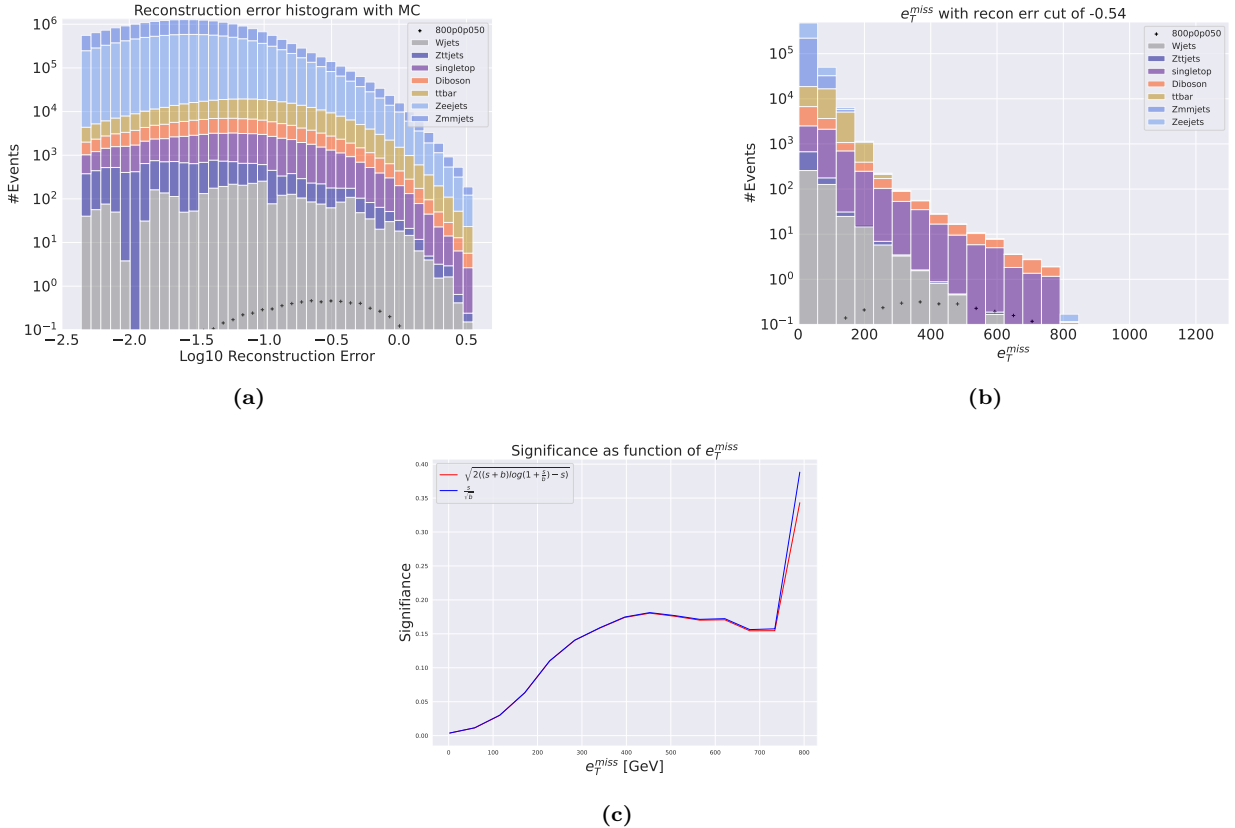


**Figure 41:** Reconstruction error (a),  $e_T^{miss}$  signal region (b) and significance as function of  $e_T^{miss}$  (c) for the deep regular autoencoder using SUSY 800p50. (a) shows that the peak of the distribution is somewhat centered in the middle of the reconstruction error range forming a bell-like shape. The peaks of the background and signal distributions are not well separated, with almost identical reconstruction error pattern. (b) shows a signal region with large background distribution. The signal region is made using a cut around  $10^{-0.64}$ . The peaks in the signal region are also somewhat separated, but the overall distributions are overlapping still. (c) shows the significance as function of  $e_T^{miss}$ . The peak significance is around 1.35 at around 400 GeV.

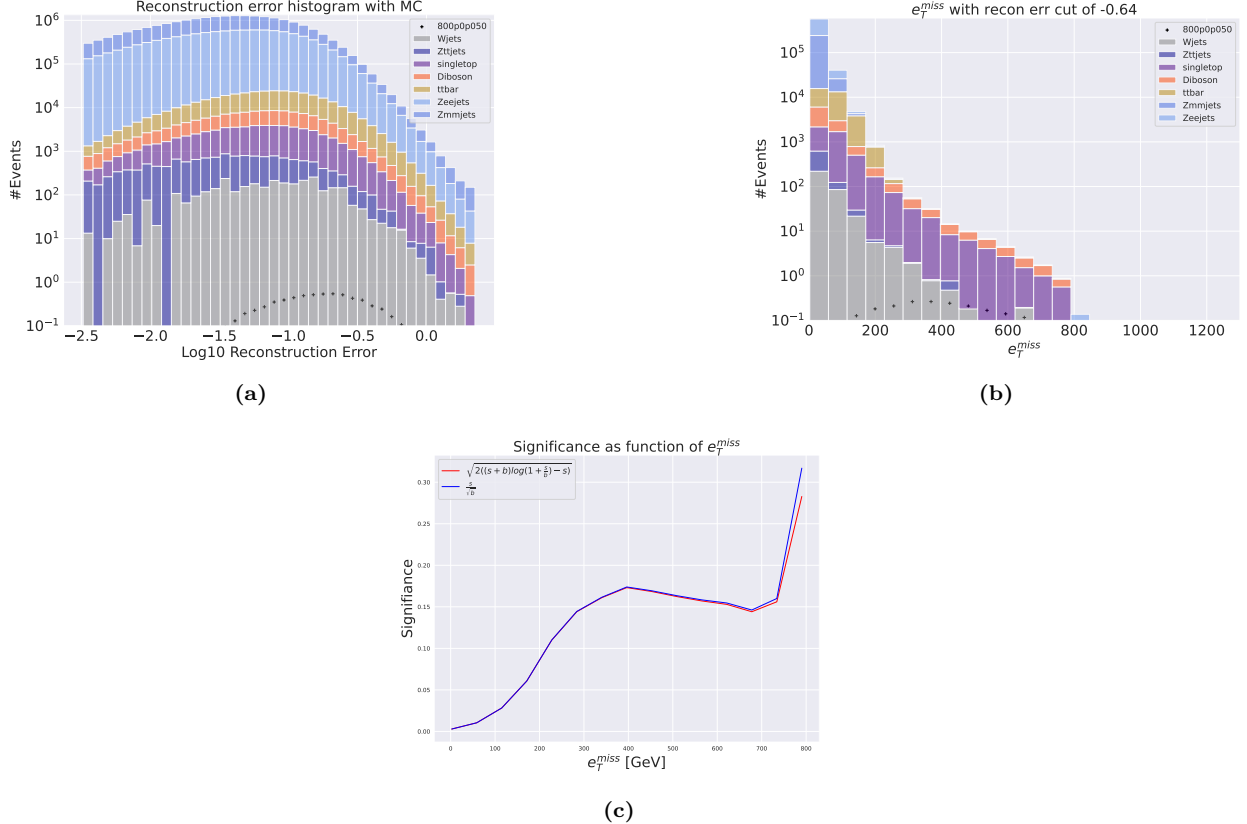


**Figure 42:** Reconstruction error (a),  $e_T^{miss}$  signal region (b) and significance as function of  $e_T^{miss}$  (c) for the deep regular autoencoder using SUSY 800p50. (a) shows that the peak of the distribution is somewhat centered in the middle of the reconstruction error range forming a bell-like shape. The peaks of the background and signal distributions are not well separated, with almost identical reconstruction error pattern. (b) shows a signal region with large background distribution. The signal region is made using a cut around  $10^{-0.54}$ . The peaks in the signal region are also somewhat separated, but the overall distributions are overlapping still. (c) shows the significance as function of  $e_T^{miss}$ . The peak significance is around 0.17 at around 450 GeV.

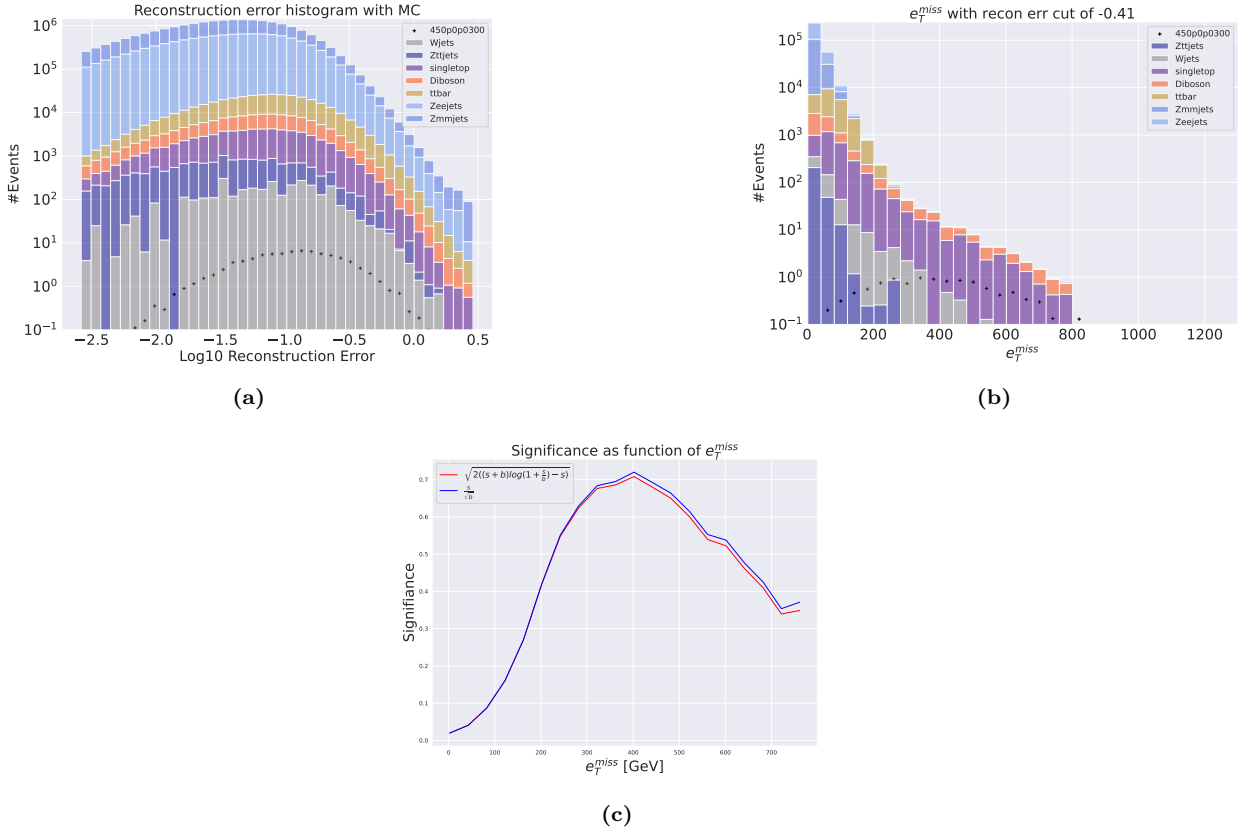


**Figure 43:** Reconstruction error (a),  $e_T^{miss}$  signal region (b) and significance as function of  $e_T^{miss}$  (c) for the deep regular autoencoder using SUSY 450p300. (a) shows that the peak of the distribution is somewhat centered in the middle of the reconstruction error range forming a bell-like shape. The peaks of the background and signal distributions are not well separated, with almost identical reconstruction error pattern. (b) shows a signal region with large background distribution. The signal region is made using a cut around  $10^{-0.41}$ . The peaks in the signal region are also somewhat separated, but the overall distributions are overlapping still. (c) shows the significance as function of  $e_T^{miss}$ . The peak significance is around 0.71 at around 400 GeV.

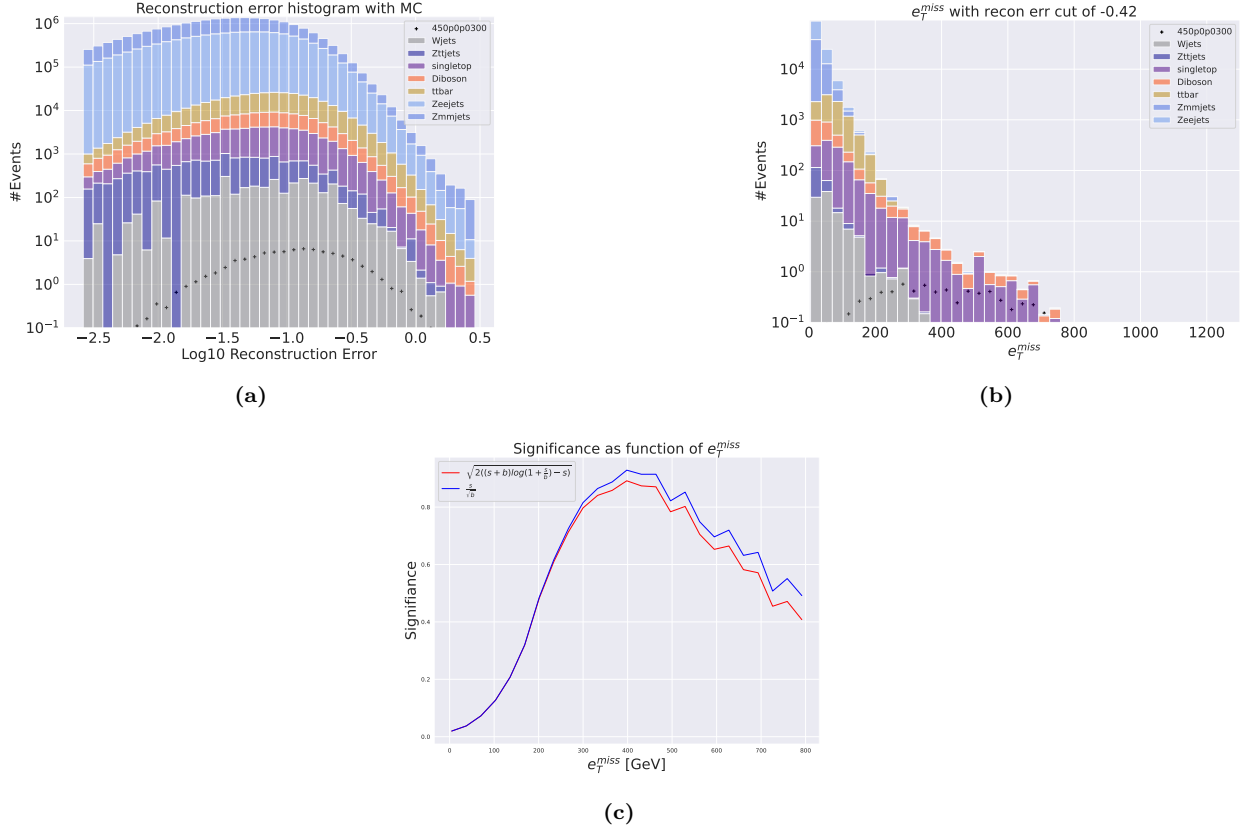


**Figure 44:** Reconstruction error (a),  $e_T^{miss}$  signal region (b) and significance as function of  $e_T^{miss}$  (c) for the deep regular autoencoder using SUSY 450p300. (a) shows that the peak of the distribution is somewhat centered in the middle of the reconstruction error range forming a bell-like shape. The peaks of the background and signal distributions are not well separated, with almost identical reconstruction error pattern. (b) shows a signal region with large background distribution. The signal region is made using a cut around  $10^{-0.42}$ . The peaks in the signal region are also somewhat separated, but the overall distributions are overlapping still. (c) shows the significance as function of  $e_T^{miss}$ . The peak significance is around 0.92 at around 400 GeV.

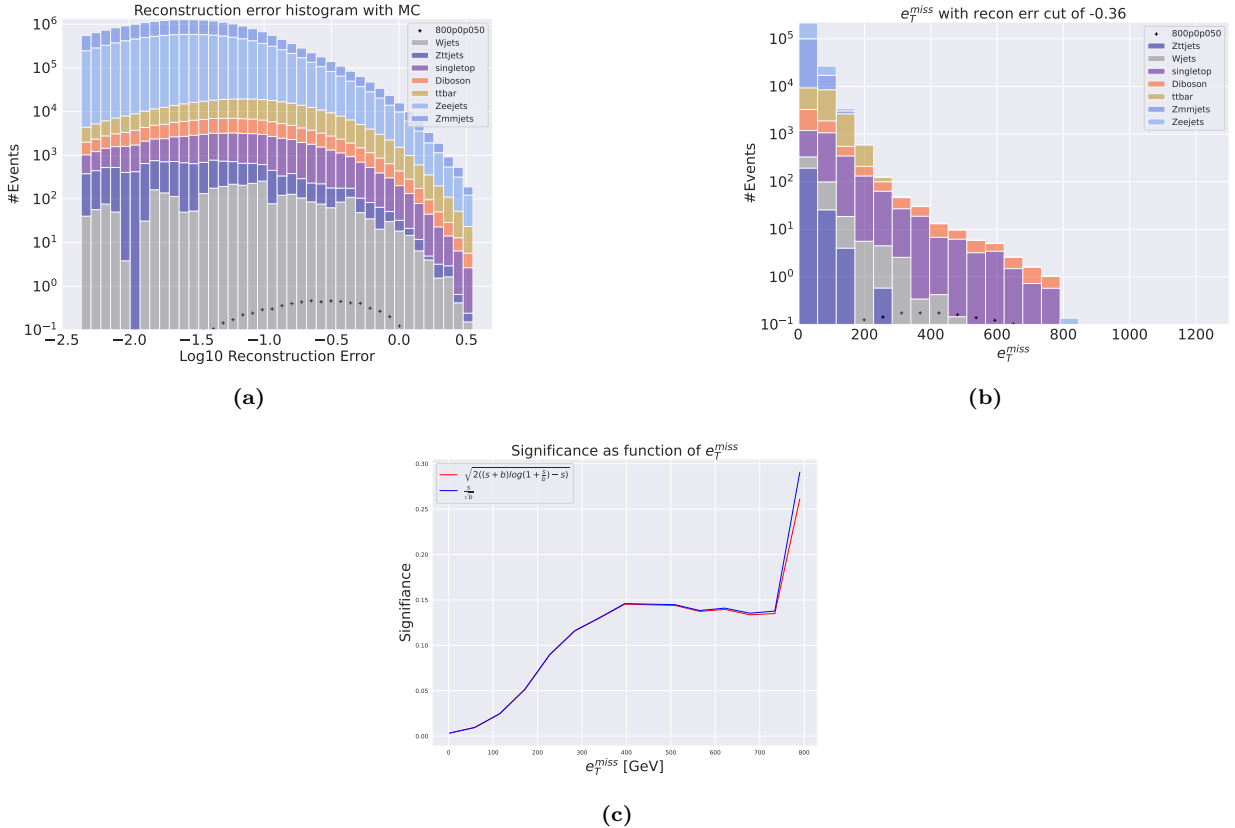


**Figure 45:** Reconstruction error (a),  $e_T^{miss}$  signal region (b) and significance as function of  $e_T^{miss}$  (c) for the deep regular autoencoder using SUSY 800p50. (a) shows that the peak of the distribution is somewhat centered in the middle of the reconstruction error range forming a bell-like shape. The peaks of the background and signal distributions are not well separated, with almost identical reconstruction error pattern. (b) shows a signal region with large background distribution. The signal region is made using a cut around  $10^{-0.36}$ . The peaks in the signal region are also somewhat separated, but the overall distributions are overlapping still. (c) shows the significance as function of  $e_T^{miss}$ . The peak significance is around 0.148 at around 400 GeV.

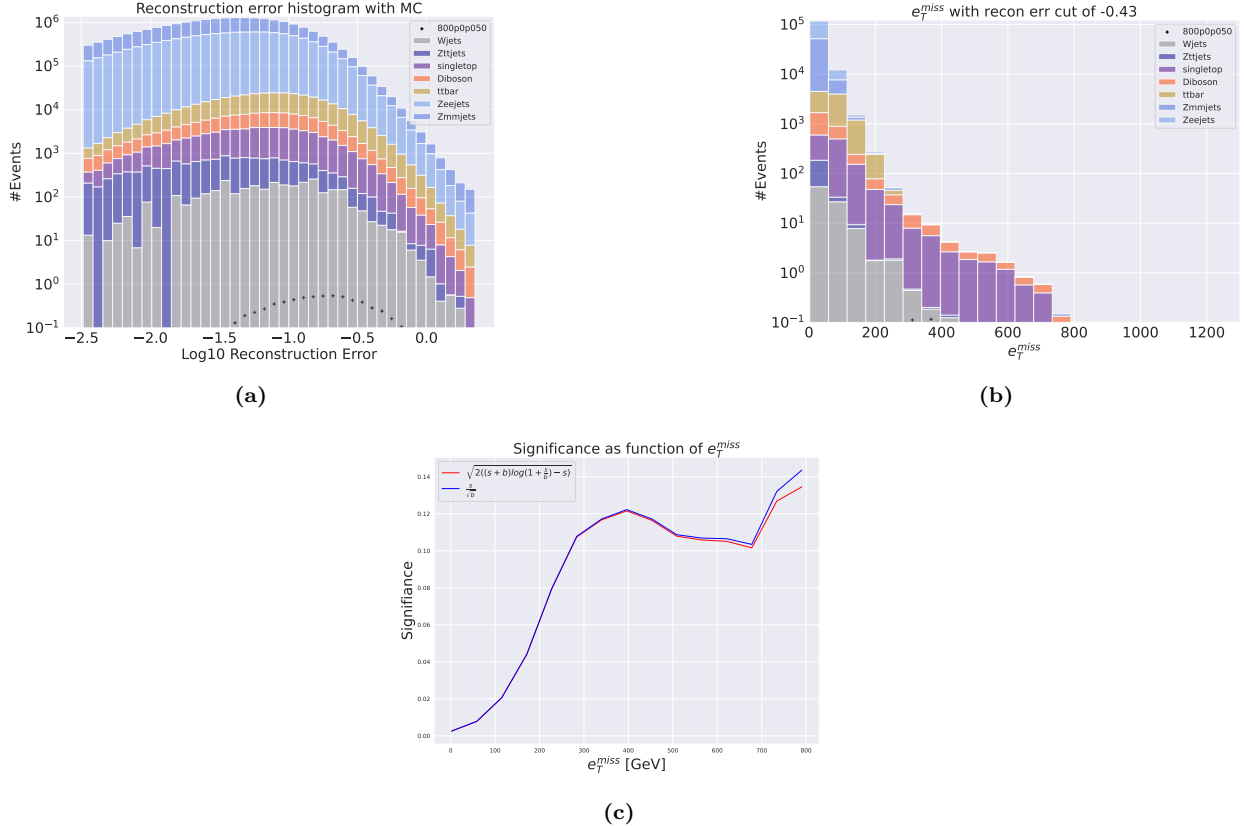


**Figure 46:** Reconstruction error (a),  $e_T^{miss}$  signal region (b) and significance as function of  $e_T^{miss}$  (c) for the deep regular autoencoder using SUSY 800p50. (a) shows that the peak of the distribution is somewhat centered in the middle of the reconstruction error range forming a bell-like shape. The peaks of the background and signal distributions are not well separated, with almost identical reconstruction error pattern. (b) shows a signal region with large background distribution. The signal region is made using a cut around  $10^{-0.43}$ . The peaks in the signal region are also somewhat separated, but the overall distributions are overlapping still. (c) shows the significance as function of  $e_T^{miss}$ . The peak significance is around 0.123 at around 400 GeV.



# Appendix B

## B.1 Algorithmic implementation

The RMM as a set of features were a bit tricky to implement, and one way to implement it was to use a dictionary containing the names of features already in the RDataFrame set. RDataFrame allows for custom c++ functions to be run on the entire dataframe, and because almost all the features in the RMM use the kinematical variables for each particle they were needed to be accessed. Each element in the dictionary contains a number ID corresponding to the column it belongs to, a name, the 4 kinematic variables  $pt$ ,  $\eta$ ,  $\phi$  and  $E$ , and the rank within its particle type. Thus,  $ele_0$  is the first electron, and its rank is 0.

```

1 rmm_structure = {
2     1: ["ljet_0", "jetPt[ljet]", "jetEta[ljet]", "jetPhi[ljet]", "jetM[ljet]", 0,],
3     2: [ "ljet_1", "jetPt[ljet]", "jetEta[ljet]", "jetPhi[ljet]", "jetM[ljet]", 1,],
4     3: [ "ljet_2", "jetPt[ljet]", "jetEta[ljet]", "jetPhi[ljet]", "jetM[ljet]", 2,],
5     4: [ "ljet_3", "jetPt[ljet]", "jetEta[ljet]", "jetPhi[ljet]", "jetM[ljet]", 3,],
6     5: [ "ljet_4", "jetPt[ljet]", "jetEta[ljet]", "jetPhi[ljet]", "jetM[ljet]", 4,],
7     6: [ "ljet_5", "jetPt[ljet]", "jetEta[ljet]", "jetPhi[ljet]", "jetM[ljet]", 5,],
8     7: [ "bjet_0", "jetPt[bjet77]", "jetEta[bjet77]", "jetPhi[bjet77]", "jetM[bjet77]", 0,],
9     8: [ "bjet_1", "jetPt[bjet77]", "jetEta[bjet77]", "jetPhi[bjet77]", "jetM[bjet77]", 1,],
10    9: [ "bjet_2", "jetPt[bjet77]", "jetEta[bjet77]", "jetPhi[bjet77]", "jetM[bjet77]", 2,],
11   10: [ "bjet_3", "jetPt[bjet77]", "jetEta[bjet77]", "jetPhi[bjet77]", "jetM[bjet77]", 3,],
12   11: [ "bjet_4", "jetPt[bjet77]", "jetEta[bjet77]", "jetPhi[bjet77]", "jetM[bjet77]", 4,],
13   12: [ "bjet_5", "jetPt[bjet77]", "jetEta[bjet77]", "jetPhi[bjet77]", "jetM[bjet77]", 5,],
14   13: [ "ele_0", "lepPt[ele_SG]", "lepEta[ele_SG]", "lepPhi[ele_SG]", "lepM[ele_SG]", 0,],
15   14: [ "ele_1", "lepPt[ele_SG]", "lepEta[ele_SG]", "lepPhi[ele_SG]", "lepM[ele_SG]", 1,],
16   15: [ "ele_2", "lepPt[ele_SG]", "lepEta[ele_SG]", "lepPhi[ele_SG]", "lepM[ele_SG]", 2,],
17   16: [ "ele_3", "lepPt[ele_SG]", "lepEta[ele_SG]", "lepPhi[ele_SG]", "lepM[ele_SG]", 3,],
18   17: [ "ele_4", "lepPt[ele_SG]", "lepEta[ele_SG]", "lepPhi[ele_SG]", "lepM[ele_SG]", 4,],
19   18: [ "muo_0", "lepPt[muo_SG]", "lepEta[muo_SG]", "lepPhi[muo_SG]", "lepM[muo_SG]", 0,],
20   19: [ "muo_1", "lepPt[muo_SG]", "lepEta[muo_SG]", "lepPhi[muo_SG]", "lepM[muo_SG]", 1,],
21   20: [ "muo_2", "lepPt[muo_SG]", "lepEta[muo_SG]", "lepPhi[muo_SG]", "lepM[muo_SG]", 2,],
22   21: [ "muo_3", "lepPt[muo_SG]", "lepEta[muo_SG]", "lepPhi[muo_SG]", "lepM[muo_SG]", 3,],
23   22: [ "muo_4", "lepPt[muo_SG]", "lepEta[muo_SG]", "lepPhi[muo_SG]", "lepM[muo_SG]", 4,],
24 }
```

The dictionary is then used in the nested for loop below. The loop is partitioned into several scenarios. Firstly, the first element in the matrix is the  $e_T^{miss}$ . Once that is set, the loop has three cases to check, the upper triangle, the lower triangle and the diagonal. The upper triangle is related to masses, and the lower triangle is related to longitudinal properties. Using this, the number ID helps ID which particle(s) to use and where to put the properties calculated based on them.

```

1 for row in range(N_row):
2     if row == 0:
3         # Calculate e_T^miss and m_T for all objects
4         for column in range(N_col):
5             if column == 0:
6                 # Set e_T_miss
7                 df[k] = df[k].Define("e_T_miss", "met_Et")
8             else:
9                 # Set m_T for all particles
10                name, pt, eta, phi, m, index = rmm_structure[column]
11                df[k] = df[k].Define(
12                    f"m_T_{name}", f"getM_T({pt},{eta},{phi},{m},{index})"
13                )
14
15     else:
16         # Calculate rest of matrix
17         for column in range(N_col):
18             if column == 0:
19                 # Set h_L for all particles
20                 name, pt, eta, phi, m, index = rmm_structure[row]
21
22                 df[k] = df[k].Define(
23                     f"h_L_{name}", f"geth_L({pt},{eta},{phi},{m},{index})"
24                 )
25             elif column == row:
26                 name, pt, eta, phi, m, index = rmm_structure[column]
27                 if index == 0:
28                     # If particle is the first of its type, calculate e_T of particle
29                     df[k] = df[k].Define(
30                         f"e_T_{name}", f"getET_part({pt},{m},{index})"
31                     )
32                 else:
33                     # If particle is not the first of its type, calculate the difference in e_T
34                     df[k] = df[k].Define(
35                         f"delta_e_t_{name}", f"delta_e_T({pt},{m},{index})"
36                     )
37
38             elif column > row:
39                 # For invariant mass
40                 # Particle 1
41                 name1, pt1, eta1, phi1, m1, index1 = rmm_structure[row]
42
43                 # Particle 2
44                 name2, pt2, eta2, phi2, m2, index2 = rmm_structure[column]
45
46                 histo_name = f"m_{name1}_{name2}"
47                 df[k] = df[k].Define(
48                     histo_name,
49                     f"getM({pt1},{eta1}, {phi1}, {m1}, {pt2}, {eta2}, {phi2}, {m2}, {index1}, {index2})",
50                 )
51             elif row > column:
52                 # For h longitudinal stuff
53                 # Particle 1
54                 name1, pt1, eta1, phi1, m1, index1 = rmm_structure[row]
55
56                 # Particle 2
57                 name2, pt2, eta2, phi2, m2, index2 = rmm_structure[column]
58
59                 histo_name = f"h_{name1}_{name2}"
60                 df[k] = df[k].Define(
61                     f"{histo_name}",
62                     f"geth({pt1},{eta1}, {phi1}, {m1}, {pt2}, {eta2}, {phi2}, {m2}, {index1}, {index2})",
63                 )

```